MONASH University

The progressive development of soil arching in geosynthetic reinforced piled embankments

Louis Evans King

Bachelor of Engineering (with Honours) in the field of Civil Engineering

A thesis submitted for the degree of Doctor of Philosophy at

Monash University in 2019

Department of Civil Engineering

Monash University, Clayton, Australia

Copyright notice

Abstract

Geosynthetic reinforced piled embankments (GRPEs) utilise soil arching and membrane actions to transfer embankment loads towards pile heads, and in turn, to a deeper founding stratum. These mechanisms reduce the stress acting on the soil directly beneath the embankment (the subsoil). When designing GRPEs, the most common approach is to assume that a single state of soil arching develops, which is independent of both subsoil and pile head settlement. In doing so, the resulting stresses that act on the geosynthetic reinforcement and subsoil are determined, which in turn allows individual elements of the GRPE to be suitably designed to withstand the imposed actions. However, it has been shown, both physically and numerically, that load transfer from soil arching and membrane actions progressively develops as subsoil undergoes consolidation. Furthermore, soil arching is dependent on whether differential settlement occurs between pile heads, which may develop when a pile exhibits a softer load-settlement response due to a defect.

In the present study, physical and numerical modelling was undertaken to gain further understanding into how soil arching develops as (i) subsoil undergoes consolidation and (ii) a defective pile undergoes additional settlement to the surrounding non-defective piles. Small-scale piled embankment models (without reinforcement) were constructed to simulate the progressive development of soil arching while being imaged using synchrotron produced X-rays. The reconstructed volumes from this imaging process were analysed using image correlation techniques in order to obtain three-dimensional displacement fields, which provided insight into the kinematics of soil arching. Centrifuge modelling was also undertaken, which allowed scaling issues to be more rigorously addressed and mechanisms more realistically simulated than possible within 1*g* small-scale models. The results from centrifuge modelling were then used to calibrate a finite element model using the software PLAXIS.

Results from X-ray imaging show that failure surfaces develop in the granular material overlying pile heads as subsoil undergoes consolidation. These failure surfaces indicate that the soil arching mechanism within granular material above a pile head is analogous to the failure mechanism that develops beneath shallow foundations, although vertically mirrored. Based on the observed failure surfaces, the progressive development of soil arching as subsoil undergoes consolidation is attributed to the mobilisation of shear strength within these failure surfaces. A design method is proposed that accounts for the progressive mobilisation of arching stresses and membrane actions as subsoil undergoes consolidation by utilising an interaction diagram approach, which is shown to match the results from centrifuge modelling closely.

Based on the results from both physical and numerical modelling, it is evident that, when a defective pile undergoes additional settlement, a portion of such settlement may propagate to the embankment surface. However, in some cases, e.g. where a pile defect is not severe or where a tall embankment

allows a plane of equal settlement to develop within the embankment fill, a defective pile may not adversely affect the performance of a GRPE. Recommendations are provided for determining whether a defective pile may or may not adversely affect a GRPEs performance, and, if this occurs, what remedial actions should be undertaken.

Declaration

This thesis contains no material which has been accepted for the award of any other degree or diploma at any university or equivalent institution and that, to the best of my knowledge and belief, this thesis contains no material previously published or written by another person, except where due reference is made in the text of the thesis.

Louis E. King

Department of Civil Engineering, Monash University, Australia

January 2019

Publications during enrolment

The following publications align with the research aims of this thesis and were produced while enrolled in the degree.

Journal papers

- King, L., Bouazza, A., Maksimenko, A., Gates, W.P., Dubsky, S. 2018. Measurement of 3D displacement field in a piled embankment using synchrotron X-ray tomography. *Canadian Geotechnical Journal*. https://doi.org/10.1139/cgj-2018-0159
- King, L., Bouazza, A., Dubsky, S., Rowe, R.K., Gniel, J., Bui. H.H. 2019. Kinematics of soil arching in piled embankments. *Géotechnique*. https://doi.org/10.1680/jgeot.18.P.104
- King, L., Bouazza, A., Gaudin, C., O'Loughlin, C.D., Bui. H.H. 2019. Behavior of geosynthetic reinforced piled embankments with defective piles. *Journal of Geotechnical and Geoenvironmental Engineering*. (*Under review*).

Conference papers

- King, L., Bouazza, A., Gniel, J., Gaudin, C., O'Loughlin, C.D. 2017. Centrifuge modelling of displacement piles and installation effects. *Proceedings of DFI-PFSF Piled Foundations & Ground Improvement Technology for the Modern Building and Infrastructure Sector*. Melbourne, Australia. 21 – 22 March 2017.
- King, D.J., King, L., Bouazza, A., Gniel, J., Bui, H.H. 2017. The development of arching in geosynthetic reinforced column supported embankments on semi-rigid inclusions. *Proceedings of the 19th International Conference on Soil Mechanics and Geotechnical Engineering*. Seoul, Korea. 17 – 22 September 2017.
- King, L., Bouazza, A., Dubsky, S. 2018. Kinematics of piled embankments with defective piles. *Proceedings of China-Europe. Conference on Geotechnical Engineering*. Vienna, Austria. 13 – 16 August 2018

Acknowledgements

I would like to begin by acknowledging the Traditional Owners of the land on which this research was conducted, the Wurundjeri people of the Kulin Nation. I pay my respects to their Elders past, present and emerging and acknowledge that sovereignty was never seeded.

I would like to express my gratitude to my supervisor Prof. Malek Bouazza for the advice, guidance and support given over that past four years. I would also like to thank my co-supervisors Dr Joel Gniel and Dr Ha Bui for their mentorship and contribution to this project.

The team from the National Geotechnical Centrifuge Facility (NGCF) at the University of Western Australia were extremely accommodating and I am thankful for the opportunity to visit and perform the centrifuge tests at their world-class facility. Further thanks go to Prof. Christophe Gaudin and Associate Prof. Conleth O'Loughlin for introducing me to the world of centrifuge modelling and providing technical oversight to my research.

I was fortunate to be granted beamtime at the Imaging and Medical Beamline (IMBL), the Australian Synchrotron. Access to the IMBL was made possible by the Australian Synchrotron and Australian Nuclear Science and Technology Organisation (ANSTO) (Program Proposal 11018, 11663 and 11980). The support of the IMBL staff, including Dr Anton Maksimenko, Dr Daniel Hausermann and Dr Chris Hall, is greatly appreciated. Imaging was also performed at the DINGO neutron imaging facility at the OPAL research reactor, ANSTO. I am grateful to the staff at DINGO, in particular, Dr Ulf Garbe for the assistance and expertise in neutron imaging.

I would also like to thank my colleagues who helped along the way: Dr Will Gates for teaching me all things CT imaging, Dr Stephen Dubsky for providing and assisting me with his digital volumetric correlation software, Peter Domelow for fabricating small-scale models and Warren Hornsey (TRI Environmental Pty. Ltd.) for performing testing on samples of geosynthetics.

I am thankful to Golder Associates for their financial support and in-house technical support. In particular, I would like to thank Dr Daniel King, Dr Chris Haberfield and Dr Gary Chapman for giving their time to answer all of my questions.

I would also like to gratefully acknowledge that this research was supported by an Australian Government Research Training Program (RTP) Scholarship.

Finally, I could not have undertaken and completed my studies without the support of my friends and family. To my grandparents Florence and Ian Evans, my parents Robert King and Jillian Evans, and my partner Sophie Jackson thank you for your love and support.

Contents

List of figures

List of symbols

a	Pile head width (m)
A_L	Load coverage area (m^2)
A_p	Penetrometer projected area (m^2) or area of pile head (m^2)
A_s	Penetrometer shaft area (m^2)
A_{uc}	Area of unit cell (m^2)
B	Trapdoor width (m) or silo width (m)
b	Clear spacing between piles (m) or span of a void (m)
b'	Equivalent axisymmetric clear spacing (m)
c'	Cohesion in terms of effective stress (kPa)
C_c	Compression index
c_h	Coefficient of horizontal consolidation (m^2/year)
C_r	Recompression index
C_s	Swelling index
c_v	Coefficient of vertical consolidation (m^2/year)
d	Pile head diameter (m)
D_{50}	Mean particle size (mm)
D_r	Relative density (%)
E	Young's modulus (kPa)
$\mathbf{E}$	Strain tensor
e	Void ratio
E_{50}	Drained triaxial secant stiffness (MPa)
E_A	Load efficacy considering Load Part A (%)
E_{A+B}	Load efficacy considering Load Part A and B (%)
e_{min}, e_{max}	Minimum and maximum void ratio, respectively
E_{oed}	Tangent stiffness for primary oedometer loading (MPa)
E_{ur}	Unload/reload stiffness (MPa)
F	Load carried by pile (kN)
$\mathbf{F}$	Deformation gradient tensor
G_s	Specific gravity
H	Height of soil (m)
h_{cr}	Critical height (m)
$h_{cr,def}$	Critical height above a defective pile (m)
H_{dr}	Maximum drainage length (m)
h_e	Embankment height (m)
h_{fs}	Maximum height of failure surfaces (m)

h_{LTP}	Height of load transfer platform (m)
I_r	Relative dilatancy index or rigidity index
J	Tensile stiffness of geosynthetic reinforcement (kN/m)
k	Coefficient of permeability (m/s)
K_0	At rest earth pressure coefficient
K_a	Rankine active earth pressure coefficient
K_p	Rankine passive earth pressure coefficient
K_{pile}	Pile axial stiffness (kN/m)
k_s	Modulus of subgrade reaction (kN/m^3)
L	Displacement gradient tensor
L_p	Pile length (m)
M	Frictional coefficient within critical state framework
m	Power law for stress level dependency in Hardening Soil model
n	Scale factor or plastic volumetric multiplier (Ladd, et al. (1977)
OCR	Overconsolidation ratio
p'	Mean effective stress (kPa)
p_a	Atmospheric pressure (≈100 kPa)
q	Surcharge pressure acting on embankment surface (kPa), deviatoric stress (kPa) or T-bar penetration resistance (kPa)
$q_{T,net}$	Net T-bar penetration resistance (kPa)
r	Radius of piezocone or log-spiral (m)
r_e	Relative element size
R_{inter}	Interface strength reduction factor
R_K	Stiffness reduction factor
R_n	Normalised roughness
R_t	Maximum surface roughness (μm)
S	Settlement (m)
s	Closest centre-to-centre spacing of adjacent piles (m)
s'_{int}	Centroid spacing where interaction occurs between failure surfaces (m)
s'	Centroid spacing (m)
s_d	Largest centre-to-centre spacing of piles (m)
S_e	Settlement within embankment due to subsoil settlement (m)
s_{int}	Centre-to-centre spacing where interaction between failure surfaces occurs (m)
S_p	Pile head settlement (m)
S_{total}	Total settlement experienced at the embankment surface (m)
s_u	Undrained shear strength (kPa)
t	Time (mins)

T	Time factor
T_u	Ultimate tensile strength of geosynthetic reinforcement (kN/m)
U	Normalised excess pore pressure
u_o	Hydrostatic pore pressure (kPa)
U_z	Vertical displacements (m)
V'	Normalised velocity
W_T	Line load (kN/m)
α	Unequal area ratio of T-bar correction
α_r	Replacement ratio
γ	Unit weight (kN/m^3) or shear strain (%)
γ_{max}	Maximum shear strain (%)
δ_{GR}	Vertical deflection of geosynthetic reinforcement relative to pile heads (m)
δ_s	Subsoil settlement between adjacent pile heads (m)
$\delta_{s,max}$	Maximum subsoil settlement (m)
Δ_{SP}	Elongation of string potentiometer cable (m)
δ_{sp}	Settlement plate displacement (m)
ΔS_{pile}	Pile head differential settlement (m)
ΔS_{surf}	Embankment surface differential settlement (m)
δ_{TD}	Trapdoor displacement (m)
Δu_e	Excess pore water pressure (kPa)
ε	Strain (%)
ε_a	Axial strain (%)
ε_v	Volumetric strain (%)
η	Settlement shape factor
θ_{Arth}	Arthur angle of orientation (˚)
θ_{coul}	Coulomb angle of orientation (˚)
κ	Slope of swelling line
κ^*	Modified swelling index
λ	Load recovery index or slope of normal consolidation line
λ^*	Modified compression index
ν	Poisson's ratio
ξ	State parameter
ρ_{min}, ρ_{max}	Minimum and maximum dry density, respectively (kg/m^3)
σ	Total stress
σ'	Effective stress (kPa)
σ'_1	Effective major stress (kPa)

σ'_3	Effective minor stress (kPa)
σ'_{GR}	Vertical stress carried by geosynthetic reinforcement (kPa)
σ'_h	Horizontal effective stress (kPa)
σ'_{LTP}	Vertical stress in LTP directly above geosynthetic reinforcement (kPa)
σ'_p	Vertical stress transferred directly to pile heads through soil arching (kPa)
σ'_s	Vertical stress acting subsoil below geosynthetic reinforcement (kPa)
σ'_{TD}	Stress acting on trapdoor (kPa)
σ'_v	Vertical effective stress (kPa)
σ'_{v0}	Initial vertical overburden stress (kPa)
τ	Shear stress (kPa)
ϕ_{cv}	Critical state or constant volume frictional angle (˚)
ϕ_p	Peak friction angle (˚)
ψ	Dilation angle (˚)
ω	Angular velocity (rad/s) or log-spiral curvature

1 Introduction

1.1 Purpose

This thesis investigates the progressive development of soil arching in geosynthetic reinforced piled embankments (GRPEs) as both subsoil and piles undergo settlement. Both the load transfer and kinematics that develop within these embankments are explored by implementing physical and numerical modelling techniques. The ultimate aim of this thesis is to provide a better understanding of the soil mechanics associated with soil arching, which can be used to further explain many of the observed phenomenon associated with soil arching in GRPEs and assist in the development of future design methods and recommendations.

1.2 Background

Highly compressible soils provide un-favourable conditions for the construction of infrastructure. These soils may be susceptible to instability issues and excessive settlements from the loading of a superstructure. Many construction methods are available to combat these issues, including specifically for embankments: geosynthetic basal reinforcement, lightweight fill, temporary surcharging, prefabricated vertical drains (PVDs), semi-rigid columns or piles. While some embankment construction methods address stability control or settlement control, methods that address both provide unique design solutions that allow the construction of an embankment to proceed rapidly. One such solution that has been increasingly adopted over the past 30 years to support road and rail infrastructure, among other structures, underlain by highly compressible soils is that of geosynthetic reinforced piled embankments (GRPEs). By transferring embankment loads to deeper and less compressible founding layers, GRPEs allow construction to proceed without the need to wait for consolidation to occur within near-surface soft clay layers. A review of 16 case studies by Almeida et al. (2007) showed an increase in the popularity of piled embankments since 1995, with more than 80% of applications related to road and rail infrastructure.

While historically GRPEs have been supported on piles, which are rigid deep foundations, the advancement of many ground improvement techniques in recent years has led to embankments being increasingly supported on semi-rigid columns, such as drilled displacement columns (DDCs) (Pearlman and Porbaha 2006; Wong and Muttuvel 2012; Gniel and Haberfield 2014; King et al. 2017a) and deep mixing method columns (Huang and Han 2009). The research undertaken as part of this study applies to both embankments supported on rigid piles or semi-rigid columns as it focuses on the localised behaviour of the soil-structure-geosynthetic interaction under the centreline of an embankment without consideration of the global embankment behaviour. Whether piles or semi-rigid columns are used, it is

common practice to construct pile caps or enlarged heads to increase the area of embankment supported on structural elements.

Piled embankments often utilise a load transfer platform (LTP), otherwise referred to as a bridging layer, overlying pile heads to facilitate the transfer of embankment loads towards pile heads and reduce both differential and total settlements experienced at the embankment surface. LTPs typically comprise a granular material with a high friction and dilation angle. Due to the differential settlement that occurs between the pile heads and the underlying soft soil (subsoil), shear stresses are mobilised within the LTP, resulting in a transfer of embankment loads towards the pile heads through a mechanism known as soil arching. Geosynthetic reinforcement, either using a single or multiple layers, is often placed within the LTP, although piled embankments may also be constructed without geosynthetic reinforcement, e.g. where relatively low compressible soils underlie the embankment or piles are spaced closely. When geosynthetic reinforcement is placed above the pile heads within the LTP, it deforms due to a differential settlement between pile heads and subsoil, which mobilises tensile loads, further transferring embankment loads towards the pile heads.

Many soil arching theories have been developed over the past three decades to estimate displacements and load transfer within GRPEs. The clear majority of these models assume that the soil arching mechanism is independent of subsoil and pile head settlement. However, observations from physical model tests, case studies and numerical modelling show that soil arching is dependent on subsoil settlement and progressively develops as consolidation occurs, and is, therefore, a time-dependent mechanism. Furthermore, piles may exhibit differences in load-settlement response for several reasons (e.g. defective piles and transition zones), and as such, an understanding of how soil arching progressively develops above piles exhibiting differential settlement is required.

1.3 Geosynthetic reinforced piled embankments (GRPEs)

1.3.1 Piles

The typical layout of a GRPE is shown in Figure 1.1. Piles may be installed into a rigid founding stratum, in which case the piles are considered end-bearing, or they may be installed with toes still founded within a compressible layer, and in this case they are referred to as floating piles. Due to the strict settlement requirements of most road and rail infrastructure projects, floating piles are not as common as end-bearing piles to support GRPEs, although they are used frequently in embankment transition zones. Concrete piles, either cast-in situ or precast, are most commonly adopted to support GRPEs (Almeida et al. 2007), although timber piles may also be used to support embankments (Van Eekelen et al. 2010). Semi-rigid columns have also been used over the past 10 years to support embankments, and while these embankments are often referred to as column supported embankments (CSEs), no such

differentiation will be made in this thesis between embankments supported on piles or semi-rigid columns.

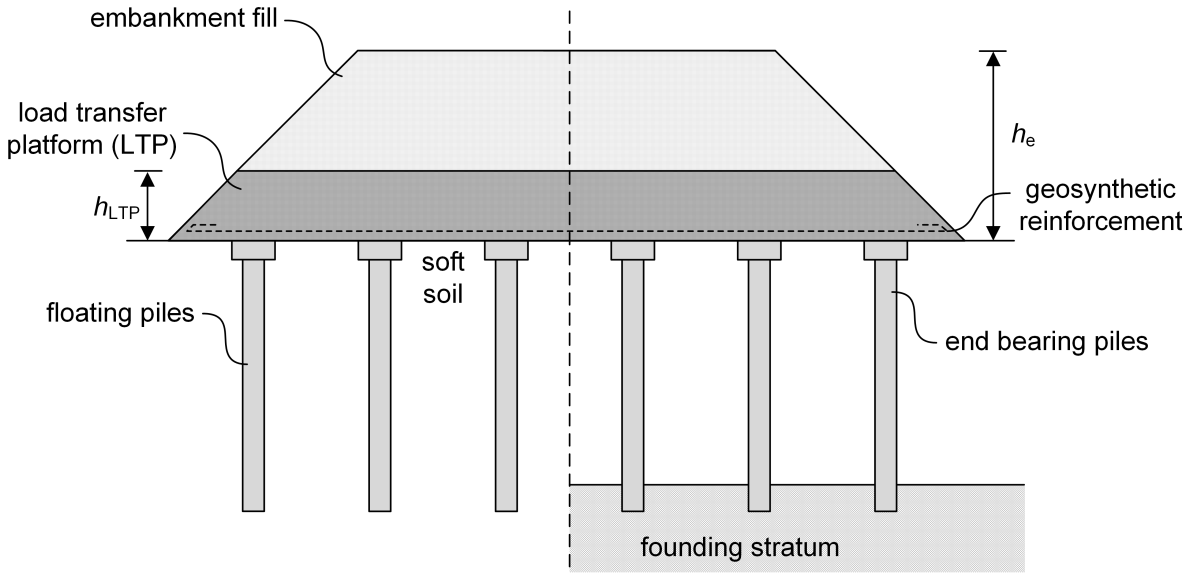

Figure 1.1: Typical geosynthetic reinforced piled embankment (GRPE)

The piles supporting a GRPE are typically installed on a square grid (Figure 1.2a), although piles may be arranged in other layouts including equilateral triangular grids (Figure 1.2b) or rectangular grids. Either square or circular pile caps (otherwise referred to as enlarged heads) may be placed on the top of the pile to increase the area of the structure supporting the base of the LTP. The centre-to-centre spacing of piles (s) and the pile cap diameter (d) (or pile cap width, a) are essential parameters that require careful refining in the design of a GRPE. As will be shown throughout this thesis, these parameters govern the settlement and load transfer within GRPEs.

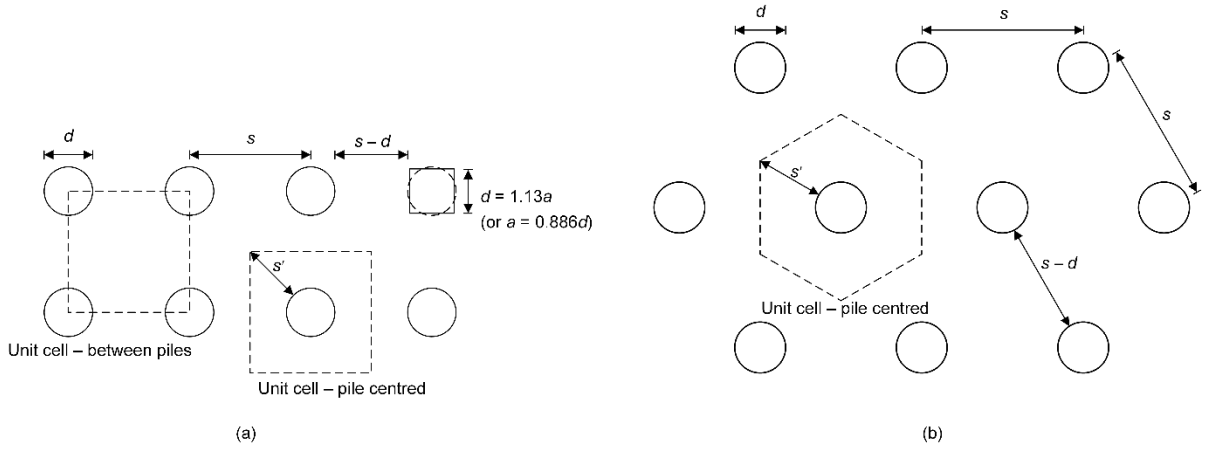

Figure 1.2: Plan view of piles arranged on a (a) square grid; (b) equilateral triangular grid

Piles arranged on a grid may be considered to have a zone of influence. For piles spaced on a square grid the shape of this zone of influence is square, whereas for piles spaced on an equilateral triangular grid this zone of influence is hexagonal. The zone of influence is often referred to as the unit cell and is shown for square and equilateral triangular arrangements in Figure 1.2. The furthest horizontal distance from the edge of the pile head to the boundary of the unit cell is referred to as the centroid spacing, s', and is another integral parameter for the design of GRPEs as it represents the furthest horizontal distance soil within the LTP may be from a structural support.

The ratio of unit cell area (A_{uc}) and the pile head area (A_p) is referred to as the replacement ratio (α_r). The replacement ratio is representative of the proportion of the embankment supported on structural elements, and while a higher replacement ratio may result in less settlement and more of the embankment load carried by piles, it also increases the cost of the project.

1.3.2 Load transfer platform

Granular materials that exhibit a high peak friction angle and undergo significant dilation during shearing are suitable to be used within the LTP. Such materials may include rock fill (King et al. 2017a), reused concrete and road pavements (Briançon and Simon 2012) or sand (Van Eekelen et al. 2010). For high-quality LTP materials to exhibit the desired properties, it is often necessary for them to be placed in a dense state. This can be difficult to achieve within the lower portion of the LTP as compaction techniques may not successfully achieve the desired density due to the presence of underlying soft soils. These high quality granular materials are typically placed and compacted to create a thickness of LTP (h_{LTP}) that corresponds to the height above the pile heads where a plane of equal settlement is predicted to develop (described in Section 2.3.1); above which lower quality fill materials may be used to produce the full embankment height (h_e).

Geosynthetic reinforcement is often placed close to the base of the LTP, either directly above the pile heads or above a thin layer of granular material to avoid the geosynthetic from being damaged from direct contact with the pile heads. To provide suitable reinforcement for a GRPE, the selected geosynthetic should have an ultimate tensile strength capable of withstanding the imposed loads while also having sufficient tensile stiffness to not excessively deform under the imposed loads. Suitable geosynthetics that exhibit such strength and stiffness include both geogrids (uniaxial or biaxial) and geotextiles, both of which are commonly made from polyester or polypropylene (Almeida et al. 2007).

1.3.3 Load distribution

When GRPEs are built over compressible soils, referred to as the subsoil, differential settlement develops over time between the surface of the subsoil and the pile heads due to the vertical loads imposed from the overlying embankment. This differential settlement mobilises two load transfer

mechanisms within the LTP overlying the pile heads, namely, soil arching and membrane actions. These mechanisms redistribute the embankment loads towards the pile heads. One of the primary intentions of GRPE design methods/recommendations is to estimate the load distribution between pile heads, geosynthetic reinforcement and subsoil. To do so, it is common practice to simplify the load distribution into three loads, which are represented in Figure 1.3 and may be summarised as:

- Load Part A – The embankment loads transferred directly to the pile heads through soil arching. Soil arching models are employed to estimate the magnitude of this load.
- Load Part B – The embankment loads transferred to the pile head through tensile forces mobilised within the geosynthetic reinforcement, referred to membrane actions.
- Load Part C – The embankment loads acting on the surface of the subsoil. This is the remaining embankment load not transferred to the pile heads through soil arching or membrane actions.

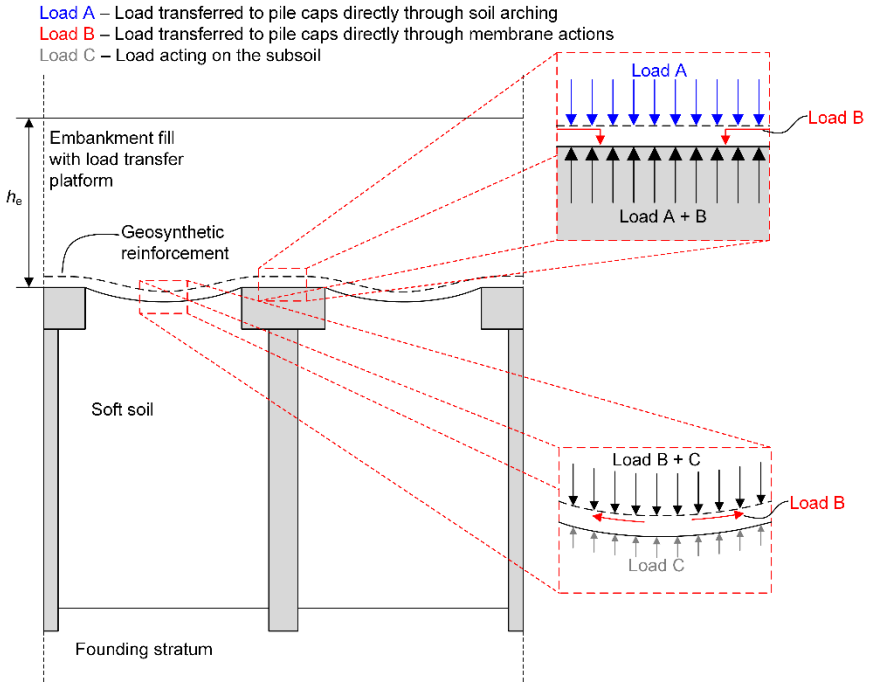

Figure 1.3: Load distribution within a GRPE

GRPE design methods typically adopt a two-step design process, where arching models are used to estimate Load Part A, while the remaining Load Parts B and C act on the surface of the geosynthetic reinforcement. The arching models employed in some of the most common GRPE national design methods, including British (BS8006), German (EBGEO) and Dutch (CUR226), estimate Load Part A as a stress acting on the pile heads independently of the subsoil settlement. However, observations from numerical modelling (Zhuang et al. 2010), physical modelling (Ellis and Aslam 2009b) and a full-scale case study (King et al. 2017a), indicate that the arching stresses are dependent on the subsoil settlement. The progressive development of these arching stresses as subsoil consolidates makes soil arching in

GRPEs a time-dependent mechanism, which is not considered by many if the national design recommendations (e.g. BS8006, EBGEO and CUR226). While soil arching within GRPEs may have been shown to be a settlement dependent mechanism, an understanding of the soil mechanics that cause this behaviour has not been developed, and still, most arching models are based on assumed failure surfaces rather than any observed kinematics.

1.3.4 Embankment settlements

Most road and rail infrastructure will have strict serviceability requirements imposed on the design, which is often what leads to GRPEs being selected as the preferred construction method over options such as temporary surcharging or PVDs. The total settlement that is experienced at the embankment surface (S_{total}) is the sum of the pile head settlement (S_p) and the settlement that develops within the embankment due to the differential settlement between pile heads and subsoil at the base of the embankment (S_e). While the pile head settlement may be estimated using any number of methods developed for determining pile settlement, the settlement that develops within the embankment is more difficult to estimate. While some methods exist for estimating S_e, it is often not considered in design methods, with design recommendations often suggesting numerical analysis be undertaken for serviceability design.

In addition to total embankment settlement, differential settlement may occur at the embankment surface if the embankment height is insufficient for a plane of equal settlement to develop within the LTP or the embankment fill. It has been shown that a plane of equal settlement develops within GRPEs at some height above the pile heads. The height at which this plane forms is referred to as the critical height (h_{cr}). When $h_e < h_{cr}$, some portion of the differential settlements that occur at the base of the embankment between pile heads and subsoil may propagate to the embankment surface, which has been shown to result in a "mushroom" like profile at the embankment surface (McGuire 2011; Sloan 2011). However, many of the methods available to predict h_{cr} are again based on assumed failure surfaces that do not match any observed modes of failure or empirical relationships. In the author's experience, there is an increasing demand to utilise GRPEs with shallow embankment heights. Without an understanding as to what mechanism results in the development of a plane of equal settlement and without an accurate method to predict the height at which one forms within an LTP or embankment fill, there is increasing risk that shallow height embankments will be constructed, and over time, experience differential settlement at the embankment surface.

1.3.5 Defective piles

Imperfections within piles may arise during the construction of a GRPE due to several reasons, including geological imperfections, inadequate ground investigation, pile construction process, loading during construction and/or during operation. Such imperfections may cause a pile to be defective, which

has been shown to cause, in most cases, the pile to exhibit a softer load-settlement response compared to non-defective piles installed and behaving as per the design (Poulos 2005). When these piles are connected by a rigid structural element such as a pile cap, the structural connection redistributes loads away from the defective pile towards the surrounding non-defective piles (Poulos 1997). However, when defective piles are installed within a large group of piles beneath an LTP, there is limited understanding as to how the overlying LTP redistributes loads due to soil arching and membrane actions away from the defective pile. Similar to the progressive mobilisation of arching and membrane actions, the settlement of a defective pile will also develop as loads are progressively applied to it through both of these actions. Thus, the transfer of loads towards and away from a defective pile within a group of piles connected by an overlying LTP will depend on complex soil-structure-geosynthetic interaction mechanisms, which are settlement dependent and will progressively develop. It is also not understood how the presence of a defective pile may affect the development of a plane of equal settlement, and whether the softer load-settlement response of a defective pile may cause additional settlement at the embankment surface.

Due to the relatively light loads carried by piles or ground improvement columns underlying an embankment, typically less than 800 kN per pile, piles or columns are often designed with shallow embedment into a founding layer. In combination with embankment footprints that require large quantities of piles, it can be difficult to ensure the quality of all piles and that their load-settlement response will meet the design requirements. For example, Michalowski et al. (2018) reported an embankment in Poland that was supported on 13,670 DDCs that were designed to be terminated at no less than 0.5 m into a founding stratum. The depth of this founding stratum was determined during construction by a significant increase in piling rig torque. Some of these columns experienced an increase in rig torque prior to reaching the founding stratum due to thin lenses of stronger soil and were prematurely terminated, i.e. floating columns were installed without any embedment into the founding stratum. It was shown that the premature termination of DDCs in some locations contributed to excessive embankment surface settlements, which among other factors, played a role in the serviceability failure of this embankment. It is also the author's experience that during the construction stage of GRPEs, when the load-settlement performance of isolated piles or columns is called into question, significant delays and expenses can be incurred if remedial actions are required.

1.4 Research hypothesis

It has been shown that soil arching exhibits a displacement or subsoil settlement dependency that is not accounted for in many of the existing soil arching theories adopted in GRPE design. Instead, many of the existing soil arching theories developed specifically for GRPEs assume failure surfaces within the LTP overlying the pile heads based on load or displacement measurements at a number of discrete

locations within a model test or field case study. However, such soil arching models fail to explain many of the observed phenomenon associated with soil arching, such as the formation of a plane of equal settlement within the embankment at some height above the pile heads, the propagation of settlement above this plane of equal settlement to the embankment surface or the progressive development of soil arching as subsoil undergoes consolidation. It is the author's position that the existing soil arching models assume incorrect failure surfaces as they contradict observations from experimental and field case studies.

The assumption made by many GRPE soil arching models is that all piles undergo uniform settlement. However, defective piles that exhibit softer load-settlement responses to other non-defective piles may undergo additional settlement. While it is assumed by recommendations such as (CUR226 2016) that soil arching will re-establish around a defective pile, between non-defective piles, this has not been studied or shown to date. It is considered likely that if a defective pile were to undergo additional settlement to the surrounding non-defective piles, then this additional settlement would cause an increase in height above the pile heads required for a plane of equal settlement to develop. If an embankment was sufficiently tall, it is likely that differential settlements would not be experienced at the embankment surface, and it may be possible that a level of redundancy exists within some GRPEs.

1.5 Research aims

Many soil arching models exist, the clear majority of which are based on assumed soil kinematics without any observed mechanism or failure surfaces. The intention of this research is not to develop another soil arching model. Instead, it is to investigate the soil mechanics within an LTP overlying pile heads as (i) subsoil consolidates and (ii) a pile undergoes additional settlement relative to the surrounding piles. It is anticipated that this will provide insight for future research to develop models and design recommendations that are based on observed and understood mechanisms without the assumptions made by many of the existing arching models. Thus, the aims of this thesis are:

- To investigate how soil arching within an LTP progressively develops as subsoil undergoes consolidation.
- To examine how soil arching within an LTP gradually develops as an individual pile (defective pile) undergoes additional settlement relative to surrounding piles (non-defective piles).
- To investigate what conditions may lead to a defective pile causing adverse effects on the performance of a GRPE.

1.6 Outline of thesis

An in-depth review of the existing literature regarding GRPEs is provided in Chapter 2 along with the current knowledge gaps. The chapter first looks at existing arching theories, both those developed for

general use and those developed specifically for GRPEs. The background is provided on how existing design methods estimate maximum strains and tensile loads in geosynthetic reinforcement as well as the settlements (both differential and total) that arise at the embankment surface due to the subsoil settlement between pile heads. The chapter also discusses the outcomes of studies that have investigated the performance and effects of defective piles before providing a summary of previous physical model tests of piled embankments.

Small-scale model piled embankments (without reinforcement) were designed and built so that imaging could be undertaken to observe the soil kinematics associated with soil arching in piled embankments. These models, along with the preliminary results from three different imaging techniques, are described in Chapter 3. The chapter also discusses the image correlation techniques that were employed to calculate three-dimensional displacement fields from computed tomography (CT) reconstructed volumes collected using synchrotron produced monochromatic X-rays.

The results from imaging small-scale model piled embankments are described in Chapter 4. The displacement fields obtained were used to estimate shear and volumetric strains in fine-grained sand overlying pile heads, both with and without a defective pile. From these results, the failure surfaces that develop above pile heads within the LTP granular material are characterised as subsoil, and defective piles progressively undergo settlement.

The small-scale physical modelling performed at 1*g* has several limitations associated with scaling. To account for many of these limitations, centrifuge modelling was performed on two GRPE models that were tested at an enhanced gravitational acceleration of 40*g*. The design and construction of these two models are discussed in Chapter 5. The chapter also describes the materials, instrumentation and testing procedure for these two models.

The results from centrifuge model tests are presented in Chapter 6. Both models comprised sections of an embankment with and without defective piles, which provides an indication of (i) how loads and settlements develop as subsoil consolidates and (ii) how a defective pile may affect an embankments performance.

The results from centrifuge model tests are then used to calibrate a finite element method (FEM) model, which is described in Chapter 7. The calibrated FEM model is then used to perform a parametric study where the parameters such as the embankment height and severity of a pile defect are varied to investigate under what conditions a defective pile may cause differential settlements to arise at the embankment surface.

The research findings are outlined in Chapter 8 along with the practical outcomes of the research. This then leads to the conclusions from the research being presented in Chapter 9.

2 Literature review

This chapter provides an overview of the key mechanisms and design principles associated with GRPEs. The load distribution within GRPEs is predominantly attributed to soil arching and membrane actions, both of which are discussed in this chapter along with some of the more widely used GRPE design methods. The background is also provided regarding the causes and effects of defective piles in both pile groups connected by a rigid structure and in groups of piles connected by an overlying LTP or embankment. Given that a large portion of the research undertaken as part of this study utilises physical modelling techniques, a review of previous physical modelling experiments is also provided.

2.1 Soil arching

Soil arching is the redistribution of loads towards or away from a structure due to its relative movement to a body of soil (Evans 1983). This relative movement mobilises shear stresses within the soil mass, which resist the relative movement between soil-structure and cause a redistribution of loads. This redistribution of loads due to soil arching has been observed in a wide variety of geotechnical problems, such that Terzaghi (1943) noted: "*Arching is one of the most universal phenomena encountered in soils in both the field and laboratory*".

2.1.1 Early arching theories

Arching within particulate materials has been studied since the 1800's, when it was observed that the stress acting on the base of a silo was not equal to the overburden stress, reportedly first identified and shown experimentally by the French military in the 1820's (Feld 1948). This observation was extended by Janssen (1895), who proposed a silo theory to estimate stresses acting on the base of a silo, described by Blight (1986). The free body diagram assumed by Janssen is shown for a parallel-sided cylindrical silo in Figure 2.1.

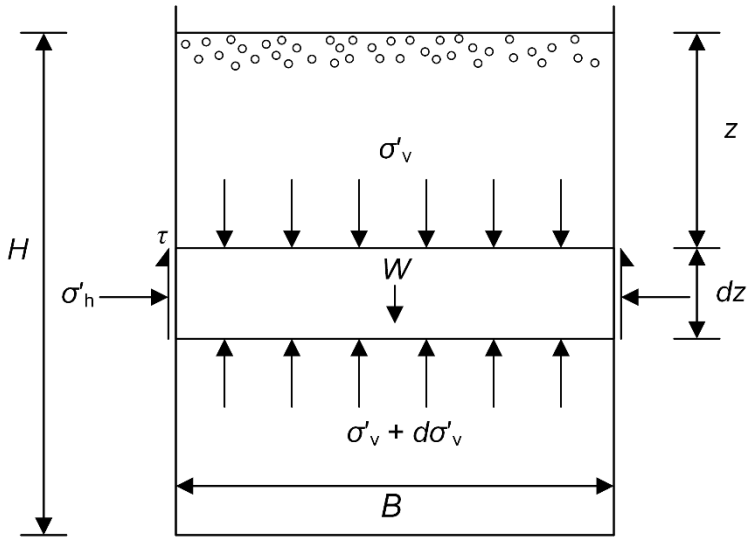

Figure 2.1: Janssen (1895) silo theory

In Janssen's silo theory, a horizontal element of thickness *dz* is considered, where vertical equilibrium within this element is achieved when:

$$\sigma'_{\mathrm{v}} + d\sigma'_{\mathrm{v}} + \frac{4\tau dz}{B} = \sigma'_{\mathrm{v}} + \gamma dz \tag{2.1}$$

Where σ'_{v} is the vertical stress acting on the top of the element, $\sigma'_{\mathrm{v}} + d\sigma'_{\mathrm{v}}$ is the vertical force acting on the base of the element, τ is the shear stress acting on the vertical boundaries of the element, γ is the unit weight of the granular material and B is the width of the silo. The shear stress on the vertical sides of the element is taken as:

$$\tau = \sigma'_{\mathrm{h}} \tan\delta \tag{2.2}$$

Where σ'_{h} is the horizontal stress acting on the vertical boundaries of the element and δ is the angle of friction between the silo wall and granular material, taken as internal friction angle of the granular material (ϕ). σ'_{h} is equal to $K\sigma'_{\mathrm{v}}$, where K is the coefficient of lateral earth pressure, which is assumed in Janssen's silo theory as equal to the Rankine active earth pressure coefficient:

$$K = K_{\mathrm{a}} = \frac{1 - \sin\phi}{1 + \sin\phi} \tag{2.3}$$

A differential equation is derived after rearranging Equation 2.1, the solution of which, when solved for the vertical stress acting at the base of a silo or trapdoor, is:

$$\sigma'_{\mathrm{TD}} = \frac{B\gamma}{4K\tan\phi}\left[1 - e^{\left(\frac{-4Kz\tan\phi}{B}\right)}\right] \tag{2.4}$$

Marston and Anderson (1913), described by Spangler and Handy (1973), adopted similar assumptions as Janssen's silo theory and applied them to the stresses acting on pipes. For a buried rigid pipe where the backfill is compressible, such that as the backfill settles above the pipe shear stresses develop along the walls of the trench, the vertical stress acting on the pipe (or trapdoor) may be estimated as:

$$\sigma'_{\mathrm{TD}} = \frac{B\gamma}{2K\tan\phi}\left[1 - e^{\left(\frac{-2Kz\tan\phi}{B}\right)}\right] \tag{2.5}$$

Essentially, the only difference between Equation 2.4 and 2.5, is that one is for a cylindrical geometry and the other is for plane strain conditions. Marston and Anderson (1913) also assumed that $K = K_a$, in line with the assumption made by Janssen (1895). Equation 2.5 may also be modified (replacing minus signs with plus signs) for a positive projecting conduit/culvert, where the fill surrounding the conduit settles more than the conduit itself. This is equivalent to a passive trapdoor test (Section 2.1.2).

Another early arching theory was proposed by Engesser (1882) who studied the stresses acting on tunnels and assumed that an "arch" in the shape of a parabola develops above a yielding support, as described by Iglesia (1991). Engesser assumed that the parabola-shaped arch extended from the edges of a yielding support, tunnel in the case of their work, at an angle of θ to the horizontal. Loads acting above the arch were assumed to be transferred to the support on the side of the arch, while the sum of the weight of the soil below the arch (W) and the vertical stress directly above the yielding support (σ'_{vr}) act on the yielding support (Figure 2.2). The vertical stress directly above the yielding support is increased due to an increase in lateral stress (σ'_{hr}) above the yielding support due to the load distribution, which may be written as:

$$\sigma'_{\mathrm{vr}} = \frac{HB\gamma K}{2H\tan\theta + BK} \tag{2.6}$$

The weight of the soil below the arch per unit length is calculated as:

$$W = \frac{\gamma B^2 \tan\theta}{6} \tag{2.7}$$

Thus, the average stress acting on the yielding support, or trapdoor, can be calculated by combining Equation 2.6 and 2.7:

$$\sigma'_{\mathrm{TD}} = \gamma B\left[\frac{HK}{2H\tan\theta + BK} + \frac{\tan\theta}{6}\right] \tag{2.8}$$

In the initial theory proposed by Engesser (1882), the coefficient of lateral earth pressure was assumed equal to the Rankine active earth pressure coefficient, $K = K_a$, and the angle at which the arch developed at the edge of the support to the horizontal was taken as the internal friction angle of the soil, $\theta = \phi$. However, these assumptions have been questioned and modified in more recent years (Evans 1983;

Handy 1985), including the modifications made for the Ground Reaction Curve (GRC) framework proposed by Iglesia et al. (1999) and described in the following section.

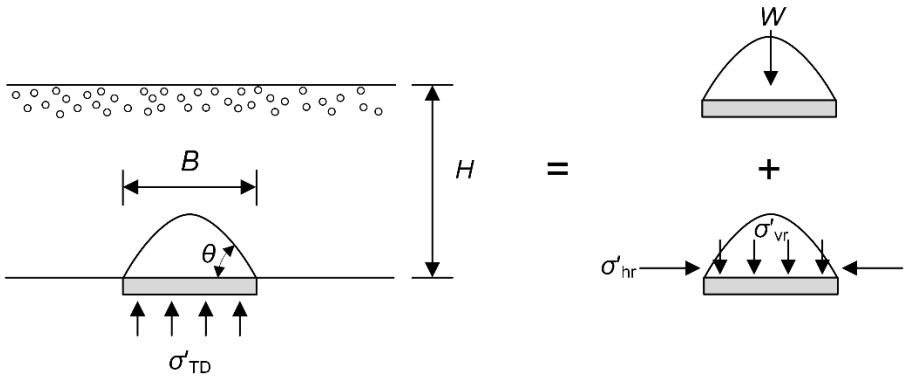

Figure 2.2: Engesser (1982) arching theory (modified from Iglesia 1991)

2.1.2 Trapdoor tests

Soil arching in the laboratory has been extensively studied using the trapdoor test since the well-known experiments performed by Terzaghi (1936). A trapdoor test employs an experimental apparatus where soil (or rock) is placed above an initially level surface, which comprises a plate (trapdoor with width B) that can be penetrated vertically upwards into the soil mass (passive arching) or vertically lowered (active arching) by a distance δ_{TD}. The supports surrounding the trapdoor remain stationary throughout the test, resulting in either an increase or decrease in stress acting on the trapdoor (σ'_{TD}) from the initial overburden condition for passive and active arching, respectively.

Terzaghi (1936) performed active trapdoor experiments on dry sand prepared in both a dense and loose state (Figure 2.3a) and observed that the vertical stress acting on the trapdoor exhibited a dependency on trapdoor displacement. Terzaghi noted that as the trapdoor was displaced vertically down, the stress acting on the trapdoor experienced a minimum after a relatively small trapdoor displacement. With increasing trapdoor displacement, the stress acting on the trapdoor increased until it approached an ultimate value similar for both densities of sand. It was also noted that the minimum stress acting on the trapdoor was less for the dense sand compared to the loose sand.

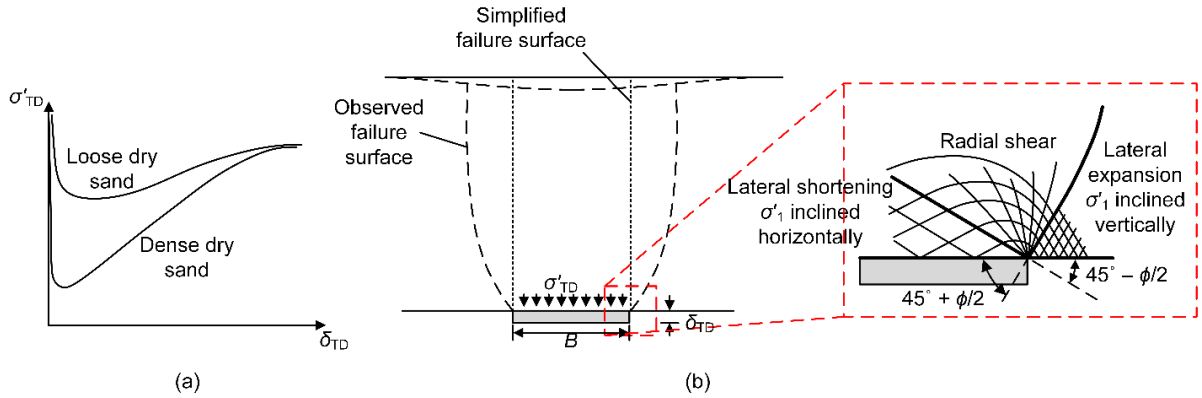

Figure 2.3: (a) Trapdoor stress-displacement relationship (modified from Terzaghi 1936); (b) failure surfaces above a trapdoor (modified from Terzaghi 1943)

Terzaghi (1943) also described the failure surfaces that develop above an active trapdoor, which are shown in Figure 2.3b. Terzaghi considered that the soil directly above the yielding trapdoor is in a state where the vertical stress decreases such that the major principal stress is inclined horizontally, where the soil is in a passive Rankine state. Directly above the stationary support adjacent to the trapdoor, the vertical stress increases due to the trapdoor displacement, with the major principal stresses becoming inclined vertically, like what would develop in an active Rankine state. Based on the Mohr-Coulomb failure criterion, the angle at which a plane of failure develops relative to the minor principle stress direction is equal to:

$$\theta_{coul} = 45^{\circ} + {}^{\phi}/_{2} \tag{2.9}$$

Thus, two failure surfaces were considered by Terzaghi to develop from the singularity point at the edge of the support adjacent to the trapdoor. Based on the assumed stress state above the trapdoor and support, the angle of inclination for these two surfaces was estimated relative to the minor principal stress direction using Equation 2.9, as shown in Figure 2.3b. Between these two Rankine zones, a radial shear zone is considered to develop.

Rather than resolving the frictional resistance along the observed failure surfaces, Terzaghi (1943) simplified the failure surfaces to vertical planes of shearing (Figure 2.3b). Terzaghi (1943) notes that the errors associated with the simplified failure surfaces are small and predictions made adopting this assumption match experimental results well. As such, Terzaghi estimated the pressure acting on an active trapdoor with dry cohesionless material without a surcharge using a similar equation and method as the silo theory proposed by Janssen (1895). However, Terzaghi (1943) showed that the earth pressure coefficient is not uniform throughout the height of the soil and that the zone of arching only extends to a height of 5*B* above the trapdoor. This resulted in Terzaghi estimating a different pressure to Janssen's silo theory.

Many researchers have performed similar trapdoor experiments to those of Terzaghi. Ladanyi and Hoyaux (1969) performed plane strain trapdoor tests using Schneebeli aluminium rods (Schneebeli 1957). It was observed in these experiments that a similar trend to Terzaghi's experiments developed, where after a small trap door displacement (approximately 8% of the trapdoor width) minimum stress on the trapdoor was experienced. This minimum stress was again followed by an increase in stress on the trapdoor with increasing displacement until an ultimate state was achieved after the trapdoor was displaced approximately 0.5*B*.

This trapdoor stress-strain relationship has also been illustrated in many experimental trapdoor studies (Evans 1983; Iglesia 1991; Santichaianaint 2002; Dewoolkar et al. 2007; Chevalier and Otani 2011; Chevalier et al. 2012; Han et al. 2017). After completing a series of centrifuge model trapdoor tests, Iglesia et al. (1999) described this progressive development of soil arching, referred to as the ground reaction curve (GRC), by classifying the progressive development of arching stresses in four stages of soil arching, described below.

Initial arching – Prior to any trapdoor displacement, the vertical stress acting on the trapdoor is equal to the initial overburden stress ($\sigma'_{v0} = \gamma H$, in the case of no surcharge applied to the soil surface). As the trapdoor is lowered, σ'_{TD} decreases rapidly. This rapid reduction in stress with small trapdoor displacement is attributed by Iglesia to the formation of an "arch".

Maximum arching – With increasing trapdoor displacement, a stress state develops which results in a minimum stress acting on the trapdoor. Under these conditions, the arching effect is most prominent, and as such, is referred to as maximum arching. Iglesia observed this stress condition to develop between trapdoor displacements of 2% and 6% of the trapdoor width. Iglesia observed that the stress acting on the trapdoor at this displacement was essentially independent the height of soil, and concluded that an "arch" must have developed within the soil overlying the trapdoor. Iglesia assumed that this arch took the shape of a parabola, and therefore adopted the equation proposed by Engesser (1882) to estimate σ'_{TD}, Equation 2.8. However, Iglesia assumed that the arch developed at an angle of $\theta = 90^\circ - \phi$ based on the test results of Evans (1983). Also, based on the assumption that the arch is a failure surface, Iglesia determined from Mohr's circle that:

$$K_E = \frac{\cos^2 \phi}{1 + \sin^2 \phi} \tag{2.10}$$

Load recovery – Beyond maximum arching, increasing trapdoor displacement results in an increase in stress acting on the trapdoor. This is attributed by Iglesia et al. (2013) to the transition of arching from a parabolic arch to an ultimate state with vertical failure surfaces. The load recovery index (λ) is the rate of stress increase with trapdoor displacement on a $\sigma'_{TD}/\sigma'_{v0}$ vs δ_{TD}/B plot. Iglesia et al. (1999) developed an empirical relationship based on the results of centrifuge model trapdoor tests to determine this index:

$$\lambda = \left[2.5 + 5.7 \log\left(\frac{B}{10D_{50}}\right)\right] e^{-0.65\left(H/B\right)} \tag{2.11}$$

Where D_{50} is the average grain size.

Ultimate state – With sufficient trapdoor displacement, it has been shown that the vertical stress acting on a trapdoor approaches a constant value, termed the ultimate state. Iglesia assumes that this state of arching corresponds to shearing along vertical planes. This corresponds to the assumptions of the silo theory proposed by Janssen (1895), and as such, Iglesia estimates the vertical stress acting on a trapdoor at the ultimate state with Equation 2.5.

The GRC proposed by Iglesia et al. (1999) is shown in Figure 2.4, where the stress acting on the trapdoor is normalised by the initial overburden stress prior to any trapdoor displacement ($\sigma'_{TD}/\sigma'_{v0}$), referred to as the stress reduction ratio (SRR), and the trapdoor displacement is normalised by the trapdoor clear spacing (δ_{TD}/B), referred to as the relative displacement.

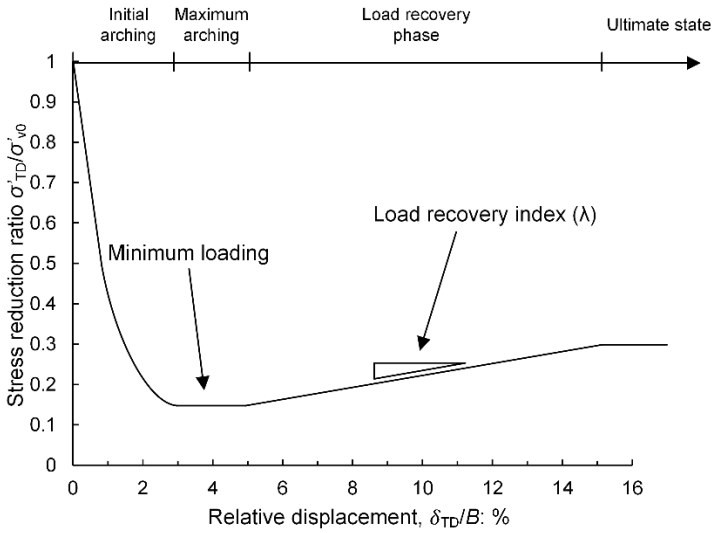

Figure 2.4: Ground reaction curve after Iglesia et al. (1999)

The failure surfaces within a soil mass overlying an active trapdoor have been studied experimentally by several researchers to investigate the vertical stress that acts on the trapdoor (Vardoulakis et al. 1981; Stone and Wood 1992; Tanaka and Sakai 1993; Santichaianaint 2002; Dewoolkar et al. 2007; Costa et al. 2009). In general, for dry sand in a dense state overlying an active trapdoor (in both centrifuge model tests and 1*g* experiments) a failure surface in the form of a shear band develops at the edge of both the supports adjacent to the trapdoor upon small displacement of the trapdoor. This shear band has been shown to form at an angle to the vertical approximately equal to the dilation angle of the sand (ψ) (Stone and Wood 1992; Dewoolkar et al. 2007; Costa et al. 2009), and exhibit a curved shape. Dewoolkar et al. (2007) attribute the curvature of this shear band to the dependency of dilation angle on stress (Bolton

1986). With increasing height above the trapdoor, the dilation angle increases due to the reduction in stress, and therefore, increases the angle at which the shear band develops to the vertical. This initial shear band that develops after a small amount of trapdoor displacement is considered to coincide with the maximum dilation angle and the state of maximum soil arching where the stress on the trapdoor is a minimum, as shown in Figure 2.5 (Dewoolkar et al. 2007).

Increasing trapdoor displacement beyond this initial movement has been shown to result in the development of sequential shear bands (Stone and Wood 1992; Dewoolkar et al. 2007; Jacobsz 2016) until eventually, almost vertical shear bands develop between the edges of the trapdoor and the sand surface. Dewoolkar et al. (2007) propose that the development of sequential shear bands correspond with soil arching transitioning from maximum arching to an ultimate state, and may be described by the mobilisation of dilatancy, as demonstrated in Figure 2.5. As the shearing approaches critical state and ψ approaches zero, as shown in Figure 2.5b by the flattening of the volumetric strain (ε_v) versus axial strain (ε_a) plot from a triaxial test, the orientation of the shear bands become increasingly vertical.

This observation of progressively and sequentially developing shear bands by Stone and Wood (1992) and Dewoolkar et al. (2007) was considered by Iglesia et al. (2013) to strengthen the case of their GRC framework. The initial shear band labelled 1 in Figure 2.5a was considered to be similar in shape to the arch assumed in the Engesser (1882) model, which is used in the GRC framework to calculate σ'_{TD} at maximum arching. However, while experimental studies suggest that the angle at which this shear band forms to the vertical is equal to ψ, Iglesia et al. (2013) still assume that it develops at an angle equal to ϕ. With increasing trapdoor displacement, the formation of near-vertical shear bands (labelled 3 in Figure 2.5a) is considered to resemble the assumed planes of sliding in the Janssen (1895) silo theory, which is used by Iglesia et al. (1999) to calculate σ'_{TD} at ultimate state.

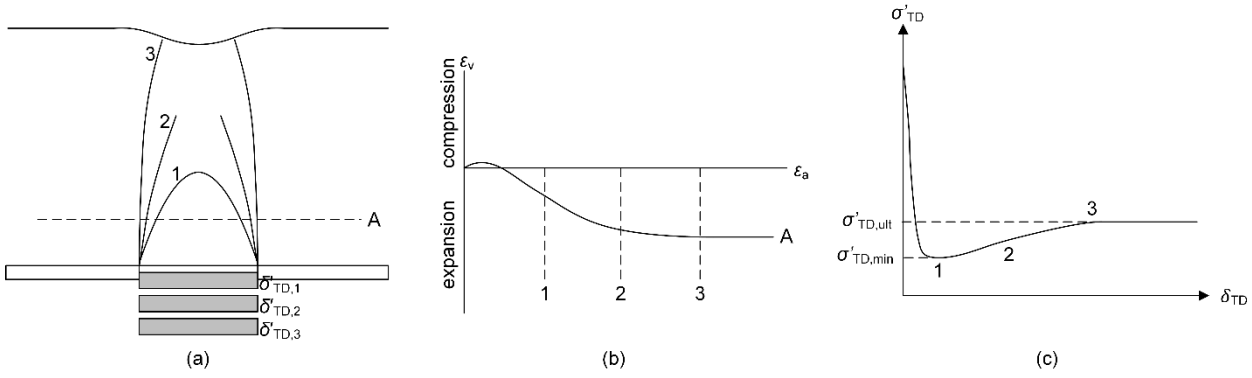

Figure 2.5: Progressive development of shear bands and soil arching (modified from Dewoolkar et al. 2007)

2.1.3 Arching in GRPEs

Principles of soil arching, much of which has been learnt from trapdoor tests, have been applied to GRPEs for over 30 years. Many arching models have been developed over this time specifically for GRPEs to estimate the load transferred directly towards the pile head (Load Part A), and as a result, the remaining load that is carried by the geosynthetic reinforcement and subsoil (Load Part B and C, respectively). These arching models were broadly grouped by Van Eekelen et al. (2013) into 5 categories of models (rigid, mechanical, empirical, frictional and limit equilibrium), which are briefly described below.

- **Rigid arch** models assume the shape and orientation of failure surfaces and estimate the stress acting on the geosynthetic reinforcement and subsoil as the weight of fill below these surfaces. Such models do not consider the mechanical properties of the load transfer platform (LTP) or embankment fill materials to affect the shape of the failure surfaces and do not consider shear stresses along the failure surfaces. An example is the model adopted by the "Nordic Guidelines for Reinforced Soil and Fills" (Rogbeck et al. 2003), which assumes that a triangular wedge failure surface develops between pile heads at an angle of 75˚ to the horizontal, as shown in Figure 2.6a.
- **Mechanical** models approximate the behaviour of an LTP using spring based models, such as the method proposed by Deb et al. (2007), which uses a Pasternak shear layer to represent the LTP granular material. Deb et al. (2007) state that the "*soil arching effect is ignored as the thickness of the granular fill is assumed to be small*". However, the use of a Pasternak shear layer, which considers shear interaction among springs within the system, is inherently modelling the load distribution from the soil arching.
- **Empirical** models simply fit an equation to an experimental dataset without the application of any theoretical soil mechanics framework. Van Eekelen et al. (2013) suggested that the method for estimating stresses on a buried pipeline proposed by Marston and Anderson (1913) is an empirical method. As shown previously, the method of Marston and Anderson (1913) is based on the same principles as the methods proposed by Janssen (1895) and Terzaghi (1943) and is more appropriately categorised as a frictional model. However, Jones et al. (1990) modified this method so that it could be used for three-dimensional piled embankment geometries, and in doing so, empirically fitted a load factor to the results of Marston and Anderson (1913).
- **Frictional** models assume failure surfaces and typically resolve the stresses acting on the pile heads and subsoil by applying a Mohr-Coulomb strength condition along these surfaces, including the Terzaghi (1943) and Janssen (1895) models described previously. Russell and Pierpoint (1997) extended the Terzaghi (1943) model to incorporate the three-dimensional geometry of GRPEs (Figure 2.6b), and Filz et al. (2012) made a further modification to consider

arching only below the critical height (Section 2.3.1) of a GRPE, which has been incorporated into their Load-Displacement Compatibility design method.

- **Limit equilibrium** models assume that an arch develops between piles, where the major principle stress direction is aligned in the tangential direction of the arch, and the minor principle stresses in the radial direction. However, it is noted that to derive a solution for the stress applied to the surface of a pile head using limit equilibrium methods, an assumption regarding the failure surfaces and the stress distribution along the failure surfaces should be made (Chen 1975). These arching models have been widely adopted in national design recommendations, and thus, some of the models will be further discussed in the following section.

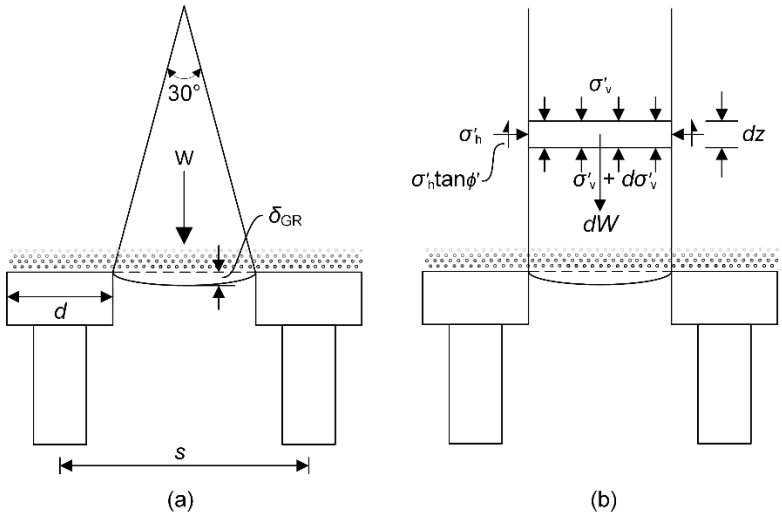

Figure 2.6: Assumed failure surfaces adopted in arching models proposed by (a) Rogbeck et al. (2003); (b) Terzaghi method adapted by Russell and Pierpoint (1997)

Hewlett and Randolph (1988)

One of the early limit equilibrium arching models that is still widely used is the Hewlett and Randolph (1988) arching model. In their experimental study, Hewlett and Randolph performed physical model tests of small-scale piled embankments, using both two-dimensional plane strain and three-dimensional arrangements. In tests where moist sand was used to model the LTP granular material, post-test examination of the underside of the sand embankment revealed the formation of "stable" arches. Based on the observations from their tests, a model was developed where it was assumed that three-dimensional hemispherical "domes" formed between piles, a two-dimensional section of which is shown in Figure 2.7a. However, given that the stable arch was only observed in tests with moist sand, this is likely a result of matric suction (apparent cohesion) rather than an indication of failure surfaces.

Hewlett and Randolph (1988) considered that two critical locations within the domes existed where failure may occur, at the crown of the arch or within the soil directly above the pile cap. By considering that the tangential stresses (σ'_θ) within the arch are related to the radial stresses (σ'_r) by the Rankine passive earth pressure coefficient, $\sigma'_\theta = K_p\sigma'_r$, the stresses within the arch are integrated and solved for the stress acting on the pile head. This stress is expressed by Hewlett and Randolph (1988) in terms of arching efficacy (E_A), defined as the proportion of the embankment load/weight transferred directly to the pile heads through arching (Load Part A). It should be noted that some studies refer to efficacy as the proportion of the embankment load transferred to the pile head through both arching and membrane actions (Load Part A and B), which will be represented in the present study by the symbol E_{A+B}.

The efficacy when a failure occurs at the crown of the arch is estimated by Hewlett and Randolph (1988) as:

$$E_{A,crown} = 1 - \left[1 - \left(\frac{a}{s}\right)^2\right](A - AB + C) \tag{2.12}$$

Where the coefficients A, B and C are equal to:

$$A = \left[1 - \left(\frac{a}{s}\right)\right]^{2(K_p - 1)} \tag{2.13}$$

$$B = \frac{s}{\sqrt{2}H}\left(\frac{2K_p - 2}{2K_p - 3}\right) \tag{2.14}$$

$$C = \frac{s - a}{\sqrt{2}H}\left(\frac{2K_p - 2}{2K_p - 3}\right) \tag{2.15}$$

Alternatively, failure may occur at the pile cap, in which case the efficacy may be calculated as:

$$E_{A,cap} = \frac{\beta}{1 + \beta} \tag{2.16}$$

Where the coefficient β is given as:

$$\beta = \frac{2K_p}{(K_p + 1)\left(1 + \frac{a}{s}\right)}\left[\left(1 - \frac{a}{s}\right)^{-K_p} - \left(1 + K_p\frac{a}{s}\right)\right] \tag{2.17}$$

Hewlett and Randolph (1988) recommend that the minimum of the efficacies calculated at the crown and pile cap is used for design purposes.

Zaeske (2001)

Zaeske (2001) performed 1:3 reduced scale 1g model tests, as described by Kempfert et al. (2004), to investigate the stress distribution in a reinforced sand layer overlying piles. Based on the observed stress

distribution, Zaeske (2001) assumed that multiple stress shell-like arches developed between piles, as shown in Figure 2.7b. Adopting similar limit equilibrium principles as Hewlett and Randolph (1988), Zaeske resolved the stresses within these arches. This led to a differential equation, which when solved for the radial stress acting at the crown of the aches, provided the vertical stress acting at the base of the LTP directly above geosynthetic reinforcement if present or the subsoil (σ'_{LTP}). This stress is given by:

$$\sigma'_{\mathrm{LTP}} = \lambda_1^{\chi}\left(\gamma + \frac{q}{h_{\mathrm{e}}}\right)\left\{h_{\mathrm{e}}(\lambda_1 + h_{\mathrm{a}}^2\lambda_2)^{-\chi} + h_{\mathrm{a}}\left[\left(\lambda_1 + \frac{h_{\mathrm{a}}^2\lambda_2}{4}\right)^{-\chi} - (\lambda_1 + h_{\mathrm{a}}^2\lambda_2)^{-\chi}\right]\right\} \tag{2.18}$$

Where q is the surcharge acting on the embankment surface, h_{a} is the height of the arch and the coefficients λ_1, λ_1 and χ are given as

$$\lambda_1 = \frac{1}{8}(s_{\mathrm{d}} - d)^2 \tag{2.19}$$

$$\lambda_2 = \frac{s_{\mathrm{d}}^2 + 2ds_{\mathrm{d}} - d^2}{2s_{\mathrm{d}}^2} \tag{2.20}$$

$$\chi = \frac{d(K_{\mathrm{crit}} - 1)}{\lambda_2 s_{\mathrm{d}}} \tag{2.21}$$

Where s_{d} is the largest centre-to-centre spacing between adjacent piles (the diagonal distance between piles on a square grid) and K_{crit} is the critical principal stress ratio, given as:

$$K_{\mathrm{crit}} = \tan^2\left(45^{\circ} + \frac{\phi}{2}\right) \tag{2.22}$$

Van Eekelen (2013, 2015)

Model experiments performed by Van Eekelen et al. (2012a) identified that the distribution of load acting on the geosynthetic reinforcement takes the form of an inverse triangle, rather than the triangularly shaped distribution that results from the stress arches assumed in the model proposed by Zaeske (2001). Considering the observed stress distribution in model tests, Van Eekelen et al. (2013) proposed a concentric arches model, which assumes that multiple stress arches develop between pile heads as shown in Figure 2.7c. Conceptually, Van Eekelen et al. (2013) described how these stress arches progressively develop from the outer arches inwards as subsoil undergoes settlement, which matches the progressive development of arching observed in laboratory and field measurements (see section below). However, as noted by Van Eekelen et al. (2013), limit equilibrium models exhibit a rigid-plastic behaviour unable of capturing the arching stress-subsoil settlement dependency.

The concentric arches model is an extension to the Hewlett and Randolph (1988), replacing the single arch with a finite thickness with multiple concentric arches. The equilibrium of stresses is calculated at

the crown of the arch for each arch radius. Based on the assumption that the tangential stress is consistent throughout the arch, the stress acting on the geosynthetic reinforcement is estimated based on the radius at which the arch intersects the geosynthetic. Due to the complex geometry associated with the concentric arches, a description of the derivation to estimate the load distribution (Load Part A, B and C) is outside the scope of this study, and readers are referred to Van Eekelen et al. (2013) for further details. A spreadsheet for estimating this load distribution (Load Part A, B and C) has also been made publically available (Deltares and Van Eekelen 2015).

Van Eekelen et al. (2015) compared the concentric arches model along with a number of analytical models, including the methods proposed by Hewlett and Randolph (1988) and Zaeske (2001), with several field case studies and model tests. Comparisons showed that the concentric arches model matched physical results, in general, more closely than other analytical methods, although discussion focused on the load distribution and geosynthetic deflections at a single point in time, rather than the progressive development or arching stresses over time or for different subsoil settlements.

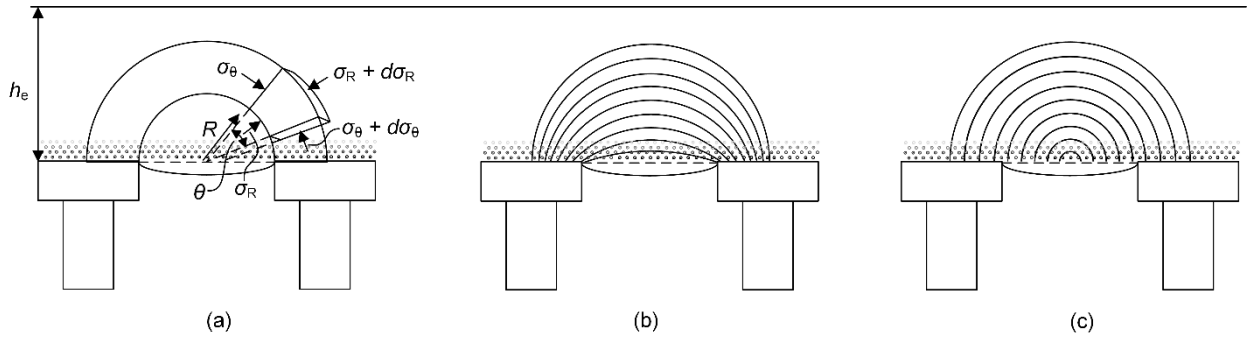

Figure 2.7: Assumed stress arches in the limit equilibrium models of (a) Hewlett and Randolph (1988); (b) Zaeske (2001); (c) Van Eekelen et al. (2013)

Comments on arching models

As described in Section 2.1.2, soil arching has been widely shown to develop as a trapdoor is displaced progressively. This behaviour has also been observed in several studies, including centrifuge modelling (Ellis and Aslam 2009a, b), full-scale field cases (King et al. 2017a, b) and numerical analysis (Lai et al. 2018). However, the soil arching models developed specifically for GRPEs described above consider only the load distribution at a single state, exhibiting a rigid-plastic behaviour independent of subsoil settlement. Further, these models fail to explicitly define how much subsoil settlement is required for this single state of arching to develop, i.e. whether the predicted stress distribution corresponds to maximum arching after a small amount of settlement or an ultimate state after a relatively large amount of subsoil settlement. These concerns were outlined by King et al. (2017b), who suggested the implementation of the GRC framework proposed by Iglesia et al. (1999) as a means for estimating the

progressive development of arching stresses as subsoil beneath a GRPE consolidates. In this method, King et al. (2017b) recommended normalising subsoil settlements by an equivalent area axisymmetric clear spacing between piles, so that the relative displacements proposed by Iglesia et al. (1999) for a plane strain trapdoor could be applied to subsoil settlements and GRPEs (see Section 4.2.1).

Some of the arching models described above assume failure surfaces to develop within the granular LTP material, including the frictional and rigid arch models shown in Figure 2.6. The vertical failure surfaces adopted in the arching model proposed by Terzaghi (1943), modified by Russell and Pierpoint (1997), are a simplification of the actual failure surfaces observed in active trapdoor tests (Figure 2.3). Similarly, the limit equilibrium models of Hewlett and Randolph (1988), Zaeske (2001) and Van Eekelen et al. (2013) assume stress arches to develop. Except for Hewlett and Randolph (1988) who based the shape of the soil arch on the observation of a stable mass of moist sand, the validity of which has already been questioned, the assumed geometry of the limit equilibrium models is based on measured stresses at discrete locations and geosynthetic deflections. None of the assumed failure surfaces or stress arches adopted in the soil arching models described are based on any observed kinematics in granular material overlying piles.

2.2 Geosynthetic reinforcement membrane action

Many of the theories regarding the development of strains and tensile forces in geosynthetic reinforcement spanning between piles are based on tensioned membrane theory introduced by Giroud (1981). Initial tensioned membrane theory assumed that the deflected shape of a geosynthetic overlying a void could be approximated by a circular curve. By assuming that strain in the geosynthetic is uniformly distributed, the strain may be estimated as:

$$\varepsilon = \frac{1}{2}\left(\frac{2\delta_{GR}}{b} + \frac{b}{2\delta_{GR}}\right)\sin^{-1}\left[\frac{1}{\frac{1}{2}\left(\frac{2\delta_{GR}}{b} + \frac{b}{2\delta_{GR}}\right)}\right] - 1 \tag{2.23}$$

Where δ_{GR} is the vertical deflection of the geosynthetic reinforcement and b is the span of the void. The deflected shape of the geosynthetic spanning a void may also be approximated as a parabola (Giroud 1995), in which case the strain in the geosynthetic may be estimated as:

$$\varepsilon = \frac{1}{2}\sqrt{1 + 16\left(\frac{\delta_{GR}}{b}\right)^2} + \frac{b}{8\delta_{GR}}\ln\left[\frac{4\delta_{GR}}{b} + \sqrt{1 + 16\left(\frac{\delta_{GR}}{b}\right)^2}\right] - 1 \tag{2.24}$$

By using truncated series expansions on both Equation 2.23 and 2.24, Giroud (1995) showed the equations for geosynthetic strain assuming both circular and parabolic deformed shapes may be approximated by:

$$\varepsilon = \frac{8}{3}\left(\frac{\delta_{GR}}{b}\right)^2 \tag{2.25}$$

However, tensioned membrane theory alone is insufficient to estimate the tensile loads that will be experienced by the geosynthetic reinforcement. Some of the common methods for estimating these tensile loads are detailed in the following section.

Jones et al. (1990)

After estimating the stresses transferred directly to the pile heads through arching (Load Part A) and assuming that the subsoil would not carry any of the embankment loads (Load Part C = 0), Jones et al. (1990) were able to estimate the load carried by the geosynthetic reinforcement (Load Part B). Jones et al. (1990) assumed that the vertical stress acting on the geosynthetic reinforcement was carried to the pile heads in concentrated strips of the reinforcement, equal in width to the width of the pile heads. In the case of an embankment with no surcharge acting on the surface, the line load (W_T) that acts on the strips of reinforcement between the pile heads is taken as:

$$W_T = s\gamma h_e\left(s^2 - a^2\,{\sigma_p'}/{\gamma h_e}\right) \tag{2.26}$$

Where σ'_p is the stress transferred to the pile head through arching, calculated by Jones et al. (1990) by empirically fitting a coefficient to the results of Marston and Anderson (1913). As shown in Figure 2.8a, Jones et al. (1990) consider the area of $s(s\text{-}a)$ to transfer the vertical load acting on the geosynthetic reinforcement towards the concentrated strips of reinforcement. It was shown by Van Eekelen et al. (2011) that this procedure applies the stress on the reinforcement twice, therefore not resulting in vertical equilibrium. Although in doing so, Jones et al. (1990) does provide a conservative estimate of the line load carried by the reinforcement.

By considering the geosynthetic reinforcement spanning between piles as a cable, Jones et al. (1990) followed the method described by Leonard (1988) to derive the tension acting in a cable under a uniformly applied load Figure 2.8b. Jones et al. (1990) estimated the tensile load (T) in the reinforcement under the uniformly applied line load of W_T by defining a maximum strain the geosynthetic could undergo, and by incorporating the deflection from Equation 2.25, estimated the tensile load as:

$$T = \frac{W_T(s-a)}{2a}\sqrt{1+\frac{1}{6\varepsilon}} \tag{2.27}$$

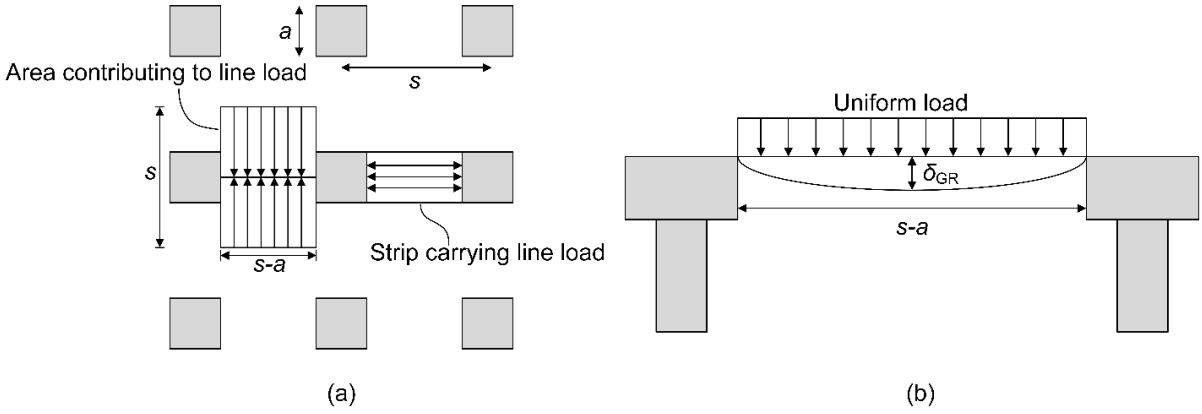

Figure 2.8: Jones et al. (1990) (a) assumed load transfer to strips of reinforcement; (b) deformed reinforcement between pile heads

Zaeske (2001)

After estimating the vertical stress acting on the surface of the geosynthetic reinforcement using Equation 2.18, Zaeske (2001) considered the loads to be carried to the pile heads through strips, similar to Jones et al. (1990) although the load was not applied twice (Figure 2.9a). Zaeske (2001) assumed that the load acting on the geosynthetic reinforcement in these strips was triangular in its distribution, rather than uniform, as shown in Figure 2.9b.

Zaeske (2001) considered the effect of subsoil support in their derivation of tensile force in geosynthetic deforming between piles. The subsoil was treated as an elastic spring with a modulus of subgrade reaction (k_s) resisting the deflection of the geosynthetic between piles. Given that the geosynthetic is assumed to carry load only in strips between the piles, the subgrade reaction is only considered beneath this strip, as identified by Van Eekelen et al. (2012b).

By treating the strip of geosynthetic reinforcement spanning between piles as an elastic cable, Zaeske (2001) showed that the loading and deformation of such a cable might be expressed by the differential equation:

$$\frac{d^2z}{dx^2} = \frac{q_z(x)}{T_h} + \frac{k_s z(x)}{T_h} \tag{2.28}$$

Where $q_z(x)$ is the load distribution applied on the geosynthetic strip between piles and T_h is the horizontal tensile load in the geosynthetic reinforcement due to its deflection. Zaeske (2001) solved this equation and presented the solution in dimensionless charts that could be used to estimate the average strain of the deformed reinforcement. This strain was then used to estimate the tensile load in the reinforcement through the equation $T = \varepsilon J$, where J is the tensile stiffness of the geosynthetic.

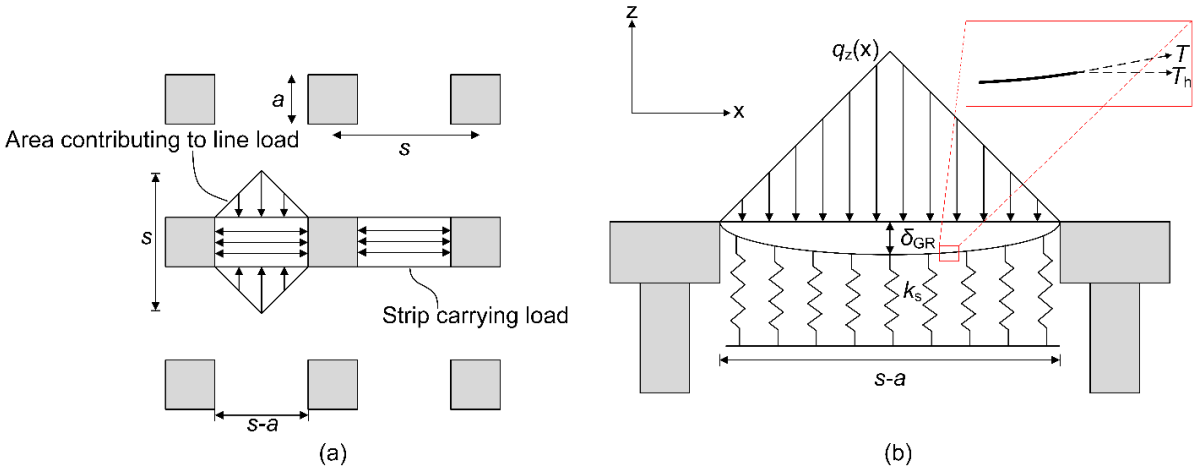

Figure 2.9 Zaeske (2001) (a) assumed load transfer to strips of reinforcement; (b) deformed reinforcement between pile heads

Van Eekelen (2012b)

The results from model-scale testing performed by Van Eekelen et al. (2012a) showed that the deflected geosynthetic reinforcement corresponded to a distributed load better represented by an "inverse-triangle", rather than the uniform or triangular distributions adopted in the methods proposed by Jones et al. (1990) and Zaeske (2001), respectively. Van Eekelen et al. (2012b) also considered the subsoil support below the entire area of geosynthetic reinforcement that deformed vertically, rather than just the strips between adjacent piles. To do so, Van Eekelen et al. (2012b) proposed a modified subsoil modulus (k_m), which may be written for piles on a square grid with square pile caps as:

$$k_m = \frac{A_L k_s}{(s-a)a} \tag{2.29}$$

Where A_L is the load coverage area, as shown in Figure 2.9a. Thus, the modified subsoil reaction modulus is equal to k_s increased by a factor to account for the load coverage area. In doing so, Van Eekelen et al. (2012b) used the same method as Zaeske (2001) to solve for the tension in the geosynthetic reinforcement under an inverse triangle load distribution while considering subsoil support over the load coverage area. Van Eekelen et al. (2012b) also provides dimensionless charts to estimate strain in the geosynthetic.

2.3 Settlements

2.3.1 Differential settlements

The differential settlement that develops in a GRPE at the base of an LTP, between the pile heads and subsoil, reduces with height above the pile heads. At some height above the pile heads, it has been shown that these differential settlements reduce such that a plane of equal settlement develops (Hewlett

and Randolph 1988; McGuire 2011; Fagundes et al. 2015). The height at which this plane of equal settlement forms within the embankment/LTP is referred to as the critical height (h_{cr}). As described previously, trapdoor tests typically do not result in the formation of a plane of equal settlement. Thus, this phenomenon is unique to the three-dimensional geometry and relatively low replacement ratio of GRPEs compared to trapdoor tests.

Design recommendations and standards for GRPEs often rely on the critical height concept to provide minimum embankment heights ($h_e > h_{cr}$) so that it can be ensured differential settlements do not develop at the embankment surface. The critical height, or minimum embankment height, is often based on an assumed soil arch geometry (Collin 2007; EBGEO 2011) or a series of physical model experiments (Chen et al. 2008; McGuire 2011). Some of the commonly adopted minimum embankment heights are shown in Table 2.1.

Table 2.1: Recommended minimum embankment height

Reference	**Minimum height**
Rogbeck et al. (2003)	$1.2(s–a)$
Filz and Smith (2006)	$1.0(s–a)$
Collin (2007)	$0.5(s–\mathrm{d})$
Chen et al. (2008)	$1.6(s–a)$
EBGEO (2011)	$0.8(s_d–d)$
McGuire (2011)	$1.15s'+1.44d$
BS8006 (2016)	$0.7(s–a)$
CUR226 (2016)	$0.66(s_d–d)$

While many of the minimum embankment heights or critical heights presented in Table 2.1 are simply based on an assumed mechanism and geometry, McGuire (2011) performed a series of bench-scale tests to determine the critical height. Testing was performed on medium-grained dense sand ($D_r = 70 – 100\%$), which due to the low confining stress in bench-scale tests and the density at which the sand was prepared at, exhibited a high peak friction angle ($\phi_p > 48^\circ$) and dilation angle ($\psi > 27^\circ$). Some of the key findings of the testing performed by McGuire (2011) in regard to the critical height were:

- Over the range of densities tested, the initial sand relative density had little effect on the critical height. It is noted, however, that the range of initial relative densities and the deviatoric response of the sand under these densities did not vary significantly in the testing performed. It is the author's opinion that it cannot be concluded from the limited testing performed by McGuire (2011) that initial density does not affect the critical height.
- While geosynthetic reinforcement reduced the magnitude of differential settlements, it did not affect the height at which a plane of equal settlement developed.
- The critical height is primarily governed by the pile spacing (s) and pile head size (a or d).

- Provided that the height of sand was greater than the critical height, the sand surface underwent uniform settlement even after large amounts of subsoil settlement. Thus, the critical height is independent of subsoil settlement.

2.3.2 Total settlement

The pile head settlement and consolidation of subsoil between piles beneath an embankment cause total settlements to be experienced at the embankment surface. The total settlement experienced at the embankment (S_{total}) is equal to the sum of the pile head settlement (S_p) and the settlement that develops within the fill as a result of subsoil settlement (S_e). The total pile head settlement, which may comprise some elastic shortening particularly when semi-rigid columns are used instead of piles, may be estimated using analytical techniques for the specific deep foundation and soil conditions.

Russell et al. (2003) proposed a method for estimating S_e, which has since been adopted by Filz et al. (2012) in their Load-Displacement Compatibility (LDC) method, and may be written as:

$$S_e = \frac{\delta_{s,max}(1 - \alpha_r)}{2} \tag{2.30}$$

Where $\delta_{s,max}$ is the maximum vertical deflection of the subsoil surface between piles, assumed to be equal to the vertical deflection of the geosynthetic reinforcement. The method proposed by Russell et al. (2003) assumes that the average differential settlement of the subsoil is equal to half of the maximum differential settlement between subsoil and piles. It is also assumed that the soil within the embankment fill undergoes no volume change as a result of shearing, and as such, all of the volume loss at the base of the embankment resulting from subsoil settlement will be experienced at the embankment surface. Results of testing performed by McGuire (2011) and Sloan (2011) show that this assumption is conservative (i.e. overestimates settlement), which is due to the materials in their tests exhibiting a strong dilative response to shearing.

2.4 Design methods

In the author's experience, four design methods/recommendations are most commonly used in practice to design GRPEs, those being BS 8006, EBGEO, CUR226 and the Load-Displacement Compatibility (LDC) method. Of these methods, the first three adopt a two-step design process to determine the load distribution amongst piles, geosynthetic reinforcement and subsoil and are commonly used across Europe. The LDC employs an iterative approach to satisfy force equilibrium and displacement compatibility and is commonly used by engineers in North America. Both of these design approaches are described below.

2.4.1 Two-step design process

Design methods that adopt a two-step design process start by assuming that soil arching is independent of subsoil settlement. This allows the design process to be broken into two steps to calculate Load Part A, B and C. Step 1 involves estimating the stress transferred to the pile caps directly through soil arching (Load Part A), which is calculated by the arching models described in Section 2.1.3. The remaining load not transferred to the pile heads through arching is then assumed to be carried by the geosynthetic reinforcement and subsoil (Load Part B and C). Step 2 estimates the tensile forces mobilised in the geosynthetic reinforcement (Load Part B) by using membrane models (as described in Section 2.2), which may or may not consider subsoil support (Load Part C).

BS 8006

The British Standards Institution "Code of practice for strengthened/reinforced soils and other fills", otherwise known as BS8006, includes a chapter regarding embankments with reinforced soil foundations on poor ground (Section 8), which provides recommendations specifically for the design of GRPEs. Published initially in 1995, BS8006 has been revised and amended several times since its initial publication, with the latest version being BS8006-1:2010+A1:2016, which was revised in 2010 and includes amendments from 2016.

In its initial version, BS8006 (1995) adopted the method proposed by Jones et al. (1990) to estimate the stress transferred directly to the pile heads through arching (Load Part A) and the tension carried in strips of reinforcement between piles (Load Part B), described previously. In its revision, BS8006 (2010) provided users with the option of using the limit equilibrium method proposed by Hewlett and Randolph (1988) to estimate stress transferred by arching to the pile caps. BS8006 in all its versions considers no subsoil support (i.e. Load Part C = 0).

EBGEO

The German Geotechnical Society (DGGT) "Recommendations for Design and Analysis of Earth Structures using Geosynthetic Reinforcements – EBGEO" was published in 2004 before being revised in 2010 and released in English in 2011 (EBGEO 2011). EBGEO recommends estimating the stress acting on the subsoil (Load Part B and C) using the multi-shell limit equilibrium method proposed by Zaeske (2001). In step 2, EBGEO again adopts the membrane action method proposed by Zaeske (2001) to estimate the tensile loads and strains in the geosynthetic reinforcement, which considers subsoil support by modelling the soil as a Winkler spring with a reaction modulus.

CUR226

The Dutch "Design Guideline for Basal Reinforced Piled Embankments" was first published in 2010, then later revised and released in English in 2016. In its initial release, CUR226 adopted many of the recommendations of EBGEO, including the Zaeske (2001) methods to calculate arching stresses and membrane actions. In the 2016 release, CUR226 adopted the concentric arches model proposed by Van Eekelen et al. (2013) to calculate arching stresses. Further, the recommended modifications to the Zaeske (2001) membrane model proposed by Van Eekelen et al. (2012b) regarding triangular load distribution and subsoil support were also adopted by CUR226 (2016).

2.4.2 Load-displacement compatibility

Numerical analysis performed by Smith (2005) highlighted the affect subsoil settlement had on the development of load transfer towards pile heads. This contradicts the assumption made by the two-step methods where arching stresses and subsoil settlement are de-coupled and leads to the main point of difference between the two types of design methods. The load-displacement compatibility (LDC) method adopts three load-displacement relationships, which are iteratively solved to satisfy load-equilibrium and displacement compatibility and estimate the load distribution and settlements among piles, geosynthetic reinforcement and subsoil. The three non-linear relationships included:

I. Stress acting on pile cap due to the LTP settling around pile cap
II. Geosynthetic deflection between piles
III. Compressibility of soil between piles

The load-deflection behaviour of the stress transferred directly to the pile cap (due to soil arching) is assumed to be linear until a limiting stress is reached. The linear response is estimated using the linear-elastic solution of Poulos and Davis (1974) for the displacement of a circular footing loaded on a semi-infinite mass. This relationship essentially approximates the stress acting on the top of the geosynthetic to reduce linearly with increasing relative displacement between the pile head and subsoil ($\delta_{s,max}$), the gradient of which is based on the elastic modulus of the LTP granular material. This reduction in stress continues until a limiting stress is reached. The limiting stress condition, which is assumed to remain constant with any increasing subsoil settlement, is estimated using the adapted Terzaghi method, modified by Russell and Pierpoint (1997). Filz et al. (2012) provided further modifications to this arching model by considering the effect of different LTP/embankment fill layers and only considering the shear stresses up h_{cr}, which is logical given that shear stresses will not develop above a plane of equal settlement.

Smith (2005) performed axisymmetric numerical analysis of a membrane deforming under a uniform load. This membrane was pinned at the edge of the pile head, and a roller boundary condition was

applied to the external boundary to represent the mid-span of the geosynthetic, where vertical deflection is greatest. An equation was fitted by Smith (2005) to the results of this modelling to estimate the deflection of the geosynthetic based on the uniform stress acting on the geosynthetic surface, the stress acting on the base of the reinforcement and the tensile stiffness of the reinforcement.

Stresses are transferred from the subsoil to the pile shafts (negative friction) as subsoil undergoes consolidation beneath an embankment until at some depth below the subsoil surface, the soil and pile settlement are equal. This load transfer is considered in the LDC method and is used to calculate vertical strains in the piles and subsoil resulting from the stresses applied to their surfaces. The total settlement of the subsoil and compression of the piles is then estimated by integrating the vertical strains over the depth of the pile.

2.5 Defective piles

The nature of constructing deep foundations below the ground surface means that the finished product cannot be visually inspected, and as such, ensuring the integrity of deep foundations can prove difficult. Defects within piles, or ground improvement columns, may arise due to a number of imperfections or conditions, which Poulos (2005) broadly grouped as geological imperfections, inadequate ground investigation, pile construction, loading during construction and loading during operation. Geological imperfections are due to the ground conditions at the site, which may include non-continuous layers, non-horizontal layers, boulders floating within the soil (Figure 2.10a), sloping bedrock, karst ground conditions, intrusions within the rock, compressible layers below founding stratum, etc.

When a ground investigation is insufficient in scope to detect and characterise many of the ground conditions associated with geological imperfections, the effects of these conditions may be intensified. A common scenario is non-homogenous ground conditions, which are incorrectly identified as homogeneous by a limited number of boreholes. As shown in Figure 2.10b, this may result in some piles not having a sufficient embedment into a founding stratum. Abdrabbo and Abouseeda (2002) presented a case study from Egypt where a 10 level building supported by 8 m long bored piles designed to be founded in sandstone, although due to an insufficient ground investigation, were approximately 1 m shallow of this founding stratum. As a result, this building experienced 1:70 vertical differential settlement. Where a limited ground investigation has been performed for an embankment spanning a large footprint supported by ground improvement columns, such as drilled displacement columns (DDCs), the rig instrumentation (most commonly torque) may be heavily relied upon to determine the depth at which a stiffer/denser founding stratum is encountered (Gniel and Haberfield 2014). In the event an increase in rig torque is incorrectly assessed as a suitable founding layer, columns may be terminated with an insufficient socket into the founding stratum, as was noted by Michalowski et al. (2018) to have contributed to the serviceability failure of an embankment supported on DDCs.

Imperfections associated with pile construction may be broadly grouped into two main categories, structural and geotechnical. Structural defects are associated with the pile structure itself and may include the pile size (diameter or length) not being as per design or the pile material being weaker than or not as stiff as designed for. Specifically for bored piles, Sliwinski and Fleming (1983) describe how the segregation of concrete, formation of cavities, displacement of reinforcement cage and necking can affect the integrity of a pile. Geotechnical defects are due to the ground conditions impacting the construction of the pile, such as the use of drilling fluid in bored piles, which can cause a reduction in the pile shaft resistance (de Lima 2017). Disturbance to the ground during the construction of the pile may also result in reduced shaft and/or base resistances as well as the presence of soft debris at the base of the pile (soft pile toe) due to insufficient cleaning of the pile base. Defects associated with construction of deep foundations are particularly common in unreinforced ground improvement columns. King et al. (2018) showed that for a typical layout adopted in piled (or column supported) embankments, the installation of full-displacement unreinforced columns such as DDCs would cause such lateral deformations within soft soils that the unreinforced columns would likely crack during construction.

Once deep foundations have been constructed, loading and deformations associated with ongoing construction activities may also cause defects. An example may include the stockpiling of material, particularly when such loads induce lateral movements and bending moments that exceed a pile's capacity. Analysis undertaken by Chen et al. (1999) and Mroueh and Shahrour (2002) showed that considerable loads were also experienced by piles adjacent to nearby tunnelling work.

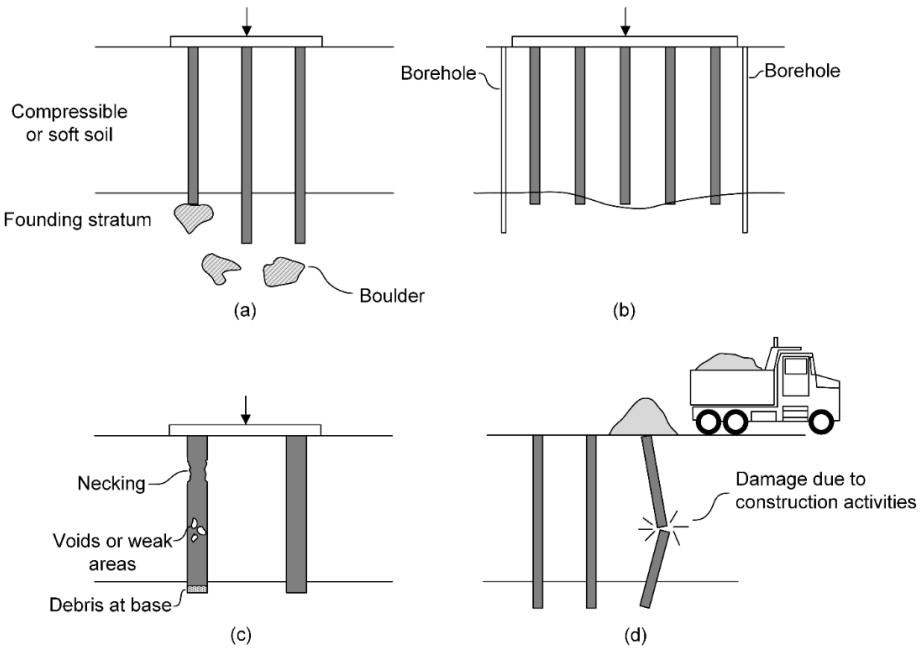

Figure 2.10: Defects arising due to (a) geological sources; (b) inadequate ground investigation; (c) construction techniques; and (d) construction actives, modified from Poulos (2005)

Poulos (1997) performed a numerical analysis to investigate the load-settlement response of piles comprising defects, both as isolated single piles and within a group (discussed in the following section). The results of this analysis for a pile comprising a reduced cross-sectional area (necking) 10% of the unaffected pile section, extending from the pile head to a depth of 8 m below the ground surface, are shown in Figure 2.11a where the applied load (P) is normalised by the ultimate geotechnical capacity of the non-defective pile (P_u). The analysis was performed for different concrete compressive strengths, and it was shown that the defective pile underwent additional settlement to the non-defective pile. It is also seen in Figure 2.11a that with reducing concrete compressive strength, the defective pile began to fail structurally due to the reduced cross-sectional area, which resulted in large settlements.

Using the same numerical techniques, Poulos (1997) also analysed the effect of soft debris at the base of a pile on the pile's load-settlement response (Figure 2.11b). This analysis looked at the effect of the Young's modulus of the soft debris (E_{bs}) relative to the Young's modulus of the founding stratum (E_b), and showed that soft debris at the pile base reduced the axial stiffness of the pile. Large settlements were shown to develop for loads approaching the ultimate geotechnical capacity of the pile. It was concluded by Poulos (1997) that while different types of defects will have different effects on the load-settlement response of a pile, the presence of defects leads to a reduction in axial stiffness of the pile.

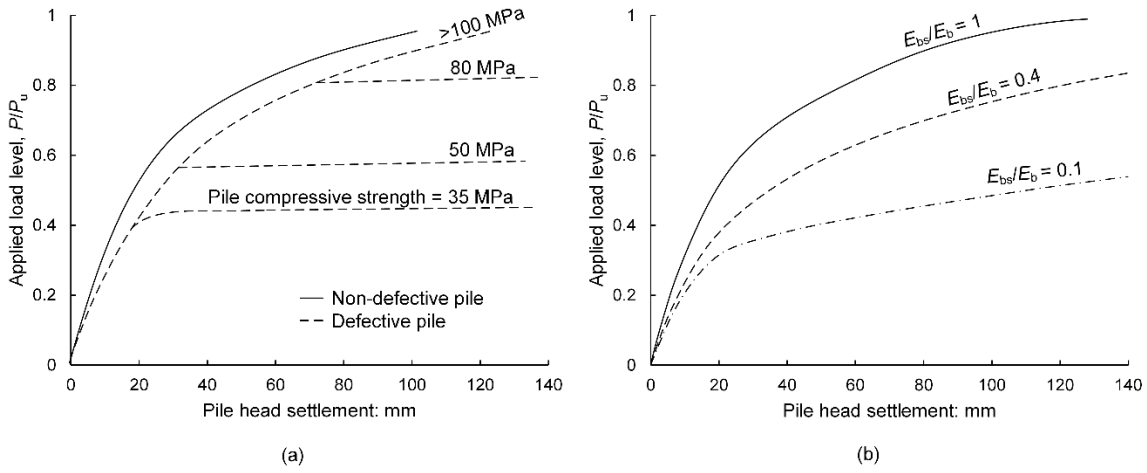

Figure 2.11: Load settlement curves for single pile comprising (a) structural defect (necking); (b) soft base, modified from Poulos (1997)

2.5.1 Defective piles within a pile group

When piles are installed in a group and structurally connected at their heads (pile cap), loads are distributed amongst the piles, such that piles comprising defects do not carry the same load as non-defective piles. Zhang and Wong (2007), also reported by Wong (2004), undertook centrifuge modelling of pile groups containing defective piles (both soft bases and shorter piles) to investigate the load distribution amongst piles within the group as well as the bending and tilting of the pile group. In

their study, Zhang and Wong (2007) modelled 2 x 2 groups of bored piles, each measuring at prototype scale 2 m in diameter and 15 m in length founded on bedrock (in the case of non-defective piles). Load testing on single piles confirmed that the presence of a soft toe reduced the mobilised base resistance of the pile, although the shaft resistance was unaffected by the soft pile toe. The findings from these tests may be summarised as:

- Both soft toes and short piles within a group of piles reduced the axial capacity of the pile group, although the reduction in axial capacity of the pile group was less than the reduction in axial capacity experienced by a single defective pile.
- The load distribution amongst piles within the group meant that non-defective piles carried some additional load compared to the defective piles, which was attributed to the difference in axial stiffness between the defective and non-defective piles.
- Differential settlements developed between defective and non-defective piles, resulting in the tilting of the pile cap. This rotation caused significant bending moments to develop within the piles and pile cap, with a maximum bending moment experienced at the pile head.

Numerical analysis performed by Kong and Zhang (2004) and Poulos (1997) showed results in agreement with the above-described centrifuge modelling, where the load was redistributed away from defective piles towards non-defective piles, and pile caps underwent rotation due to the presence of defective piles.

2.5.2 Defective piles supporting embankments

LTPs and embankments do not provide a "rigid" structural connection between piles underlying an embankment in the same way that pile caps connect piles within a group. Instead, LTPs and embankments provide a "flexible" connection between piles within a group, and therefore, will behave vastly different to a pile group connected by a pile cap. The transfer of embankment loads within a GRPE towards pile heads is due to soil arching (Section 2.1) and membrane actions (Section 2.2), and thus, the interaction between defective piles, non-defective piles and the overlying LTP is an extremely complex soil-structure-geosynthetic interaction problem. To date, this interaction has not been studied either numerically or physically.

Recommendations provided in the Dutch design guidelines CUR226 (2016) suggest that redundancy may exist within a GRPE if an embankment is of sufficient height. CUR226 states that "*... if one pile fails, the arching will re-establish itself. If the embankment is sufficiently high, the load will be transferred to the surrounding piles via this newly re-established arching.*" Based on the recommended minimum embankment height of $0.66(s_d - d)$, see Table 2.1, it is assumed by CUR226 that if a pile is to fail, or comprise a defect such that its axial stiffness is significantly reduced, then arching will re-establish itself if $h_e > 0.66(2s_d - d)$, as shown in Figure 2.12. However, this state of arching is not based

on any understanding of soil mechanics or any observed failure mechanism. It is simply an assumed shape of soil arching extended from an analytical model that is also not based on any observed soil kinematics.

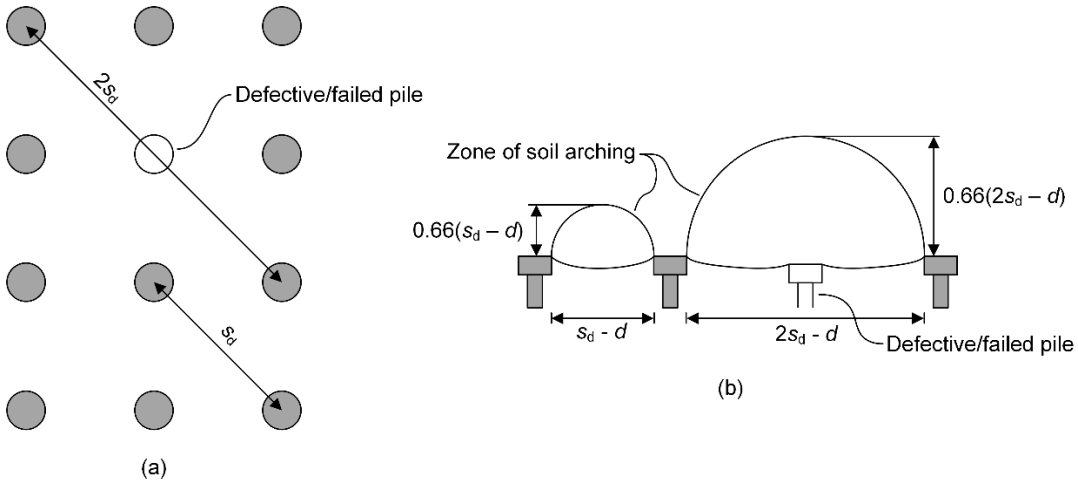

Figure 2.12: Assumption of CUR226 (2016) regarding defective piles (a) plan view; (b) cross-section

2.6 Physical modelling experiments

A large number of physical modelling experiments have been undertaken over the past 30 years to investigate piled embankments, both with and without geosynthetic reinforcement. Some of these studies are described and discussed in the following section, with studies divided into 1*g* model tests and centrifuge model tests.

Table 2.2: Previous studies comprising 1*g* model tests

Reference	LTP/embankment granular material	Pile arrangement	Geosynthetic reinforcement	Subsoil or displacement control	Imaging	Comments
Hewlett and Randolph (1988)	Sand (density not described)	2D plane strain and grid of piles	No reinforcement	Foam rubber chips	Coloured sand layers viewed through a transparent window	This study was one of the first experimental investigations into soil arching in piled embankments, which led to the commonly used Hewlett and Randolph (1988) arching model. However, the experiment does not consider scaling effects or sand density. Further, a series of tests were performed with moist sand. After the foam settled beneath the moist sand, the sand within the zone of arching was inspected from the underside. It was observed that a stable soil arch formed, which is the basis of the Hewlett and Randolph method. This arch is likely a result of soil suction and is not an indication of a "stable" arch or failure surface.
Low et al. (1994)	Sand prepared at D_r = 41% (+/- 8%)	2D plane strain	Single layer of geotextile, J = 400 kN/m	Foam	Transparent windows, no displacement field.	This study used a plane strain geometry, which did not scale geosynthetic stiffness. The study expanded on the Hewlett and Randolph (1988) method, considering geosynthetic reinforcement. The authors note that scaling has not been rigorously considered and centrifuge modelling or full-scale studies are needed to validate the model.
Zaeske (2001) described by Kempfert et al. (2004)	Sand (density not described)	2x2 square grid of piles	Tests performed with and without reinforcement	Soft peat	No imaging	This series of tests resulted in the development of a widely-used soil arching model which has since been adopted by EBGEO. Without the original manuscript, critical analysis of the testing is not possible. However, it is noted that the 2x2 pile grid will likely comprise boundary effects and the depth of subsoil (400mm) would likely have resulted in small subsoil settlement in-line with maximum arching conditions.
Villard et al. (2004) and Chew et al. (2006)	Sand (compacted but density not described)	Piles on a triangular grid	Two layers of uniaxial geotextile J = 577 kN/m	Excavation of underlying subsoil	No imaging	This test facility incorporated a grid of piles. The results from testing comprised observable boundary effects. Further, the excavation of soil does not simulate the gradual consolidation of subsoil and led to a non-symmetric settlement contour map. Soil arching is likely effected by the excavation process, rather than more uniform subsoil settlement.

Reference	LTP/embankment granular material	Pile arrangement	Geosynthetic reinforcement	Subsoil or displacement control	Imaging	Comments
Jenck et al. (2005) and Jenck et al. (2007)	Aluminium rods	2D plane strain	No reinforcement	Foam	DIC performed on photographs through transparent window	This testing utilised aluminium rods, which were reported to have a friction angle of ϕ = 24 degrees, significantly lower than a typical LTP granular material. DIC was applied to pairs of images as the foam settled over a period of 80 minutes. The 2D nature of this model and the materials used means that it is well suited to the calibration of a purely 2D numerical model although provides little insight into the mechanism of soil arching in piled embankments.
Hong et al. (2007) and Hong et al. (2011)	Sand D_r = 72.8%	2D plane strain	No reinforcement	Tests were conducted using a device with a mechanical tray or soft clay	Coloured sand layers viewed through transparent window	This paper describes testing where soil arching is investigated in plane strain model tests with observations through a transparent window. Strain-controlled tests where subsoil consolidation is simulated by a mechanical tray as well as stress controlled tests with soft clay subsoil were both performed. The failure surfaces after small displacement indicate the formation of shear bands above the pile heads, However, after significant displacement of the mechanical tray, an almost semi-circle zone of soil collapses, and leaves a stable zone of sand still in place above the collapsed zone. This observation is inconsistent with other studies (Rui et al. 2016; Cui et al. 2017), although may occur if the sand was partially saturated. The tests performed only consider a single span between two cap beams.
Oh and Shin (2007)	Silty sand (weathered granite, compaction not described)	3x3 square grid of piles	Biaxial geogrid, T(@ 5% strain) = 8.5 kN/m (MD) and 13.4 kN/m (CD)	1.5 m thick deposit of marine clay	No imaging	The study installed piles through a 1.5 m thick marine clay layer. The authors then used a geosynthetic reinforcement with a low axial stiffness and concluded that the effect of the geogrid is negligible. However, the thickness of the soft subsoil meant that the subsoil settlement was insufficient to engage significant tensile loads within such a low stiffness geosynthetic. The conclusion that the geosynthetic reinforcement is negligible is, therefore, based on subsoil conditions and reinforcement properties that would not be used in the field. Further, the material used as embankment fill (silty sand) is unlikely to exhibit friction and dilation angles, although not reported, representative of typical LTP granular material.
Chen et al. (2008)	Sand prepared at D_r = 55% (+/- 7%)	2D plane strain	Geosynthetic with T(@ 8% strain) = 0.35, 1.4 and 22.5 kN/m	Water bag with water released to simulate subsoil consolidation	No imaging	These 2D plane strain model tests showed that arching stresses developed as subsoil consolidated. However, the scaling of geogrid is questionable and 2D nature of model tests is not realistic. As a result, the comparison made to existing design methods is of little value.

Reference	LTP/embankment granular material	Pile arrangement	Geosynthetic reinforcement	Subsoil or displacement control	Imaging	Comments
McGuire (2011)	Sand prepared at D_r between 70% and 100%	Single column, 2x2 and 5x5 square grids	Biaxial geogrid , J = 4.3 - 25.8 kN/m	Mechanical tray	No imaging	This bench scale study focused on identifying the critical height for a range of pile spacing's, pile geometries, sand densities and geosynthetic stiffnesses. It was shown that the critical height was dependent on pile spacing and diameter, and not measurably affected by the relative density over the range of 70-100%. The stiffness of geosynthetic reinforcement did not affect the critical height.
Sloan (2011)	Well compacted crushed rock	2x2 and 3x3 square pile grids	3 to 5 layers biaxial geogrid	Geofoam, dissolved to remove subsoil support	No imaging	This study comprised a full-scale embankment built over short concrete piles/columns with a geofoam that was dissolved to simulate subsoil consolidation. The results closely matched the critical height as determined using method proposed by McGuire (2011). Results were consistent with LDC method predictions.
Briançon and Simon (2012)	LTP comprising gravel (compaction not described) and embankment fill comprising marly/chalky material	Full-scale GRPE	2 layers of biaxial geogrid T(@ 10% strain) = 58 kN/m and one layer of geotextile T(@ 10% ε) = 79 kN/m	Field study with site underlain by soft deposits	No imaging	This study formed part of the French Amélioration des Sols par Inclusions Rigides (ASIRI) project, and studied four instrumented sections with difference reinforcement arrangements. The testing showed the development of relatively higher strains at the edge of pile caps and that differential settlement between pile heads and subsoil develops during construction. However, the compressibility of the subsoil at the test location was less than what is commonly encountered below GRPEs in the field. As a result, the subsoil consolidation and relative displacement is small and the arching stresses do not reach a maximum.
Eskişar et al. (2012)	Samples comprising either sand or dry clay prepared at approximately D_r = 80%	2x2 square grid of piles	Two types of geogrid tested J = 15 and 67 kN/m. Scaling not described. Geogrid not laterally restrained	Mechanical tray	X-ray CT, no image correlation performed. Voxel size = 1000 x 293 x 293 micron (height x length x width)	This is the only experimental study (prior to the current study) to show the 3D soil arching in piled embankments. However, it did not consider scaling rigorously. For example, the plate was mechanically lowered 5 mm before any imaging was performed. This displacement corresponds to a relative displacement of 17%, well beyond what would occur in any piled embankment performing as per design. Progressive development of soil arching was not studied, only a single state was imaged. The scaling of the geogrid is not considered, with apertures up to 5 mm x 5 mm, which means that sand grains (d_{50}<0.2 mm) did not interlock with the geogrid, which is evident in the CT images although not described by the authors. The resolution of the CT images means that strain localisations cannot be observed. Given that the height of the voxels was 1 mm, and the width of the shear band for a sand with a d_{50} = 0.12 is approximately 1.2 mm (10 x d_{50}), strain localisation cannot be observed.

Reference	LTP/embankment granular material	Pile arrangement	Geosynthetic reinforcement	Subsoil or displacement control	Imaging	Comments
Van Eekelen et al. (2012a)	Sand or crushed recycle construction material (compacted, although D_r not described)	2x2 square grid of piles	Uniaxial and biaxial geogrids and geotextiles with a range of axial stiffnesses, J = 757 - 2904 kN/m	Water soaked foam cushion	No imaging	One of the more comprehensive experimental programmes, which tested many reinforcement arrangements. The study did not scale the geosynthetic as it attempted to induce equivalent stresses in the model as would be expected in the prototype by applying a surcharge to the surface. This approach still incorrectly scales the stress gradient within the embankment fill materials due to the scaled height of the embankment. This study showed that the stress distribution acting on the geosynthetic follows the shape of an inverse triangle. This finding is not in-line with the assumptions made by other membrane models, and is later used to develop the concentric arches model proposed by Van Eekelen et al. (2013).
Xing et al. (2014)	Gravel, well compacted. Sand (D_r = 70%) overlying the gravel	Group of 6 piles on an equilateral triangular grid surrounded by circular steel casing	One test with two layers of biaxial geogrid T(@ 10% strain) = 40 kN/m, one test without any reinforcement	Site underlain by highly compressible deposits	No imaging	Large-scale study with a static load test. Results show that EBGEO predicts pile efficacy well. However, the authors note that "EBGEO can be used in the design of pile-supported embankments with a triangular arrangement". However, this statement is only true if the piles are on a square grid rotated 45° to the longitudinal direction. EBGEO states that "*other triangular grid shapes (e.g. 60°) are not dealt with in these recommendations*". The equilateral triangular grid adopted in this study is one of these "other" arrangements that EBGEO should not be applied to. Further, none of the discussion provided in this study addresses subsoil settlement or the progressive development of soil arching.
Chen et al. (2016)	Sand and gravel layers	3x5 square grid of piles	Single layer of uniaxial geogrid with J = 2459.5 kN/m	Water bag, water released to simulate subsoil consolidation	No imaging	The tests were performed at the full-scale facility at Zhejiang University, which is capable of simulating high-speed train loadings. The study measured the geogrid strain during construction of the embankment due to lateral spreading by preventing drainage from the water bags. The measurement of lateral loads is considered not realistic, as the subsoil is modelled by a waterbag, and hence will not exhibit the same frictional properties (and resistance) to a soft clay or working platform. The study compares measured geogrid tensile loads to BS8006 and recommends amendments that they consider are more accurate. This is not verified with comparisons to other experimental or field case studies. Further, the simulation of load development during construction is flawed, as subsoil settlement is only simulated due to the water bags deforming under the imposed loads. There is no control over the waterbag deflection nor is it measured during “construction”.

Reference	LTP/embankment granular material	Pile arrangement	Geosynthetic reinforcement	Subsoil or displacement control	Imaging	Comments
Rui et al. (2016)	Sand, three coarse and one medium grained (D_r = 85%)	2D plane strain	No reinforcement	Mechanical tray	DIC performed on photographs through transparent window	This study performed 2D plane strain model tests visualising deformations through a transparent window with DIC applied to pairs of photographs to obtain displacement and strain fields. While the study indicates that several piles were modelled with a mechanical tray lowered between the piles, describing the test as a "multi-trapdoor" test, no discussion of interaction between failure surfaces above adjacent piles is provided. The geometry of most the tests are more closely described as trapdoor tests rather than a piled embankment model test. A plane of equal settlement was observed in only a select few tests. The geometry of these tests that developed a plane of equal settlement had replacement ratios equivalent to piled embankments. Other tests that did not develop a plane of equal settlement had much larger replacement ratios, similar to conventional trapdoor tests.
Xu et al. (2016)	Sand and sand with fibres to investigate influence of fill cohesion	2x5 square grid of piles	Biaxial geogrid, J = 500 kN/m and aperture size of 40 mm x 40 mm	Sand mixed with EPS beads	No imaging	Model tests were performed with a subsoil substitute made from a mixture of sand and expanded polystyrene (EPS) beads. Piles tested were both end-bearing and floating within the sand-EPS mixture. It is considered that floating piles in this mixture will not exhibit a load-settlement response that is relatable to GRPEs in the field. The shaft and end-bearing resistance of the piles in this mixture will be significantly different to piles founded within clay. Also, the paper models fill with cohesion by mixing sand with fibres. However, it is not discussed what prototype material they are attempting to model. A clayey sand would likely have some cohesion, although not exhibit the same friction angle as a clean sand. The fibre sand-mixture used in the study is shown to have the same ϕ =38° as the clean sand.
Cui et al. (2017)	Sand (ρ_d = 1500 kg/m^3, although min and max densities or void ratios not described)	2D plane strain	No reinforcement	Mechanical tray	Coloured sand layers viewed through transparent window	This study observed different failure surfaces in 2D plane strain models with different embankment heights. It was shown that arching stresses develop progressively as the mechanical tray was lowered. However, only three piles were modelled in a 2D arrangement. Again, these 2D failure surfaces observed are likely different to those that would develop within a piled embankment. An interesting finding is that different failure surfaces developed with different embankment heights.

Table 2.3: Previous studies comprising centrifuge model tests

Reference	*N*	LTP/embankment material	Pile/column arrangement	GR	Subsoil or displacement control	Comments
Lee et al. (2005)	50	Sand (Dense, although D_r not describe)	Square grid of 37 piles installed at 1*g*	No reinforcement	Kaolin clay prepared in centrifuge	Using different pile cap sizes, the study investigated replacement ratios ranging from 6 to 30%. The study also comprised a relatively thin (2 m in prototype) embankment with a tank applied at the sand surface, which was filled during the test. The results indicated the benefit of installing pile caps to increase the replacement ratio, which reduced settlements. Although, beyond 25%, no significant benefit was observed. It was also observed that piles under the centre of the tank carried more load than piles under the edges/corner of the tank.
Weber et al. (2006)	50	Sand (density no described)	Sand compaction piles installed in-flight using specially designed instrument	Geosynthetic reinforcement used although properties not described	Natural clay prepared under consolidation at 1*g*	The study installed sand compaction piles in-flight using an innovative device. The study installed limited instrumentation, with no measurements of pile loads, geosynthetic tensions, subsoil stresses or subsoil settlements. Therefore, the results are rather limited, although the installation of sand compaction piles in-flight is an example of advanced centrifuge modelling techniques.
Kitazume and Maruyama (2007)	50	Sand, rained in-flight	Groups ranging from 3x6 to 7x6 square grid of deep mixing columns. Columns prepared in consolidated clay at 1*g*	No reinforcement	Kaolin clay prepared in centrifuge	The study investigated the stability of deep mixing columns under embankment slopes. By raining in the embankment sand in-flight, the embankment height could be increased until failure was observed. The failure of columns was observed through a transparent window. It was shown that columns under the embankment slope don't fail simultaneously. Instead columns fail progressively, starting with the forefront column and failing backwards in sequence.
Ellis and Aslam (2009a,b)	10 to 60	Sand (D_r = 90 to 95%)	3x3 and 4x4 square grid of piles	No reinforcement, although tests with geogrid were reported in Aslam (2008).	Foam	This study was one of the first to show the progressive development of soil arching to be well described by the ground reaction curve (GRC). An interaction diagram is proposed, which allows geosynthetic stiffness and subsoil support to be considered. This interaction diagram considers the mobilisation of Load Part A, B and C as subsoil settles.

Reference	*N*	LTP/embankment material	Pile/column arrangement	GR	Subsoil or displacement control	Comments
Baudouin et al. (2010)	27.8	Sand (Dr not described)	3x3 square grid of piles	No reinforcement	Clay (with some sand), normally consolidated in-flight	This study incorporated normally consolidated subsoil, through which the piles are installed at 1*g*. The study applied loads at the embankment surface to simulate different structures. Only small replacement ratios (less than 5%) were investigated, which are typically too low for embankments supported on soft clays although may be appropriate when firm-stiff clays are present.
Blanc et al. (2013) and Blanc et al. (2014)	20	Sand (D_r = 74%)	Large group of piles on square grid	Biaxial geotextiles, J = 2960 kN/m and 4760 kN/m in longitudinal and transverse directions respectively (prototype scale)	Mechanical tray, details of which are provided in (Rault et al. 2010). Note, other tests using this device were also reported by Girout et al. (2016) and Girout et al. (2018), although layouts and findings were similar to those reported by others	This study investigated low replacement ratios (α_r < 5%) and shallow embankment heights (h_e <1.8 m), and as a result, the majority of tests resulted in differential settlement developing at the embankment surface. It was shown that geosynthetic reinforcement improves load transfer to pile heads, which reduces the stress acting on the subsoil and differential settlements.
Fagundes et al. (2015) and Fagundes et al. (2017)	20	Sand (D_r = 57%)				The models tested as part of this study comprised model geometries with α_r > 4.91% and h_e = 1-7.2 m, both with and without geosynthetic reinforcement. It is shown that the critical height was in close agreement with the method proposed by McGuire (2011), and not so much with BS8006 (2010). It was also shown that arching stresses develop progressively with subsoil settlement, and the maximum arching stress was well approximated by the Hewlett and Randolph (1988) method.
Okyay et al. (2014)	12 and 20	Sand (D_r = 85%)		No reinforcement		This study covered many of the geometries tested as part of Blanc, et al. 2013 and 2014, although applied cyclic loading to the sand surface by filling and emptying a water tank. This loading simulated the cyclic loading of an LNG storage tank. It was shown that while the unloading-reloading of a tank resulted in a reduction in load transfer to pile heads, a small amount of subsoil settlement remobilised arching stresses. It was concluded that cyclic loading-unloading of a tank does not influence the behaviour of the LTP. However, it is the opinion of the author that this conclusion is incorrect. If arching stresses reduce after an unloading-reloading cycle, then additional stress will be experienced by the subsoil. While it is shown that a small amount of subsoil settlement will remobilise arching stresses, this will still result in some additional subsoil settlement. Cumulatively over many cycles this may result in excessive surface settlement.

Limitations of physical model tests

Some of the apparent issues and limitations with previous physical model studies investigating piled embankments include:

- Many of the model tests reported did not consider the density of the model LTP granular material to be of importance, such that many studies did not report the density at which material was prepared at. Furthermore, several tests used sand to model the LTP granular material and prepared it at $D_r < 70\%$. Given that LTP material typically comprises well compacted granular material, which exhibits high peak friction and dilation angles, many of the studies have not selected and prepared a granular material that will appropriately model the deviatoric response of the prototype material.
- Several of the studies have not rigorously considered the scaling of the geosynthetic reinforcement. Of critical importance to accurately modelling membrane actions is the scaling of the axial stiffness (J) of the reinforcement. For 1g reduced scale model tests, this is very difficult, as the appropriately scaled stiffness is very small, such that it is difficult to find a commercial product with a repeatable stiffness. Most centrifuge model tests did include reinforcement.
- Several studies that performed two-dimensional model tests essentially modelled multiple trapdoors adjacent to each other without considering how the plane strain arrangement may influence soil arching or how the geometry between two- and three-dimensional arrangements could be related, e.g. ensuring similitude between replacement ratios. Some of these studies made comparisons of the test results to analytical design models and concepts such as the critical height, both of which are typically three-dimensional in nature. Thus, many of the conclusions in these two-dimensional model tests are not justified.
- Only two of the studies reported in Table 2.2 implemented image correlation techniques to determine full-field displacement vectors, both of which were plane strain 1g model tests (Jenck et al. 2005; Rui et al. 2016). Only one model test observed the three-dimensional arching mechanism, although image correlation techniques were not utilised and the resolution of the images was insufficient to observe any failure mechanism in detail (Eskişar et al. 2012). Thus, none of the physical model tests have shown the three-dimensional kinematics of soil arching.

2.7 Summary

The load transfer in GRPEs, under the centreline, is predominantly due to soil arching and membrane actions. In two-dimensional active trapdoor tests, it has been shown that soil arching cannot be described by a single state. As the trapdoor is lowered, soil arching progressively develops, which is well described by the ground reaction curve proposed by Iglesia et al. (1999). The dependency exhibited

between arching stresses and trapdoor displacement are explained by the mobilisation of dilation and shear strength as well as the development of sequential failure surfaces that propagate to the soil surface.

The clear majority of existing GRPE design methods predict arching stresses (loads towards the pile heads) without any consideration of subsoil settlement. However, it has been shown that arching stresses progressively develop as subsoil undergoes consolidation. The progressive development of soil arching in piled embankments cannot be explained by the formation of sequential failure surfaces propagating to the embankment surface, as this contradicts the observations that a plane of equal settlement develops independently of the amount of subsoil settlement. Thus, the three-dimensional nature and low replacement ratio adopted in piled embankments result in a different soil arching mechanism to trapdoor tests.

Several studies have performed two-dimensional plane strain model testing of piled embankments, both with and without reinforcement, and observed soil deformations through a transparent window. These tests typically observed similar failure mechanisms as shown to develop in trapdoor tests. This is expected, as the simplified geometry adopted in these tests comprised multiple active trapdoors (used to simulate subsoil consolidation) separated by stationary supports (used to model the pile heads). However, the three-dimensional geometry of piles on a square grid is not accurately modelled using a plane strain geometry. To date, no physical modelling has been performed investigating the three-dimensional displacement field and failure mechanism within LTP granular material overlying pile heads. Thus, the soil arching models described are based on assumed kinematics, rather than any observed or known mechanism.

Defective piles have been shown to result in a softer load-settlement response than non-defective piles. The presence of defective piles within a group connected by a pile cap has been studied physically and numerically, and results show defective piles lead to a reduction in stiffness of the pile group as well as rotation of the pile cap. However, defective piles within a group of piles supporting an embankment have never been studied. Given that the load acting on the defective pile within a GRPE will progressively develop as subsoil undergoes consolidation, which may, in turn, cause the defective pile to undergo additional settlement to surrounding non-defective piles, predicting the settlement of a defective pile and the behaviour of the overlying LTP is extremely complex. Thus, the interaction between defective piles, non-defective piles and an LTP must consider the progressive development of load transfer and settlements, rather than just a single state of arching to develop around the defective pile as is the assumption made by CUR226 (2016).

2.8 Proposed research

The research undertaken as part of this thesis investigates the progressive development of soil arching and load transfer within GRPEs as (i) subsoil consolidates and (ii) a defective pile settles. When

designing GRPEs, the global embankment behaviour must be considered (e.g. lateral sliding and stability); however, such behaviour is not considered as part of this study. This study focuses only on the load distributions and settlements that arise under the centreline of an embankment, where lateral resistances and movements are not considered.

The behaviour of GRPEs under these conditions will be modelled both physically and numerically. The physical modelling will be undertaken at two scales, 1*g* and centrifuge. 1*g* model tests will obviously incorporate scale limitations; however, such limitations can be accepted given the additional information that can be obtained at such scales. Advanced CT imaging can be used to image small-scale 1*g* model tests, and with the application of image correlation techniques, can reveal the kinematics of granular material overlying pile heads as subsoil undergoes consolidation. With the soil kinematics obtained, the failure surfaces that develop within an LTP overlying pile heads as the subsoil progressively settles, both with and without a defective pile, can be investigated. With three-dimensional displacement fields, understanding can be gained of phenomenon such as the critical height, the propagation of settlements above the critical height to the embankment surface and how these are both affected by the presence of a defective pile.

Centrifuge modelling will be undertaken to ensure many of the limitations of the small-scale 1*g* model tests are removed due to appropriately scaling stresses and more accurately simulating mechanisms. The cost of performing tests within a geotechnical centrifuge is that less information is collected, e.g. displacements are only measured at discrete locations. However, in satisfying many scaling conditions, the results from centrifuge modelling are appropriate for calibrating numerical models. A suitably calibrated finite element method (FEM) model will then be used to simulate a range of geometries and materials to investigate when a defective pile may cause adverse effects on the performance of a GRPE.

3 Measuring three-dimensional displacement fields in model tests

Small-scale physical models provide a means to investigate phenomenon, such as pre-failure mechanisms, within a laboratory or facility where advanced experimental techniques can be undertaken that may otherwise not be implemented on larger models or full-scale studies. To measure displacements and strains within physical models, conventional pointwise measuring techniques such as linear variable differential transformers (LVDTs) and strain gauges only provide measurements at a small number of discrete locations, while techniques such as particle image velocimetry (PIV) or digital image correlation (DIC) only provide surface displacement fields. To accurately measure three-dimensional full-field displacements, it is necessary to scale models so that non-destructive imaging techniques can be employed to visualise grains or material texture within a model comprising geomaterials.

This chapter outlines three non-destructive imaging techniques that were performed on small-scale model piled embankments with the aim of obtaining sufficient spatial resolution and contrast within the scans so that digital volume correlation (DVC) analysis could be undertaken. The design and scaling of the models are introduced, providing insight into the limitations of the small-scale model testing. Finally, details are provided of the image analysis undertaken to obtain information regarding the kinematics of granular material (and soil arching) within a piled embankment.

3.1 Design of model

Small-scale models were designed to simulate the arching mechanism that occurs in a load transfer platform (LTP) overlying pile heads. The models were designed so that they were small enough to be placed on an imaging rotation stage (sample stage) and small enough in diameter so that radiation, whichever form proved most suitable, could penetrate the sample without the resulting images suffering artefacts or requiring excessive scan times. At the time of designing the models, the ability of the proposed radiation sources (laboratory X-rays, neutrons and synchrotron X-rays) to penetrate a sample of fine-grained sand was not well understood. Imaging of samples comprising silica sand greater than 100 mm in diameter had not been performed at any of the proposed testing facilities. It was, therefore, necessary to design the models to be as small as possible while satisfying a number of scaling issues. Objectives of the small-scale 1*g* model experiments are outlined in Table 3.1.

Table 3.1: Objectives of small-scale 1*g* model experiments

Objectives	**Comments**
Model the progressive development of soil arching in piled embankments	Displacement controlled plate ("settlement plate") which was progressively lowered to simulate subsoil consolidation
Model the arching mechanism around a defective (soft) pile	Displacement controlled central pile that was lowered to simulate a relatively softer load-settlement response compared to surrounding non-defective piles
Investigate the three-dimensional nature of soil arching	Computed tomography (CT) imaging was applied on model piled embankments to observe the mechanism of soil arching
Investigate the progressive development of soil arching in a piled embankment	Digital volume correlation (DVC) analysis was applied to pairs of CT volumes to obtain three-dimensional displacement fields at various settlement plate displacements. The settlement plate was lowered without the need to remove the model from the sample stage, thus allowing displacement vectors within the sand mass to be estimated directly from DVC analysis
Investigate the arching mechanism around a defective column	Comparison made between displacement fields around a defective pile to those around a non-defective pile
Investigate the effect material properties have on the arching mechanism	Sand was prepared at two different densities to simulate different deviatoric responses.

3.2 Scaling

Physical modelling is often undertaken at geometric scales smaller than the prototype. While this approach offers many advantages (e.g. control of boundary conditions, rapid testing and control of materials), it introduces experimental issues, mostly because of the soil constitutive behaviour being stress dependent. Thus, scaling of the model must be carefully considered so that results from model testing can be extrapolated to learn about the behaviour of a prototype. The following section describes the scaling and limitations associated with the small-scale model tested at 1*g*.

3.2.1 Dimensional analysis

Dimensional analysis is a procedure employed to investigate the variables governing a phenomenon. It can be used to simplify a problem by reducing the number of variables that need to be studied experimentally while also providing insight into how variables should be scaled in model tests. The premise underlying dimensional analysis is that a dimensionally homogeneous equation describing a

phenomenon can be reduced to a series of non-dimensional products (Buckingham 1914). While dimensional analysis can be used to obtain a partial theoretical solution, it does not provide insight into any mechanisms. As such, an understanding of the physical phenomenon should be obtained prior to performing dimensional analysis, often based on experimental observations.

The Buckingham π theorem considers that a phenomenon characterised by n variables can be expressed by $n - r$ dimensionless products (π), where r is equal to the rank of the dimensional matrix (Langhaar 1980). When studying mechanics based problems, the dimensions of variables can typically be reduced to a combination of mass (M), length (L) and time (T).

The case of an unreinforced piled embankment with dry cohesionless granular material will be studied to investigate the scaling of variables for model testing. It is first assumed that the maximum stress acting on the pile heads (σ'_p) is a function of the pile head diameter (d), the pile centre-to-centre spacing (s), the height of the embankment (h_e), embankment fill unit weight (γ) and the friction angle of the LTP material (ϕ). Like many arching models, this assumes that the stress distribution resulting from soil arching is independent of subsoil settlement and is similar in principle to the ultimate bearing capacity of a foundation. Based on this assumption, it can be written that:

$$f\left(\sigma'_p, d, s, h_e, \gamma, \phi\right) = 0 \tag{3.1}$$

By simplifying the units of the relevant variables using the dimensions M, L and T, a dimensional matrix can be written as:

	σ'_p	d	s	h_e	γ	ϕ
M	1	0	0	0	1	0
L	-1	1	1	1	-2	0
T	-2	0	0	0	-2	0

The rank of this dimensional matrix is $r = 2$, which according to the Buckingham π theorem, means that the physical phenomenon of stress acting on a pile head within an unreinforced piled embankment can be expressed by 4 dimensionless groups. Through further examination of the problem it can be seen that the following dimensionless groups can be used to express the problem:

$$f\left(\frac{\sigma'_p}{d\gamma}, \frac{s}{d}, \frac{h_e}{d}, \phi\right) = 0 \tag{3.2}$$

Which may be rearranged so that:

$$\frac{\sigma'_{\mathrm{p}}}{d\gamma} = f\left(\frac{s}{d}, \frac{h_{\mathrm{e}}}{d}, \phi\right) \tag{3.3}$$

Regarding physical modelling, the partial relationship deduced from dimensional analysis presented in Equation 3.3 provides a means to check whether similitude between model and prototype is achieved. Similitude is achieved when the dimensionless groups in Equation 3.3 are equal in both model and prototype (Harris and Sabnis 1999). From dimensional analysis, it is evident that a model piled embankment should be geometrically scaled such that ratios of s/d and h_e/d are kept constant, while the soil should exhibit the same frictional behaviour between model and prototype. Given that the constitutive behaviour of soil is stress dependent, the strength of the model soil will be different to the prototype soil if the stress conditions between the two are not consistent.

It is also apparent from Equation 3.3 that the dimensionless group $\sigma'_p/\gamma d$ should remain constant. Given that in an ideal model the stress conditions in both model and prototype remain equal, then γd should also remain constant. Thus, if the physical model is geometrically scaled such that d is reduced by a length factor n, then γ should be increased by n. The unit weight of soil is the product of the soil density (ρ) and gravitational acceleration (g), and as such, unit weight can be scaled by subjecting the model to an enhanced gravitational field (ng), i.e. performing the test within a centrifuge. However, in 1g conditions, the unit weight can only be increased by using artificial materials with heavier particles. Using granular materials with heavier particles than the prototype soil would likely introduce additional limitations regarding material constitutive behaviour. Herein lies the major limitation of 1g modelling; dimensional analysis shows that in a model piled embankment, exact similitude cannot be achieved as we are unable to replicate the prototype stress conditions in the model. While exact similitude is not always possible, provided the engineer is willing to accept the discrepancy between the dimensionless products in model and prototype, it may be said that first-order similarity is achieved (Harris and Sabnis 1999).

Scale factors have been extensively studied by others, including relationships for scaling geosynthetic reinforcement (Altaee and Fellenius 1994; Muir Wood 2004; Viswanadham and König 2004), which was not considered in the previous dimensional analysis. The relevant scale factors associated with the modelling of GRPEs at 1g are presented in Table 3.2.

Table 3.2: Scale factors for modelling piled embankment at 1*g*.

Parameter	**Scale factor**
Length (a, s, h_e)	$1/n$
Stress (σ'_p)	$1/n$
Soil friction angle (ϕ)	1
Soil-geosynthetic friction angle (ϕ_{sg})	1
Unit weight (γ)	1
Geosynthetic reinforcement tensile stiffness (J)	$1/n^2$
Geosynthetic reinforcement ultimate tensile strength (T_u)	$1/n^2$

3.2.2 Stress conditions

The stress within an embankment is predominantly governed by the weight of the embankment fill (γh_e). As such, a small-scale physical model of a piled embankment will experience less stress than that of a prototype. As noted previously, this is of concern since the constitutive behaviour of the granular material is stress dependent. To account for this, a surcharge can be placed on the surface of the model embankment, which may result in stresses at the base of the model embankment being equivalent to those at the base of a prototype. However, the stress gradient within the zone of soil arching will not be the same in both model and prototype. This is demonstrated in Figure 3.1.

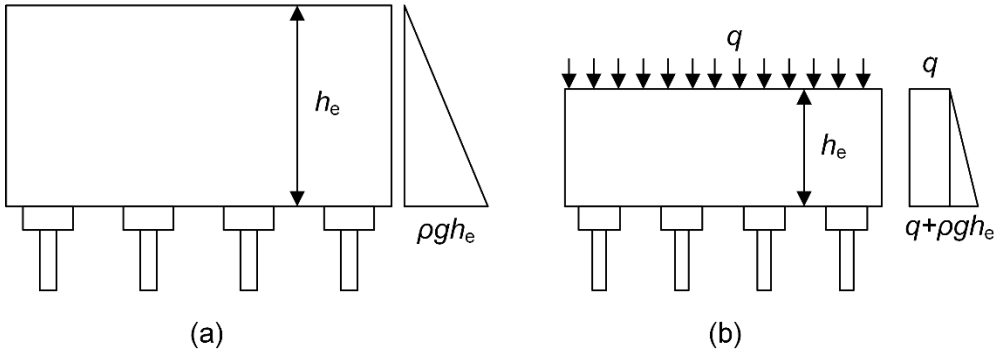

Figure 3.1: Stress conditions within embankment fill for (a) prototype; (b) model

In the testing undertaken as part of this study, a surcharge of 6.3 kPa was applied to the surface of the model sand. This resulted in a vertical stress of approximately 8 kPa at the base of the model sand. In prototype scale, this is equivalent to the stress at the base of an approximately 0.45 m high embankment. While a higher surcharge on the model sand surface would have resulted in stresses equivalent to a higher embankment, this may have made the model unstable on the imaging rotation stage. As such, the constitutive behaviour of the soil under higher embankment loads was replicated using the equivalent state parameter method (Been and Jefferies 1985; Altaee and Fellenius 1994), described in Section 3.3.5.

3.2.3 Geometric considerations

It has been shown that all geometric elements of the model should be scaled by the same factor n to ensure geometrical similitude between model and prototype. Although in soil-structure interaction problems, it is also necessary to consider the scaling between particle size and structural elements, which may lead to particle scale effects. When selecting an appropriate pile head diameter and LTP granular material for the model tests, scaling the ratio between the average sand grain size to the enlarged head diameter must be considered.

A typical rule of thumb is the ratio between structural dimension to particle size should be greater than 30 (Ovesen 1979; Randolph and House 2001). However, where localised deformations (shear bands) are expected to be a governing mechanism, Foray et al. (1998) observed that shaft friction was dependent on the ratio of pile diameter to shear band thickness up to a limiting value of 20 (when a shear band thickness of $10 \times D_{50}$ is assumed). More specifically to soil arching, the localised deformations above a trapdoor have been shown to be susceptible to particle size effects for ratios between trapdoor width, B, and average particle diameter, D_{50}, of up to 1000 (Kutter et al. 1994). Several studies investigating the behaviour of LTPs overlying piles in centrifuge tests have adopted the approach where they ensure the ratio between pile head diameter, d, and the D_{50} of the LTP granular material is greater than a minimum value, typically in the range 20 to 35 (Blanc et al. 2013; Okyay et al. 2014). However, given the wide range of structural dimension to particle size similitude conditions reported in the literature, it is difficult to adopt a single condition with great certainty. It is therefore worth revisiting the cause of grain size effects on the development of shear bands.

Stone and Wood (1992) showed that the grain size effects within trapdoor tests were due to the mobilisation of dilation. They noted that "*the relative displacement across a localisation necessary for the attainment of critical state condition is a function of particle size. Thus, to observe similar stages in the development of localisations in soils of different particle size, the soil within the localisations must be at similar points on their respective cumulative dilatancy curves…*" To achieve similar stages of shear band development between model and prototype, it is, therefore, necessary to scale the grain size by the same factor n that the structural dimensions are scaled by. This was demonstrated by Kutter et al. (1994) in a series of centrifuge model tests investigating the particle size effects on the collapse of sand overlying cavities in centrifuge models. In the case of piled embankments, this means that the model LTP granular material will undergo similar mobilisation of dilation as the prototype material if the soil particle size is scaled by the same factor as the structural element it interacts with. As the LTP granular material is in direct interaction with the pile head, the following similitude condition should be maintained:

$$\frac{d_{\mathrm{p}}}{D_{50,\mathrm{p}}} = \frac{d_{\mathrm{m}}}{D_{50,\mathrm{m}}} \tag{3.4}$$

Where the subscripts m and p denote model and prototype dimensions, respectively. This ratio will be shown to be satisfied in the following section where materials are introduced.

3.3 Model setup

3.3.1 Pile arrangement

Two small-scale model piled embankments were designed and constructed to study the soil arching mechanism that develops within piled embankments, both with and without defective piles. The model's dimensions were geometrically scaled down by approximately 50 times that of a typical full scale piled embankment ($n \approx 50$). The first of the models (Figure 3.2) comprised four piles arranged on a square grid with a centre-to-centre pile spacing of s = 45 mm and pile head diameter of d = 15 mm, resulting in a replacement area ratio of α_{r} = 0.087. All piles within the square pile arrangement model were rigid, i.e. no defective piles were present within the model.

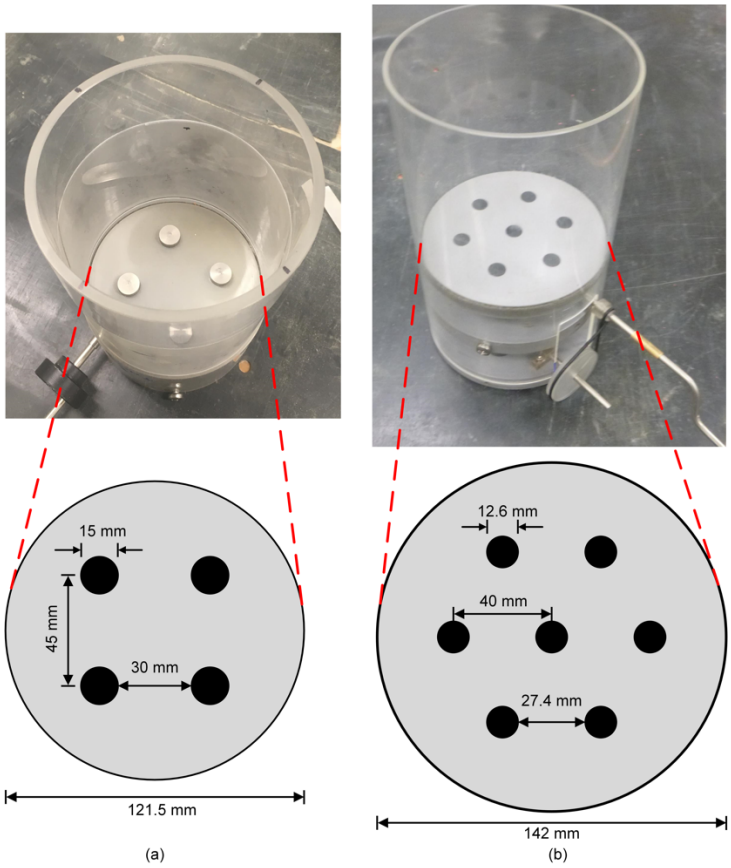

Figure 3.2: Model piled embankments with piles arranged on a (a) square; (b) equilateral triangular arrangement

The second model comprised piles arranged on an equilateral triangular grid with s = 40 mm, d = 12.6 mm and α_r = 0.09. The central pile within this model was displacement controlled, meaning that it could be kept rigid (simulating a non-defective pile) or lowered (simulating a defective pile undergoing settlement). All other piles within the triangular pile arrangement model were rigid.

3.3.2 Sand

Commercially available silica sand, commonly referred to as 'superfine' UWA sand, was used to model LTP material in the model tests. The silica sand is fine to medium-grained and sub-angular with an average effective particle size of 0.18 mm. This sand has been used extensively in physical model testing in Australia over the past three decades. As such, the properties of UWA sand have been well documented in previous studies (Stewart 1992; Cheong 2002; Bagbag et al. 2017; Chow et al. 2018b). In addition to these properties, four direct shear box tests were performed at the Monash University soils laboratory to determine the peak friction (ϕ_p) and maximum dilation (ψ_{max}) angles under low stresses. Four shear box tests were performed. Two of these tests were undertaken on samples classified as dense (D_r = 88% and 91%) and two tests classified as medium dense (D_r = 63% and 68%). The tests were performed under a normal stress of 8.2 kPa, and corrected for using the method described by Lehane and Liu (2013) for shear box testing at low-stress levels. The shear stress and volumetric response of thee shear box tests are presented in Figure 3.3. Properties of UWA sand are presented in Table 3.3.

Table 3.3: Properties of UWA sand (after Chow et al. 2018b)

Property	**Symbol**	**Value**
Specific gravity	G_s	2.67
Particle size	D_{10}, D_{50}, D_{60}	0.12, 0.18, 0.19 mm
Minimum dry density	ρ_{min}	1497 kg/m^3
Maximum dry density	ρ_{max}	1774 kg/m^3
Critical state friction angle	ϕ_{cv}	31.6°
Peak friction angle (88%<Dr<91%)	ϕ_p	46° †
Peak friction angle (63%<Dr<68%)	ϕ_p	40° †
Maximum dilation angle (88%<Dr<91%)	ψ_{max}	14° †
Maximum dilation angle (63%<Dr<68%)	ψ_{max}	9 ° †
Coefficient of uniformity	C_u	1.67
Coefficient of curvature	C_c	1.02
Slope of critical state line	λ	0.029*
Void ratio on critical state line at p' = 1 kPa	Γ	0.917*

*After Chow et al. (2018a)

† From shear box tests performed at Monash University with a normal stress of 8.2 kPa

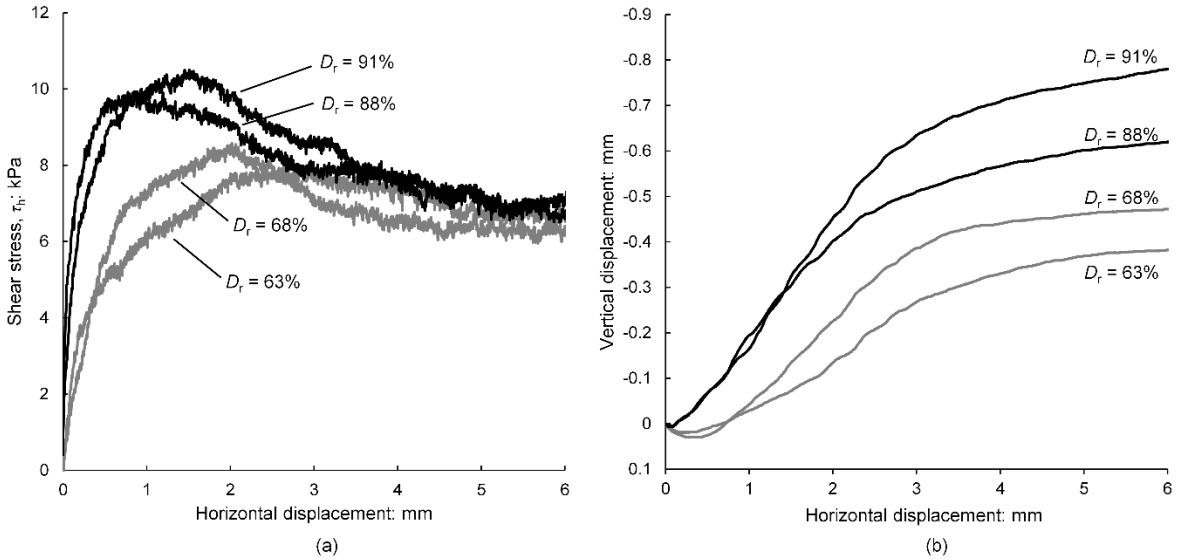

Figure 3.3: Results from shear box testing on samples of UWA sand under a normal stress of 8.2 kPa

UWA sand was selected to model the LTP material as it exhibits relatively high peak friction and dilation angles, similar to what would be expected of the high-quality granular fill that is commonly used within LTPs. Further to its mechanical properties, the average grain size of 0.18 mm suitably scales to a grain size of about 9 mm at prototype, thus simulating similar mobilisation of shear bands as a gravel at prototype scale (common LTP granular material grain size) and satisfying the similitude condition in Equation 3.4.

UWA sand is composed of predominantly silica sand grains, which are light in colour due to their partial transparency. However, upon visual inspection, it is evident that there are trace grains darker in colour as seen in Figure 3.4a. Scanning electron microscopy (SEM) of the sand was undertaken in combination with energy-dispersive X-ray spectroscopy (EDS) to investigate the sand mineralogy, particularly regarding the darker grains. Results from EDS confirmed that the majority of grains were silica (SiO_2); although, a trace amount of denser grains consisting of titanium, iron and oxygen were also observed. Three denser grains detected by EDS are shown in an SEM image in Figure 3.4b, while the remaining grains are silica (SiO_2). These titanium-iron trace grains are likely a derivative of the mineral ilmenite ($FeTiO_3$). It is also evident from the SEM images that the silica grains are predominantly sub-angular in shape while the trace titanium-iron grains are approximately sub-rounded in shape. Using sand with trace dense grains improves the image texture within reconstructed CT volumes, which is described later.

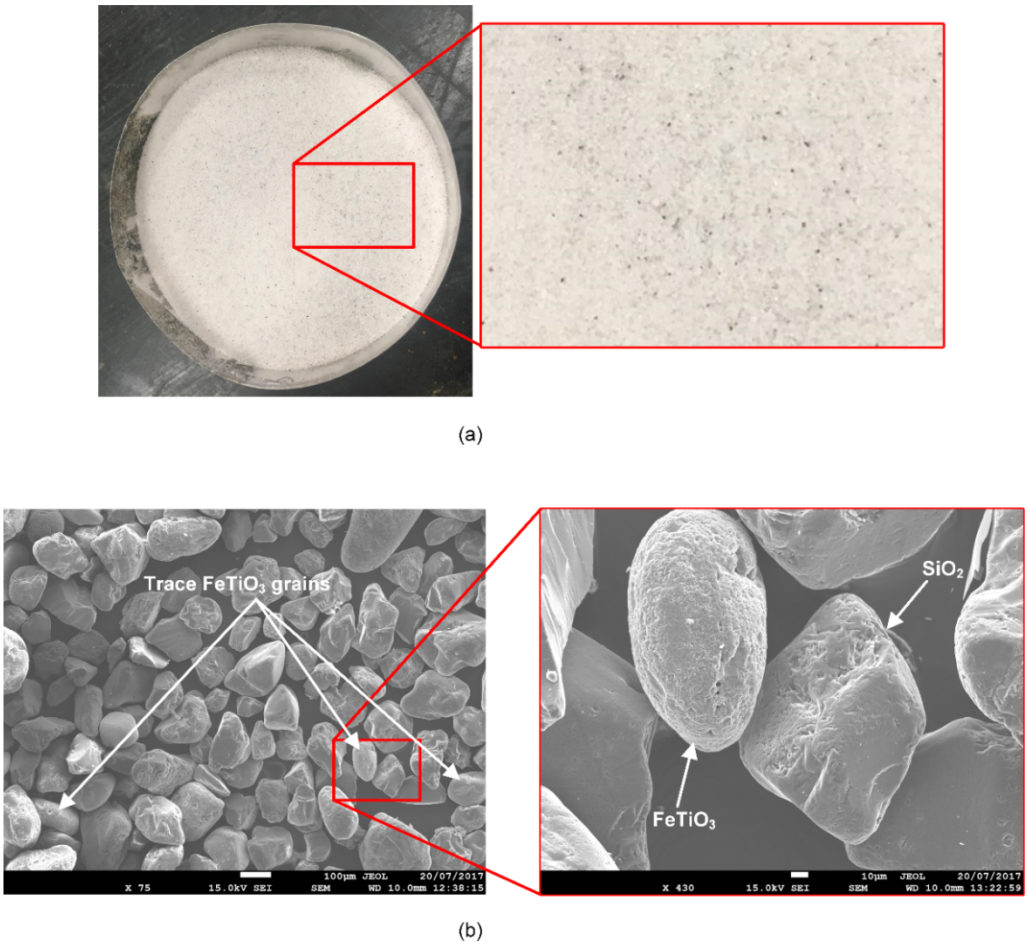

Figure 3.4: (a) Photo of UWA sand; (b) SEM images of UWA sand

3.3.3 Displacement control

The subsoil settlement of the model was simulated by lowering a mechanical device, referred to as the settlement plate. This approach of simulating subsoil settlement mechanically has been adopted in many other studies at both lab-scale tests (Eskişar et al. 2012; Rui et al. 2016) and in centrifuge tests (Blanc et al. 2013; Okyay et al. 2014; Fagundes et al. 2015). The settlement plate is a rigid plate, and as such, simulates a flat deformed surface. However, the subsoil beneath an embankment comprising geosynthetic reinforcement will not undergo uniform settlement between the pile heads, which has been shown through numerical modelling (Halvordson et al. 2010; Jones et al. 2010). Thus, the settlement plate results in greater volume loss beneath the model sand compared to what would develop in the field beneath an embankment.

The settlement plate was lowered at a rate of 0.1 mm/min using a hand-driven worm-drive gearing mechanism located beneath the settlement plate. Displacement was monitored using a dial gauge attached to the settlement plate, which was used to ensure a consistent rate of displacement. The hand-drive attachment was easily removed from the shaft connecting it to the worm drive, which allowed the

model to remain on the imaging station during the displacement of the settlement plate. This was important for the application of image correlation techniques to ensure the model remained in the same position between CT scans.

The central pile in the triangular model was controlled using a similar device as the settlement plate, although smaller and located within the pile shaft itself. In tests where only non-defective piles were modelled, this central pile was kept stationary. This central pile was lowered in tests where the objective was to investigate the formation of soil arching above a defective pile undergoing additional settlement due to its softer load-settlement response. Given that a defective pile will attract load and undergo settlement at the same time as subsoil undergoes settlement, it was important for the two processes to occur simultaneously in the model. This was achieved by attaching the two displacement controls using a belt so that they were displaced at the same time using the one hand-drive, as shown in Figure 3.5. The diameter of the gears connected by the belt could be varied to achieve different rates of displacement for the central defective pile relative to the settlement plate. Due to the demand for beamtime at the imaging facilities, only enough time was granted to test one gear ratio. In the arrangement tested, the diameter of the gear controlling the settlement plate displacement was 7.72 mm, and the diameter of the gear controlling the central pile displacement was 27.78 mm. This resulted in a gear ratio of 1:3.6.

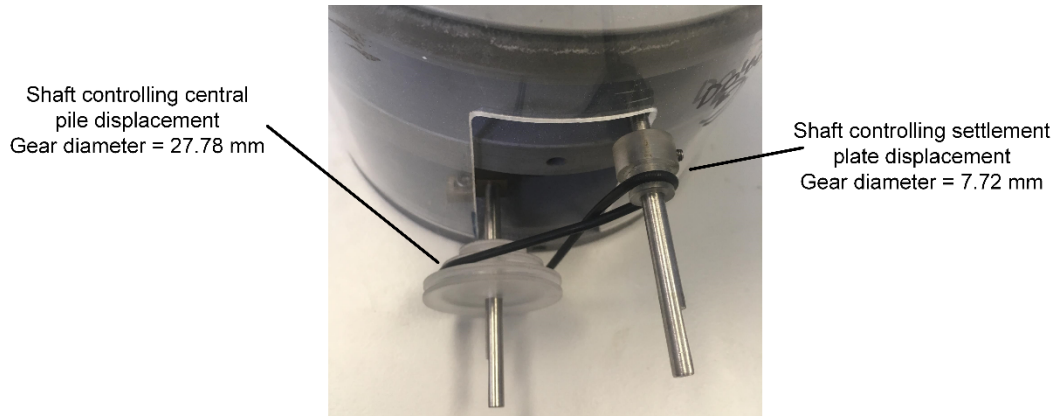

Figure 3.5: Gears and belt controlling the settlement plate and the central pile displacement.

3.3.4 Surface roughness

It is considered that the failure mechanism within the LTP granular material above pile heads may be dependent on the roughness of the pile heads, like the dependency shown by the failure mechanism below shallow foundations. Roughness testing was performed on the pile heads using a stylus profiler. The measured pile head maximum roughness, R_t, defined as the vertical height between a maximum and minimum on a surface profile over a length of approximately the average sand particle diameter, D_{50}, was between 15 and 20 μm. The corresponding normalised roughness ratios, R_n, which is expressed

as $R_n = R_t/D_{50}$, are between 0.083 and 0.11. The interface between a soil and a structural element is typically considered smooth for R_n values of less than 0.02, and rough for R_n value of 0.1 and greater (Kishida and Uesugi 1987; Fioravante 2002). The pile head normalised surface roughness values are on the border of intermediate-rough, and as such, it is expected that the frictional resistance mobilised at the soil-pile head interface will be close to the shear strength of the soil.

The surface of the settlement plate was also measured. The settlement plate, due to its smooth finish, resulted in values of R_t between 1.2 and 1.4 μm. These values correspond in a normalised roughness of about 0.007. It may, therefore, be expected that the resistance along the interface between sand and settlement plate will be low, with no dilation occurring (Fioravante 2002).

3.3.5 Sample preparation

As noted previously, the models were tested under only one surcharge pressure. To investigate the behaviour of LTP granular material under larger embankment loads, due to either greater embankment heights or loading applied to the embankment surface, the equivalent state parameter concept was utilised (Altaee and Fellenius 1994). In the critical state soil mechanics framework, it has been shown that soil undergoing deformation will approach a *critical state* where plastic deformation continues without volume change or change in effective stress (Roscoe et al. 1958). In an $e - \ln(p')$ space, the critical state is represented by the critical state line (CSL), which may be written as:

$$e_f = \Gamma - \lambda \ln(p') \tag{3.5}$$

Where the subscript f denotes that the void ratio corresponds to failure at the critical state, Γ is the void ratio at critical state at $p' = 1.0$ kPa and λ is the slope of the critical state line in an $e - \ln(p')$ space. Been and Jefferies (1985) proposed that the stress-strain behaviour of a soil is dependent on the void ratio and the mean effective stress, which is captured within a parameter called the *state parameter* (ξ). The state parameter, as defined by Been and Jefferies (1985), is the difference between the current void ratio (e) and the void ratio at critical state (e_f) at the same mean effective stress, which may be written as:

$$\xi = e - e_f \tag{3.6}$$

Or:

$$\xi = e + \lambda \ln(p') - \Gamma \tag{3.7}$$

The equivalent state parameter concept described by Altaee and Fellenius (1994) suggests that the deviatoric behaviour of sand may be described by the state parameter over a wide range of stresses and densities. This provides a means to test soils at 1g while replicating the constitutive behaviour of the same soil under higher stresses with an equivalent state parameter. If the soil within the zone of arching is initially (prior to any settlement plate displacement) at a stress state of approximately $p' = 5$ kPa

within the model, then a sample prepared at D_r = 63% will have an equivalent ξ to sand prepared at D_r = 94% under p' = 90 kPa, as shown in Figure 3.6. Thus, the deviatoric behaviour of medium dense sand at model scale will be similar to the behaviour of a dense sand at field scale under an embankment height of about 8 m. As such, the testing was performed with sand within the models prepared at two densities, dense (D_r = 94% +/- 2%) and medium dense (D_r = 63% +/- 2%). Sand was air-pluviated into the models using a funnel at a set drop height of 1 m. In the case of dense sand, the model was further vibrated to prepare a dense sample.

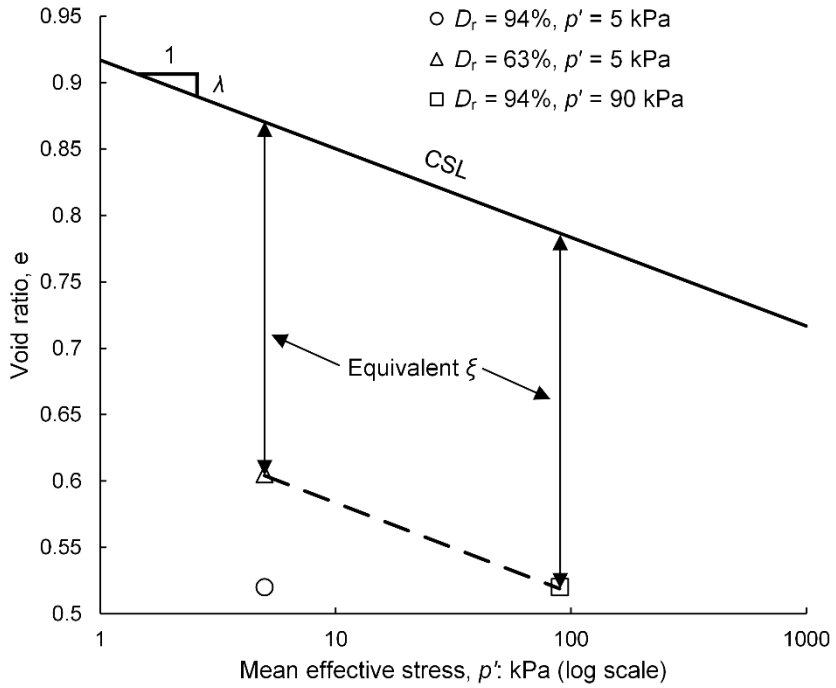

Figure 3.6: The equivalent state parameter concept

3.4 Computed tomography

X-ray computed tomography (CT) was developed in the 1960s as a medical diagnostic tool. In the proceeding decades, X-ray CT imaging was applied to many other fields including geomaterials (Petrovic et al. 1982; Hainsworth and Aylmore 1983; Wellington and Vinegar 1987). While X-rays produced from an X-ray tube are the most widely used radiation source for CT scans, other forms of radiation may also be implemented, including neutron CT and synchrotron X-ray CT, both of which were used in the current study.

CT imaging works by collecting a series of projected images of an object as it is positioned between a radiation source and detector and rotated around a central axis. The projections (radiographs) are two-dimensional images composed of pixels, the values of which are defined by line integrals. The line integrals in a projection represent the total interaction suffered by radiation as it passes through the object (Kak and Slaney 2001). By collecting projections of an object as it is rotated around an axis,

reconstruction algorithms may be implemented to provide a three-dimensional volume composed of CT values that represent the interaction between the radiation and the object at specific locations (voxels) within the volume.

In the proceeding sections, three radiation sources are introduced: laboratory X-rays, neutrons and synchrotron X-rays. Preliminary imaging was undertaken using each of these sources to investigate which method would result in reconstructed CT volumes appropriate for the application of image correlation techniques to estimate three-dimensional full-field displacements. For such correlation techniques to be implemented, CT volumes must possess image texture, which is essentially a high density of voxel information. This is achieved through high spatial resolution and contrast, which are used to assess the suitability of each radiation source for the proposed experimental program.

3.4.1 Laboratory X-ray CT

To produce X-ray radiation, traditional X-ray tubes use an electron gun (cathode) to bombard a metal target (anode) with electrons. Around 99% of the energy from the incoming high-speed electrons is transformed into heat upon interaction with the anode, with the remaining 1% converted into and emitted as X-rays (Carmignato et al. 2018). The emitted X-rays comprise a range, or spectrum, of energies, which may be tuned by altering the electron acceleration voltage. The energy of the X-rays will affect the interaction of the radiation with the sample, and as such, is an important consideration of X-ray imaging. Filters may be implemented to narrow the spectrum of X-ray energies, which may, in turn, improve the acquired image quality and reduce artefacts. Laboratory X-ray CT utilising X-ray tubes has become a common non-destructive imaging technique with access to facilities becoming increasingly cheaper. It is, therefore, a suitable technique to apply prior to using more advanced radiation sources.

Method

Laboratory X-ray CT imaging was undertaken at the X-ray microscopy facility for imaging geo-materials (XMFIG) using a high-resolution Zeiss Xradia 520 Versa. Electrons were accelerated at a voltage of 140 keV and radiographs collected as the model was rotated 360˚ around its vertical axis. The acquired projections were reconstructed using the software XM Reconstructor (Xradia 2011) to obtain CT volumes with a voxel size measuring 47.2 x 47.2 x 47.2 µm.

Imaging was initially undertaken using silica sand within the model comprising piles arranged on a triangular pattern (model diameter of 142 mm). Sand was pluviated into the model, and the settlement plate lowered approximately 1 mm while on the sample rotation stage (Figure 3.7). However, preliminary scans indicated that the reconstructed volumes did not provide any detail of individual sand grains, with general density changes also not clearly evident. 1 mm diameter glass beads were used as

an alternative to fine-grained sand within the model to investigate the ability of laboratory X-ray CT to image volumes of predominantly silica-based granular material up to 142 mm in diameter. The glass beads were analysed using X-ray Fluorescent Spectroscopy, which confirmed that they were mostly silica. X-Ray CT scanning of the sample required approximately 12 hours, including positioning and readout time.

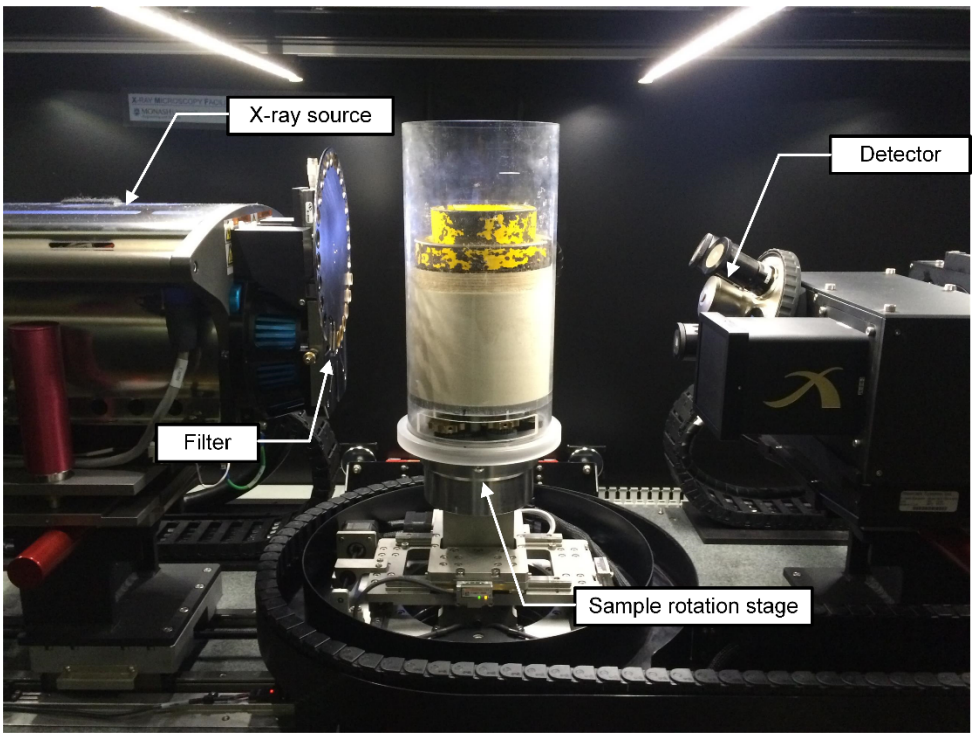

Figure 3.7: Model piled embankment within the XMFIG X-ray CT facility

Preliminary results

Reconstructed CT volumes of the triangular model comprising glass beads suffered from beam hardening artefacts. Beam hardening is an artefact that arises due to the broad spectrum of X-ray energies emitted from the X-ray source. The low energy X-rays are attenuated more rapidly than high energy X-rays, which results in the beam shifting towards higher energies as it passes through the sample, referred to as hardening (Jin et al. 2015). While this can be somewhat corrected for during the CT reconstruction, the artefacts could not be completely removed using a linearization algorithm (Brooks and Di Chiro 1976). A horizontal CT slice taken through the middle of the sample is presented in Figure 3.8. In this slice, the bright region within the centre is the result of beam hardening.

Glass beads can be identified within the slice shown in Figure 3.8. Thus, DVC analysis could be applied to pairs of CT volumes collected using this setup and technique, although errors would likely occur around the centre of the volume where artefacts are most prominent. However, the 1 mm diameter glass beads, or a sand grain with an equivalent D_{50}, would not satisfy the similitude conditions described

previously. Given that X-ray CT imaging of fine-grained sand could not produce reconstructed volumes with any discernible grains or image texture, it is considered that this technique is not suitable for the imaging of such large diameter samples of fine-grained silica sand where the intention is to apply DVC analysis. Although, it is shown that this experimental setup and imaging technique could be utilised if larger grains were able to be used within the model while still satisfying scaling requirements.

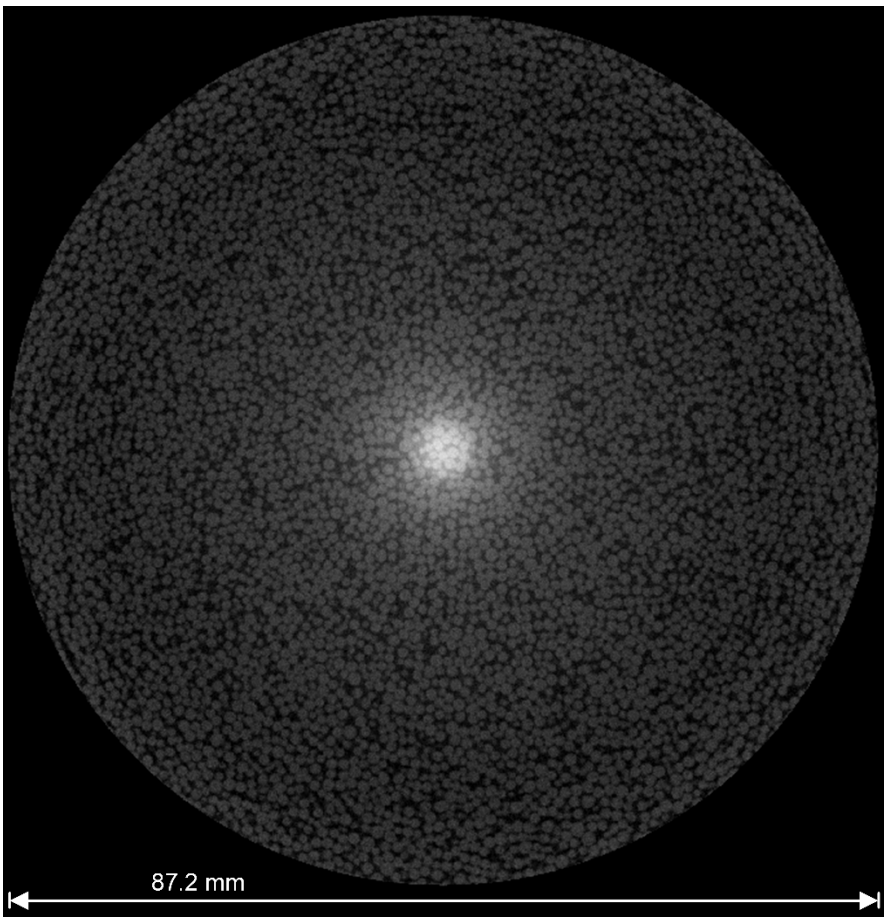

Figure 3.8: Horizontal tomography slice from X-ray CT through a sample containing glass beads

3.4.2 Neutron CT

While X-rays interact with electrons, resulting in the X-ray attenuation coefficient being related to the atomic number of the element, neutrons interact with the nuclei of atoms. This different interaction allows neutron imaging to provide contrast between elements that may have relatively close atomic numbers. A major advantage of neutrons is that from the view of a neutron, the nuclei of an atom takes up a small cross-sectional area of the entire atom compared to an electron cloud. Therefore the probability of an incident neutron being absorbed or scattered by an atom (i.e., the neutron scattering cross-section) is typically lower than that of an incident X-ray, which results in neutrons achieving superior material penetration (Anderson et al. 2009). For this reason, neutron imaging was performed on the small-scale model piled embankments in the expectation that images could be obtained with

fewer artefacts and more contrast between grains and voids than were observed in images obtained from laboratory X-ray CT.

Method

The most common source of neutrons for imaging is from dedicated research facilities where neutrons are produced by fission or spallation (Banhart 2008). Neutron radiographs for this study were collected at the DINGO imaging station of the Australian Centre for Neutron Scattering (ACNS), Lucas Heights, Australia. Commissioned during 2013-2014, DINGO uses thermal neutrons from the OPAL research reactor. The neutron flux has been measured at 5.3 x 10^7 n/s/cm^2 at an L/D (length/diameter) ratio of 500. To facilitate the imaging of relatively large samples, the neutron beam can be up to 200 mm horizontal x 200 mm vertical. See Garbe et al. (2015) for further details of the DINGO imaging station.

The model comprising piles on a square grid was used for preliminary imaging (model diameter = 121.5 mm). The outer confining PVC shell used for imaging with X-rays was replaced with a 1.8 mm thick aluminium shell, as aluminium is penetrated by neutrons with less interaction than PVC. Also, the surcharge placed at the top of the sand surface was applied using a stand that allowed the steel mass to be placed above the neutron beam to avoid it becoming activated by neutrons. Otherwise, the sample was prepared and placed on the rotation stage in the same manner as the laboratory X-ray CT process. The final model set up on the DINGO rotation stage is shown in Figure 3.9.

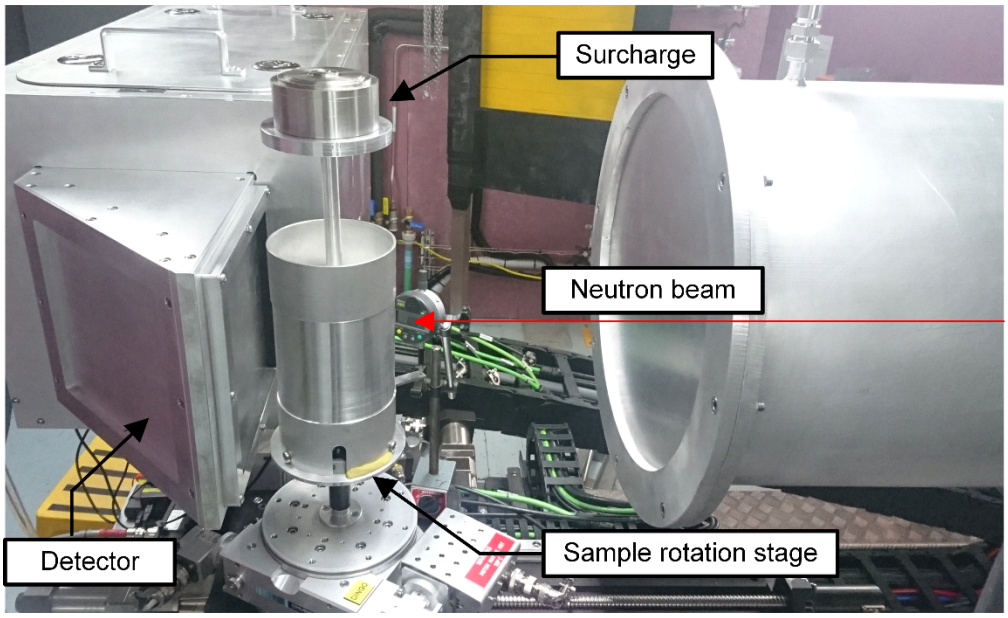

Figure 3.9: Model piled embankment within DINGO neutron imaging facility

1896 radiographs measuring 2048 x 2048 pixels were acquired over approximately 17 hours, which includes readout and positioning time. CT volumes were then reconstructed using a filtered back

projection algorithm implemented in the software Octopus (Dierick et al. 2004). The resulting CT volumes comprised voxels measuring 63 × 63 × 63 μm.

Preliminary results

A CT slice taken 2 mm above the pile heads after the settlement plate was displaced 1.8 mm vertically down is presented in Figure 3.10, with the corners of the slice positioned above the centres of the four piles. It is evident in this slice that the CT volumes did not suffer any significant artefacts, other than some minor ring artefacts resulting from imperfections within the detector. The darker regions in Figure 3.10 indicate areas of lower density while the lighter regions are indicative of relatively higher density material. Regions of relatively higher porosity, where soil has undergone shearing and dilation, are present in localised regions above the pile heads.

The enlarged section of the slice presented in Figure 3.10 possesses a blurred granular-like texture due to the fine-grained sand. However, the spatial resolution and contrast achieved by neutron CT results in the sand grains not being clearly identifiable. Given the time to collect one scan required 17 hours, and that the study intended to perform up to 10 scans per sample at incrementally increasing settlement plate displacements, neutron imaging would require a significant amount of beamtime to acquire the proposed scans.

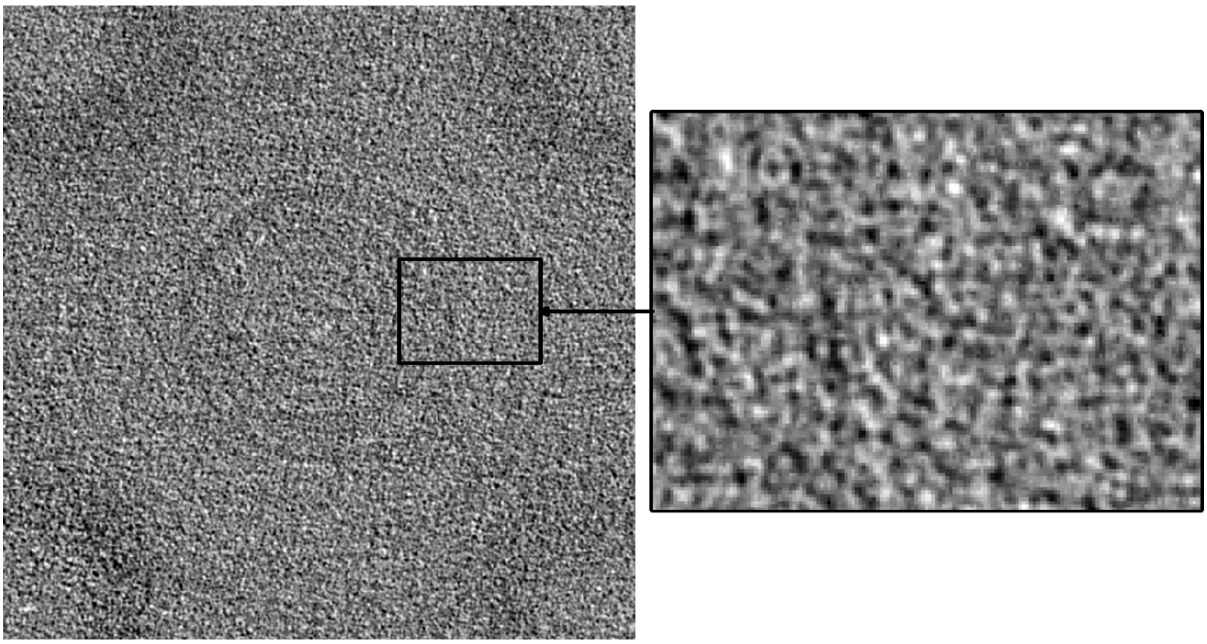

Figure 3.10: Horizontal tomography slice from neutron CT

3.4.3 Synchrotron X-ray CT

Synchrotron light sources accelerate electrons to speeds close to the speed of light, using magnetic fields to maintain the trajectory of the electrons around a closed path, which in turn emits electromagnetic

radiation ranging from infrared to gamma rays. When undertaking imaging, monochromators may be used to cut a narrow band of energy out of this broad spectrum, which can produce images with phase contrast and remove the issue of beam hardening. Insertion devices, such as wigglers, are used in synchrotrons to achieve a high photon flux of this narrow energy band, producing high brightness for imaging and CT. This brightness makes synchrotron X-ray CT preferable over conventional laboratory X-ray sources as it can obtain high-resolution images of dense and large objects in significantly shorter times (Brunke et al. 2008).

Method

Experiments were conducted using the Imaging and Medical Beamline (IMBL) at the Australian Synchrotron (ANSTO, Victoria, Australia), within the third hutch (mode 3B). Imaging within this hutch allows the sample to be located 135 m from the source (Figure 3.11), which produces highly coherent X-rays suitable for phase-contrast imaging. Samples are positioned using a three-dimensional (3D) robot controlled sample stage, which allows a large variety of sample sizes to be placed within the path of the beam. The detector system utilises a photo-sensitive device coupled with a bright lens to a suitable X-ray sensitive scintillator (Hall et al. 2013). The sensor used is a pco.edge camera system mounted on a vertical motor-driven slide set within a light-tight enclosure. A mirror is used to view a phosphor plate set orthogonally to the direction of the beam. For this experiment, the sensor was equipped with a Nikon Micro-Nikkor 50 mm/f 1.6 macro lens allowing the slide to be used as a zoom control. The scintillator was a 12-micron thick terbium-doped gadolinium oxy-sulfide (Gadox, P43) screen with aluminium powder coat as an optical block.

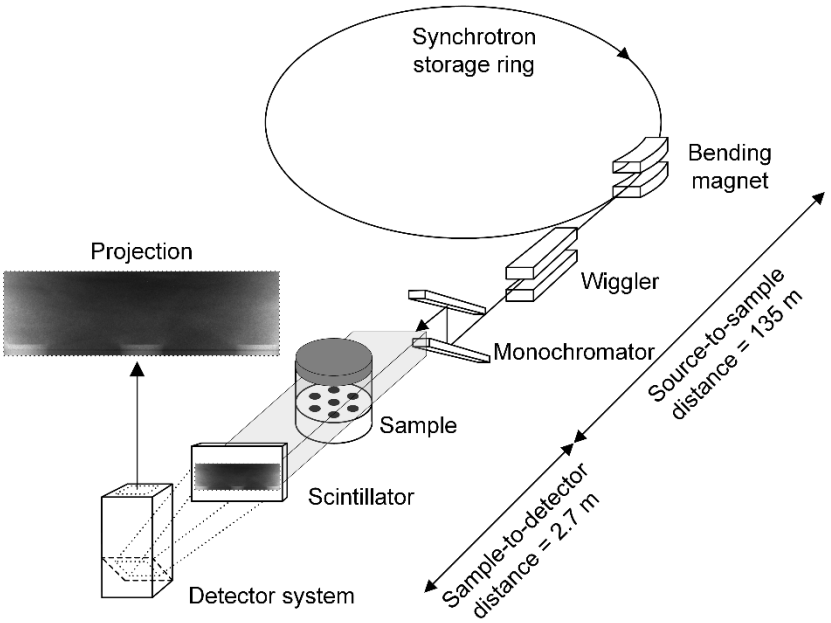

Figure 3.11: Concept and setup for imaging within the IMBL mode 3B

The camera system used was capable of producing an image of 2560 pixels wide. This limited the voxel size to 34.9µm in width to capture the Region of Interest (ROI), which measured approximately 89 mm wide to capture the sand spanning between the outer piles within the model comprising piles on a triangular grid. While the IMBL beam in mode 3B is sufficiently wide to image the entire ROI, it is only 30 mm in height, with roll off observed in the lower and upper sections of the beam. The robot controlled sample stage could position the model in the path of the beam at precise locations for scans to be performed at different heights of the model. Several scans were undertaken with sufficient overlap between scans to reduce the effects of roll off and allow the scans to be stitched together to capture the full height of the ROI, from the pile heads to above the critical height.

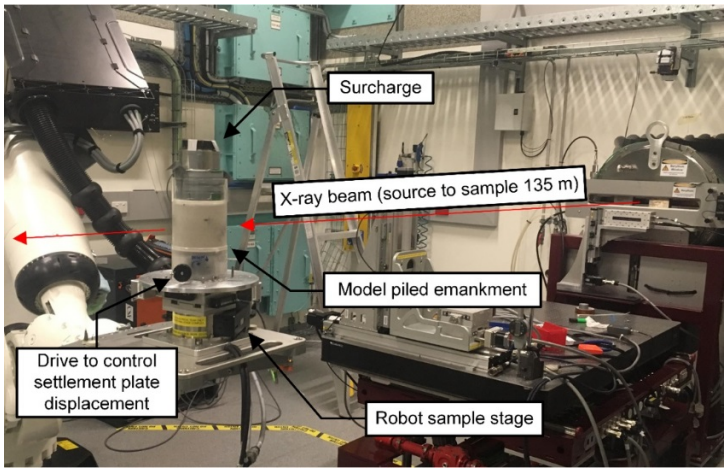

Figure 3.12: Model piled embankment within the IMBL third hutch

Preliminary results

To investigate the optimal imaging technique, two modes of the X-ray imaging available on the IMBL were tested: monochromatic and pink beams (see Figure 3.13). In the first approach, a double Laue reflection silicon monochromator was used at a distance of 21.6 m from the source to extract a narrow band of the broad energy spectrum. The monochromator was tuned to produce an X-ray beam consisting of photons with an energy of 60 keV. The exposure time of a single image under these conditions to achieve sufficient photon counts was 1 second. The pink beam mode is composed of a much broader and higher energy spectrum, which is shaped by utilising multiple attenuators to absorb the low-energy part of the beam. The higher energy X-rays (although technically gamma-rays as most of the photons are above the 100keV formal boundary) used in pink beam imaging can penetrate through high density and large diameter objects much easier than low energy photons. This results in the pink beam requiring an exposure time of only 0.5 seconds per projection to achieve sufficient photon counts. However, the images collected using the monochromatic beam possessed an essential property that was not present in images obtained using the pink beam – the phase contrast enhancement, which is acutely sensitive to the interfaces between different materials (Diemoz et al. 2012).

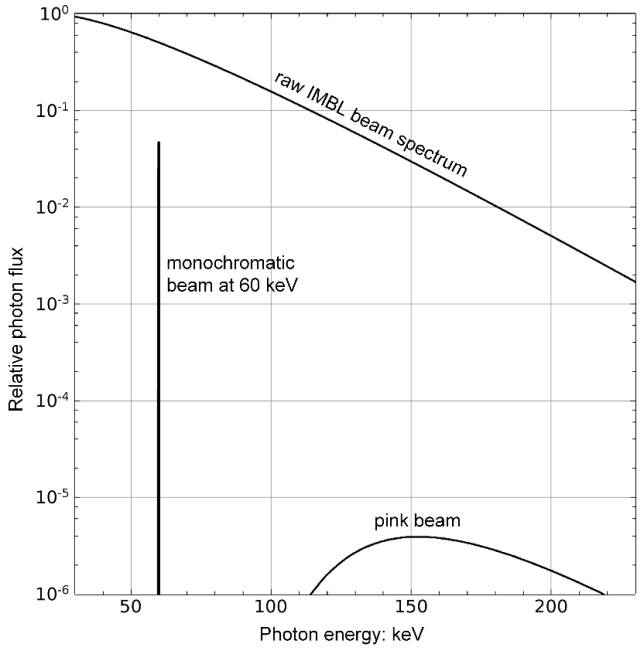

Figure 3.13: Beam spectra used in the monochromatic and pink beam imaging modalities

Each scan comprised of 1800 radiographs taken at rotation increments of 0.1˚. The radiographs were first stitched together to obtain the full height of the ROI and then reconstructed using the software package X-TRACT developed by CSIRO (Gureyev et al. 2011; Hall et al. 2013). A standard filtered back projection algorithm for the CT processing was used. While the monochromatic images contain the phase contrast component, the phase retrieval step was omitted in the CT reconstruction. Although phase retrieval may improve the material differentiation, it adds blurring into the reconstructed image. The blurring introduced by this step was found to remove small features, which given the size of the grains relative to the voxel size, reduced the image texture resulting from sand grains in the reconstructed CT volumes.

Two CT scans were recorded after the settlement plate was lowered approximately 1.5 mm to select the appropriate imaging modality. One scan was performed with the 60 keV monochromatic beam and another with the pink beam. Both scans had the same voxel size of 34.9 μm. A projection with the flat field and background subtracted using both modes is shown in the top row of Figure 3.14 (after scans were stitched), where the piles (lighter regions) can be seen to be penetrating through the settlement plate and into the sand. A reconstructed CT slice taken within the sand sample, passing through the exposed pile heads, is shown in the middle row of Figure 3.14. A sub-volume from this slice (bottom row of Figure 3.14) highlights the difference in contrast capabilities between the monochromatic and pink beams. Texture within the sand mass is evident in the monochromatic CT reconstructions due to the contrast between sand grains and air voids. The central pile, which is made from PVC, is seen to have minimal texture in the monochromatic CT slice, although some ring artefacts, again due to imperfections of the detector. However, the pink beam CT slice has consistent texture throughout both

the sand mass and pile, which is due to the strong component of the scattered radiation and higher noise produced by the high-energy photons rather than any sand grains or material structure. The ilmenite grains within the sand, seen as white spots in the monochromatic beam CT slice, are not present in the pink beam CT slice because the modulation of the absorption contrast alone is not sufficient, which is further suppressed by the scattered radiation. Moreover, the polychromatic beam does not contain the phase enhancement observed in the monochromatic beam and, thus, produces brighter but less informative images. By using a lower energy X-ray beam, a greater differential attenuation between materials occurs, which in turn increases absorption contrast. Thus, images obtained using the lower energy monochromatic X-ray beam (relative to the pink beam) and containing the phase component, which is specifically sensitive to the interfaces between materials, comprised greater contrast between grains and voids and more pronounced texture. To acquire such CT images on large diameter samples of sand using laboratory produced monochromatic X-rays would require long scan times, which becomes increasingly unfeasible if a large number of consecutive scans are undertaken for the implementation of DVC analysis.

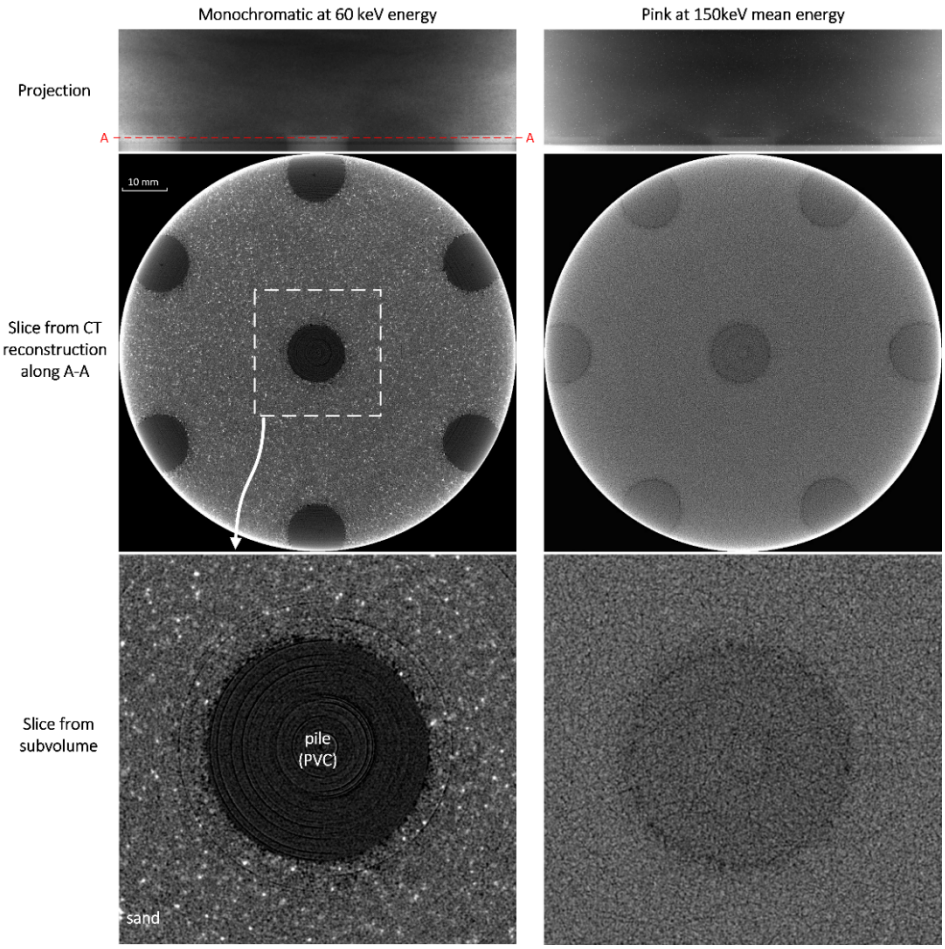

Figure 3.14: Monochromatic (left) and pink beam (right) imaging; (top row) projections, (middle row) CT reconstructed slices along plane A-A and (bottom row) sub-volume of CT slice

3.4.4 Conclusions of imaging

Three radiation sources and imaging techniques were investigated to determine which method is best suited for imaging samples of fine-grained silica sand with a diameter of up to 142 mm while achieving sufficient spatial resolution and contrast for the application of DVC. The findings of preliminary imaging using the three sources may be summarised as:

- Laboratory X-rays: The polychromatic X-ray beam resulted in significant artefacts and provided no contrast between grains and voids, such that no image texture could be observed within reconstructed CT volumes of fine-grained silica sand. This method was shown to be useful for larger grained (1 mm) glass beads, although such grains do not satisfy similitude conditions. Monochromatic beam could be utilised, although the low brilliance of a monochromatic laboratory X-ray beam would likely require long scan times to achieve sufficient photon counts through such a large sample.
- Neutrons: The penetration capabilities of neutrons allowed general density changes within the sand mass to be observed, although the reconstructed CT volumes possessed a blurred texture (Figure 3.15a). Preliminary DVC analysis (described in the proceeding section) performed on CT volumes obtained from neutron imaging resulted in many spurious measurements (Figure 3.15b). Given the time required to collect these scans and the quality of reconstructed CT volumes, this technique was found not suitable for the proposed experimental programme.
- Synchrotron X-rays: The imaging undertaken using monochromatic synchrotron X-rays resulted in CT volumes well-suited for DVC analysis within relatively short scan times compared to the other imaging techniques. Reconstructed CT volumes possessed a fine image texture (Figure 3.15c) due to the high brilliance, coherent and low energy monochromatic X-ray beam achieved at the IMBL facility. The reconstructed CT volumes resulted in displacement vectors being estimated from DVC analysis without any spurious measurements evident (Figure 3.15d). This setup was selected as the preferred imaging method and was applied to several models, the results of which are presented in the following chapter.

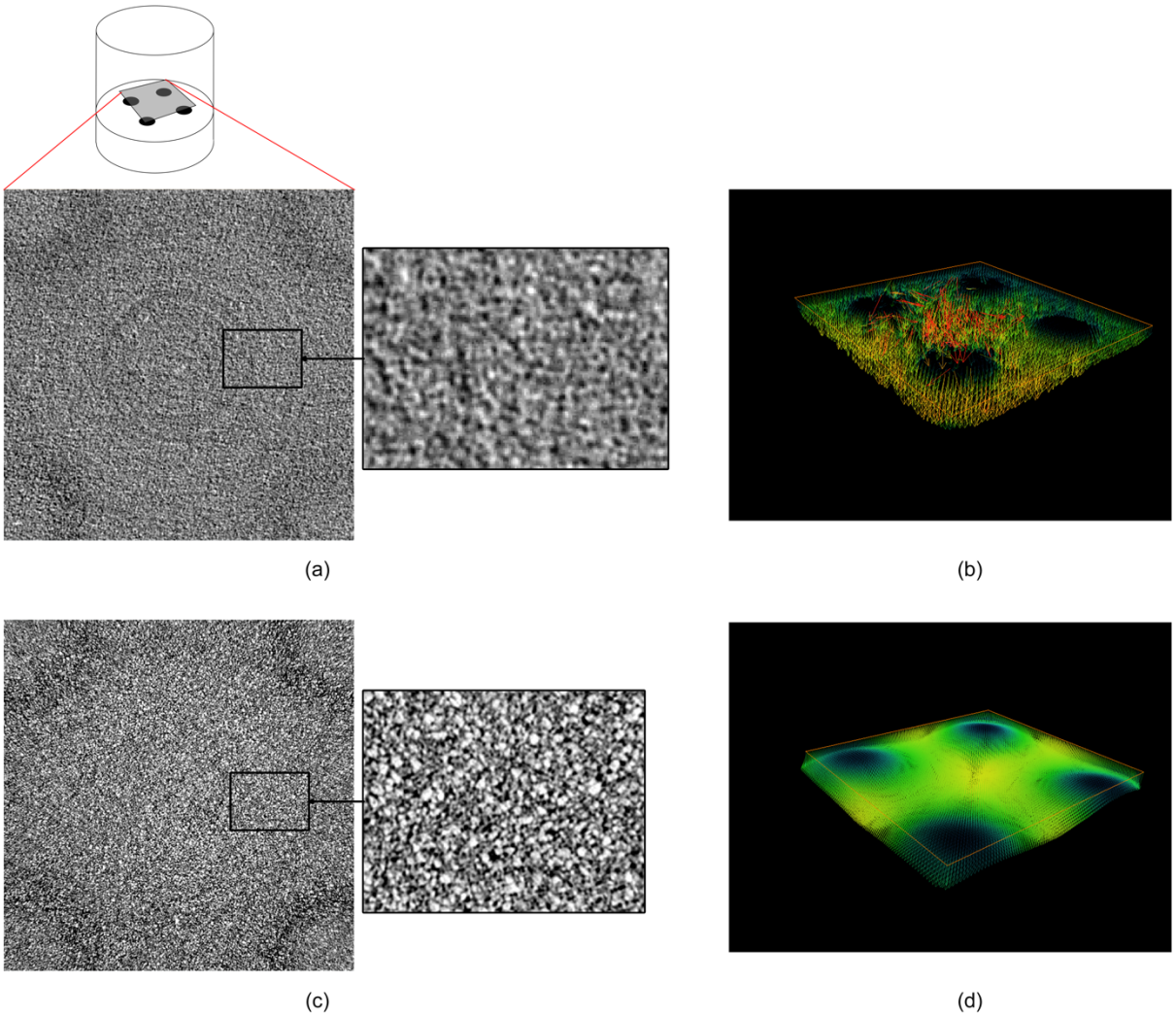

Figure 3.15: (a) Neutron CT slice; (b) slice of displacement vectors from neutron CT; (c) synchrotron X-ray CT slice; and (d) slice of displacement vectors from synchrotron CT

3.5 Characterisation of kinematics

3.5.1 Calculation of displacement field

Digital volume correlation (DVC) is a 3D extension to the more widely known methods of Particle Image Velocimetry (PIV) and Digital Image Correlation (DIC). PIV refers to the accurate, quantitative measurement of velocity vectors at a very large number of points simultaneously, most commonly within a fluid (Adrian 2005). In the field of fluid mechanics, tracer particles are typically added to a flow and illuminated along a planar field by a light source (Raffel et al. 2007). The modern form of PIV takes digital images of these illuminated particles and applies post-processing techniques to estimate the displacement field between two images. With a known time interval between the two images, referred to as the inter-frame time, the velocity vectors can be estimated by dividing displacements by the inter-frame time.

To estimate a displacement field, PIV divides a digital image into sub-regions called interrogation windows. Each interrogation window of the digital image is made up of pixels, each with its own grey-scale value. By comparing two images, before and after a time interval, it is possible to find the displacement between them by implementing an algorithm that searches for similar pixel patterns. The search algorithm utilises cross-correlation, or other image correlation methods, to search for similar pixel patterns. The maximum correlation function within the correlation plane is taken as the most common displacement of the particles (or material) within the interrogation window.

PIV has found increasingly widespread application to geotechnical research since White et al. (2003) developed the open-source software GeoPIV. Geotechnical research, particularly when studying granular materials, often focuses on displacement fields without considering time. Thus, the term DIC is commonly used interchangeably with PIV by geotechnical researchers. DIC in the field of geotechnics is typically applied to 2D plane strain model tests, utilising the image texture within digital photographs of soils, either naturally or by artificially seeding (Stanier and White 2013) to achieve sufficient pixel information to perform cross-correlation. Higher image texture has been shown to increase the precision of DIC analysis (White et al. 2003; White and Take 2005).

Over the past two decades, digital volume correlation (DVC) has been increasingly applied to CT volumes (Bay et al. 1999; Elsinga et al. 2006) due to the advancement of imaging technologies that allow higher spatial and temporal resolution to be achieved. DVC utilises similar concepts to DIC where a CT volume is discretised into sub-regions known as interrogation volumes. Cross-correlation is applied in three dimensions to search for similar voxel grey-scale patterns between pairs of CT volumes to estimate the 3D displacement vectors for each interrogation volume.

The DVC software applied in the present study was developed by Dubsky et al. (2012) for imaging of biological tissue using synchrotron X-ray CT. This software utilises an iterative multi-pass method (Scarano and Riethmuller 1999), where a first pass analysis is performed on a larger interrogation volume followed by a second analysis on a smaller interrogation window offset by the displacement calculated by the initial pass. This iterative approach reduces the errors associated with sand grains leaving the interrogation volume between scans. In the present study, a final interrogation window measuring 32 x 32 x 32 voxels was used with a 50% overlap between interrogation volumes. The universal outlier method (Westerweel and Scarano 2005) is also applied to the displacement vector field to remove spurious measurements. DVC analysis was implemented using the high-performance computing (HPC) facility called MASSIVE. It is noted that no post-processing was performed on the reconstructed volumes before performing DVC analysis.

3.5.2 Calculation of strain field

Partial derivatives of the displacement vector field were calculated by fitting a polynomial to the displacement field and differentiating the fitted polynomial (Dubsky et al. 2012), which allowed the second-order displacement gradient tensor, **L**, to be derived:

$$\mathbf{L} = \begin{bmatrix} \frac{\partial u}{\partial x} & \frac{\partial u}{\partial y} & \frac{\partial u}{\partial z} \\ \frac{\partial v}{\partial x} & \frac{\partial v}{\partial y} & \frac{\partial v}{\partial z} \\ \frac{\partial w}{\partial x} & \frac{\partial w}{\partial y} & \frac{\partial w}{\partial z} \end{bmatrix} \tag{3.8}$$

The deformation gradient (**F*)* is calculated from the displacement gradient by the relationship:

$$\mathbf{F} = \mathbf{L} + \mathbf{I} \tag{3.9}$$

Where **I** is the identity matrix. Through polar decomposition theorem, the deformation gradient can be decomposed into the product of a proper orthogonal tensor (**R**) and a symmetric tensor (**U**), such that:

$$\mathbf{F} = \mathbf{RU} \tag{3.10}$$

Equation 3.10 can be rearranged to give:

$$\mathbf{U} = (\mathbf{F}^{\mathrm{T}}\mathbf{F})^{1/2} \tag{3.11}$$

The symmetric tensor may be used to calculate any number of strains, of which the Biot strain was used in the present study, which is written as:

$$\mathbf{E}_{\mathrm{Biot}} = \mathbf{U} - \mathbf{I} \tag{3.12}$$

The principle engineering strains, ε_1, ε_2 and ε_3, are equal to the eigenvalues of the strain tensor $\mathbf{E}_{\mathrm{Biot}}$ and the eigenvectors are the inclination of the principal strains to the x, y and z axes. In the proceeding results section, strains are presented using natural strains, which were calculated by the relationship:

$$\varepsilon_{\log} = \log_e(1+\varepsilon) \tag{3.13}$$

The maximum natural shear strain, $\gamma_{\log,\max}$, was then estimated using the relationship:

$$\gamma_{\log,\,\max} = \varepsilon_{\log,1} - \varepsilon_{\log,3} \tag{3.14}$$

Where $\varepsilon_{\log,1}$, $\varepsilon_{\log,2}$ and $\varepsilon_{\log,3}$ are the major, intermediate and minor natural principal strains respectively. The volumetric natural strain may then be written as:

$$\varepsilon_{\log,\,v} = \varepsilon_{\log,1} + \varepsilon_{\log,2} + \varepsilon_{\log,3} \tag{3.15}$$

3.6 Measurement procedure

As noted, monochromatic synchrotron X-ray CT scans were found to obtain volumes with sufficient voxel information to conduct DVC analysis on models comprising up to 142 mm of fine-grained silica sand. The experimental procedure utilising this technique and subsequent image analysis undertaken to measure three-dimensional full-field displacements and strains may then be summarised by the flowchart depicted in Figure 3.16.

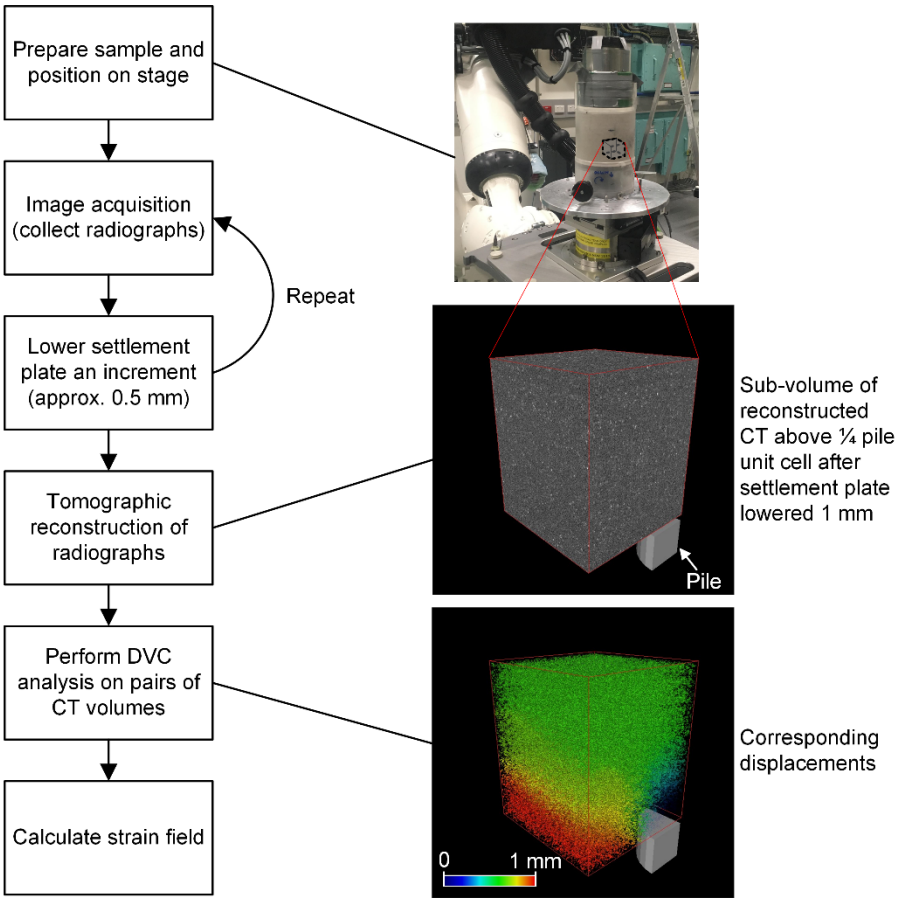

Figure 3.16: Flowchart of experimental procedure and image analysis performed to measure displacement and strain fields

3.7 Summary

Small-scale model piled embankments (without geosynthetic reinforcement) were designed and constructed to simulate the progressive development of soil arching as subsoil undergoes settlement and as a defective pile undergoes additional settlement to the surrounding non-defective piles. Imaging was performed using three types of radiation, and it was found that Synchrotron X-Ray CT imaging using monochromatic photons produced superior images in respect to spatial resolution, contrast and

artefacts compared to images collected using laboratory produced X-rays and neutrons. The monochromatic X-ray beam produced high-resolution reconstructed volumes with a fine texture due to the size and mineralogy of the sand grains as well as the phase contrast enhancement achieved by the monochromatic X-ray beam. The reconstructed volumes were well suited to the application of digital volume correlation, which utilises cross-correlation techniques to estimate three-dimensional full-field displacement vectors. These displacement fields can be used to calculate strains, which in turn, provide insight into the failure surfaces and soil kinematics associated with soil arching in piled embankments.

4 Small-scale model tests – results and discussion

As shown in Chapter 2, many soil arching models assume a failure surface as part of their derivation of arching stresses within a piled embankment. However, these assumed failure surfaces are not based on any observed soil kinematics other than some surface displacements or 2D plane strain observations that are more representative of a trapdoor test than a piled embankment. Understanding the soil displacements and strains within an LTP overlying a grid of piles is essential for the development of more advanced arching models, but also to explain many of the phenomenon observed in piled embankments, such as the formation of a plane of equal settlement and the propagation of settlements from the base of the embankment to the surface.

This chapter details the results from monochromatic synchrotron X-ray CT scanning undertaken on small-scale model piled embankments, which were used to calculate three-dimensional displacement and strain fields. The results allow the failure surfaces that develop above pile heads within the LTP granular material to be characterised.

4.1 Test program

A total of six model tests were imaged using synchrotron produced X-rays. Tests were undertaken using either the square model (SQR) or equilateral triangle model (EQT) arrangements and comprised UWA fine-grained sand prepared in either a dense (D) or medium dense (MD) state. One of the aims of the study was to investigate the arching mechanism around a defective pile. As described in Chapter 2, a defective pile typically experiences a softer load-settlement response to other non-defective piles. Therefore, to study the soil kinematics above a defective pile, the central pile in two of the triangular model tests (names ending with 'DEF') was lowered to simulate the additional settlement that may be experienced by a defective pile. Details of the tests performed are provided in Table 4.1.

Table 4.1: Model test details

Test name	Model	Central pile defective?	Relative density, D_r
SQR-D	Square	No	95%
SQR-MD	Square	No	62%
EQT-D	Triangle	No	94%
EQT-MD	Triangle	No	64%
EQT-D-DEF	Triangle	Yes	96%
EQT-MD-DEF*	Triangle	Yes	61%

*Test terminated early due to equipment malfunction

4.2 Model tests without defective piles

4.2.1 Results

The results from DVC analysis are presented in the following sections at specific settlement plate displacements to highlight the progressive development of the soil arching mechanism. In 2D trapdoor tests, the trapdoor vertical displacement is often normalised by the trapdoor clear spacing when studying the progressive development of load transfer resulting from soil arching (Iglesia et al. 1999). However, the layout of the piles in a grid means that no single clear spacing between the piles exists, and as such, the subsoil settlement (or settlement plate displacement) beneath an embankment cannot be compared directly with normalised trapdoor displacements. So that the progressive development of soil arching can be investigated with comparisons made to trapdoor soil arching theories, an equivalent area unit cell concept is used to calculate an equivalent axisymmetric clear spacing, described by King et al. (2017a) and depicted in Figure 4.1. This method calculates an axisymmetric unit cell with diameter D that has an area equal to that of the actual unit cell. The axisymmetric clear spacing (b') is then taken as $b' = D - d$. For the pile arrangement and geometry of the square and triangular models used in the current study, the equivalent axisymmetric clear spacing's are equal to 35.8 mm and 29.4 mm, respectively. Settlement plate displacements in the following sections have been normalised by b'.

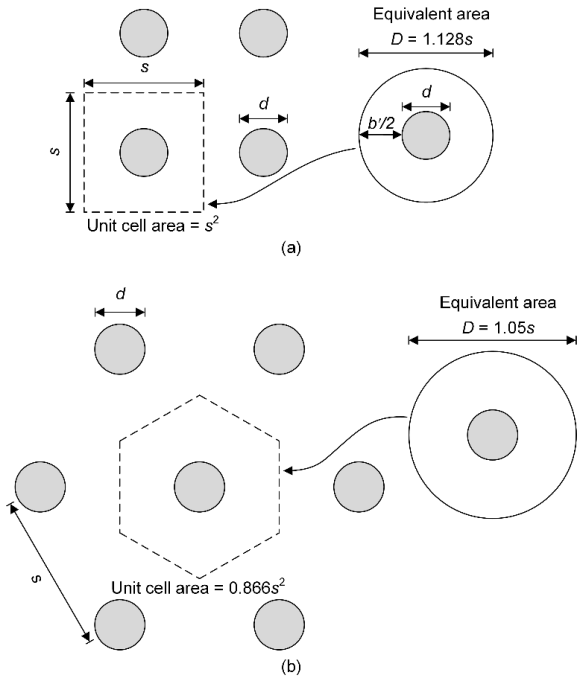

Figure 4.1: Equivalent area unit cell for piles on a (a) square grid; (b) equilateral triangular grid

Incremental displacements have been used to show the mechanism governing soil arching at specific settlement plate displacements, meaning that displacement vectors are estimated only between scans at the two noted displacements and are not cumulatively added together. In doing so, the state of the soil

arching mechanism is shown at the specified settlement plate displacement. The vertical displacements of the sand, U_z, have also been normalised by the settlement plate displacement δ_{sp}.

Figure 4.2 shows the normalised incremental vertical displacements at increments of normalised settlement plate displacement (δ_{sp}/b') for both square and triangular models comprising dense and medium dense sand. Due to the symmetrical nature of the models, each slice shown in Figure 4.2 is divided in two, with dense samples shown on the left side and medium dense samples shown on the right side. For both densities, the displacements within the sand were a minimum at shallow heights directly above the pile heads and a maximum at shallow heights directly above the settlement plate. With increasing height above the pile heads, the difference between these settlements decreased until an almost uniform settlement was achieved, i.e. the critical height.

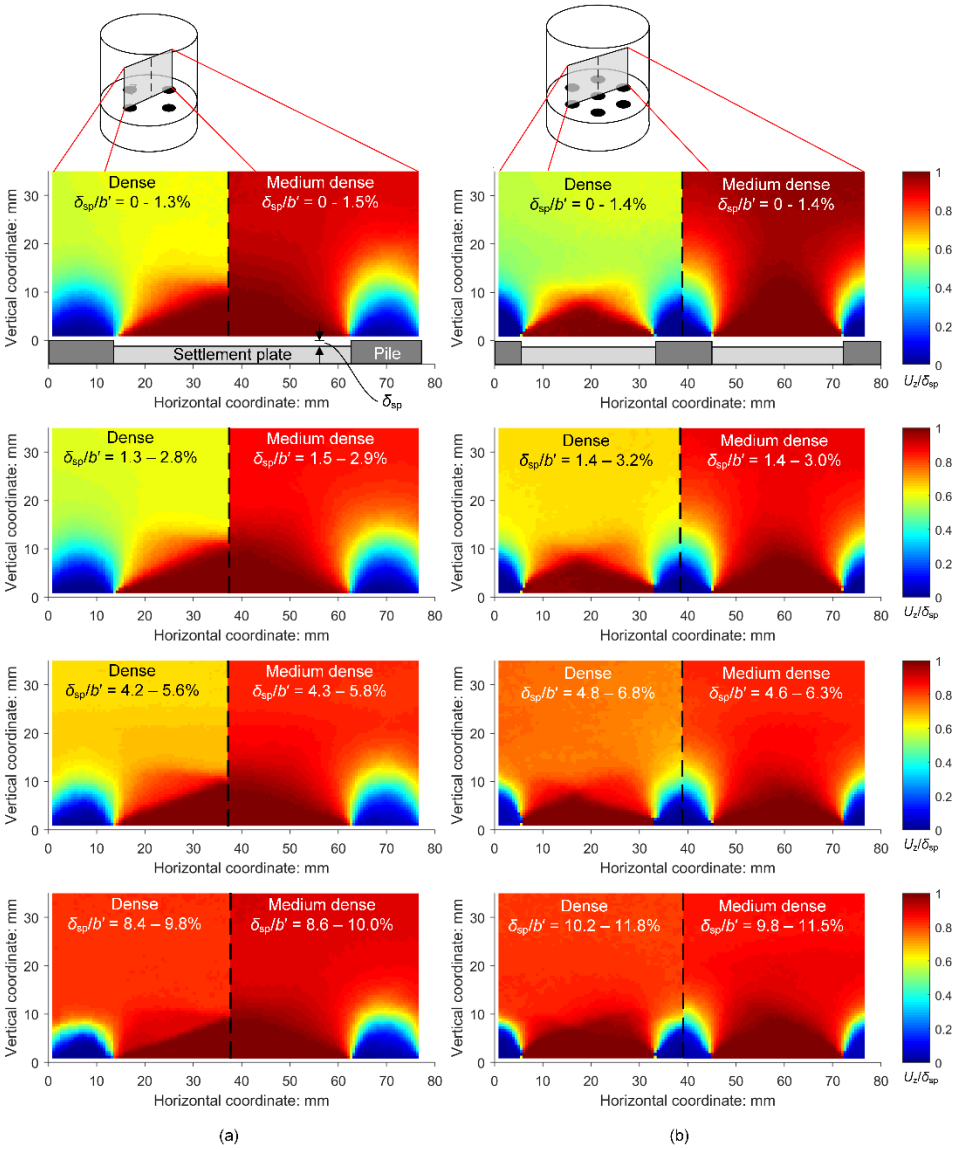

Figure 4.2: Slices of incremental normalised vertical displacements with dense sand on the left and medium dense sand on the right of each slice for (a) square model; (b) triangular model

Similar behaviour regarding the progressive development of soil arching is observed between both square and triangular models. The dense samples resulted in less settlements propagating to the embankment surface compared to the medium dense samples at values of $\delta_{sp}/b' < 4\%$. With increasing settlement plate displacement, the soil displacements in the models comprising dense sand increased. After further settlement plate displacement ($\delta_{sp}/b' > 8\%$) the displacements within models comprising dense sand began to resemble those of the models comprising medium dense sand.

The incremental maximum natural shear strains ($\gamma_{max,log}$), again for both the square and triangular models comprising dense and medium dense sand, are presented in Figure 4.3. The shear strains show localisations of strain (shear bands) propagating from the edge of the pile heads into the sand mass. These shear bands developed within the first increment of δ_{sp}/b' from 0% to approximately 1.4%. In the models comprising dense sand, two shear bands developed at the pile head-settlement plate interface. One of the shear bands (Type 1) formed above the pile head, which developed at an inclination to the horizontal of between 55˚ and 65˚. This shear band intersected the equivalent Type 1 shear band propagating from the opposite side of the same pile head, forming a triangular wedge above the pile head. The second shear band (Type 2) formed away from the pile heads and was orientated at approximately 25˚ to 35˚ to the horizontal. Type 2 shear bands were initially linear and passed through the equivalent shear band propagating from an adjacent pile head. At some distance into the soil mass Type 2 shear bands became curved and appear to have interacted and converged with a Type 1 shear band from an adjacent pile. Both shear bands in the dense sand, Type 1 and 2, were present throughout all slices, regardless of settlement plate displacement. There was a trend in both models comprising dense sand for the Type 1 shear bands forming the wedge above the pile heads to develop larger shear strains with increasing settlement plate displacement. The Type 2 shear bands that formed above the settlement plate became either more localised (square model) or experienced less shear strain (triangular model) with increasing values of δ_{sp}/b'. It is also noted that Type 1 and 2 shear bands formed at approximately 90˚ to each other above the edge of the pile heads.

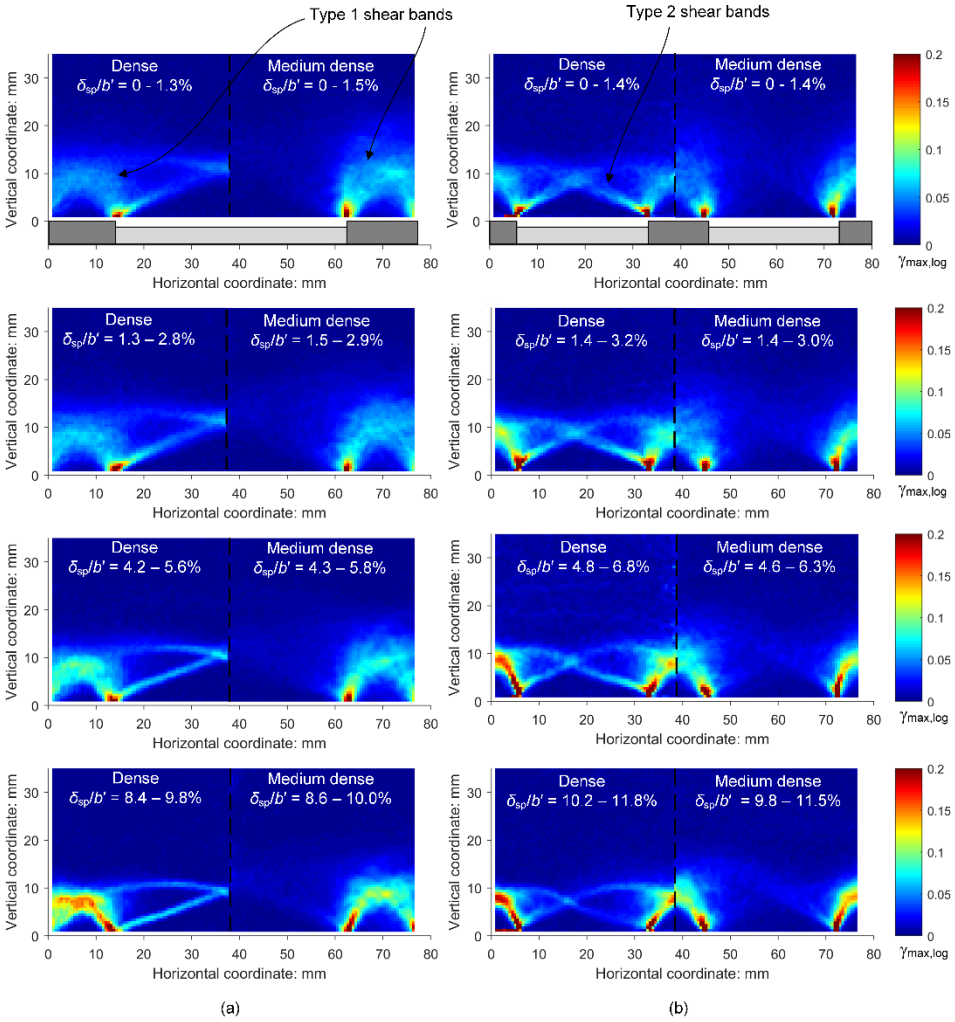

Figure 4.3: Slices at equivalent position as Figure 4.2 of incremental maximum shear strain for (a) square model; (b) triangular model

The shear strains for the models comprising medium dense sand presented in Figure 4.3 show only one shear band propagating from the edge of the pile head-settlement plate interface, which is equivalent to the Type 1 shear bands observed in the models comprising dense sand, and hence is assigned the same nomenclature. Again, these Type 1 shear bands developed at an angle of between 55˚ and 65˚ to the horizontal. There is evidence in the slices through models comprising medium dense samples that failure occurred in the regions above the settlement plate and extending from the top of the Type 1 shear bands. Although shear strains in these regions developed in a non-localised mode, representative of diffuse failure (Darve et al. 2004). Again, there was a trend in the medium dense samples for increasing shear strain to develop in the Type 1 shear bands with increasing settlement plate displacement.

The incremental volumetric strains (ε_v) are presented in Figure 4.4. It is evident that maximum volumetric strain, and hence dilation, occurred in the models comprising dense sand within both Type 1 and 2 shear bands at values of $\delta_{sp}/b' < 6\%$. It is likely that these small displacements mobilised

maximum dilatancy at points within the shear bands. After which, less volumetric strain occurred as the sand within the shear bands began to approach constant volume shearing (critical state). A similar response regarding mobilisation of dilation is observed in the models comprising medium dense sand, although less dilation occurred compared to the corresponding dense samples at similar values of δ_{sp}/b' and dilation occurred mostly within the Type 1 shear bands.

It is also shown in Figure 4.4 for both models and sand densities that non-uniform strain is mobilised within the shear bands. After small settlement displacement ($\delta_{sp}/b' < 2\%$) high volumetric strain developed in regions of the shear bands close to the pile heads. After more settlement plate displacement, volumetric strain is mobilised in regions further away from the pile heads. For example, the shear band along the outer boundary of the Prandtl radial shear zone observed in both models comprising dense sand is not clearly evident in slices of volumetric strain after small amounts of settlement plate displacement. After more settlement plate displacement, strain is mobilised in these regions that are further from the pile head-settlement plate interface.

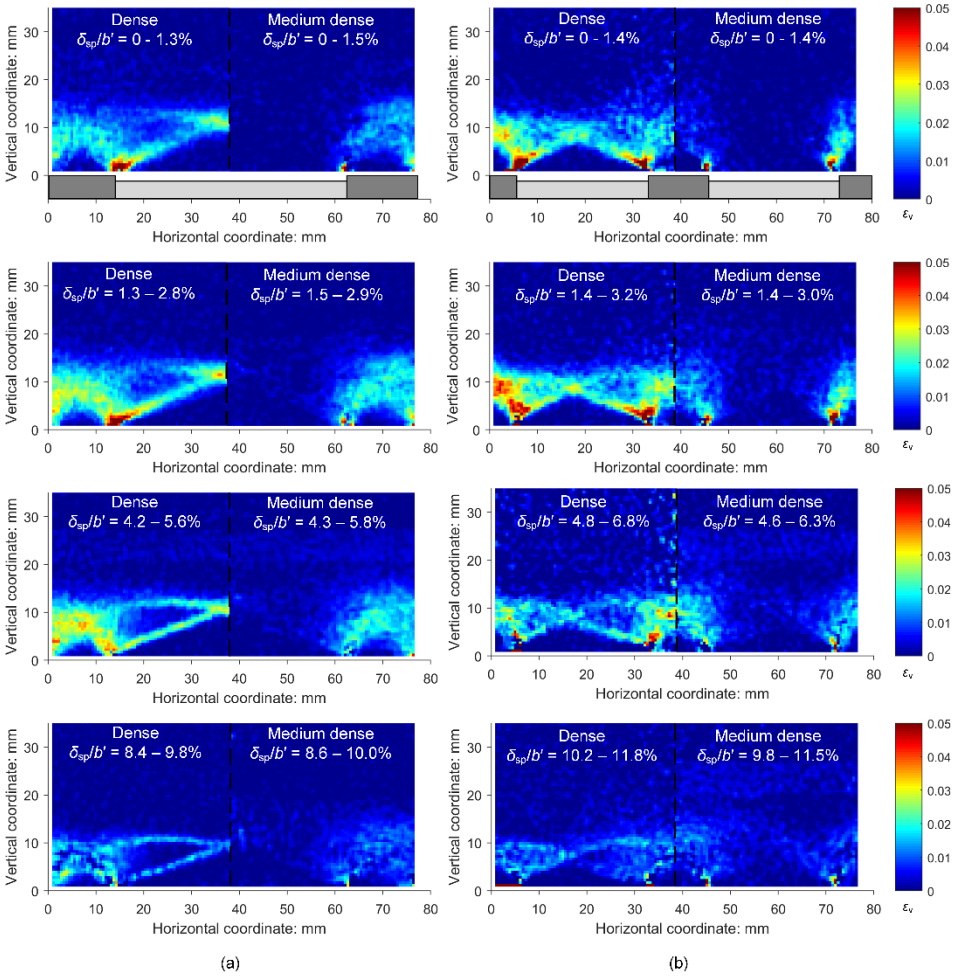

Figure 4.4: Slices at equivalent position as Figure 4.2 of incremental volumetric strain for (a) square model; (b) triangular model

4.2.2 Analysis

It is noted that the displacement (Figure 4.2) and strain fields (Figure 4.3 and Figure 4.4) do not resemble the failure mechanism assumed in many of the widely-used soil arching design models. No physical arch-like shape was observed. Instead, strain localisations propagated from the edge of the pile heads and, in the case of dense sand, interacted with localisations propagating from adjacent pile heads. The following discussion does not provide a new soil arching design model. The analysis instead focuses on describing the observed kinematics, which may assist the development of future design models.

Failure mechanism – dense sand

One of the most widely studied failure mechanisms in geotechnical engineering is that of shallow foundations. General shear failure of a shallow foundation is expected to be the governing mode of failure when a shallow foundation is placed at shallow depths on dense sand (Vesic 1973). General shear failure of shallow foundations is typically characterised by three zones (Terzaghi 1943), as shown in Figure 4.5, with defined failure surfaces dividing the zones. Zone I is a triangular wedge where soil remains in an elastic state of equilibrium. Zone II is referred to as the Prandtl radial shear zone, and Zone III is the passive Rankine zone, both of which are plastic zones.

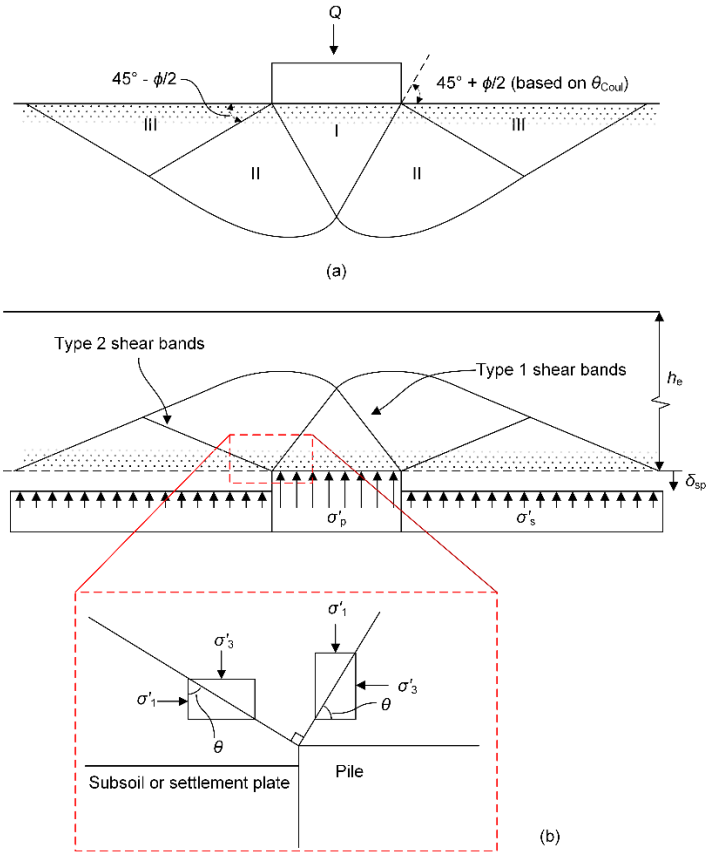

Figure 4.5: (a) General shear failure of a shallow foundation; (b) failure mechanism observed in dense sand samples in model piled embankments (not to scale)

Based on observations from DVC analysis on samples of dense sand, the pattern and shape of shear bands that develop within sand above a pile in an LTP are analogous to that of general shear failure beneath a shallow foundation, although vertically mirrored and without consideration of interaction with failure surfaces above adjacent piles (Figure 4.5). The observation of such a failure mechanism in the model piled embankments comprising dense sand is, in-part, due to the direction of principal stresses as the settlement plate is lowered. Directly above the pile heads, the sand material is in an active state after the settlement plate is lowered, with the major principal stress direction inclined vertically. The sand directly above the settlement plate is in a passive state, where the minor principal stress direction is inclined vertically. The sand between these two zones undergoes radial shear as the principal stress direction rotates between these two active and passive zones. The direction and rotation of principal stresses between these zones are described similarly by Terzaghi (1943) regarding an active trapdoor. Thus, the three zones observed below a shallow foundation experiencing general bearing failure (elastic, radial Prandtl shear and Rankine passive zones) are also present within granular material overlying a pile head.

For general shear failure of a rough footing, the failure surfaces extending from the edge of the foundation between Zones I and II are typically assumed to develop at an angle equal to $45^\circ + \phi_m/2$ to the horizontal (Meyerhof 1951), where the subscript m refers to mobilised. This angle is based on the Mohr-Coulomb criterion with an associated flow rule. When defined relative to the minor principal stress direction, this angle is referred to as the Coulomb angle of orientation, θ_{Coul}. Considering the minor principal stresses near the ground surface adjacent to a loaded shallow foundation are vertically inclined, the angle of the surfaces separating Zones II and III in Figure 4.5a is equal to $45^\circ - \phi_m/2$ to the horizontal, based on θ_{Coul}. It is noted that these failure surfaces are based on slip line theory. However, given that the surfaces are evident after large amounts of deformation, it is more appropriate for these surfaces to be classified as shear bands rather than slip lines.

Studies investigating the development of shear bands in granular materials have shown that the angle at which they develop relative to the minor principal stress direction is more suitably estimated using a non-associated flow rule (Vardoulakis 1980; Desrues et al. 1985; Vermeer 1990). Based on experimental observations, Arthur et al. (1977) proposed the following angle of shear band orientation:

$$\theta_{Arth} = 45^\circ + \frac{(\phi_m + \psi_f)}{4} \tag{4.1}$$

Where the subscripts m and f refer to mobilised and failure, respectively. This angle was shown to be a close approximation for the solution obtained through bifurcation analysis by Vardoulakis (1980). Given that shear bands form initially at or slightly before peak strength, in the following analysis the shear band orientation will be estimated assuming $\phi_m = \phi_p$ and $\psi_f = \psi_{max}$ at the onset of localisation.

Based on $\phi_p = 46^\circ$ and $\psi_{max} = 14^\circ$ (Table 3.3, dense sand), the angles at which the two shear bands (Type 1 and 2) developed were estimated using the θ_{Coul} and θ_{Arth} relationships and are shown in Table 4.2 along with the measured angles from DVC analysis. Note, the Type 1 shear band angles were estimated based on the assumption that the minor principal stress direction is horizontally orientated above the pile heads, while in the vicinity of the Type 2 shear bands (directly above the settlement plate) the minor principal stress direction is inclined vertically. It is evident that the shear band angles of orientation based on θ_{Arth} lie within the range of measured angles for both Type 1 and 2 shear bands comprising dense sand, while θ_{Coul} overestimates the angle of shear band orientation relative to the minor principal stress direction.

Table 4.2: Estimated and measured shear band angles of orientation to the horizontal for models comprising dense sand

Shear band	θ_{Coul}	θ_{Arth}	$\theta_{measured}$
Type 1	68˚	60˚	55˚ – 65˚
Type 2	22˚	30˚	25˚ – 35˚

Failure mechanism – medium dense sand

The model tests comprising medium dense sand were shown to develop a different failure mechanism to those comprising dense sand. The absence of the Type 2 shear bands in the results from DVC analysis on medium dense model tests makes the failure mechanism analogous to that of punching or local shear failure of a shallow foundation, although again vertically mirrored. Punching shear failure of a shallow foundation is shown in Figure 4.6a and is characterised by a triangular wedge pushing vertically downwards directly below the footing, similar to Zone I for general shear failure. The soil in this wedge is in an elastic state of equilibrium with minor principal stresses inclined horizontally beneath the footing. The failure surfaces that develop from the edge of the footing and bound this zone are typically assumed to develop at an angle to the horizontal of $45^\circ + \phi_m/2$, based on θ_{Coul}.

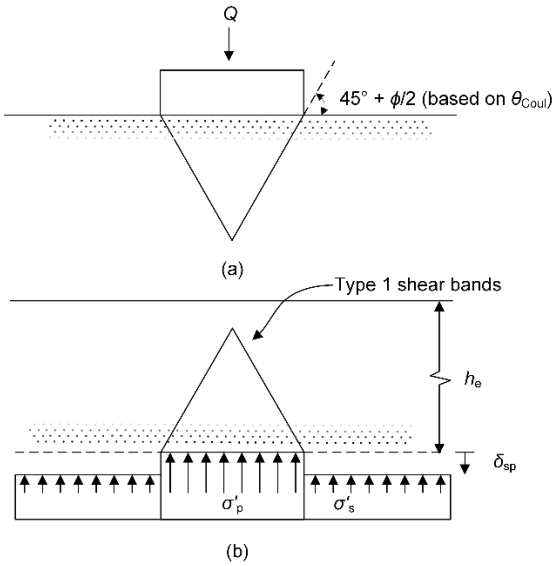

Figure 4.6: (a) Punching shear failure of a shallow foundation; (b) failure mechanism observed in medium dense sand samples in model piled embankments

Given that punching shear failure can be expected to develop beneath foundations placed on loose sands and/or on dense sands at great depths (Vesic 1973) it is logical that the model piled embankments comprising relatively lower density sand exhibited a similar mechanism. In the models comprising medium dense sand, Type 1 shear bands developed above the pile heads, forming a triangular wedge (Figure 4.6b). Extending from the edge of the pile heads above the settlement plate and from the top of the Type 1 shear bands was a diffuse failure. As noted, no significant difference was observed in the orientation of Type 1 shear bands in the results from DVC analysis on model tests comprising medium dense sand compared to tests with dense sand. However, the medium dense sand exhibits a lower peak friction angle of $\phi_p = 40^\circ$ and maximum dilation angle of $\psi_{max} = 9^\circ$ (Table 3.3, medium dense sand) compared to the dense sand. The angles at which the Type 1 shear bands develop were also estimated using the θ_{Coul} and θ_{Arth} relationships and are shown in Table 4.3 along with the range of measured angles. Again, the angle predicted by θ_{Arth} is within the range of measured angles while the angle based on θ_{Coul} is on the upper limit of this range.

Table 4.3: Estimated and measured shear band angles of orientation to the horizontal for models comprising medium dense sand

Shear band	θ_{Coul}	θ_{Arth}	$\theta_{measured}$
Type 1	65	57	55° – 65°

Interaction with adjacent piles

As observed in Figure 4.3 for the dense samples, when piles are spaced on a close enough grid the shear bands that develop within the overlying granular soil in a piled embankment interact with shear bands

developing above adjacent pile heads. Similar interaction of closely spaced shallow foundations has been studied experimentally (Stuart 1962; Das and Larbi-Cherif 1983; Kumar and Saran 2003; Lavasan and Ghazavi 2012), where it has been shown that the bearing capacity of closely spaced foundations is dependent on their width, spacing and the underlying granular materials frictional behaviour. By applying the concepts of the failure mechanism proposed by Stuart (1962) to piled embankments, three cases are expected to arise within LTPs comprising a dense granular material with relatively shallow embankment heights. These three cases are described in terms of the spacing between piles when interaction occurs between shear bands, s_{int}.

- Case A (Figure 4.7a) – When piles are spaced on a grid with a centre-to-centre spacing, s, such that $s > s_{int}$, then failure surfaces will not overlap. Thus, the strain localisations will develop without influence from adjacent piles.
- Case B (Figure 4.7b) – With a closer pile spacing of $s = s_{int}$, the Rankine passive zones will overlap. In this case, the log-spiral failure surface bounding the Prandtl radial shear zone will intersect the Type 2 shear band extending from the adjacent pile head. However, in this condition, the shape and orientation of Type 1 and 2 shear bands do not change, and the origin of the log-spiral is located at the edge of the pile head.
- Case C (Figure 4.7c) – When $s < s_{int}$, the Prandtl radial shear zones are influenced by the Type 2 shear bands extending from the edges of adjacent pile heads. As a result, failure surface bounding the Prandtl radial shear zone does not extend as high into the embankment fill as in case A and B. While this failure surface may still be approximated by a log-spiral, its origin is no longer the edge of the pile head, instead it is below the pile head, which results in a greater radius than in cases A and B (described in more detail below).

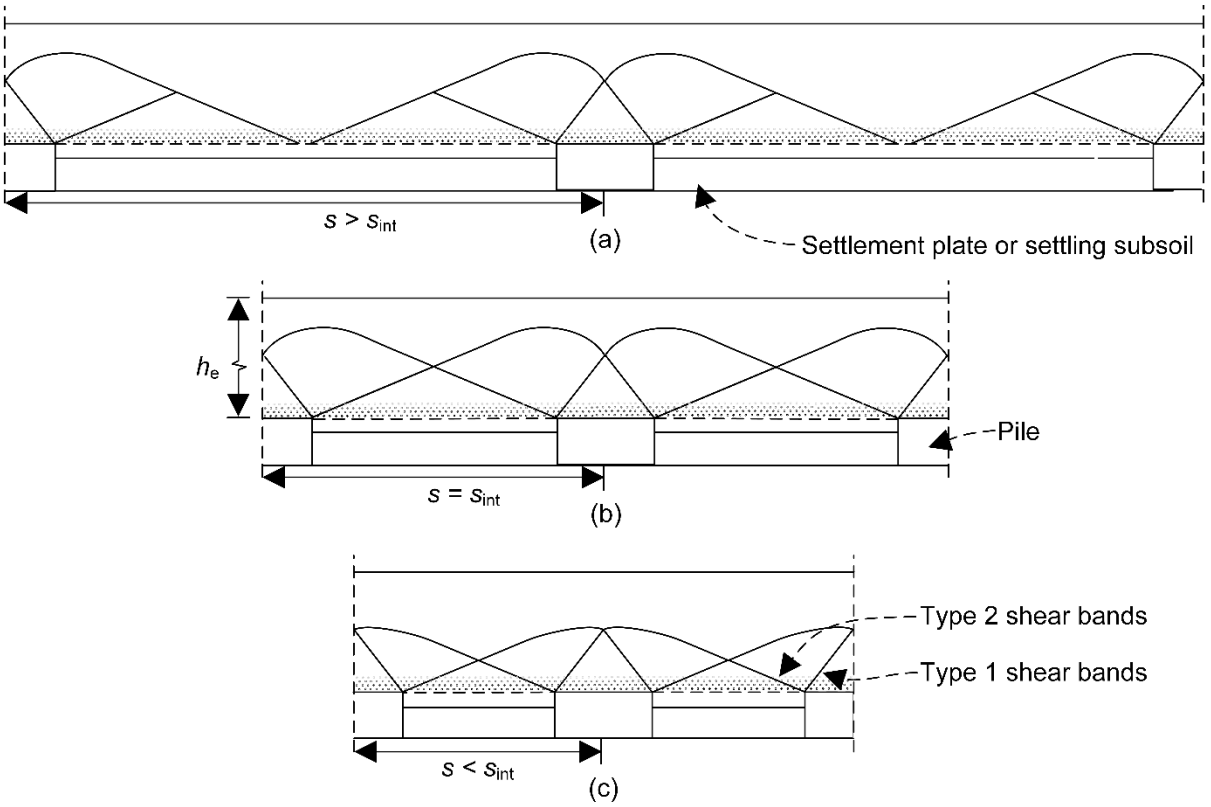

Figure 4.7: Interaction of failure surfaces in a piled embankment LTP for pile spacing's (a) $s > s_{int}$; (b) $s = s_{int}$; (c) $s < s_{int}$

A fourth case may also develop if piles are spaced close enough, where the soil between the piles will "lock" in place, and the system will behave as a single foundation, known as a blocking effect. However, the spacing required for this condition to develop is likely smaller than any spacing adopted in an economical piled embankment design. It is noted that the pile spacing at which piles interact, s_{int}, is dependent on the pile head diameter and the soil's deviatoric behaviour. For the material and geometries tested in the small-scale model tests, the failure surfaces observed as shear bands in the dense samples shown in Figure 4.3 are most closely represented by Case C described above.

Regarding LTP granular material that does not exhibit high peak friction and dilation angles, as is the case for the medium dense sand tested, Type 2 shear bands may not form. Given that the Type 2 shear bands are largely responsible for the interaction of failure surfaces between adjacent piles, it is likely that the failure mechanism within such granular material will be less dependent on pile spacing. Such behaviour may be expected in embankments of significant height, where suppression of dilation occurs, or when the LTP granular material is poorly compacted or of poor quality such that the granular material does not exhibit a large difference between peak and residual shear strength.

Progressive development of soil arching

As noted in Chapter 2, soil arching has been shown to progressively develop in active trapdoor tests as a trapdoor is displaced vertically downwards (Terzaghi 1936; Ladanyi and Hoyaux 1969; Vardoulakis et al. 1981; Iglesia et al. 1999; Dewoolkar et al. 2007; Costa et al. 2009). In trapdoor tests, the progressive development of arching stresses with trapdoor displacement is commonly attributed to failure surfaces developing sequentially as well as the mobilisation of friction and dilation angles. Where failure surfaces have been observed in trapdoor tests, it has been shown that they propagate to the soil surface after a sufficient amount of trapdoor displacement has occurred, which in turn results in surface differential settlement. However, the presence of a plane of equal settlement within piled embankments, which has been shown to develop regardless of the amount of subsoil settlement that occurs (McGuire 2011), does not correspond to the theory of sequentially developing failure surfaces that propagate to the embankment surface. It was shown in Section 4.2.1 that the failure surfaces that developed after a small amount of settlement plate displacement were still present after more than 10% normalised settlement plate displacement. Thus, the progressive development of soil arching stresses in piled embankments may not be attributed to the sequentially developing failure surfaces.

General shear failure of a shallow foundation typically exhibits a load-settlement response as shown in Figure 4.8a, which is characterised by a peak load followed by a drop in resistance with increasing settlement (Vesic 1963). In the stress-controlled conditions of a shallow foundation, this load-settlement response often results in a catastrophic failure of the footing if the ultimate bearing capacity is reached (Vesic 1973). Based on the observed failure mechanism within the small-scale model tests comprising dense sand, it is considered that a similar load-settlement response develops within piled embankments. Although, given that soil arching develops due to subsoil settlement, the mechanism is strain controlled and does not result in catastrophic failure provided the strength of the piles, subsoil and geosynthetic reinforcement (if present) are not exceeded. Instead, the amount of embankment load transferred to the pile heads increases rapidly as subsoil initially undergoes consolidation, reaching a maximum before a reduction in load transfer is experienced with ongoing subsoil consolidation. This behaviour has been shown in centrifuge tests performed by Ellis and Aslam (2009a, b), where an embankment comprising dense sand prepared at D_r = 90 - 95% was tested. The typical load-settlement response of these tests is shown in Figure 4.8b. In Figure 4.8b the load transfer resulting from soil arching is quantified by the stress reduction ratio (SRR), which is the ratio of the stress acting on the subsoil, σ'_s, to the initial overburden stress prior to any settlement or displacement, $\gamma h_e + q$, where q is the surcharge applied to the embankment surface. Given that σ'_s reduces from the initial overburden stress as a result of soil arching transferring loads towards the pile heads, the SRR is inversely proportional to the stress acting on the pile heads. As such, the similarities in the responses shown in Figure 4.8a and b, although rotated

and inversed, may be attributed to them undergoing a similar failure mechanism, and thus, similar load-settlement settlement behaviour.

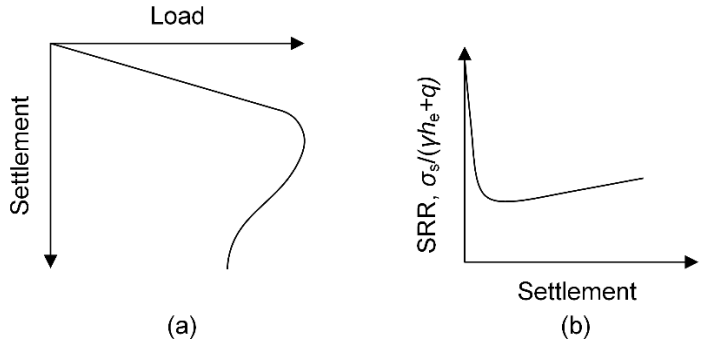

Figure 4.8: (a) Load-settlement behaviour of a shallow foundation on dense sand (after Vesic 1963); (b) stress reduction ratio-settlement behaviour of piled embankment with dense sand (after Ellis and Aslam 2009b)

The load-settlement response of a shallow foundation founded on dense sand that exhibits a significant difference between peak and residual strength is explained by the mobilisation of shear strength within shear bands (Yamaguchi et al. 1976; Perkins and Madson 2000; Conte et al. 2013). Under small settlements, the shear strength is mobilised within shear bands at points close to the footing. As the footing is further displaced downwards into the soil, shear strength is mobilised in regions further away from the footing. Thus, plastic strains within the shear bands propagating from the edge of the footing are non-uniform, and as such, peak strength is not mobilised simultaneously throughout the entire length of the shear bands. As a result, the average shear strength within the shear bands will develop as the footing is displaced vertically into the underlying soil. This average shear strength will be less than the peak shear strength and will approach critical state strength with increasing footing settlement.

The mobilisation of strains within shear bands as well as the behaviour regarding strength and dilation of granular material may also be used to explain the progressive development of soil arching in piled embankments given the observed failure mechanism. The slices of volumetric shear strain shown in Figure 4.4 indicate the amount of dilation the material within shear bands is undergoing. Given that the maximum rate of dilation is typically associated with peak shear strength (Bolton 1986), these volumetric strains indicate regions where material may have mobilised close to peak shear strength. It was shown in Figure 4.4 that maximum dilation appears to have mobilised rapidly (after small settlement plate displacement) in regions of shear bands close to the pile heads. After relatively large amounts of settlement plate displacement ($\delta_{sp}/b' > 8\%$), significantly less volumetric strain, and hence dilation, was observed in slices, suggesting that the sand within the shear bands was approaching residual shear strength.

The progressive development of soil arching stresses observed in tests presented by Ellis and Aslam (2009b) and shown in Figure 4.8b may be explained by the mobilisation of shear strength within shear bands propagating from the pile heads. As noted in Chapter 2, this SRR-settlement behaviour has been shown by several authors to be well described by the GRC framework proposed by Iglesia et al. (1999), which will be used in this discussion to relate the observed kinematics to expected arching stress versus subsoil settlement behaviour. Similar to Iglesia et al. (1999), the progressive development of soil arching is grouped into four stages, which are described below and the first three of which are presented in Figure 4.9.

- Initial arching – Small subsoil settlement results in a rapid reduction in SRR as shear strain within failure surfaces propagating from the pile heads is initially mobilised.
- Maximum arching – The full length of the failure surfaces are undergoing dilation, with some sections experiencing a maximum rate of dilation corresponding to peak shear strength. The average shear strength along the length of the shear bands is a maximum, although less than peak shear strength.
- Load recovery phase – Much of the soil within the shear bands has already experienced peak shear strength and is undergoing softening. Soil within shear bands approaches residual shear strength (critical state) with increasing subsoil settlement.
- Ultimate phase – Soil within the shear bands is undergoing critical state shearing. Any additional subsoil settlement will result in uniform arching stresses.

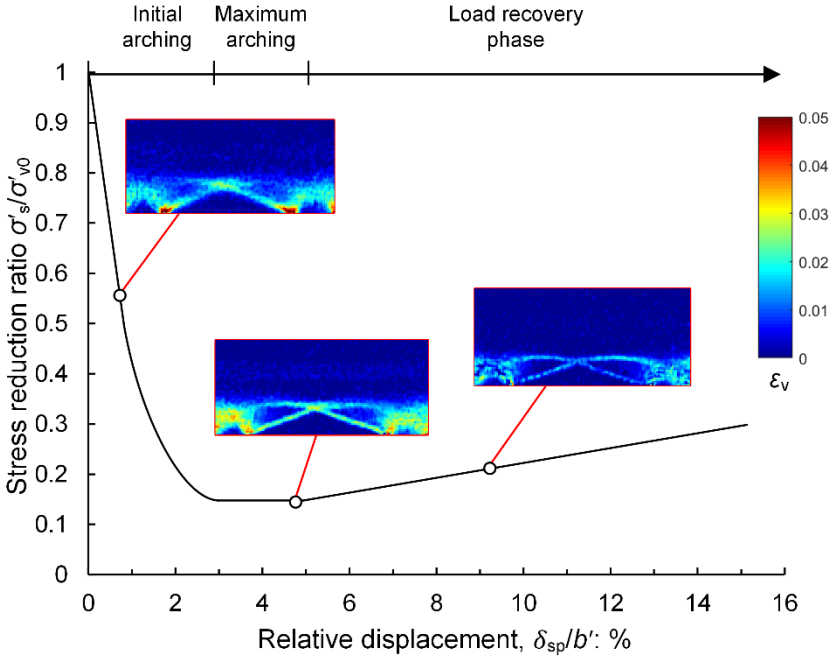

Figure 4.9: Ground reaction curve (modified from Iglesia et al. 1999) with observed volumetric strains from the square model comprising dense sand

Not all piled embankments will experience the SRR-settlement behaviour shown in Figure 4.8b and Figure 4.9. For this behaviour to arise the LTP granular material used must be a high-quality angular fill and well compacted, such that the material exhibits high peak friction and dilation angles. Also, the embankment must not be of a height such that the embankment stresses cause suppression of dilation. As shown in Section 4.2.1, the response of the medium dense samples displayed a similar failure mechanism to a shallow foundation undergoing punching shear failure, which typically develops when a footing is placed on loose sand and/or at great depths. A typical load-settlement response for a shallow foundation undergoing punching shear (Vesic 1963) is shown in Figure 4.10a where no clear maximum load is experienced.

Centrifuge modelling presented by Fagundes et al. (2015) provides an example of the SRR-settlement response that may arise when LTP material is prepared at a relatively lower density. The tests performed by Fagundes et al. (2015) incorporated sand prepared at D_r = 57%. An example SRR-settlement response for a model piled embankment with piles arranged on a square grid with prototype dimensions of s = 2.82 m, d = 1 m and an embankment height of h_e = 7.2 m is presented in Figure 4.10b. The similarities between Figure 4.10a and b, where no clear peak load is observed, further suggests that embankments of large heights and/or incorporating poorly compacted low-quality granular fill may exhibit a failure mechanism and load-settlement response similar to the punching failure of a shallow foundation. In such embankments, the average mobilised shear strength along the failure surfaces does not exceed a value significantly greater than the residual shear strength. As such, the load transfer resulting from soil arching does not exhibit a prominent peak followed by a reduction due to softening as there is not a significant difference between peak and residual shear strength.

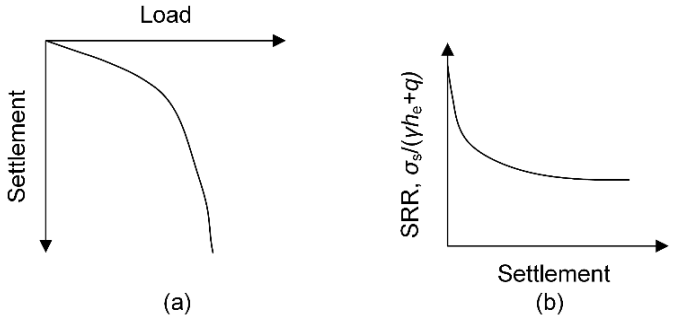

Figure 4.10: (a) Load-settlement behaviour of a shallow foundation on loose sand (after Vesic 1963); (b) stress reduction ratio-settlement behaviour of piled embankment with medium-dense sand (after Fagundes et al. 2015)

Critical height

As the subsoil beneath a piled embankment displaces vertically downwards, differential settlement develops between pile heads and subsoil at the base of the LTP. As noted previously, the height at which

these differential settlements reduce such that a plane of equal settlement forms is referred to as the critical height. Previous studies investigating the critical height in laboratory tests have typically determined h_{cr} visually in 2D plane strain model tests (Hewlett and Randolph 1988; Jenck et al. 2007) or observed surface deformations in 3D physical model tests (McGuire 2011; Fagundes et al. 2015), which only determine if the embankment height is greater or less than h_{cr}. DVC analysis of model piled embankments allows h_{cr} to be estimated using 3D geometries and with greater accuracy than the surface observation method. The h_{cr} of a model piled embankment is investigated in the present study by taking the vertical displacements throughout the height of the sand at locations above ($U_{z,above}$) and amid ($U_{z,amid}$) the piles, as shown in Figure 4.11 for both model geometries. The above pile location is directly above the centres of the piles, while the location amid piles is the furthest distance from the pile edge within the pile unit cell, s'. The differential settlement between these two locations is expected to be the maximum differential settlement at a given height in the sand.

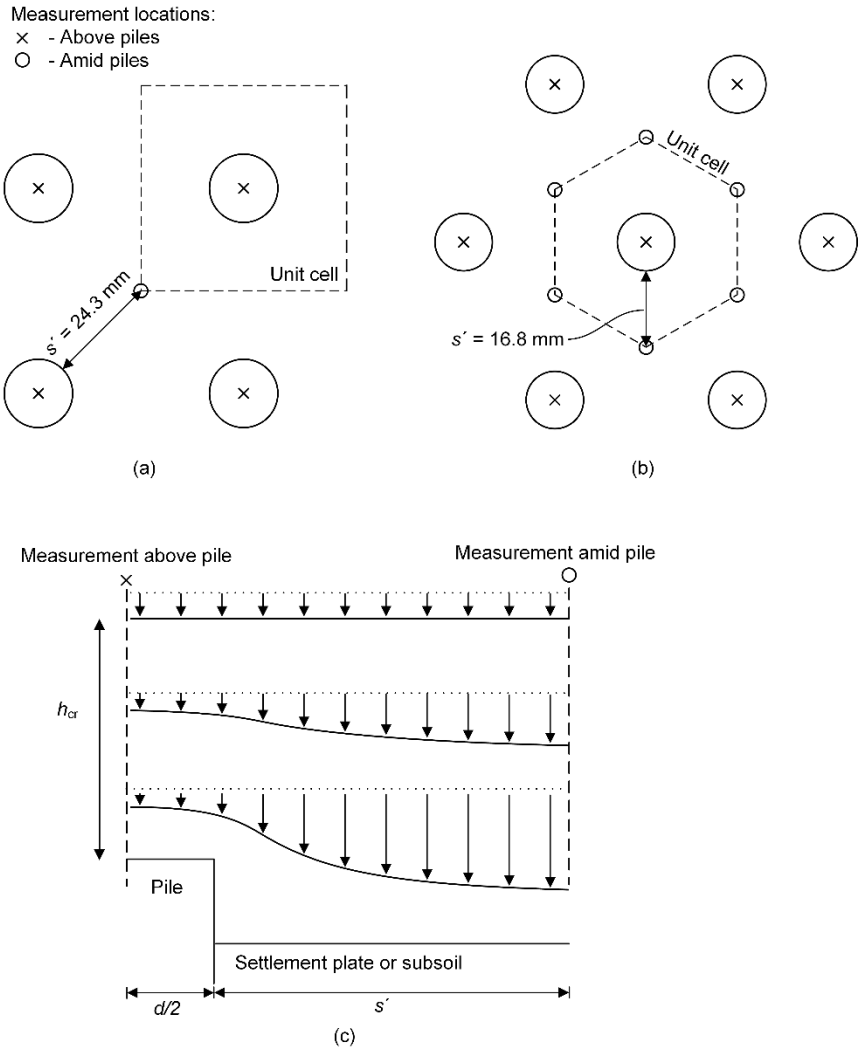

Figure 4.11: (a) Measurement locations within square model; (b) measurement locations within triangular model; (c) section view of vertical displacements (displacement exaggerated)

The incremental normalised vertical displacements from both the above and amid pile locations are shown at different increments of δ_{sp}/b' in Figure 4.12 for both model layouts and sand densities. It is shown in Figure 4.12 that for all model layouts and densities, a plane of equal settlement develops at some height within the sand when the displacements above piles become equal, or close, to the displacements amid piles. Both models comprising dense sand (Figure 4.12a and c) show a similar trend, where the displacement lines progressively shift (more settlement transferred to the embankment surface) with increasing settlement plate displacement. In contrast, the medium dense samples (Figure 4.12b and d) do not undergo such a transition – the behaviour of the displacement lines is rather consistent, with relatively little deviation for all settlement plate displacements.

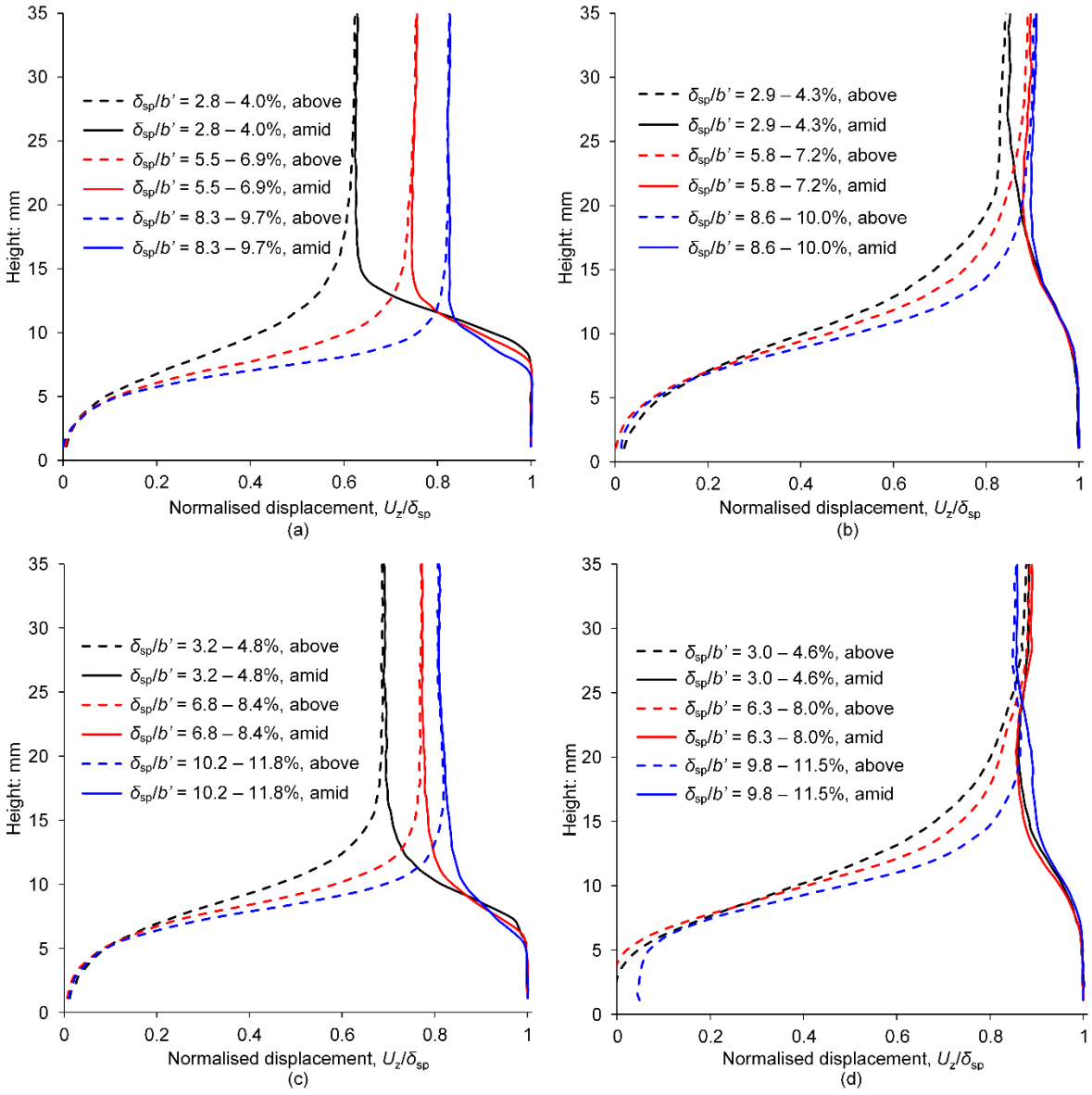

Figure 4.12: Displacements within model tests at locations defined in Figure 4.11 for: (a) square layout dense sand; (b) square layout medium dense sand; (c) triangular layout dense sand; (d) triangular layout medium dense sand

A common definition adopted for the critical height of a piled embankment is the height at which differential settlements are no longer measurable (Filz et al. 2012). This definition causes difficulty in estimating h_{cr} consistently in model tests, as the term "measurable" is dependent on the accuracy of the measuring technique. Due to the sub-voxel accuracy that can be achieved by DVC analysis, it is necessary to define h_{cr} in terms of a finite value. An angular distortion of 1/500 has been used in the present study to define "equal settlement". Thus, the critical height is the height at which the angular distortion over the length of $s' + d/2$ falls to below this limit, which may be written as:

$$\frac{U_{\mathrm{z,amid}} - U_{\mathrm{z,above}}}{s' + {}^{d}/_{2}} \leq {}^{1}/_{500} \tag{4.2}$$

The critical height is determined using this limiting angular distortion from the total displacements, rather than incremental, estimated by DVC analysis and is shown in Figure 4.13 normalised by the pile head diameter and plotted against the normalised settlement plate displacement for both model arrangements comprising dense and medium dense sand. The critical heights presented in Figure 4.13 increase with increasing settlement plate displacement, although, they tend to asymptote towards a consistent height. This trend suggests that a certain amount of displacement (or subsoil consolidation) is required for the full critical height to be realised. However, once the critical height has been established after sufficient settlement plate displacement, there is little effect on the critical height with increasing settlement plate displacement. This is consistent with the observation that the same failure surfaces were present throughout all settlement plate displacements. A similar observation was made by McGuire (2011), who performed model tests with a comparable settlement plate mechanism and observed that uniform settlement was experienced above h_{cr} even at large magnitudes of simulated subsoil settlement.

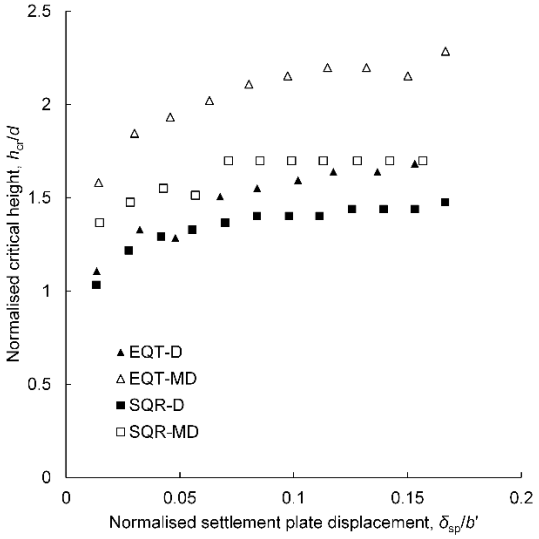

Figure 4.13: Normalised critical height plotted against normalised settlement plate displacement

The clear majority of methods for predicting the height at which a plane of equal settlement develops, or providing a minimum embankment height, estimate such heights solely on the centre-to-centre and pile head diameter without consideration of the LTP granular material properties. However, the results in Figure 4.13 show that for the same pile arrangement, models comprising dense sand resulted in lower values of h_{cr} than the models comprising medium dense sand. This observation shows that a soil's deviatoric response will also govern the height at which a plane of equal settlement develops within a piled embankment, in addition to the pile spacing and pile head diameter.

Height of failure surfaces

One such method for predicting h_{cr} is to estimate the maximum height that failure surfaces extend into the embankment (h_{fs}). Naughton (2007) assumed that $h_{cr} = h_{fs}$, and estimated h_{fs} as the height of a log-spiral curve with its origin at the mid-span between piles. However, the failure surface assumed by Naughton (2007) does not correspond with those observed in the present study, the origin of the log spiral is not centred at the mid-span between piles. A slice of normalised total vertical settlement in the square model comprising dense sand after the settlement plate was lowered 3 mm ($\delta_{sp}/b' = 8.4\%$) is plotted in Figure 4.14 with the failure surfaces overlaid, as determined from the corresponding shear strain. h_{cr} determined from DVC analysis using Equation 4.2 is also shown in Figure 4.14 along with h_{fs}. It is evident that while h_{cr} is likely dependent on h_{fs}, the two are not equal since differential settlements still occur above h_{fs}. Given that a failure surface is a region where soil is undergoing localised deformation, it is logical that it will not correspond to a plane of equal settlement. However, it is considered important to be able to estimate h_{fs}, as it is likely that the height at which a plane of equal settlement develops is strongly dependent on h_{fs}.

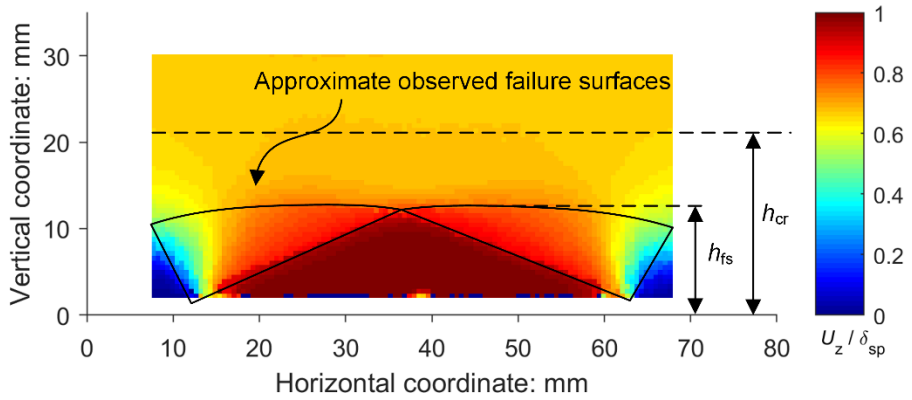

Figure 4.14: Slice of normalised vertical settlement with corresponding failure surfaces

In shallow foundations, the Prandtl radial shear zone is bound by a log spiral with its origin centred at the edge of the shallow foundation (note the difference with the assumption made by Naughton (2007) where the centre was taken at the mid-span between piles). A similar failure surface is expected to develop in piled embankments comprising dense LTP granular material when s' is greater than the

spacing between the edge of the pile head and the outermost extent of the pile unit cell when the interaction occurs between shear bands, s'_{int} (Figure 4.7). The failure surfaces associated with this pile layout and LTP material are shown in Figure 4.15. The radius, r, of the log spiral failure surface between points A and B with its origin centred at the edge of the pile head may be written as:

$$r = r_0 e^{\theta \tan \omega} \tag{4.3}$$

Where r_0 is the initial radius, θ is the angle from the x-axis and ω is a constant that represents the curvature of the log spiral (ω is the angle between the radial line and normal). Conventionally, bearing capacity analysis of a shallow foundation has taken ω to be equal to ϕ. Although, as shown previously, the orientation of shear bands was better estimated by the using a non-associated flow rule. Thus, the present analysis adopts:

$$\omega = \frac{\phi + \psi}{2} \tag{4.4}$$

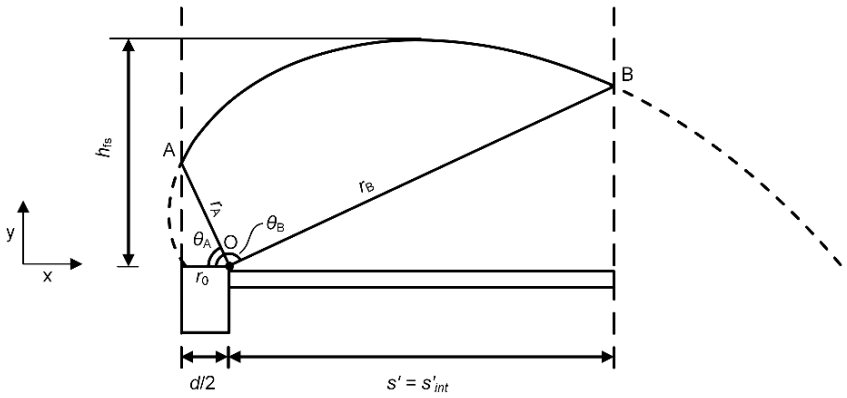

Figure 4.15: Failure surfaces within dense LTP material when $s' = s'_{int}$

It is considered that the peak friction and dilation angles should be used in estimating the geometry of the failure surfaces, for the same reason as noted previously, that shear bands form initially at or slightly before peak strength. The Cartesian coordinates for this failure surface can be expressed as:

$$x = r \cos\theta = r_0 \cos\theta \, e^{\theta \tan \omega} \tag{4.5}$$

$$y = r \sin\theta = r_0 \sin\theta \, e^{\theta \tan \omega} \tag{4.6}$$

By adopting the Arthur et al. (1977) angle of shear band orientation, it is assumed that $\theta_A = 45^\circ + \omega/2$ and $\theta_B = 135^\circ + \omega/2$. It is therefore known that at point A, the radius of the log spiral is given by:

$$r_A = \frac{d}{2\cos\left(45 + \frac{\omega}{2}\right)} \tag{4.7}$$

With this known radius, the initial radius of the log spiral may be written as:

$$r_0 = \frac{d}{2\cos\left(45 + \frac{\omega}{2}\right) e^{\left(45+\frac{\omega}{2}\right)\tan\omega}} \tag{4.8}$$

Differentiating Equation 4.6 then gives:

$$\frac{dy}{d\theta} = r_0 e^{\theta \tan\omega}(\sin\theta \tan\omega + \cos\theta) \tag{4.9}$$

The top of the log spiral, where $dy/d\theta$ is equal to zero, corresponds to h_{fs}. Thus, by letting Equation 4.9 equal zero, the angle from the origin of the log spiral at which the top of the log spiral is located (θ_{fs}) may be calculated as:

$$\theta_{fs} = 90 + \omega \tag{4.10}$$

The maximum height at which the failure surfaces develops when $s' \geq s'_{int}$ may then be written as:

$$h_{fs} = \frac{d\sin(90+\omega)\, e^{(90+\omega)\tan\omega}}{2\cos\left(45 + \frac{\omega}{2}\right) e^{\left(45+\frac{\omega}{2}\right)\tan\omega}} \qquad \text{when } s' \geq s'_{int} \tag{4.11}$$

As noted previously, when pile spacing is small enough, interaction between shear bands propagating above adjacent piles will occur. The location of point B in Figure 4.15 will be the point at which Type 2 shear bands first intersect. With the angle from the origin of the log spiral at which point B forms known (135˚ + ω/2), the spacing between piles at which interaction first occurs may be calculated as:

$$s'_{int} = \frac{d\cos\left(135 + \frac{\omega}{2}\right) e^{\left(135+\frac{\omega}{2}\right)\tan\omega}}{2\cos\left(45 + \frac{\omega}{2}\right) e^{\left(45+\frac{\omega}{2}\right)\tan\omega}} \tag{4.12}$$

When piles are arranged on a grid such that $s' < s'_{int}$, the origin of the log spiral bounding the radial shear zone is shifted, resulting in a h_{fs} lower than when $s' \geq s'_{int}$. It is assumed that the origin of the log spiral shifts below the pile head along the same inclination of the Type 2 shear band, so that the log spiral passes through points A and B, as shown in Figure 4.16. The two radii along the log spiral shown in Figure 4.16 are written as:

$$r_A = r_0 e^{\theta_A \tan\omega} \tag{4.13}$$

$$r_B = r_A e^{(\theta_B - \theta_A)\tan\omega} \tag{4.14}$$

Using geometrical relationships, it can be shown that:

$$r_A = \frac{s' + \frac{d}{2}}{r_A e^{(\theta_B - \theta_A)\tan\omega} \sin(\theta_B - 90) - \sin(\theta_A - 90)} \tag{4.15}$$

$$r_A = \frac{\frac{d}{2}\tan\left(\frac{\pi}{4} + 90\right) - s'\tan\left(\frac{\pi}{4} - 90\right)}{\cos(\theta_A - 90) - e^{(\theta_B - \theta_A)\tan\omega}\cos(\theta_B - 90)} \tag{4.16}$$

Letting $\theta_B = 135^\circ + \omega/2$, Equation 4.15 and 4.16 can be solved using iterative techniques to find r_A and θ_A. Again, the angle from the origin of the log spiral that results in the highest point of the failure surface occurs at $\theta_{fs} = 90^\circ + \omega$. Thus, h_{fs} may be written as:

$$h_{fs} = r_0 \sin(90 + \omega)\, e^{(90+\omega)\tan\omega} - y_{os} \qquad \text{when } s' < s'_{int} \tag{4.17}$$

Where y_{os} is the vertical distance that the new log spiral origin is located below the pile head surface. With r_A and θ_A previously solved, r_0 and y_{os} may be calculated as:

$$r_0 = \frac{r_A}{e^{\theta_A \tan\omega}} \tag{4.18}$$

$$y_{os} = r_A \cos\left(\theta_A - \frac{\pi}{2}\right) - \frac{d}{2}\tan\left(\frac{\pi}{4} + \frac{\omega}{2}\right) \tag{4.19}$$

The maximum height of failure surfaces is estimated using this approach and is shown in Figure 4.16, where it is normalised by d and plotted against s'/d for a range of ω values. It is worth noting that for small s'/d ratios, the log spiral does not extend above the height of point A in Figure 4.16. In this case, h_{fs} is taken as the height of point A, which is independent of pile spacing.

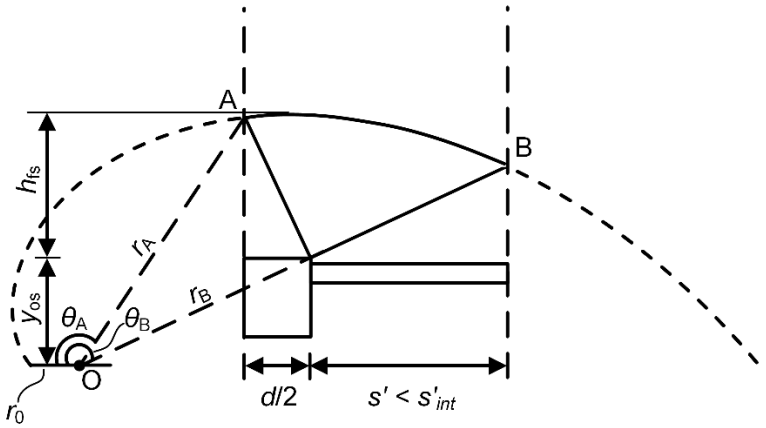

Figure 4.16: Failure surfaces within dense LTP material when $s' < s'_{int}$

Two commonly used methods for calculating h_{cr}, McGuire (2011) and BS8006 (2016), are also plotted in Figure 4.16. McGuire (2011) performed bench-scale tests where h_{cr} was determined from surface measurements, and a relationship was fitted to the results. BS8006 (2016) assumes a hemispherical arch develops between piles, the height of which between diagonally adjacent piles on a square grid is taken

as h_{cr}. Thus, neither of these relationships are based on observed failure surfaces or an understanding of the kinematics associated with soil arching. It is shown that for values $s'/d > 1$, both methods estimate a critical height greater than h_{fs}. h_{fs} is also shown to increase almost linearly with increasing s'/d until $s' = s'_{int}$, after which the failure surfaces develop without interaction and are independent of pile spacing. Both methods for estimating h_{cr} exhibit a similar, albeit steeper gradient, linear increase in h_{cr} with increasing s'/d. This behaviour is likely because of the dependency of h_{cr} on h_{fs}.

The proposed method for estimating h_{fs} is based on the assumption that shear bands interact with other shear bands propagating from adjacent pile heads, as shown within models comprising dense sand. Given that high-quality rock fill often used in LTP granular material will likely exhibit similar deviatoric behaviour to this dense sand, this mechanism is expected to develop in shallow embankments where h_{cr} is important to the performance of the embankment. If, however, poor quality LTP material is used or the embankment is of great height, such that the LTP material does exhibit high peak friction and dilation angles, then diffuse failure may develop in place of Type 2 shear bands. In this case, the interaction between failure surfaces will not occur as strongly, and the maximum height of the diffuse failure surfaces propagating from the top of the Type 1 shear bands may be conservatively calculated using Equation 4.11.

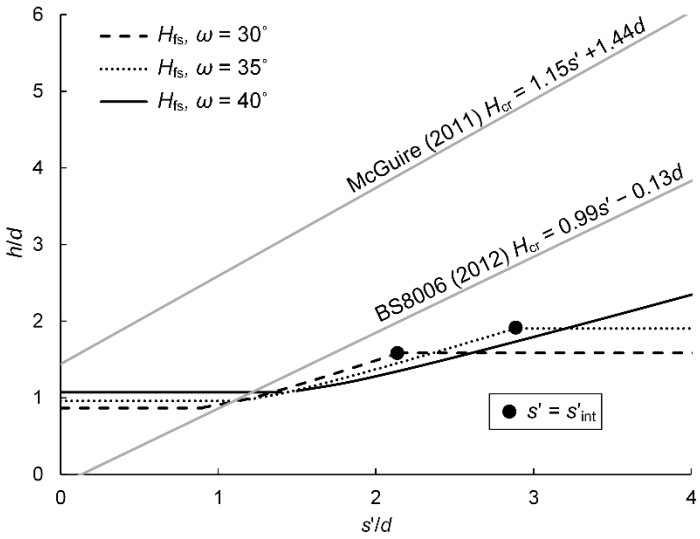

Figure 4.17: h_{fs}/d plotted against s'/d for different values of ω ($= \frac{\phi + \psi}{2}$)

Surface settlement

The total settlement of an embankment surface comprises the sum of the pile head settlement and settlement that develops within the embankment fill, S_e. While some settlements developing within the embankment fill may result from compression of the fill itself, the amount that develops post-construction is often small and therefore neglected. The majority of settlement that develops within the

embankment fill is a result of subsoil settlement propagating to the embankment surface. As shown in Figure 4.12, the vertical settlement within the sand is almost constant above h_{cr} with increasing height above the pile heads. Thus, no settlement reduction occurs above $h_{cr,}$ and the displacement from the settlement plate that propagates above h_{cr} will be experienced at the embankment surface. The ratio of the vertical settlement experienced in the sand above the critical height, equal to S_E, to the settlement plate displacement is referred to as the surface settlement ratio.

The surface settlement ratio using incremental and total displacement measurements are plotted against normalised settlement plate displacement in Figure 4.18a and b respectively. The incremental displacements again provide insight into the progressive development of soil arching, while the total displacements show how settlements may affect the design and performance of an embankment. Similar behaviour was observed for both models comprising dense samples, where initial incremental surface settlement ratios were a minimum and less than those of the models comprising medium dense samples. With increasing settlement plate displacements, the incremental surface settlement ratios for the two densities approached each other. The initially smaller surface settlement ratios experienced by the models comprising dense sand is due to the sand undergoing dilation, and hence volume change. This was also shown in Figure 4.4, where volumetric strain showed more dilation occurring in failure surfaces at small settlement plate displacements. As a result of this volume change, not all the volume loss at the base of the embankment from the displacement of the settlement plate propagates to the embankment surface. As the sand within the zone of arching approaches constant volume shearing towards the end of the tests, again shown by slices of volumetric strain in Figure 4.4, higher surface settlement ratios are experienced by the models comprising dense sand. In contrast, the models comprising medium dense sand undergo less dilation, and hence, result in higher surface settlement ratios compared to the dense sample until the sand in both models approaches critical state shearing within the failure surfaces.

The method for estimating S_e proposed by Russell et al. (2003), which has since been adopted by the Load-Displacement Compatibility (LDC) method (Filz et al. 2012), may be written as:

$$S_e = \frac{\delta_s(1-\alpha_r)}{2} \tag{4.20}$$

Where δ_s is the maximum differential settlement between subsoil and pile heads. This method assumes that the average differential settlement of the subsoil is equal to half of the maximum differential settlement between subsoil and piles. It is also assumed that the soil within the embankment fill undergoes no volume change as a result of shearing, and as such, all of the volume loss at the base of the embankment resulting from subsoil settlement will be experienced at the embankment surface.

The present study results in a greater volume loss at the base of the sand compared to a full-scale piled embankment as the settlement plate is flat and rigid compared to the non-uniform subsoil profile that develops beneath piled embankments. To consider different deformed surface profiles between piles, Equation 4.20 is modified to:

$$S_e = \delta_{subsoil}(1 - \alpha_r)\eta \quad (4.21)$$

Where η is the settlement shape factor, which is the ratio between the average subsoil settlement between the piles and δ_s. In the present study, $\eta = 1$ (flat settlement plate), $\delta_s = \delta_{sp}$ and the replacement ratio for the two models is approximately $\alpha_r = 0.09$. Based on the assumption of no volume change, as per Russell et al. (2003), then the surface settlement ratio estimated from Equation 4.21 is equal to 0.91 for both models. This is shown in Figure 4.18a to closely match the incremental surface settlement ratio after approximately 15% normalised settlement plate displacement for both dense and medium dense samples, which corresponds to when soil would likely be undergoing critical state shearing, and hence, the assumption of no volume change is valid.

It is shown in Figure 4.18b that the assumption of no volume change within the sand results in a conservative estimate of the surface settlement ratio for the dense samples, although provides a close match for the medium dense samples. The dense samples, as shown in Figure 4.4, underwent more dilation than the medium dense samples. This dilation resulted in the soil undergoing volume change within the dense sand, and thus, not all of the volume loss that occurred at the base of the embankment propagated to the embankment surface. However, the medium dense sand underwent minimal dilation, and hence volume change. Thus, the assumption of no volume change made by Russell et al. (2003) is valid for the medium dense sand and results in a close agreement between the measured surface settlement ratio medium dense samples and the ratio estimated using Equation 4.21.

It was also shown by McGuire (2011) that the assumption of no volume change resulted in a conservative estimate of surface settlement, noting that McGuire's tests comprised dense sand. McGuire (2011) investigated this volume change and showed that in addition to the soil's stress-dilation behaviour, the rate of soil dilation was dependent on pile spacing, initial soil density, embankment height and whether reinforcement was present or not. In the author's opinion, given the difficulty in quantifying the volume change that an LTP granular material may undergo due to dilation, the assumption of no volume change is prudent for estimating the surface settlement ratio for design purposes. However, the assumption of Russell et al. (2003) to adopt $\eta = 0.5$ is not based on any rigorous analysis and may warrant further investigation.

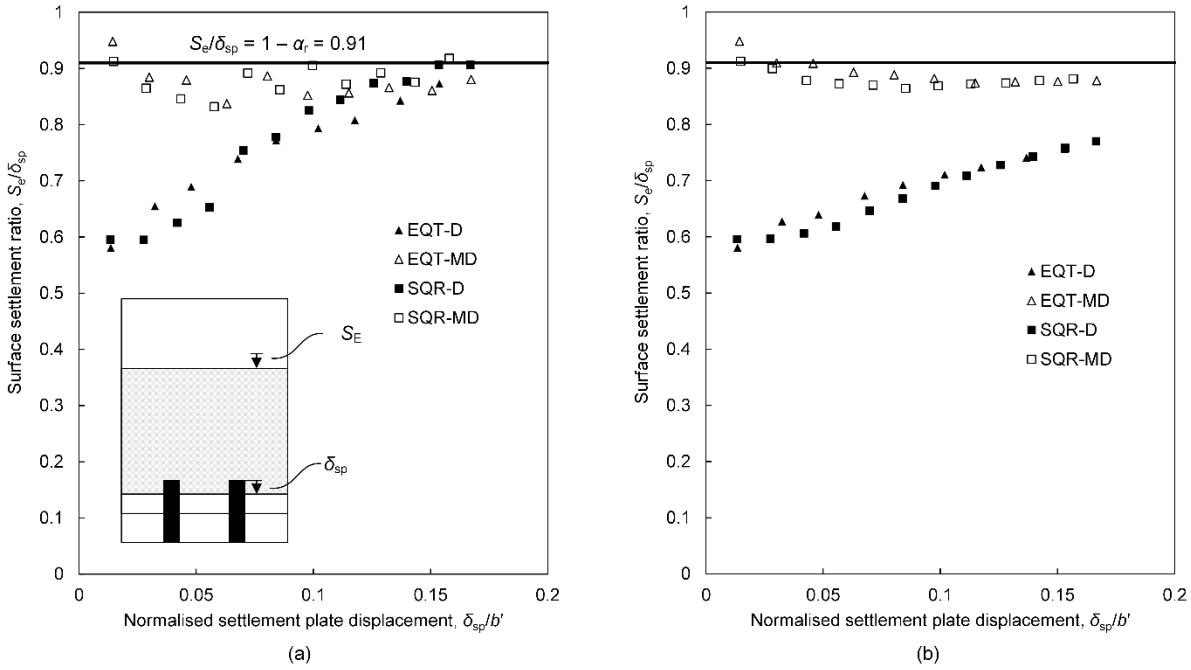

Figure 4.18: Surface settlement ratio versus relative displacement for (a) incremental displacements; and (b) total displacements

4.3 Model tests with defective piles

Two tests were performed using the model with piles arranged on an equilateral triangular grid (EQT) and the central pile displaced vertically downwards. The central pile was driven downwards in these tests at a ratio of central pile displacement to settlement plate displacement of approximately 1:3.6. Displacing the central pile vertically downwards while the surrounding piles remain stationary simulates the differential settlement that may develop between pile heads when a defective pile is present. For the following discussion, the central pile will be referred to as the defective pile.

4.3.1 Results

The incremental normalised vertical displacement is presented in Figure 4.19 for model tests comprising a central defective pile at two increments of normalised settlement plate displacement for both dense and medium dense sand samples. Again, the symmetrical nature of the slices means that slices can be divided in two about a central line of symmetry, with the model tests comprising dense and medium dense sand displayed in the left and right half of each slice, respectively. The normalised displacements in Figure 4.19 show the additional settlement that the soil directly above the central pile underwent compared to the surrounding non-defective piles. However, even with this additional settlement experienced by the defective pile at the base of the embankment sand, differential settlements reduced with height above the pile heads, such that a plane of equal settlement developed. Thus, for the arrangement modelled, a critical height still formed in the presence of the defective pile. Again, it is

also evident that with increasing settlement plate displacement, greater amounts of settlement propagated to the sand/embankment surface above the critical height for samples of dense sand, while medium dense samples did not experience much of a change

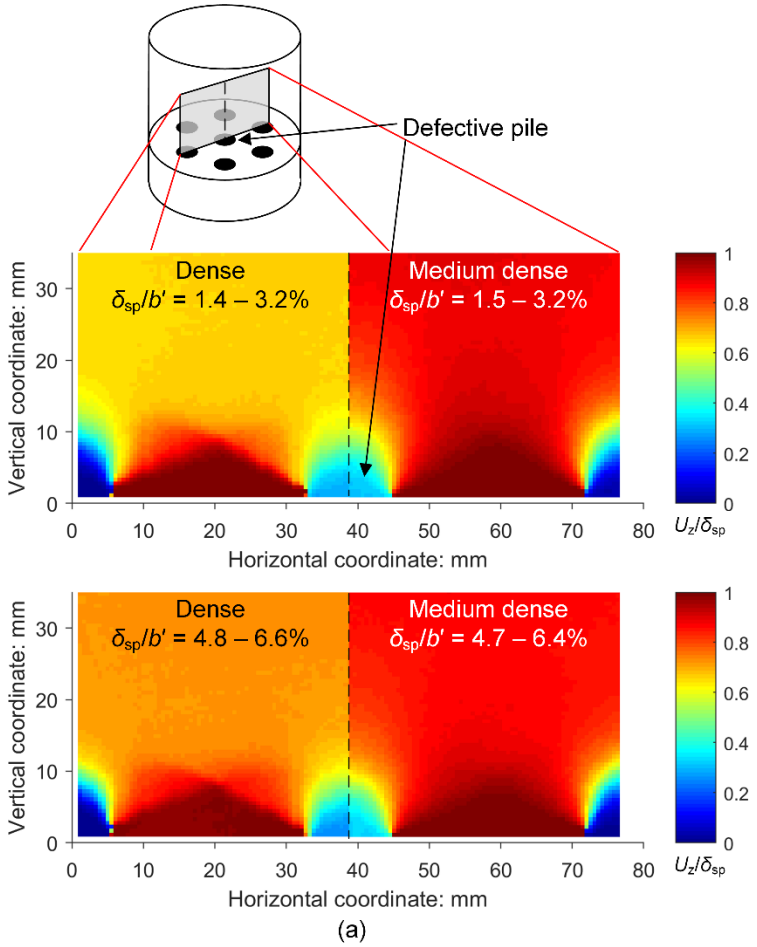

Figure 4.19: Slices of incremental normalised vertical displacements with dense sand on the left and medium dense sand on the right of each slice for triangular model comprising defective pile

The incremental maximum natural shear strains are shown in Figure 4.20 for models comprising a central defective pile at the same location and increments as presented in Figure 4.19. It is evident in Figure 4.20 that the same failure surfaces as observed in Figure 4.3 for models without a defective pile, still develop above the non-defective pile heads, although differences are present in the amount of shear strain mobilised within these surfaces. The failure surfaces above non-defective pile heads appear to be unaffected by the presence of an adjacent defective pile and exhibit similar magnitudes of shear strain to what was observed in tests without a central defective pile. In both models comprising dense and medium dense sand, the Type 1 shear bands above the defective pile did not mobilise as much shear strain as the corresponding shear band above the adjacent non-defective pile. In the dense sand above the defective pile, the extension of the Type 1 shear band that bounds the Prandtl radial shear zone and was previously defined by a log spiral, mobilised only a small amount of shear strain compared to the

same shear band above the non-defective pile. The only shear band propagating from the defective pile head in the dense sand that mobilised significant shear strain is the Type 2 shear band, which appears to be interacting with the shear band propagating from the adjacent non-defective pile head.

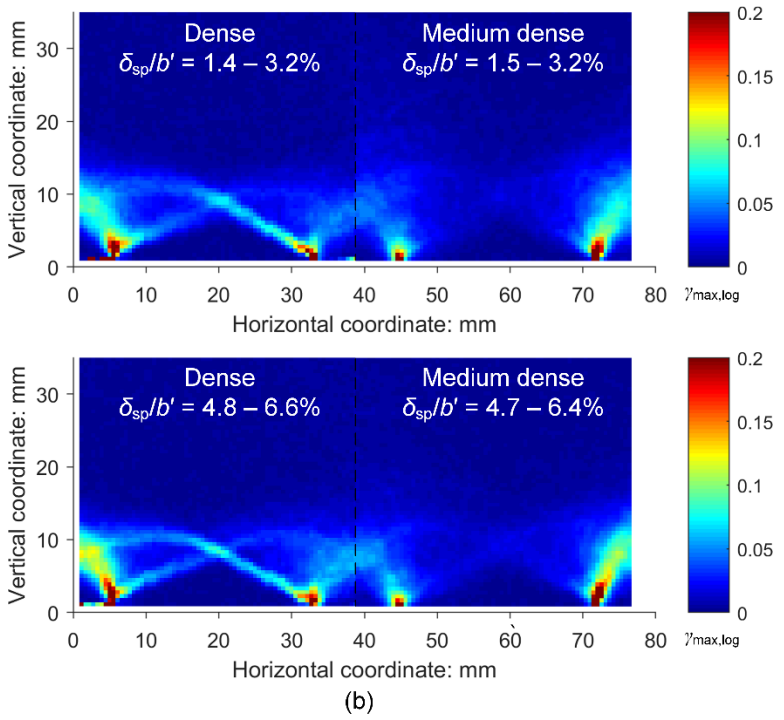

Figure 4.20: Slices at equivalent position as Figure 4.19 of incremental maximum shear strain for triangular model comrpising defective pile

4.3.2 Analysis

Load transfer

The differential settlement between pile heads and settlement plate (or subsoil settlement) is responsible for mobilising shear bands that propagate into the granular material overlying pile heads. In model tests comprising a defective pile, the differential settlement between the defective pile head and settlement plate ($\delta_{sp,def}$) is less than the differential settlement between non-defective pile heads and the settlement plate, i.e. $\delta_{sp,def} < \delta_{sp}$. This reduced differential settlement is why it was observed in Figure 4.20 that generally less shear strain was mobilised \within the shear bands developing above the defective pile head compared to the non-defective pile heads. In mobilising less shear strain above the defective pile head, less load would be transferred towards this pile through soil arching. This issue of load transfer towards a defective pile is investigated further in Chapter 6 and Chapter 7.

Settlements

As shown in Figure 4.19, a plane of equal settlement still developed within the sand mass when a defective pile was present. This is further demonstrated in Figure 4.21 where the incremental normalised vertical displacements taken throughout the height of the sand mass are presented for three locations, amid piles, above the non-defective piles and above the central defective pile. It is evident that at some height above the non-defective pile heads the vertical displacements within the sand mass approach each other and become approximately equal. The height at which this occurs is termed the defective pile critical height ($h_{cr,def}$).

It is also shown in Figure 4.21a that models comprising dense sand underwent the same progressive transition as was observed for models without a defective pile, where increasing settlement propagated above the critical height to the embankment surface with increasing increments of settlement plate displacement. Such a transition is not evident in Figure 4.21b for the sample comprising medium dense sand, which was also noted in the model tests without a defective pile. Thus, the displacement lines and shape of failure surfaces were similar between tests both with and without a central defective pile.

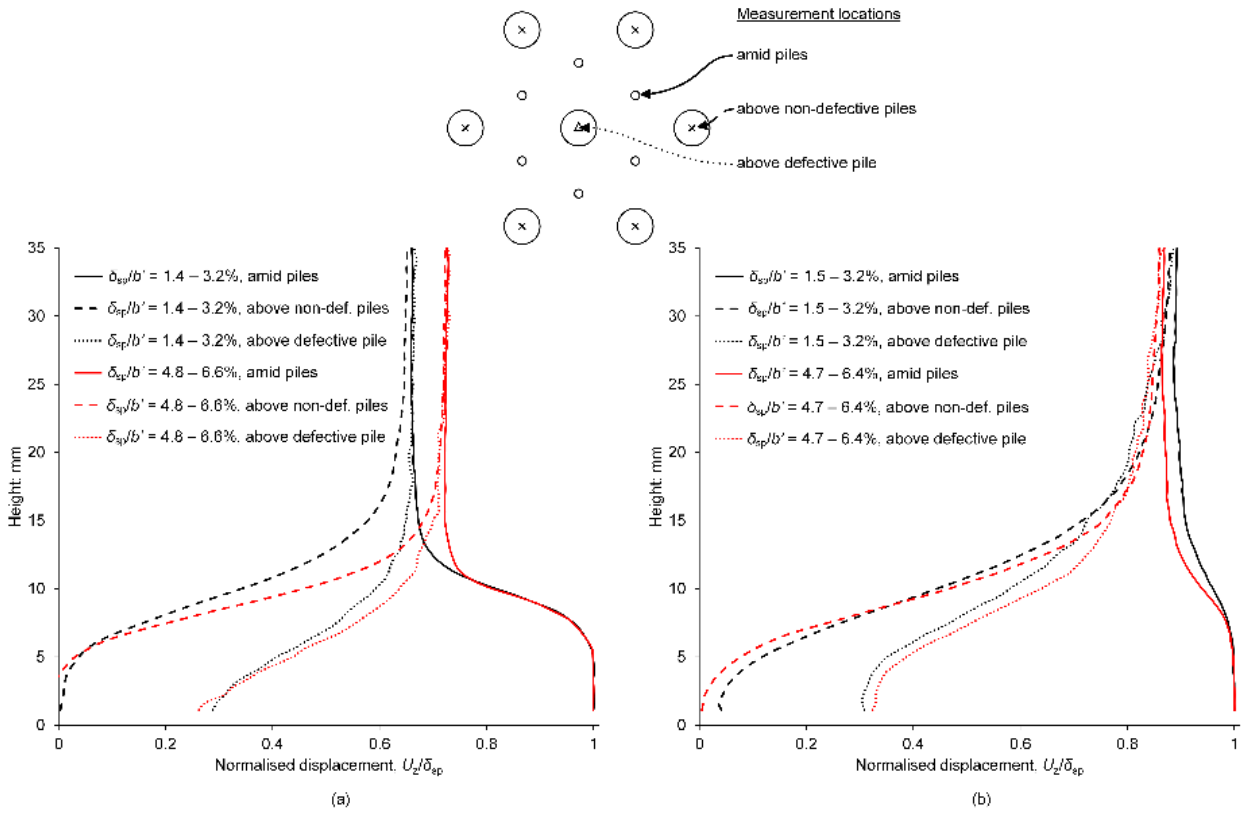

Figure 4.21: Displacements within model tests with defective pile comprising (a) dense sample; (b) medium dense sample

The critical height estimated using the relationship expressed in Equation 4.2 is presented in Figure 4.22 for model tests comprising piles on an equilateral triangular arrangement both with and without a defective pile. Unfortunately, the worm drive controlling the displacement of the central defective pile failed during the test comprising a defective pile and medium dense sand after a normalised settlement displacement of 8%, which meant that the test did not extend to displacements that allowed the final critical height to be determined. It is still evident, however, that the defective pile caused an increase in critical height for both dense and medium tests. It should be noted that the height at which failure surfaces extended into the sand above a defective pile ($h_{fs,def}$) appeared to be approximately equal to the case without a defective pile, i.e. $h_{fs,def} = h_{fs}$. However, the height at which a plane of equal settlement developed above a defective pile was greater than what developed in the case without a defective pile, i.e. $h_{cr,def} > h_{cr}$.

As shown previously, differential settlement still exists at the height at which failure surfaces extend into the sand. While strain localisations do not propagate above this height, soil still undergoes some shearing due to this differential settlement. This shearing is required for a plane of equal settlement to develop some height above the failure surface. Given that the defective pile essentially results in additional volume loss at the base of the embankment, the height above the failure surfaces required for shearing to even-out settlements and form a plane of equal settlement is greater than when a defective pile is not present due to this additional volume loss.

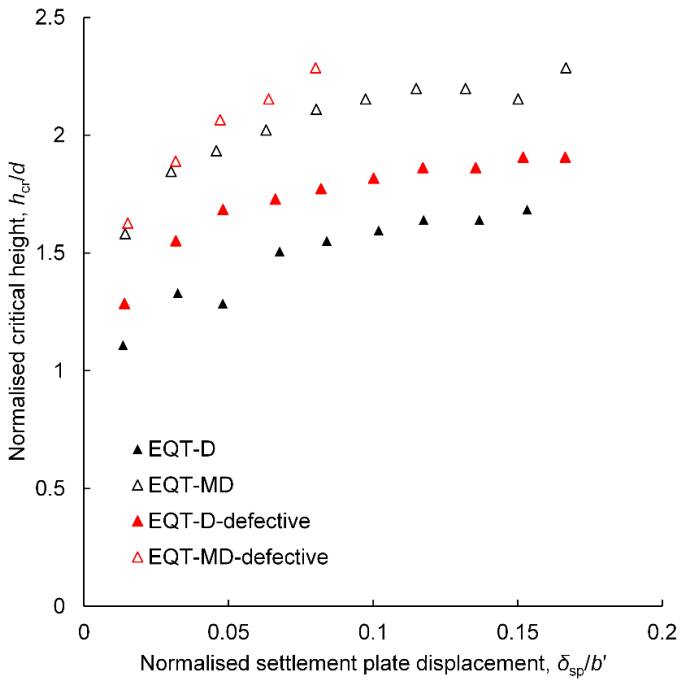

Figure 4.22: Normalised critical height plotted against normalised settlement plate displacement for model tests comprising piles on a triangular grid both with and without a central defective pile

The surface settlement ratio measured from total displacements in model tests comprising piles arranged on an equilateral triangular arrangement, both with and without a central defective pile, are plotted against the normalised settlement plate displacement in Figure 4.23. Other than a small discrepancy between model tests comprising dense sand at small settlement plate displacements ($\delta_{sp}/b' < 5\%$), the surface settlement ratio between models both with and without a defective pile match closely. Thus, the defective pile in the model tests did not result in any additional settlement propagating to the embankment surface.

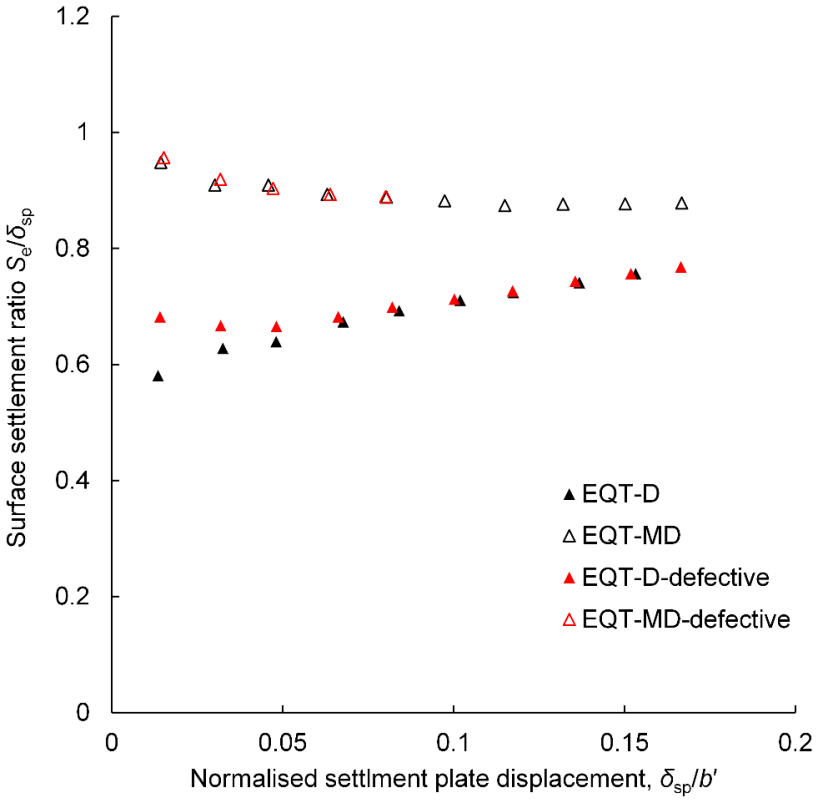

Figure 4.23: Surface settlement ratio versus relative displacement for models both with and without a defective pile

The model tests did not investigate different rates of defective pile displacement, which would have simulated different severities of pile defects. Different rates of defective pile displacement would likely result in different outcomes. However, for the geometries and displacements tested, the results from Figure 4.22 and Figure 4.23 show that the defective pile did not adversely affect the performance of the sand surface. It should be noted that the defective pile increased the height at which the plane of equal settlement developed. As such, if a relatively shallow embankment was constructed where $h_e \approx h_{cr}$, then the presence of a defective pile would likely result in differential settlements.

4.4 Summary

Synchrotron X-ray CT imaging has been undertaken on small-scale model piled embankments. By applying DVC analysis to pairs of CT volumes, full-field 3D displacement and strain fields were obtained, which provided insight into the kinematics of soil arching in piled embankments. Model tests were performed on two pile arrangements, square and equilateral triangle grids, and on samples of sand prepared in a dense and medium dense state.

The key findings from studying the displacement and strain fields from model tests without a defective pile may be summarised as follows:

- The failure mechanism within an LTP above pile heads is analogous to that of a circular shallow foundation, although vertically mirrored. Similar to shallow foundations, the failure mechanism is dependent on the soil state, including relative density and initial mean stress.
- The failure surfaces associated with soil arching in piled embankments do not take the form or resemble a simple arch-like shape, which is the assumption made by many arching based models. Instead, failure surfaces in the form of shear bands were observed to develop above pile heads within the LTP granular material, which in the case of dense sand, interacted with the failure surfaces propagating from adjacent pile heads.
- The observed failure mechanism within the model tests explains the observation of the progressive development of soil arching in piled embankments. The progressive development of soil arching may be attributed to the mobilisation of friction and dilation angles with relative shearing within shear bands.
- The critical height of a piled embankment is dependent on not only the clear spacing between piles and the pile head geometry but also on the deviatoric response of the LTP granular material. This is not considered in the majority of the currently available methods for predicting the critical height.
- A method for estimating the maximum height of failure surfaces above pile heads in an LTP is presented, which provides insight into the development of a plane of equal settlement.

Testing was also carried out on models comprising a central defective pile. The defective pile was lowered at a rate of approximately 1:3.6 of the settlement plate displacement. For this rate of defective pile displacement and the model geometry tested, the findings may be summarised as:

- The same failure surfaces as observed in tests without a defective pile developed above the defective pile head.
- Less strain was generally mobilised within the shear bands propagating from a defective pile head compared to a non-defective pile head.

- A plane of equal settlement developed at a height above the defective pile head, although this critical height was greater than for model tests without a defective pile.
- The defective pile did not affect the amount of settlement that propagated above the critical height to the embankment surface.

5 Centrifuge model tests – methodology

5.1 Introduction

It has been shown in Chapter 3 that to achieve similitude between model and prototype, equivalent stresses should be maintained between the two. This was not achieved in the 1*g* model tests described in Chapters 3 and 4. However, by subjecting small-scale models to enhanced gravitational fields by spinning them around a circular path using a geotechnical centrifuge, the scaling of small-scale models can be significantly improved.

Centrifuge modelling was performed on model GRPEs, both with and without defective piles, to overcome many of the limitations associated with the 1*g* small-scale model tests. These tests were also able to model the subsoil and pile head settlement using soil, rather than mechanically simulating these mechanisms. This chapter details the experimental apparatus, materials, model construction and testing procedure undertaken as part of this test program.

5.1.1 Background

Equivalent stresses between model and prototype may be achieved by using a geotechnical centrifuge, which rotates a small-scale model around a circular path and induces centripetal accelerations. The enhanced gravitational field can be expressed in terms of earth's gravity (g) with the following equation:

$$ng = r\omega^2 \tag{5.1}$$

Where n is the acceleration scale factor, r is the radius of the circular path the body is travelling, and ω is the angular velocity of the body. To accurately model a large-scale structure, it is preferable to achieve a close match between the acceleration scale and the geometrical scale factor. Many centrifuge scaling laws have been developed through dimensional analysis, some of which are shown in Table 5.1. Garnier et al. (2007) provided a thorough overview of the current knowledge of scaling laws and similitude conditions in geotechnical centrifuge modelling, which the reader is referred to for a more comprehensive list.

Table 5.1: Centrifuge scaling factors

Parameter	Units	Scale factor
Linear dimension	m	n
Area	m^2	n^2
Volume	m^3	n^3
Force	N	n^2
Work	Nm	n^3
Energy	J	n^3
Stress	N/m^2	1
Strain	-	1
Consolidation time	days	n^2
Creep time	days	1

5.2 Design of model

Appropriately scaling all aspects of a centrifuge model can prove difficult and expensive. Consequently, this has led to previous studies investigating the behaviour of GRPEs to use surrogate materials (not soil) or simulate mechanisms mechanically. Regarding the modelling of the soft subsoil, Ellis and Aslam (2009a) used various grades of expanded polystyrene, which compressed under the weight of embankment fill, while Blanc et al. (2013) built a "mobile tray" device to simulate subsoil consolidation mechanically. Other studies have also conducted centrifuge modelling of GRPEs without geosynthetic reinforcement (Baudouin et al. 2010; Okyay et al. 2014). To the author's knowledge, model GRPEs incorporating soft clay to model subsoil behaviour and geosynthetic reinforcement have never been studied in a geotechnical centrifuge.

In this study, importance was placed on appropriately modelling the pile-soil interaction, to ensure that pile load-settlement behaviour was replicated. This was necessary to investigate the load transfer towards a defective pile and its resulting settlement. It is not possible to model this soil-structure interaction with surrogate materials that are not soils. As such, the behaviour of the soft subsoil below the embankment was not replicated using mechanical devices or surrogate materials, instead, clay was used. This resulted in longer model preparation and testing times compared to what could have been achieved by other techniques, and as such, limited the scope of testing to two models.

The installation of piles for centrifuge model tests at 1*g* has been shown to result in different load-settlement responses to piles installed in-flight (Dyson and Randolph 2001). Given that displacement piles and ground improvement columns are commonly used to support embankments built over soft soils, full-displacement model piles were pushed into the subsoil in-flight. The piles and their installation method simulate jacked piles, rather than driven displacement piles. The design of the centrifuge model and testing was governed by the objectives outlined in Table 5.2.

Table 5.2: Objectives of centrifuge model

Objectives	Comments
Investigate installation effects of full-displacement piles and whether soft clay undergoes strength increase, as this phenomenon may reduce the effects of a defective pile	Piles installed in-flight to replicate installation process. In situ testing undertaken before and after pile installation to measure strength profile, and identify whether increase due to installation is evident.
Investigate the progressive development of soil arching (without defective pile)	Pile loads measured within a section of the embankment with no defective piles.
Investigate the progressive development of settlements	Displacements of pile heads, geosynthetic and embankment surface measured within an area of the embankment where no defective piles are present.
Model a defective pile surrounded by piles installed as per design (non-defective)	Short pile installed that does not penetrate founding strata. Surrounding piles installed to founding strata. Subsoil model using clay, rather than simulating consolidation using other techniques. Piles installed in-flight to model the load-settlement behaviour of piles.
Investigate the effect of a defective pile on embankments performance and compare area of the **embankment** with piles installed as per design.	Instrumented area with a defective pile as described above for area without defective pile. Each model, therefore, comprises an instrumented zone including a defective pile and an instrumented zone with all piles installed as per design.
Investigate the "disturbed volume" resulting from the arching mechanism.	Undertake in situ testing after consolidation from embankment has occurred to observe density changes in embankment fill from arching.

5.3 Apparatus

5.3.1 Centrifuge

Testing was performed at the University of Western Australia (UWA) centrifuge facility. An Accutronic Model 661 beam centrifuge was used in the current study (Figure 5.1). The centrifuge has a 40 g-tonnes capacity and can test smaller packages up to 200*g*. The Model 661 platform supports a 'strongbox' with the internal dimensions of 650 mm long, 390 mm wide and 325 mm in height. The strongbox is

positioned at a radius of 1.8 m from the centre of rotation. Details of the facility, in its initial state, have been provided by Randolph et al. (1991), although some advancements have since been made. A wireless data acquisition system has been developed by UWA and was used to transfer data to the control room during testing in real-time (Gaudin et al. 2009).

Figure 5.1: UWA beam centrifuge

5.3.2 Actuator

The model 661 centrifuge and strongbox allow an actuator to be fixed on top of the model and controlled while in-flight. The actuator used in the current study comprised two orthogonal motion controlled axes, vertical and horizontal, which was used to install piles and perform in situ soil characterisation testing. The axes can be load or displacement controlled using Proportional-Integral-Derivative (PID) controllers over a stroke of 260 mm in the vertical direction and 180 mm in the horizontal. Further details regarding the actuator control system developed by UWA are provided by De Catania et al. (2010).

5.3.3 Soil characterisation equipment

Soil characterisation was performed in-flight using model T-bar, piezoball and piezocone penetrometers (Figure 5.2). A T-bar penetrometer was used to characterise the undrained shear strength (s_u) profile of the clay layers. The model T-bar comprised a 5 mm diameter horizontal bar, 20 mm in length. A load cell is located directly behind the horizontal bar to measure penetration resistances during both penetration and extraction of the T-bar. A piezoball measuring 15 mm in diameter and with a pore pressure transducer located at the mid-face position was used to measure pore pressures during dissipation tests within clay layers. Dissipation tests were also undertaken using a piezocone measuring 10 mm in diameter, which measured pore pressures in the u_2 position. Both piezoball and piezocone penetrometers were also fitted with load cells directly behind the ball/cone to measure penetration resistances.

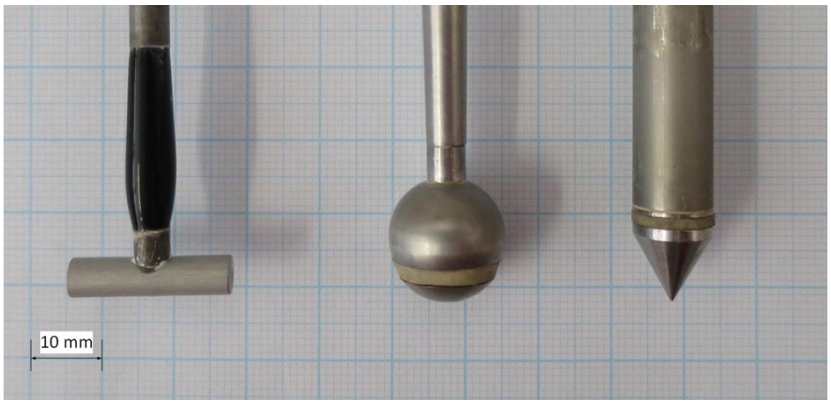

Figure 5.2: Penetrometers used in centrifuge model tests; from left to right, T-bar, piezoball and piezocone

5.4 Model layout

The testing program considers two models with differing soil conditions. Each of the models comprised two instrumented zones. The first zone (Zone 1) included piles installed to the same toe level, simulating a section of the embankment where all piles were constructed to the same depth, as may be proposed for GRPEs at the design stage. A second zone (Zone 2) included a single pile installed to a shallower depth relative to the surrounding piles, modelling a defective pile that exhibits a softer load-settlement response. To measure the performance of the model embankments, instrumentation installed included pile load cells (PLC), string potentiometers (SP), laser displacement transducers (LDT) and a single pore pressure transducer (PPT). The piles around the outer perimeter of the strongbox were installed only to reduce boundary effects. As such, no instrumentation was installed within or around these piles. The instrumentation and model layout used for both models are shown in Figure 5.3.

The pile geometry and embankment height were selected to represent common GRPE characteristics, although the pile spacing selected is towards the upper end of the range of spacing typically adopted in Australia to maximise the effect due to a defective pile. The piles were installed on a square grid with a centre-to-centre spacing of 75 mm, equivalent to a prototype spacing of 3 m. With a pile head diameter of 20 mm, this pile spacing corresponds to a replacement ratio of α_r = 5.6%. The embankment height was consistent throughout the entire model, thus, modelling a section near the centreline of an embankment where no lateral thrust will be generated.

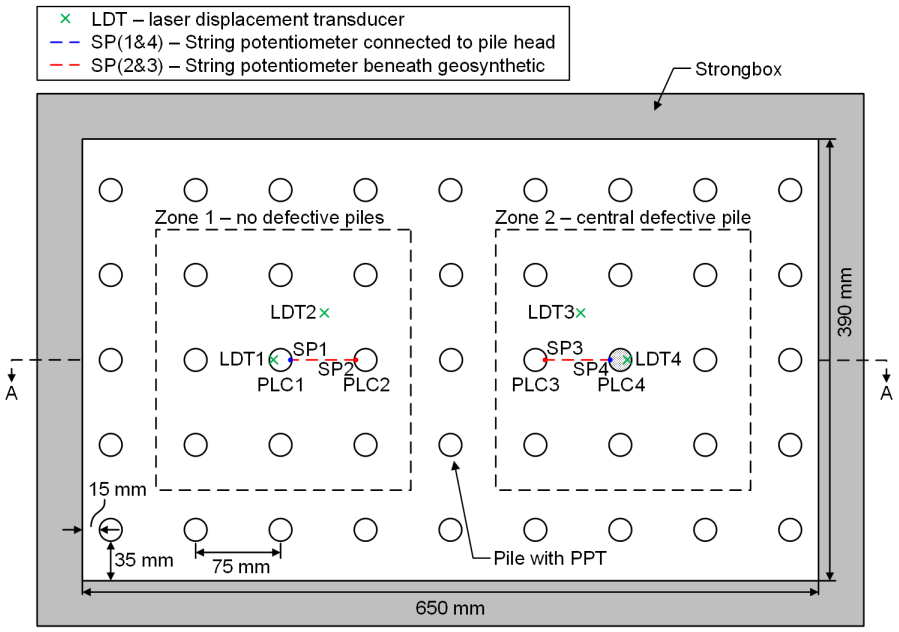

Figure 5.3: Plan view of the pile layout and instrumentation for both Model 1 and 2.

The first model (Model 1) was designed to simulate an embankment supported on 'floating piles'. This was achieved by preparing a founding layer of firm clay at the base of the strongbox. The Model 1 piles were installed through the very soft clay layer (subsoil) and into this firm clay layer (Figure 5.4a). It is noted that a thin drainage layer was installed at the base of the model comprising of coarse-grained silica sand with a layer of geotextile to separate the sand and clay layers. This drainage layer allowed the firm clay layer to drain freely from the base of the strong box.

The second model (Model 2) was designed to simulate an embankment supported on end-bearing piles. A founding layer of medium dense sand was prepared in Model 2, in which the pile toes were embedded into (Figure 5.4b). A further point of difference between the two models is the placement of the geosynthetic reinforcement. In Model 1, the geosynthetic was placed directly over the pile heads. Due to the impermeable nature of the geosynthetic reinforcement used, this prevented free-drainage from the very soft clay layer. A 10 mm thick sand layer was placed above the clay and pile heads in Model 2, before the geosynthetic reinforcement was placed, to facilitate two-way drainage within the very soft clay layer. Hydraulic connectivity between the sand above and below the geosynthetic reinforcement was maintained by a gap around the outer edge of the geosynthetic reinforcement, which allowed the sand directly above the clay and pile heads in Model 2 to act as a free-drainage layer.

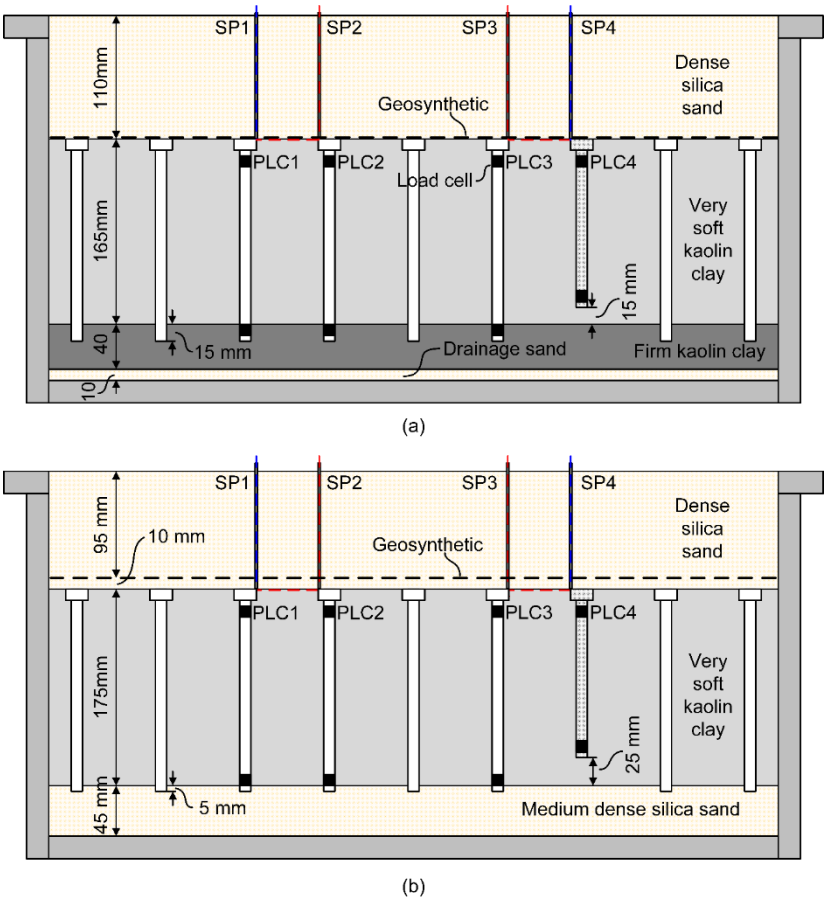

Figure 5.4: Section through centreline (A-A shown in Figure 5.3) of (a) Model 1; (b) Model 2

5.5 Experimental setup

5.5.1 Model piles

The model piles were fabricated from 1.6 mm thick hollow aluminium tubing with an outer diameter of 10 mm. The bases of the piles were sealed with epoxy to ensure a full-displacement pile was modelled. A 200 mm diameter enlarged pile head made from solid aluminium was placed on the top of the pile shaft. All piles were 180 mm in length, except for a single defective pile which was 150 mm in length and installed in the centre of the Zone 2 instrumented area of both models. At prototype scale, these dimensions scale to a 400 mm diameter pile shaft, an 800 mm diameter enlarged pile head, a non-defective pile length of 7.2 m and a defective pile length of 6 m. The models comprised 45 no. piles in total, 24 no. of which were installed around the perimeter of the strongbox to minimise boundary effects. Strain gauges were attached to two piles within each of the instrumented zones, with one of these strain gauged piles being the defective pile. Dimensions of the instrumented and non-instrumented piles are shown in Figure 5.5.

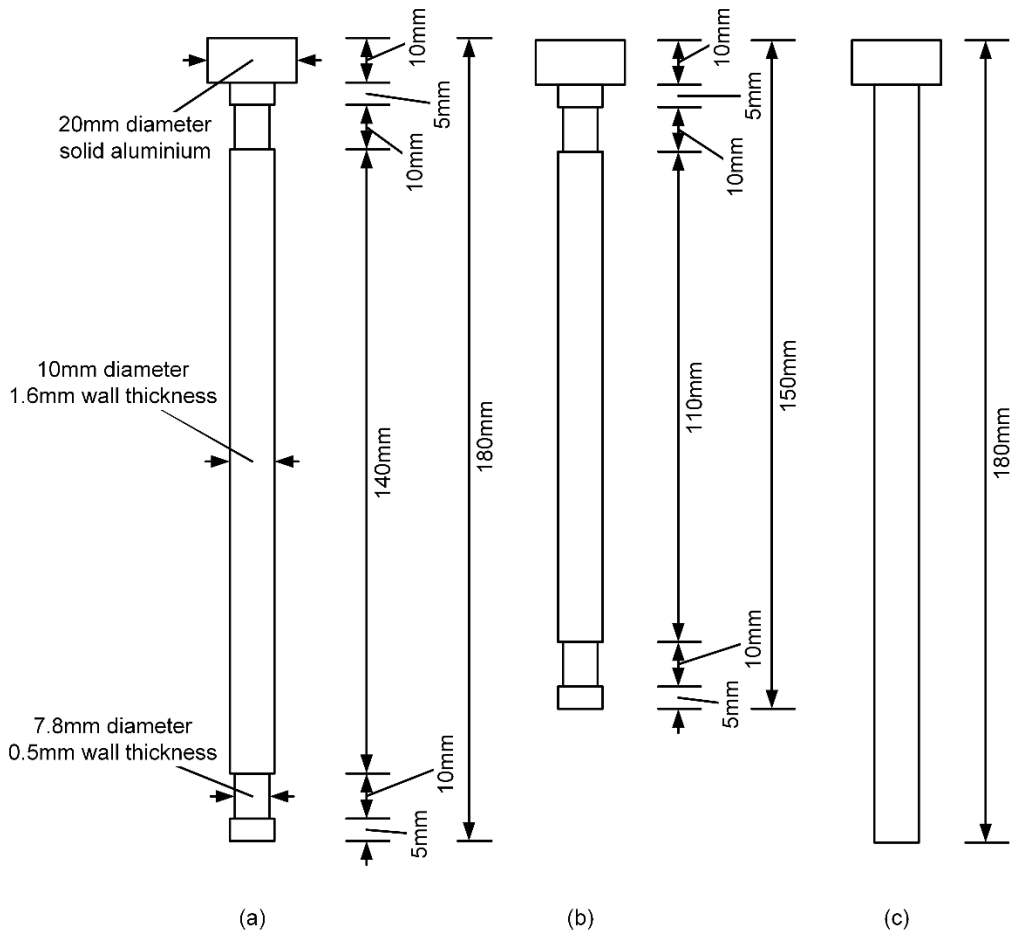

Figure 5.5: Dimensions (in model scale) of (a) non-defective piles with recesses for strain gauges; (b) defective pile with recesses for strain gauges; (c) non-instrumented non-defective piles

The pile shaft surface roughness was measured using a TR200 surface roughness tester developed and manufactured by Time Group. The pile surface roughness was measured as R_t = 3.2 μm. Pile shafts, when installed in the fine-grained sand to a D_{50} of 0.18 mm, have a relative roughness of R_n = 0.018. As such, it can be assumed that for lengths of pile penetrating sand, the mobilised shaft friction will be low and no dilation will occur (Fioravante 2002).

Regarding interface shear resistance in clays, Lemos and Vaughan (2000) undertook direct shear and ring shear clay interface testing, including samples of kaolin against smooth steel, to investigate the effects of interface roughness on the ultimate shear resistance. It was observed that for samples with high clay content, the ultimate interface shear resistance was not affected by roughness and the ultimate resistance can be approximated by the soil-soil residual strength.

Load cells

The pile shafts instrumented with strain gauges were recessed at the strain gauge locations to induce more strain in the aluminium pile (therefore increasing the strain gauge output signal), as shown in

Figure 5.6a. After the strain gauges were bonded to the aluminium shaft and the electrical wires fed into the hollow tube, epoxy resin was placed over the strain gauges, as shown in Figure 5.6b. Effort was made when applying epoxy to create a smooth and consistent diameter shaft to reduce any frictional effects from the load cells.

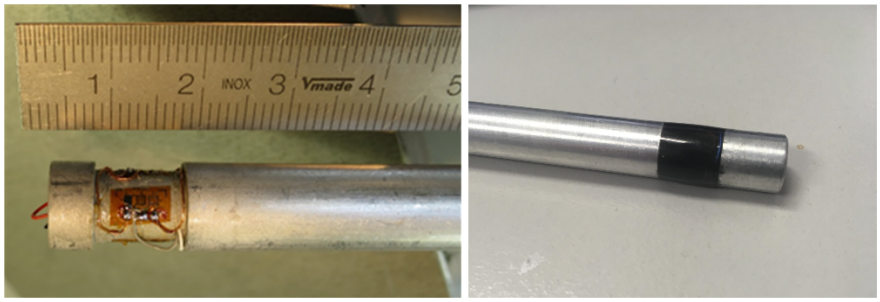

(a) (b)

Figure 5.6: Model pile load cells: (a) strain gauges attached to pile shaft; and (b) finished instrumented pile, with epoxy covering strain gauges

The strain gauges used were Micro-Measurements 120 ohm tee rosettes. Initial trials to measure axial loads in piles implemented two opposite 90-degree tee rosettes connected to form a bridge. It was found during trials that the strain gauge arrangement did not produce repeatable calibration factors. Poor repeatability is considered to have been due to the slightly non-axial loading conditions. To reduce the error that was experienced with the first strain gauge arrangement, the final model pile load cells comprised 2 bridges at each load cell, which when positioned around the pile shaft averages the strains. It is noted that similar observations were made by Aslam (2008).

Pore pressure transducer

One pile was installed near the centre of the model, between the two instrumented zones, with a pore pressure transducer (PPT) built into its shaft. A miniature pressure sensor, made by Kyowa, was fitted at the mid-point of the pile shaft Figure 5.7a. A porous filter was placed over the pressure sensor, as shown in Figure 5.7b, which prevented soil from coming into contact with the sensors diaphragm and was shaped to create a smooth pile shaft. The porous stone was saturated prior to being installed in-flight.

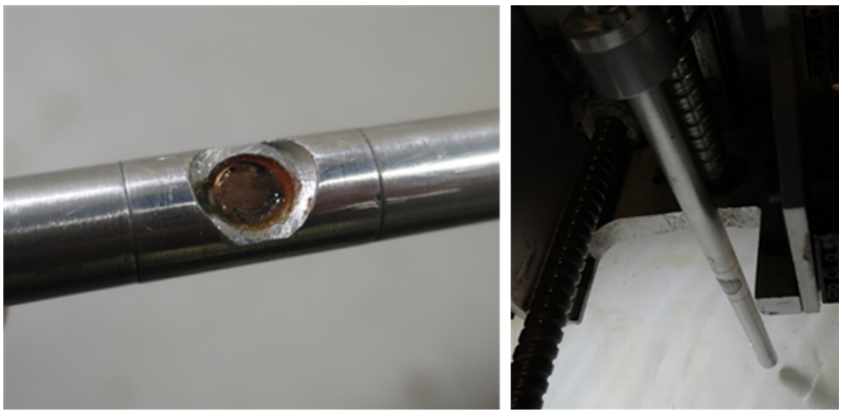

(a) (b)

Figure 5.7: Model pile instrumented with pore pressure transducer: (a) pressure sensor within pile shaft; and (b) pile with porous stone being jacked into subsoil in-flight

5.5.2 Geosynthetic reinforcement

Tensile reinforcement within an LTP may comprise either geotextiles or geogrids. Ideally, a centrifuge model would incorporate a reinforcement with all geometric dimensions scaled down by a factor of n. However, in practice, this is rather difficult, and no commercially available product will satisfy such scaling. Given that this centrifuge study was not designed to investigate the lateral stability of the embankment slopes, the interlocking of LTP granular material and geogrid was not considered critical to the model's behaviour. Instead, the centrifuge tests focused on modelling a material without apertures, similar to a geotextile.

Studies investigating the scaling of geosynthetics (Springman et al. 1992; Viswanadham and König 2004) have shown that the similitude conditions for both ultimate tensile capacity (T_u) and stiffness (J) are:

$$T_{u,m} = \frac{1}{n} T_{u,p} \tag{5.2}$$

$$J_m = \frac{1}{n} J_p \tag{5.3}$$

In the design of a GRPE, the ultimate tensile strength of the reinforcement is of importance to ensure the selected material can withstand the applied loads. However, rarely is the ultimate tensile strength of the geosynthetic reinforcement exceeded under working conditions. Design recommendations such as BS8006 (2016) suggest that the geosynthetic reinforcement should not exceed a maximum strain of 6%, while strain under working conditions is often limited to 4% or less. The ultimate tensile strength of a geogrid or a geotextile used for tensile reinforcement is typically achieved at about 10% strain, well above any strain expected in a suitably designed GRPE. Therefore, when considering the scaling of

geosynthetic reinforcement for the centrifuge tests, the ultimate tensile strength was not scaled as the geosynthetic tensile stresses in the centrifuge tests were expected to be lower than the ultimate tensile strength of the material. Emphasis was instead placed on scaling the axial stiffness of the geosynthetic reinforcement to ensure the mobilised tensile loads were modelled appropriately.

The material selected as the model reinforcement was 200 microns thick linear low-density polyethylene (LLDPE) geomembrane, which is a material commonly used for lining systems where large strains may be expected. The LLDPE material provides a relatively lower axial stiffness compared to other geomembrane materials such as high-density polyethylene. The 200 micron thick LLDPE was the thinnest commercially available geosynthetic tested that could provide repeatable strength properties.

Tensile testing of the LLDPE geomembrane was undertaken in accordance with AS 3706.2, at a strain rate of 300 mm/min, room temperature of 22.5 ˚C and relative humidity of 45 %. The results of the testing are shown in Figure 5.8a. It was observed that material began to yield at less than 2% strain, although failure in all samples was not achieved until over 100 % axial strain. In the region of interest, less than 10 % axial strain, the material can be simplified to a bilinear behaviour. This simplified bilinear behaviour assumes a model stiffness of 90 kN/m (J_p = 3600 kN/m) up to 2.7% strain and 0.5 kN/m stiffness (J_p = 20 kN/m) for strains greater than 2.7%.

The simplified tensile behaviour of the selected LLDPE geomembrane in prototype scale is plotted along with a selection of commonly used geogrids and geomembranes in Figure 5.8b. While the model reinforcement does not exhibit linear load-displacement behaviour, it is within the region of typical tensile stiffnesses of commonly used geosynthetic reinforcements, which is critical to modelling the differential settlement between subsoil and pile heads that causes soil arching to develop.

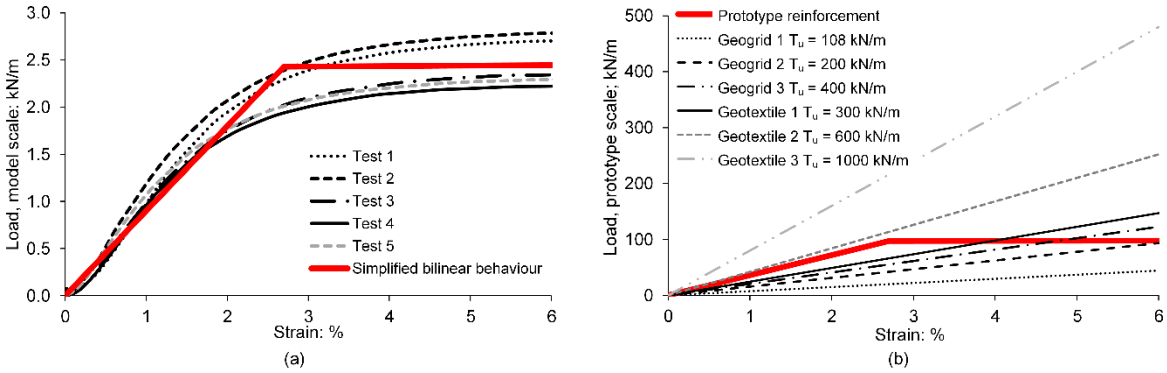

Figure 5.8: Tensile behaviour of the model geosynthetic reinforcement: (a) tensile tests at model scale; (b) behaviour at prototype scale with common geosynthetics used for reinforcement

5.5.3 Displacement measurements

Instrumentation beam

The linear displacement measuring instruments were positioned on an "instrumentation beam", which spanned the length of the strongbox (Figure 5.9) and allowed displacement to be measured from above the model. The beam was made from 10 mm thick mild steel, which deflected under the enhanced gravitational field of 40*g*. To ensure the linear displacements measured by each instrument were measuring the models behaviour, without the instrumentation beam deflection, all measurements were corrected for the deflection of the beam. The deflection of the beam at 40*g* (with instrumentation attached) at the location of each piece of instrumentation was measured prior to the embankment test. Measurements of the beam deflection before and after the test confirmed that the beam did not undergo any plastic deformation during the test, and beam deflections remained constant throughout the entire test duration.

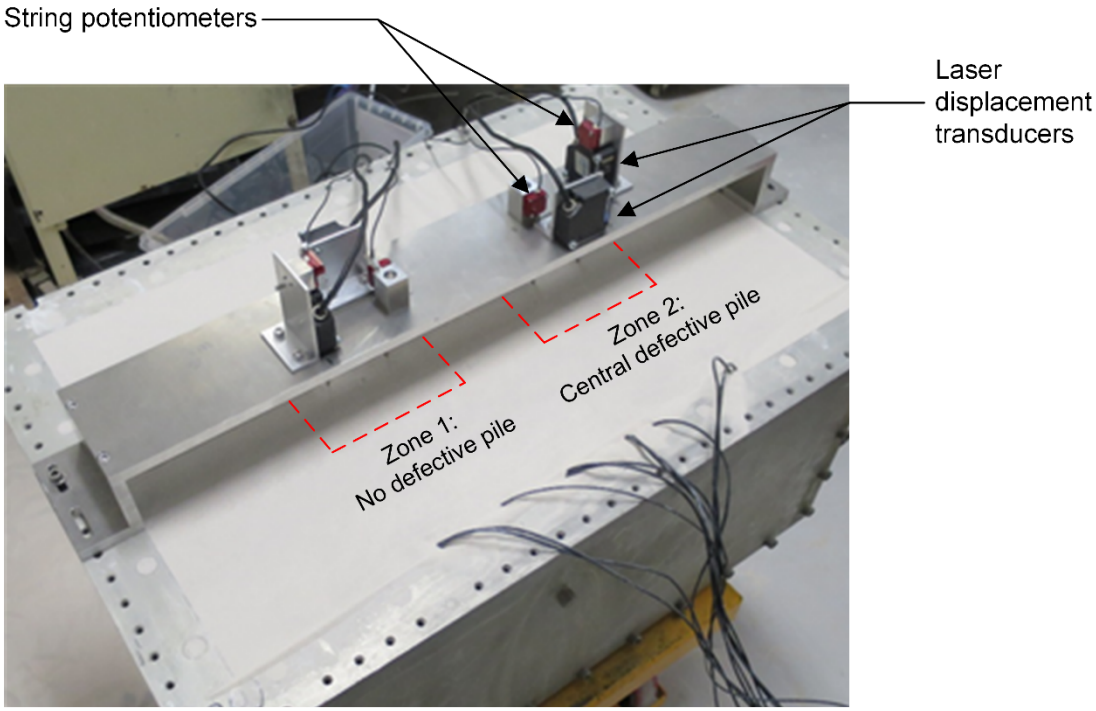

Figure 5.9: String potentiometers and laser displacement transducers on the instrumentation beam above strongbox

String potentiometers

String potentiometers (SP) were used to measure pile head settlement and subsoil settlement. String potentiometers comprise a cable, which is connected to a spring-loaded spool. A potentiometer is used to then measure the rotation of the spool, providing the displacement of the cable. The cables of string potentiometers, produced by TE Connectivity Ltd, were attached to pile heads as shown in Figure 5.10.

The cables were fed through a 2 mm diameter hollow aluminium tube, which prevented the cable from interacting with the embankment sand.

Cables measuring the settlement of pile heads were fixed directly to the pile heads. The cables measuring the deflection of the subsoil (subsoil settlement) between pile heads were fed through a pile head, beneath the geosynthetic and fixed to an adjacent pile head, as shown in Figure 5.10. Both cables were fixed within the pile heads by a grub screw, which clamped them in place.

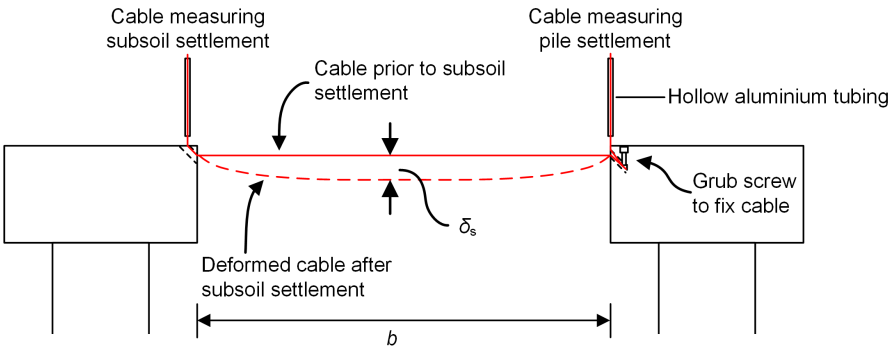

Figure 5.10: String potentiometer cables attached to pile heads to measure subsoil settlement and pile settlement (not to scale)

The difference in the displacements of the cable attached to the pile head and the cable passing beneath the embankment sand is taken to be equal to the elongation of the SP cable due to subsoil settlement, Δ_{SP}. This assumes that the two pile heads undergo uniform settlement, and as such, cannot be applied to estimate the cable elongation if differential settlement between piles is experienced. Thus, the subsoil settlement may only be estimated within the Zone 1 instrumented area, where all piles are of the same length, and uniform settlement between all piles can be assumed. The elongation ratio of the SP cable at the subsoil surface due to subsoil settlement between directly adjacent piles, ε_s, which is similar to the strain of the geosynthetic reinforcement, may be written as:

$$\varepsilon_s = \frac{\Delta_{SP}}{b} \tag{5.4}$$

Where b is the clear span between directly adjacent piles, equal to 55 mm in the centrifuge model tests. The subsoil settlement between two adjacent piles (δ_s) may then be estimated using tensioned membrane theory. Assuming the deflected shape of the geosynthetic reinforcement may be represented by a parabolic curve (Giroud 1995), δ_s may be approximated by:

$$\delta_s = b\sqrt{\frac{3}{8}\varepsilon_s} \tag{5.5}$$

Studies have shown that the maximum subsoil settlement, or geosynthetic deflection, between diagonally adjacent piles on a square grid is equal to $\delta_{s,max} = \sqrt{2}\delta_s$ (Zhuang and Ellis 2014; Fagundes et al. 2017), which in combination with Equation 5.4 and 5.5, allows $\delta_{s,max}$ to be estimated from the string potentiometer measurements.

Laser displacement transducers

Laser displacement transducers (LDT), utilising laser triangulation principles to measure linear distances, were used to measure embankment surface displacements. The sensors were also positioned on the instrumentation beam and were directed towards the sand surface at locations directly above pile heads and at the mid-point between piles to measure both total and differential surface settlements.

5.6 Material properties

5.6.1 Kaolin clay

Piled embankments are typically built over highly compressible clayey soils. Kaolin clay was used in both models to replicate the behaviour of a very soft subsoil material beneath the embankment. In Model 1, the founding layer also comprised kaolin clay, although consolidated under a press to achieve a stiffer response to the very soft subsoil layer. Dry kaolin powder was mixed with water and de-aired under a vacuum to form a slurry with a moisture content of 120%, which was then poured carefully into the strongbox. This kaolin clay has been used extensively in physical model testing over the past 25 years, and as such, the properties have been well defined (Stewart 1992; Watson 1999; House et al. 2001; Acosta-Martinez and Gourvenec 2006).

Table 5.3: Properties of kaolin clay (after Stewart, 1992)

Property	**Symbol**	**Value**
Liquid limit	*LL*	61 %
Plastic limit	*PL*	27 %
Specific gravity	G_s	2.6
Angle of internal friction	ϕ	23˚
Critical state friction constant	*M*	0.92
Slope of normal consolidation line	λ	0.205
Slope of swelling line	κ	0.044
Parameter Λ, = $(\lambda - \kappa)/\lambda$	Λ	0.785
Coefficient of vertical consolidation (at OCR = 1 and σ'_v = 20 kPa)	c_v	1.8 m^2/yr*

*House et al. (2001)

5.6.2 Silica sand

The same silica sand (UWA sand) as used for the small-scale models described in Chapter 3 was used in the centrifuge tests to model the behaviour of LTP granular material and embankment fill. The properties of this material are provided in Table 3.3. As noted in Chapter 3, the scaling of LTP granular material should consider the ratio d/D_{50}, such that the soil particle size is scaled proportionally to the model geometry. Given that the model was geometrically scaled by n = 40, the UWA sand models a gravel sized LTP granular material with D_{50} = 7.2 mm, typical of a high quality crushed rock fill.

5.7 Model construction

5.7.1 Founding layer

The key difference between the two models was the founding conditions of the piles. The piles in Model 1 were terminated 15 mm (in model scale) into a firm clay, while the piles in Model 2 were embedded 5 mm into a medium dense sand.

Model 1

Prior to constructing the firm clay layer, a 10 mm thick sand drainage layer was placed at the base of the strongbox to ensure free-drainage at the base of the clay. The firm clay founding layer was constructed by carefully pouring kaolin slurry over the drainage sand before placing the slurry under a consolidation press (Figure 5.11a). Vertical stress was incrementally applied to the surface of the kaolin, until a final stress of 394 kPa (100 kN) was achieved. This stress was applied to the surface for a period of two weeks, at which point in time the settlement of the clay was essentially constant, and the firm clay layer was 40 mm thick.

Model 2

The Model 2 founding layer was constructed from UWA silica sand, which was air-pluviated into the strongbox using a hopper (Figure 5.11b). The UWA sand hopper has an adjustable height, speed and opening width to control the density of the prepared sample. By adjusting these parameters, a 45 mm thick layer of sand was prepared at a relative density of D_r = 54% (medium dense). The surface of the sand layer was levelled to ensure that all non-defective piles penetrated an equal length into the sand founding layer.

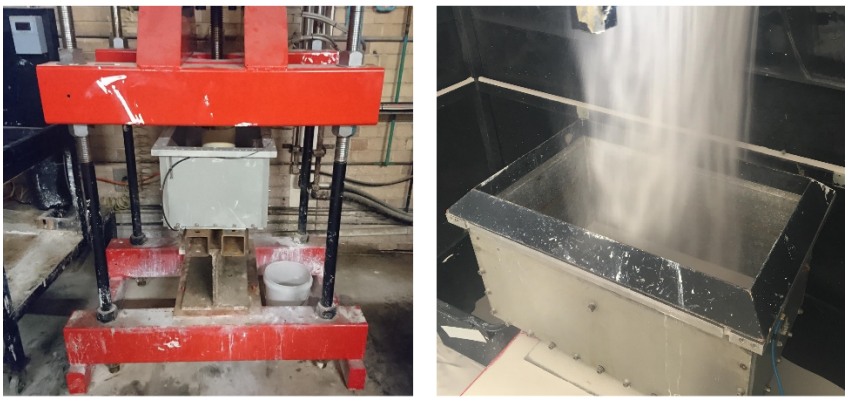

(a) (b)

Figure 5.11: Preparation of founding layers: (a) Model 1 clay in consolidation press; (b) Model 2 sand pluviated

5.7.2 Clay subsoil

The clay subsoil in both model tests was prepared in the same manner. Kaolin slurry was poured carefully over the prepared founding layer. The strongbox was then transferred to the centrifuge and consolidated under self-weight at 60*g* for a minimum of 80 hours. The surface of the kaolin was then scraped level, removing a thin layer of kaolin (up to 5 mm thick around the edges of the strongbox) from the clay surface. Given the embankments were tested at an acceleration of $n = 40g$, this very soft clay layer was slightly over-consolidated (OCR = 1.5). In situ testing was undertaken to confirm that a similar undrained shear strength profile was achieved in the clay subsoil in both models.

5.7.3 Installation of piles

Both models comprised a group of 45 piles that were pushed (jacked) into the subsoil using an electrically driven actuator. The outer-most row of piles was installed to reduce potential boundary effects due to the strongbox walls on the instrumented zones of the embankment. As the actuator was not able to reach the 24 piles within the outer row while in-flight, these piles were jacked into the subsoil at 1g at a constant penetration rate of 3 mm/s. After installing the outer piles, the remaining 21 piles were then jacked into the subsoil in-flight. All piles installed in-flight in Model 1 were jacked into the clay at a centrifugal acceleration of 40*g* and at a penetration rate of 1 mm/s. The medium dense sand founding layer in Model 2 meant that the same acceleration level and penetration rate would have resulted in pile resistances that would have approached or potentially exceeded the capacity of the pile load cells. To avoid this, the piles in Model 2 piles were installed in-flight at 1 mm/s at 40*g* to a depth of 177 mm (i.e. 2 mm penetration in the sand), before reducing the centrifugal acceleration to 30*g* and the penetration to 0.1 mm/s for the final 3 mm penetration into the sand.

Similar to the dependency of penetrometer resistance on penetration rate (Roy et al. 1982; Chung et al. 2006; Lehane et al. 2009), the pile installation resistance and soil state (in regard to drainage conditions) will depend on the installation rate. The installation rate of the pile, v, may be expressed as a normalised velocity, V', (Finnie and Randolph 1994), written as:

$$V' = \frac{vd}{c_{\mathrm{h}}} \tag{5.6}$$

Where d is the pile diameter and c_{h} is the horizontal coefficient of consolidation, which is used in place of c_{v} as the radial flow is the governing mechanism of consolidation around an advancing pile tip or penetrometer (Lehane et al. 2009). Based on values of c_{h} estimated from piezocone dissipation tests undertaken at approximately the mid-depth of the very soft clay layer, the normalised velocity of pile installation is in the range, V' = 40 – 60. While no exact normalised velocity defines the boundary between partially drained and undrained conditions around an advancing pile tip, studies have found that a normalised velocity in the range of 20 to 30 results in a minimum penetrometer resistance (Finnie and Randolph 1994; Colreavy et al. 2016), with greater normalised velocities experiencing some viscous strain rate effects. It is, therefore, expected that the pile installation at 1 mm/s results in an undrained condition in the soil surrounding the penetrating pile tip with potentially some minor viscous strain rate effects.

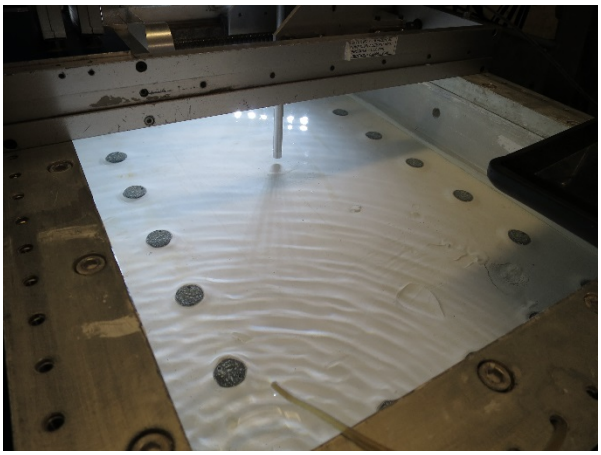

Figure 5.12: Model pile being jacked into the kaolin sample

5.7.4 Geosynthetic reinforcement

The geosynthetic reinforcement was clamped in a frame around the strongbox perimeter to provide lateral restraint to the geosynthetic (Figure 5.13). Samples of geomembrane were cut and aligned in the frame along its machine and cross directions. The reinforcement was then clamped in the frame using screws while being pulled taught. It is considered that any pretension applied to the geosynthetic reinforcement may affect the load distribution, since a pretension applied to the reinforcement may

increase its secant tensile stiffness. However, the effect of pretensioning geosynthetic reinforcement was shown to be negligible by Blanc et al. (2013) who performed several centrifuge tests on GRPEs with different pretensions applied to the geosynthetic. As such, pretensioning was not considered in the present study.

The model geosynthetic reinforcement was positioned directly above the pile heads in Model 1 (i.e. at the embankment/clay interface). As the geomembrane is essentially impermeable, free drainage was prevented at the clay surface in Model 1. To facilitate free drainage at the clay surface in Model 2, a 10 mm thick layer of sand was placed above the pile heads before placing the geosynthetic reinforcement. Given that the reinforcement did not extend to the sidewalls of the strongbox, a hydraulic connection was maintained between the sand below and above the reinforcement in Model 2. This hydraulic connection allowed the sand above the pile heads (and clay surface) to act as a drainage layer.

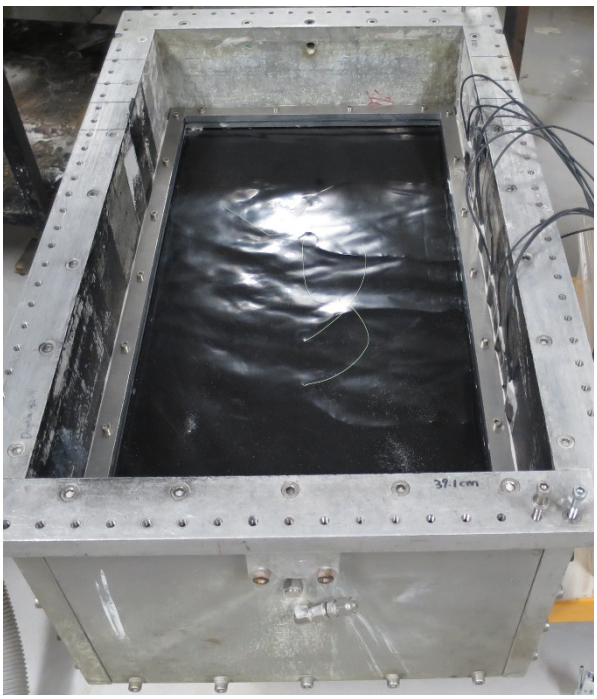

Figure 5.13: Geosynthetic reinforcement in clamp

5.7.5 Embankment sand

The granular material within LTPs and embankment fill is typically well compacted, and therefore, embankment material within centrifuge models should be prepared dense. The sand within both models was again air pluviated using the sand hopper, although adjustments were made such that dense samples were created. The sand was levelled flush with the top of the strongbox after sand was pluviated to create a consistent height of embankment sand across the entire model. By weighing the strongbox before and after the pluviation of sand into the strongbox, it was confirmed that the relative density of the embankment sand was 88% and 90% in Model 1 and 2, respectively.

As noted previously, the cables measuring pile head settlement and subsoil settlement were fed through protective aluminium tubes. These tubes were held vertically in place by a bracing cable while sand was pluviated into the strongbox (Figure 5.14).

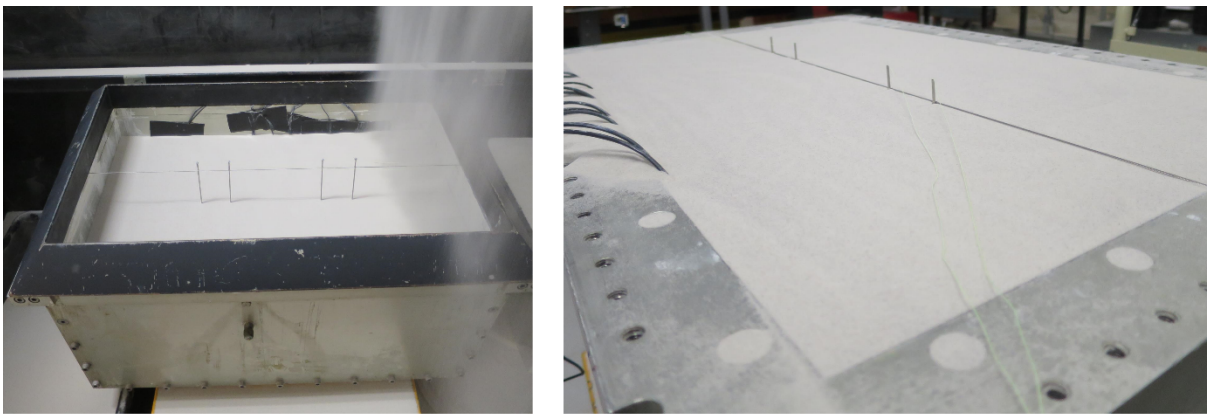

(a) (b)

Figure 5.14: (a) Pluviation of the sand around the protective tubing; (b) finished surface of embankment sand

5.8 Testing procedure

To model the behaviour of a GRPE comprising defective and non-defective piles, the construction sequence of the pile installation and embankment as well as the embankment consolidation process need to be modelled appropriately. The experimental procedure adopted to model this behaviour may be divided into four phases, which are described below:

a) *Subsoil and pile construction*: The founding layer and the subsoil were prepared before the piles were installed (as described earlier). Excess pore pressures from pile installation were allowed to dissipate for a minimum of 12 hours before embankment construction commenced.

b) *Embankment construction*: SPs were attached to pile heads before the geosynthetic reinforcement was clamped and placed in position. The SP cables were located within the protective aluminium tubes. The embankment was constructed by pluviating sand until it was flush with the top of the strongbox. The beam supporting the instrumentation was then placed over the top of the strongbox with instrumentation attached and the strongbox was then transferred to the centrifuge (Figure 5.15a). Given that the embankment was created at 1*g*, the model embankment construction sequence simulates the prototype condition where the embankment is created in a single stage.

c) *Embankment consolidation*: The centrifuge was spun at 40*g*, such that the soft clay layer underwent consolidation from the enhanced self-weight of the embankment. Consolidation was deemed complete on the basis of displacement measurements of the embankment surface (LDT

measurements). Consolidation durations were ten days in Model 1 and two days in Model 2. Ideally, the centrifuge is not stopped for the duration of the test; however, due to some counterbalance issues while Model 1 was consolidating, the centrifuge was spun down and stopped for approximately 1 minute before being returned to 40*g*. Model 2 was spun at 40*g* continuously without stopping for the duration of the embankment consolidation phase.

d) *Post-test investigation*: In-flight 'rod penetrometer' tests (described in Chapter 6) were performed to assess potential changes in the density of the sand used as the embankment fill. The embankment was then removed from the model at 1*g*, and topographical scans were performed (also at 1*g*) using a laser displacement sensor moving on a three degree of freedom actuator to quantify spatial vertical deformation of the soil layer directly beneath the geosynthetic reinforcement (Figure 5.15b). In the event that differential settlements were measured at the embankment surface by the LDTs (as was the case for Model 2), a topographical scan was performed on the embankment surface.

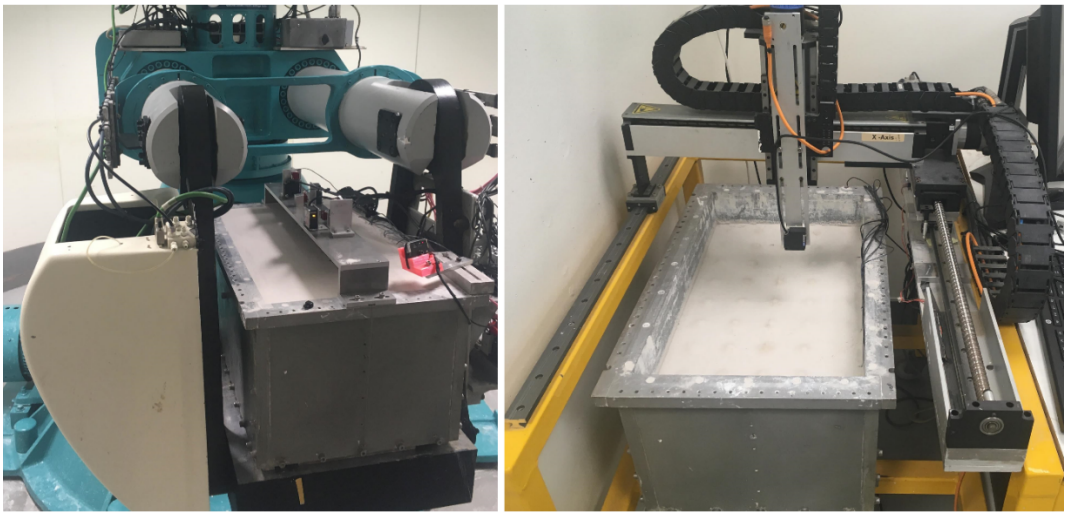

(a) (b)

Figure 5.15: Testing procedure: (a) finished model on centrifuge platform; (b) post-test topographic surface scanning

5.9 Summary

Centrifuge modelling has been utilised to address many of the scaling issues identified with performing small-scale model tests at 1*g*. The materials and instrumentation utilised in this physical model testing have been described. It was shown that by replicating many of the materials and construction methods, e.g. consolidating subsoil and installing piles in-flight, it is possible to simulate the complex soil-geosynthetic-structure interaction that occurs within GRPEs, particularly those incorporating defective piles. The methodology presented in this chapter forms the basis for the test results and analysis discussed in the following chapter.

6 Centrifuge model tests – results and discussion

Centrifuge modelling was undertaken, where two models were constructed and tested at enhanced gravitational fields to investigate the behaviour of GRPEs both with and without defective piles. The experimental apparatus, instrumentation materials, model construction and testing procedure were detailed in the previous chapter. This chapter presents the results from the centrifuge model tests and provides discussion relating to several key aspects of GRPE behaviour that the centrifuge model tests can provide insight into.

6.1 Centrifuge In situ testing

6.1.1 Undrained shear strength

T-bar penetrometers were initially developed to determine the undrained shear strength of soft clays in centrifuge testing and later applied to field investigations (Stewart and Randolph 1994). T-bars have a large projected area, typically 5 to 10 times that of the shaft, which results in a "full-flow" mechanism, meaning that the soil is assumed to flow around the penetrometer without a gap forming. This enables plasticity solutions to be employed to derive factors relating penetration resistance, q, to undrained soil shear strength, s_u. The probe to shaft area ratio of a T-bar also results in fewer corrections to the measured penetration resistance to estimate the net resistance, $q_{T,net}$, compared to a conventional CPT.

The correction applied to the T-bar penetration resistance to account for overburden stress and pore pressure may be written as:

$$q_{T,net} = q - [\sigma_v - u_0(1-\alpha)]\frac{A_s}{A_p} \quad (6.1)$$

Where σ_v is the total vertical stress, α is the unequal area ratio and is taken as 0.79 for the UWA T-bars (Colreavy et al. 2016), u_0 is the hydrostatic pore pressure, A_s is the T-bar shaft projected area and A_p is the T-bar probe projected area.

The clays in both models were characterised using a model scale T-bar penetrometer with a diameter of 5 mm, which was penetrated at 1 mm/s such that the response (in this clay) was expected to be undrained (Colreavy et al. 2016). T-bar tests were conducted at the testing acceleration of 40*g*. In both models, two T-bar tests were performed within the clay units prior to the installation of the piles (M1TB1, M1TB2, M2TB1 and M2TB2). Another T-bar test was performed in each model after the piles were installed (M1TB3 and M2TB3).

Soil buoyancy, as well as changes in bar weight and lateral pressure acting on the load cell with depth, may lead to a tensile skew in T-bar penetration resistances (Sahdi et al. 2014). These effects on the net

resistance can be corrected by performing a cyclic episode of the T-bar at a prescribed depth. The net resistance or undrained shear strength can then be adjusted to ensure that once the soil has become fully remoulded the penetration and extraction values are equal (Randolph et al. 2007). Each T-bar was moved vertically by ± 10 mm for a minimum of ten cycles about the mid-depth of the very soft clay layer. The undrained shear strength was determined from the corrected penetration resistance using the commonly adopted T-bar bearing factor of 10.5 (Martin and Randolph 2006). An example of this cyclic correction applied to M1TB1 (Model 1, T-bar 1) is shown in Figure 6.1 where the degradation factor is plotted, which is the ratio of the undrained shear strength after n penetration/extraction cycles ($s_{u\text{-}n}$) to the initial undrained shear strength ($s_{u\text{-}in}$).

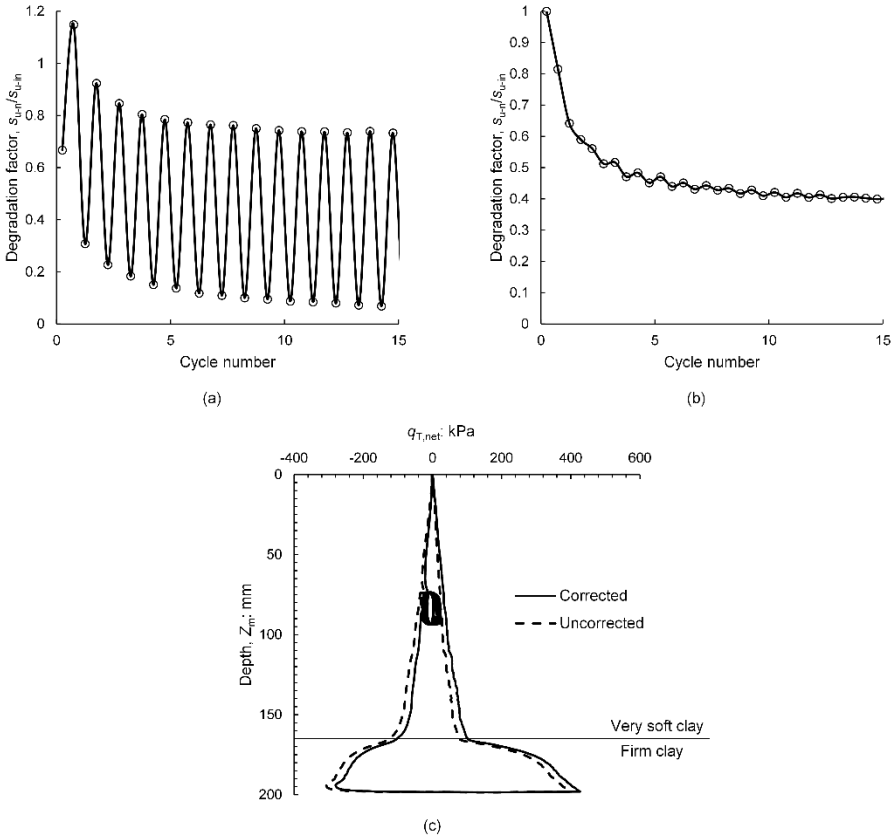

Figure 6.1. T-bar cyclic correction applied to M1TB1: (a) strength degradation without correction; (b) strength degradation corrected; (c) net T-bar resistance

The profiles of the undrained shear strength for both models estimated from T-bar tests are shown in Figure 6.2. Also shown in Figure 6.2 is the theoretical undrained shear strength profile proposed by Ladd et al. (1977), which may be written as:

$$\frac{s_u}{\sigma'_{v0}} = \left(\frac{s_u}{\sigma'_{v0}}\right)_{nc} \mathrm{OCR}^n \tag{6.2}$$

Where $(s_u/\sigma'_{v0})_{nc}$ is the normally consolidated undrained shear strength ratio, OCR is the overconsolidation ratio, σ'_{v0} is the vertical effective stress, and n is the plastic volumetric strain ratio. The best agreement between the measured and theoretical s_u profiles was obtained using $(s_u/\sigma'_{v0})_{nc}$ = 0.15 (assuming an average effective unit weight, γ' = 6.5 kN/m^3 established from sample cores taken after the tests, described later), which is typical for UWA centrifuge kaolin samples (Gaudin et al. 2006; Morton et al. 2014; O'Beirne et al. 2015), and n = 0.7, which is at the lower end of the typical range, n = 0.7 – 0.9 (Mitchell and Soga 2005). For an OCR of 1.5, Equation 6.2 gives s_u/σ'_{v0} = 0.20.

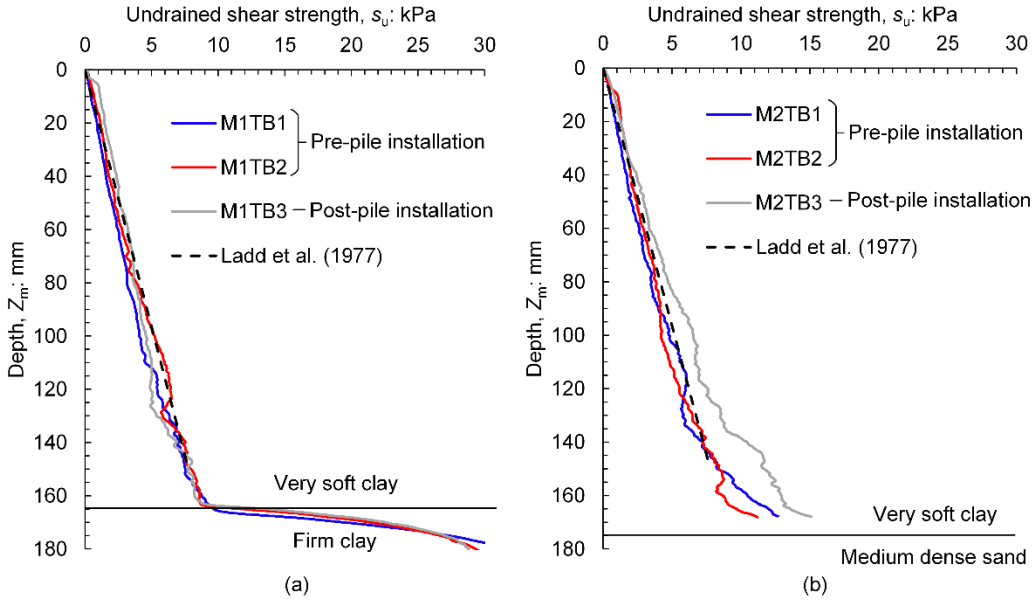

Figure 6.2. Undrained shear strength profiles: (a) Model 1; (b) Model 2.

Figure 6.2 shows that the sample strength before pile installation was consistent between the two models, with all T-bar tests undertaken prior to pile installation matching the profile predicted using Equation 6.2 closely. T-bar tests M1TB3 and M2TB3 were undertaken a minimum of 12 hours (model scale) after pile installation to allow for dissipation of excess pore pressures generated during pile installation. T-bar M1TB3 in Figure 6.2a, which was performed 37 mm from the edge of the closest pile, shows a similar undrained shear strength profile to the tests undertaken prior to the installation of the piles, suggesting no strength increase in the very soft clay layer at this location resulted from the installation of full-displacement piles. T-bar test M2TB3 in Figure 6.2b, performed 29 mm from the edge of the closest pile, shows an increase in undrained shear strength of about 30% relative to the T-bar tests conducted before pile installation, indicating that the soil is stronger adjacent to the pile due to radial consolidation following pile installation.

6.1.2 Coefficient of consolidation

A piezocone test with a dissipation phase was performed in Model 1 to estimate the horizontal coefficient of consolidation. The penetration of the piezocone was stopped at a depth of 77 mm below the surface of the very soft clay layer and the pore pressure, measured at the shoulder of the cone in the u_2 position, was monitored. The results are plotted using the non-dimensional time factor defined as:

$$T^* = \frac{c_h t}{r^2 \sqrt{I_r}} \tag{6.3}$$

Where t is the time since the start of the dissipation test, r is the radius of the piezocone and I_r is the rigidity index. The rigidity index was estimated using the solution proposed by Kulhawy and Mayne (1990):

$$I_r = \left(\frac{2}{3}\right) M \frac{1+e_0}{C_c} \ln(10) \frac{\left[1+\ln(\mathrm{OCR})\exp^{\Lambda}\right]}{\Lambda(1-\Lambda)\mathrm{OCR}^{\Lambda}} \tag{6.4}$$

Where Λ is a dimensionless parameter that relates swelling with compression. Using Equation 6.4 and the parameters provided in Table 5.3 for kaolin clay, the rigidity index was calculated as I_r = 67. Solutions proposed by Teh and Houlsby (1991) were used to estimate c_h by obtaining the best match between the test results and the solution provided in Table 6.1.

Table 6.1. Time factor at cone shoulder from Teh and Houlsby (1991)

Degree of consolidation	Modified time factor at cone shoulder, T^*
20%	0.038
30%	0.078
40%	0.142
50%	0.245
60%	0.439
70%	0.804
80%	1.6

The analysis undertaken by Teh and Houlsby (1991) is based on an ideal test where a monotonic decrease in pore pressure is observed from the moment the piezocone penetration stops, and the dissipation test commences. However, the redistribution of pore pressures during the initial stages of the dissipation test often leads to an initial increase in pore pressure before dissipation is observed. To account for this, the initial pore pressure (u_i) was estimated using the back extrapolation on a square-root time plot described by Sully et al. (1999).

Figure 6.3 plots the normalised excess water pressure ($U = \Delta u_e/\Delta u_{ei}$) against T^* for M1CPT1. The best match between results from the dissipation test and the Teh and Houlsby (1991) solution was found

using c_h = 4.4 m^2/year. Randolph and Hope (2004) performed piezocone tests on UWA kaolin and showed that c_h obtained from a piezocone was typically 2.2 times larger than c_v measured in a Rowe cell. Using this relationship, the c_v may be estimated as 2.0 m^2/year based on the results of piezocone testing.

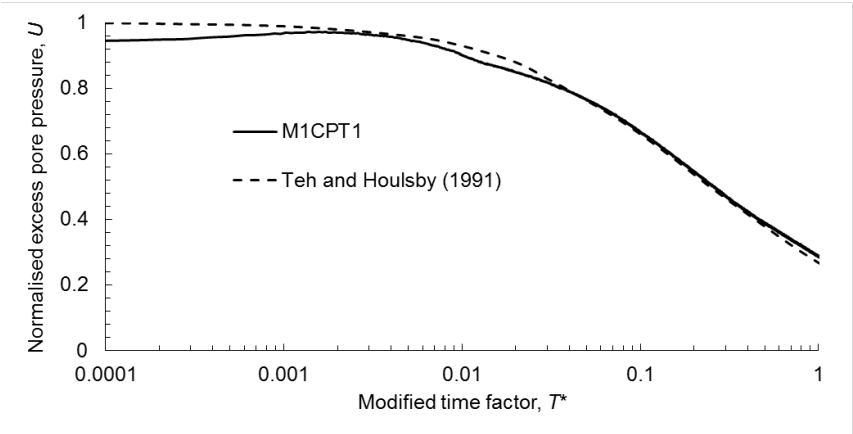

Figure 6.3: M1CPT1 non-dimensional pore pressure-time response.

House et al. (2001) performed Rowe cell tests on normally consolidated UWA kaolin clay, to which Cocjin et al. (2014) fitted the following expression:

$$c_v = (0.3 + 0.16\sigma'_v)^{0.47} \quad (6.5)$$

Based on σ'_v = 20 kPa, which is approximately the effective vertical stress at the depth of the dissipation test, a value of c_v = 1.8 m^2/year is estimated using Equation 6.5. Given the close agreement between the estimated value of c_v from both piezocone tests on the clay with an OCR = 1.5 and Rowe cell tests on normally consolidated clay, the effect of the clay being slightly overconsolidated does not appear to be significant on the rate of consolidation. As such, the value of c_v = 1.8 m^2/year is assigned to the slightly overconsolidated very soft clay for future analysis as it is based on laboratory testing rather than an empirical relationship between c_h and c_v.

6.1.3 Pile installation resistance

Pile penetration resistance was measured during each pile installation using a load cell located between the actuator and the pile head. The installation resistances of the instrumented piles and the average resistances from the non-instrumented piles for both models are shown in Figure 6.4. Figure 6.4 excludes the penetration resistance for PLC4 in Model 2 as the load cell failed during this installation. The penetration resistances confirmed that the piles achieved consistent embedment into the founding layer. Figure 3 also shows the increased resistance experienced in Model 2 piles compared to Model 1 due to the bottom layer conditions.

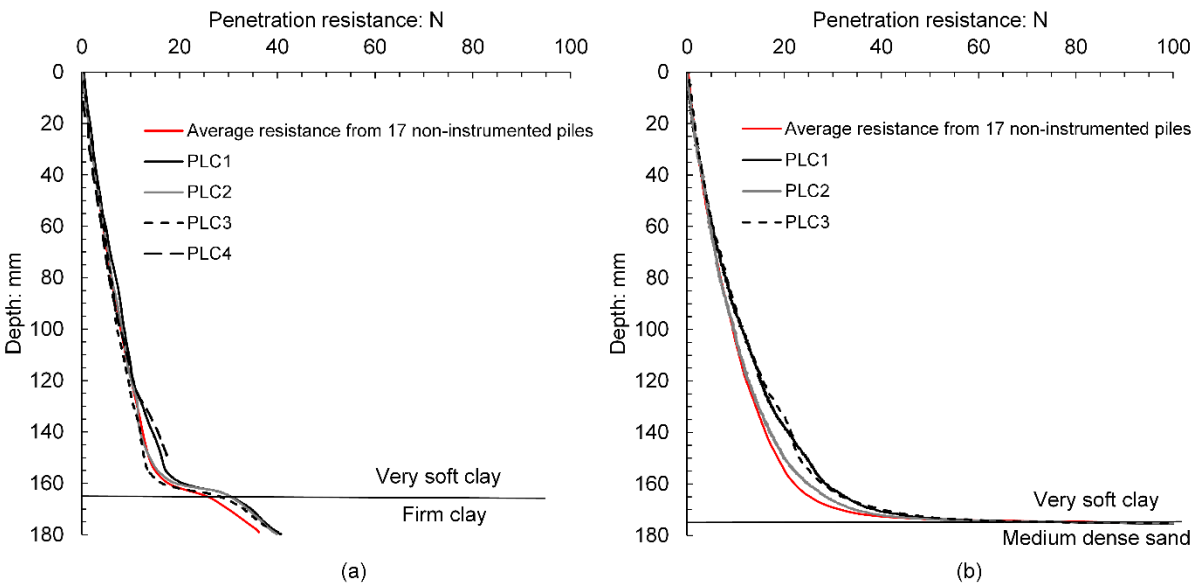

Figure 6.4: Pile installation resistance profiles: (a) Model 1; (b) Model 2.

6.2 Results

The results from the embankment consolidation stage of the test and the post-test examination are presented in the following section.

6.2.1 Embankment and pile head settlements

Embankment and pile head settlements, S, are normalised by the embankment height, h_e, and are plotted in Figure 6.5 against the time factor, T, given by:

$$T = \frac{c_v t}{H_{dr}^2} \tag{6.6}$$

Where t is the dissipation time and H_{dr} is the maximum drainage path length (before consolidation). The very soft clay layer is considered to govern the rate of consolidation in both models due to its thickness and compressibility relative to other subsoil units, and as such, c_v = 1.8 m^2/year was adopted in Equation 6.6. Dissipation time, t, was taken from the moment the centrifuge began spinning, rather than the moment when the centrifuge reached 40g as settlement of the Model 2 occurred as the centrifuge was ramping up to the target acceleration. During the ramp up, dissipation time was corrected by a factor equal to n_t^2/n^2, where n_t is the centrifugal acceleration factor at time t and n is the target acceleration factor of the test (n = 40), both of which are multiples of earth's gravity (ng).

As noted previously, the geosynthetic reinforcement was placed directly above the clay surface in Model 1. Since the geosynthetic reinforcement was a geomembrane, free drainage at the top of the clay in Model 1 was prevented, resulting in one-way drainage towards the base of the strongbox (H_{dr} = 205

mm). These drainage conditions resulted in a longer consolidation period than was required for Model 2, where a sand drainage layer was placed between the kaolin surface and the geosynthetic reinforcement, resulting in two-way drainage (H_{dr} = 88 mm). The placement of sand between the pile heads and the geomembrane is equivalent to a layer of protective granular material between pile heads and geosynthetic reinforcement often used in the field.

The time history of Model 1 and 2 settlements are presented in Figure 6.5. As noted previously in Chapter 5, Model 1 was ramped down and back up to 40*g* due to some counterbalance issues during the test. In addition to this, there were some temperature fluctuations within the centrifuge that affected measurements that were corrected during this ramp down/up. This period is represented by a dashed line in Figure 6.5, 6.6, 6.10 and 6.12.

Figure 6.5a shows that surface settlements above the defective and non-defective piles in Model 1 were identical. This observation indicates that the defective pile did not cause any differential settlement to develop at the embankment surface. This is also reflected in the Model 1 pile head settlements shown in Figure 6.5b, where the defective and non-defective piles underwent essentially identical settlement.

The time history of the embankment surface settlements for Model 2 is presented in Figure 6.5c. In Zone 1, where no defective piles were installed, the total normalised settlement of the Model 2 embankment surface was S/h_e = 0.07, almost half of that in Model 1 (S/he = 0.13), which is attributed to the much stiffer founding layer for the end-bearing piles in Model 2. However, differential settlement occurred at the Model 2 embankment surface as a result of the defective pile. This is evidenced by the difference in settlement measured by the LDT above the defective pile and the LDT above the non-defective pile. This differential settlement was confirmed by a linear topographic scan down the centreline of the strongbox (post-test), which also indicated that the width of the depression was 70 – 90 mm in model scale. Measurements of pile head settlement (presented in Figure 6.5d) show that the differential settlement observed at the embankment surface was a result of the defective pile undergoing additional settlement relative to that of the non-defective piles.

Given that uniform settlement was experienced at the embankment surfaces in areas where no defective pile was present for both models tested, it is evident that the embankment height was greater than the critical height, i.e. $h_e > h_{cr}$. However, as shown in Chapter 4, a defective pile increased the height above the pile heads that is required for a plane of equal settlement to develop, i.e. $h_{cr,def} > h_{cr}$. The localised depression observed at the Model 2 embankment surface is due to this locally increased critical height above the defective pile, and it can be concluded that for the this model $h_{cr} < h_e < h_{cr,def}$.

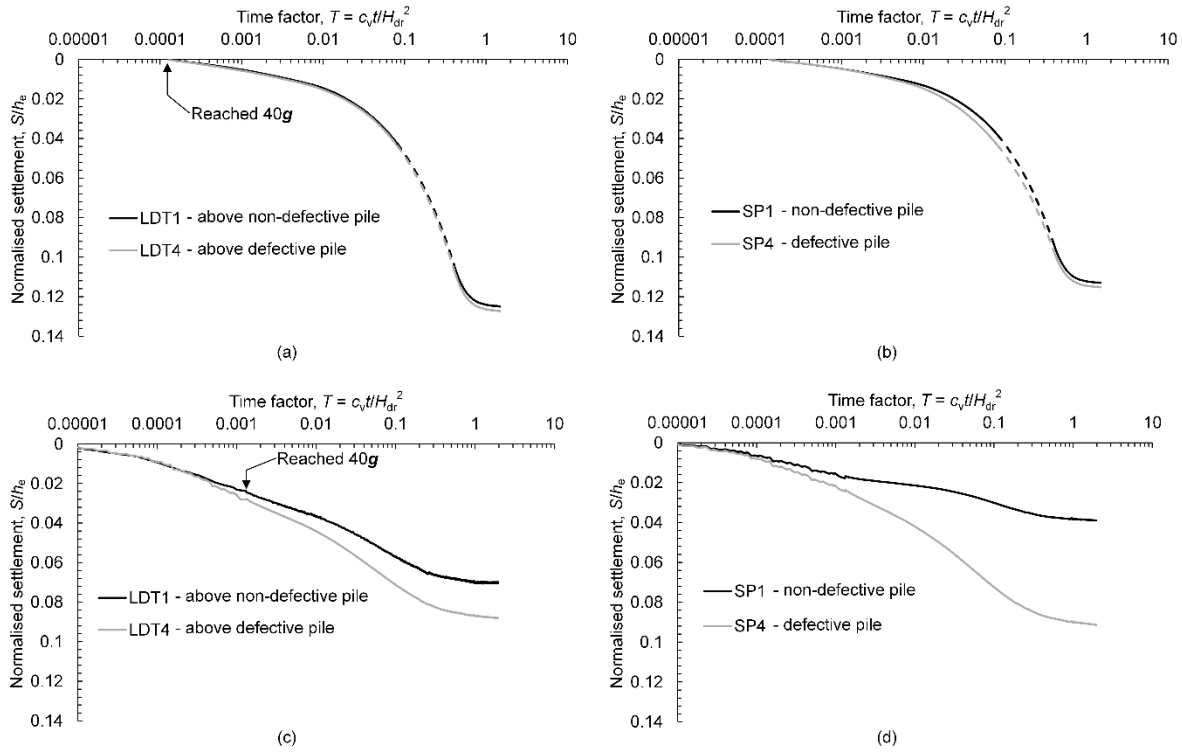

Figure 6.5: Normalised settlements plotted against time factor during consolidation phase for (a) Model 1 surface; (b) Model 1 piles; (c) Model 2 surface; and (d) Model 2 piles. Note, dashed line in Model 1 represents a period where data was not constantly (also shown in Figure 6.6, 6.10 and 6.12)

6.2.2 Dissipation of excess pore pressures

The flattening of the settlement-time curves in Figure 6.5 indicates the end of consolidation due to the stress increase imparted by the embankment. This is confirmed by Figure 6.6, which plots the time history of excess pore pressure, Δu_e, measured at the mid-height of a pile shaft installed near the middle of the strongbox normalised by the increase in total stress due to the placement of the embankment fill, γh_e. It is evident that that pore pressures follow a similar trend to the settlements, with excess pore pressures almost constant and dissipated by $T \approx 1$, consistent with when the settlements in Figure 6.5 become essentially constant.

Model 2 was slowly ramped up to an acceleration of 40*g* (3 mins in model time), which in combination with the two-way drainage in this model, meant that pore pressure dissipation began as soon as the target acceleration was reached. Model 1 was quickly ramped up to 40*g* (90 seconds model time), which along with one-way drainage resulted in a Mandel-Cryer type (Mandel 1953; Cryer 1963) increase in pore pressure after the target acceleration was reached. This effect is commonly observed in consolidation problems, e.g. Yin and Zhu (1999), Gourvenec and Randolph (2010) and Bienen et al. (2015) and is not considered to affect the rate of excess pore pressure dissipation.

Approximately 90% of excess pore pressure dissipated by $T = 0.84$ (measured at a depth of $z = 0.44H_{dr}$) in Model 1, which agrees well with the theoretical $T = 0.848$ for 90% (average one-dimensional) consolidation. In contrast, excess pore pressures dissipated much more rapidly in Model 2, with 90% dissipation complete at $T = 0.15$. The seemingly faster consolidation in Model 2 is considered to be due to a reduction in the stress acting on the soft clay, brought about by the load transfer (resulting from both arching and membrane actions) towards the pile heads. This load transfer was more significant in Model 2 compared to Model 1, as also demonstrated through the pile load measurements presented later. While two-way drainage also increases the rate of consolidation, the drainage path length is accounted for in the non-dimensional time factor (Equation 6.6).

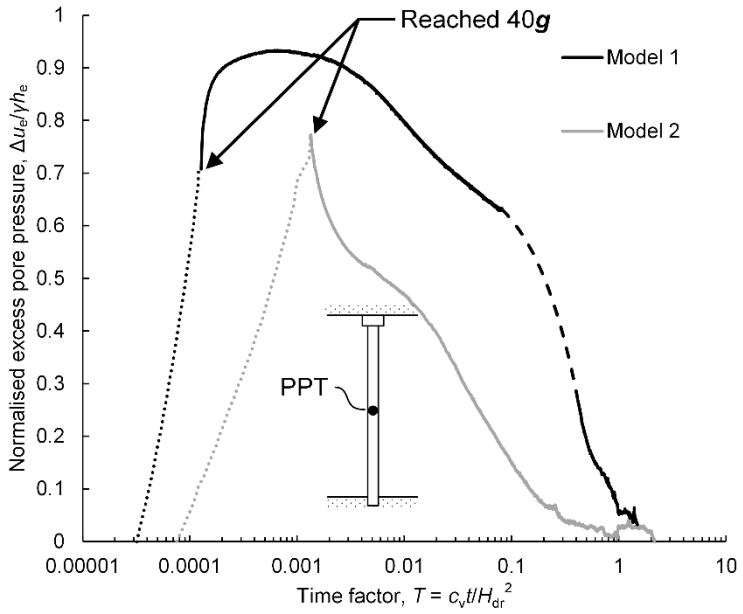

Figure 6.6: Normalised excess pore pressure plotted against time factor for both models, where the initial ramp up to 40*g* is represented by dotted line.

6.2.3 Subsoil settlement

The deflection of the SP cable between pile heads provides an indication of the differential settlement between pile heads and subsoil (subsoil settlement). Using the method outlined in Section 4.2.1, an equivalent axisymmetric clear spacing of $b' = 64$ mm is calculated for the pile geometry adopted in the centrifuge model testing. This clear spacing is then used to normalise subsoil settlements and to plot the GRC in later sections.

As noted in Chapter 5, the elongation of the SP cable is proportional to the square of the subsoil settlement, such that small subsoil settlement may result in strains that are too small to be measured. This was the case for Model 1, where the subsoil did not undergo sufficient settlement to induce measurable SP cable elongation. The subsoil underwent more settlement (and hence, more SP cable

elongation) in Model 2 due to the relatively stiffer load-settlement response of the piles, which allowed the settlements to be estimated. The normalised subsoil settlement, $\delta_{s,max}/b'$, between non-defective piles in Model 2 is plotted against T in Figure 6.7. It is noted that the deflected shape of the SP cable between the defective pile and adjacent non-defective piles in Model 2 cannot be approximated by a parabola, and settlements are therefore not presented.

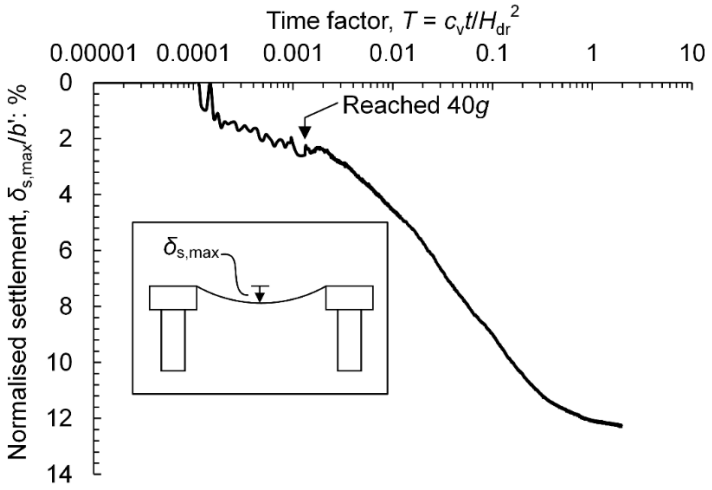

Figure 6.7: Model 2 normalised subsoil settlement plotted against time factor.

6.2.4 Final deformations

Figure 6.8 shows the surface profile of the soil directly beneath the geosynthetic, as quantified from the topographical scans conducted at 1g after the consolidation phase of the tests. It is noted that the two sharp depressions present between x = 100 and 200 mm in the Model 1 surface are the result of penetrometer tests performed after the consolidation phase of the test. The profile in Figure 6.8a confirms that the defective pile in Model 1 underwent uniform settlement with the surrounding non-defective piles. In contrast, the Model 2 profile shown in Figure 6.8b confirms that the defective pile underwent additional settlement relative to the non-defective piles. It is also shown in Figure 6.8b that all non-defective piles in Model 2, independent of their proximity to the defective pile, underwent uniform settlement. This indicates that the presence of a defective pile did not cause adjacent non-defective piles to undergo additional settlement.

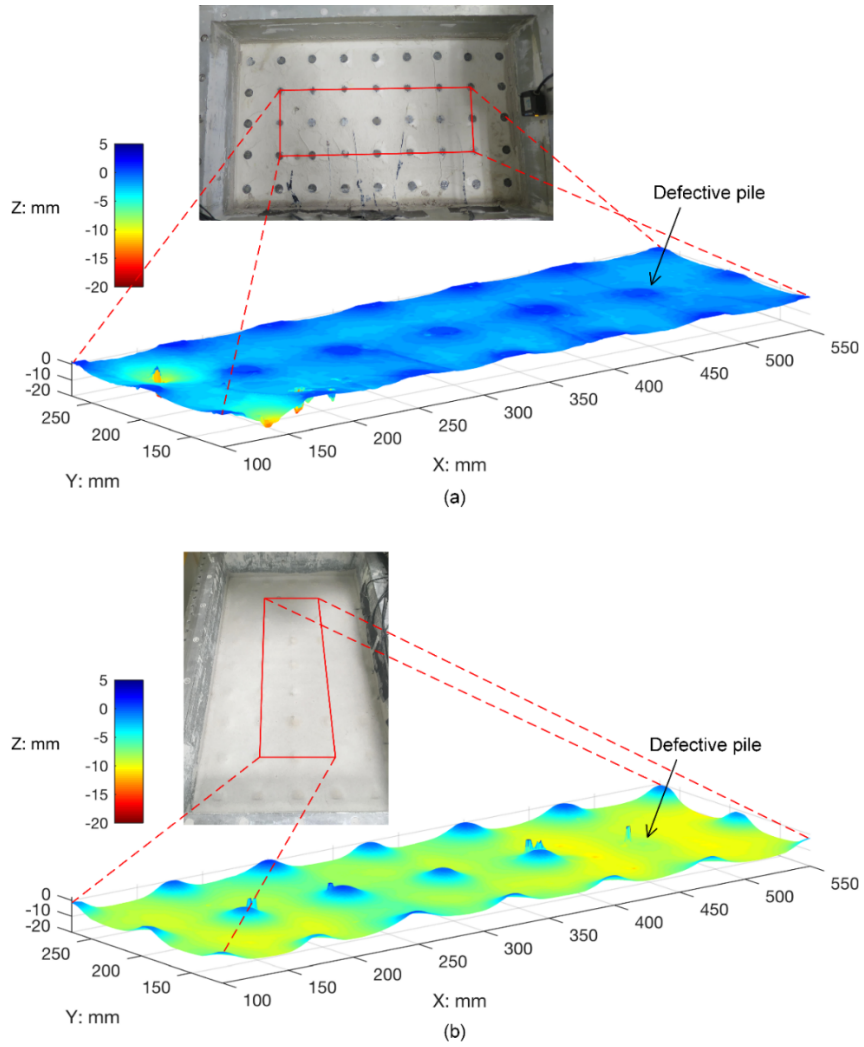

Figure 6.8: Surface profile of the soil layer underlying geosynthetic reinforcement for (a) Model 1 clay; and (b) Model 2 sand. Note, x and y dimensions are relative the bottom left corner of the strongbox in plan view

The final deformed profile in model scale, taken along the centreline of the models through the defective pile, based on LDTs, SPs and topographical scans is shown in Figure 6.9 and the corresponding displacements are presented in Table 6.2. These deformation profiles highlight the uniform settlement in Model 1 and the differential settlement in Model 2 between defective and non-defective piles. The final deformed profile also shows that the geosynthetic reinforcement underwent significantly less deflection in Model 1 than in Model 2, which is a result of the different pile founding conditions between the two models.

It is shown in the final deformed profile of Model 2 (Figure 6.9b) that the localised depression at the embankment surface above the defective pile was approximately within the confines of a single pile unit cell. Based on all deformation measurements, the defective pile did not cause additional settlements outside of the surrounding unit cell.

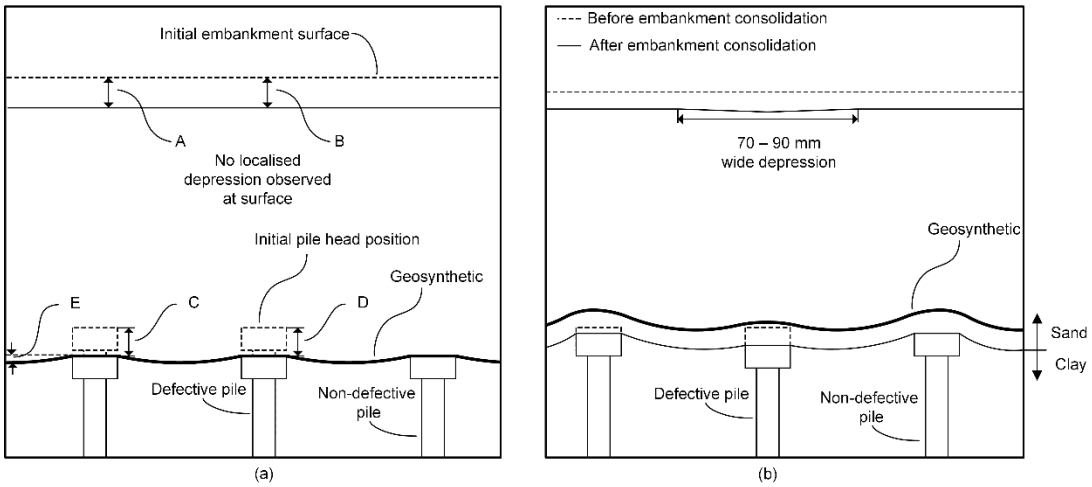

Figure 6.9: Final deformed profile in model scale taken along the centreline of the embankment through the Zone 2 instrumented area of (a) Model 1; (b) Model 2.

Table 6.2. Vertical displacements in mm in model scale at locations depicted in Fig. 10 at the end of consolidation

Location	**Model 1**	**Model 2**
A – Embankment surface away from defective pile	13.7	7.2
B – Embankment surface above defective pile	13.9	9.0
C – Non-defective pile head settlement	12.4	4.0
D – Defective pile head settlement	12.6	9.3
E – Geosynthetic deflection between non-defective piles	2.4	7.7

6.2.5 Pile loads

The load transfer in GRPEs is quantified by the efficacy (E_{A+B}), which is given as:

$$E_{A+B} = \frac{F}{\gamma h_e s^2} \tag{6.7}$$

Where F is the load carried by the pile. Efficacy may also be defined as the load transferred to the pile directly through arching without membrane actions (E_A). However, the direct measurement of soil stresses required to make this separation between arching and membrane actions is extremely challenging, particularly at small scales (Weiler and Kulhawy 1982; Dunnicliff 1988). This study has not attempted to make this separation and the measured loads from both actions are used to calculate efficacy.

Load cells were installed along pile shafts at two locations, at the top of the pile shafts 10 mm below the base of the pile heads and at the bottom of the pile shafts 10mm above the pile toes. The efficacy measured from pile load cells during the consolidation phase of both models are plotted against T in Figure 6.10. Even after Model 1 reached 40g pile loads developed slowly during the initial stages

(Figure 6.10a and b). This period of slow load development coincided with the initial rise in excess pore pressure measurements shown in Figure 6.6. In this initial period of rising/high excess pore pressures due to the Mandel-Cryer effect, subsoil settlement would have been somewhat prevented, resulting in minimal load transfer towards the pile heads from soil arching and membrane actions. Once excess pore pressures began to dissipate load transfer developed more rapidly, resulting in an increase in pile efficacy. It is evident from Figure 6.10a that the Model 1 non-defective piles attracted more load than the defective pile. However, while the defective pile carried less load than non-defective piles, it did not undergo any additional settlement. It is noted that measurement issues were encountered with the load cells at the base of the Model 1 pile shaft after a time factor of about 0.4, where load cells experienced significant drift. These load cells were replaced and the issue of drift rectified before testing Model 2.

The pile efficacy time history for Model 2 measured at the top and bottom of the pile shaft is shown in Figure 6.10c and d, respectively. Significantly more load transfer towards pile heads developed in the Model 2 test compared to Model 1. This is in line with the observation that the geosynthetic reinforcement and subsoil underwent more deflection in Model 2. As noted, the progressive development of soil arching and membrane actions is related to subsoil settlement, and it is evident that efficacy continues to increase over time as differential settlement develops between the pile heads and the subsoil (shown in Figure 6.7). Similar to Model 1, the Model 2 non-defective piles carried additional load relative to the defective pile; however, this difference is significantly greater in Model 2. It is also worth noting that the defective pile in both Model 1 and 2 experienced similar pile efficacy measured in the load cells at the top of the pile shafts by the end of the tests, in the range of approximately 17% to 22%.

The Model 2 non-defective pile heads carried an efficacy of 80% to 95% by the end of the consolidation stage. The remaining load not transferred to the piles through arching and membrane actions acted on the surface of the subsoil. Given that the pile efficacy at the pile heads level was less than 100% in both model tests, it is reasonable to assume that contact was maintained between the geosynthetic reinforcement and the underlying soil, as some load must have been carried by the subsoil.

In both model tests, there is no evidence to suggest that non-defective piles directly adjacent to a defective pile were affected by the defective pile exhibiting a relatively softer load-settlement response. Loads measured by all non-defective piles were consistent, with almost no difference between loads measured in piles directly adjacent (PLC3) or further away (PLC1 and PLC2) to a defective pile. CUR226 (2010) claims that if a pile fails and the embankment height is sufficient then arching will re-establish itself between the surrounding piles. While the Model 2 embankment height may not have been sufficient for a plane of equal settlement to develop above the defective pile, the observation that all non-defective piles carried the same load regardless of their proximity to the defective pile

contradicts this assumption made by CUR226. If soil arching was to "re-establish" between the piles surrounding a failed or defective pile then it would be expected that these piles carry a significant additional load to other non-defective piles, which was not observed.

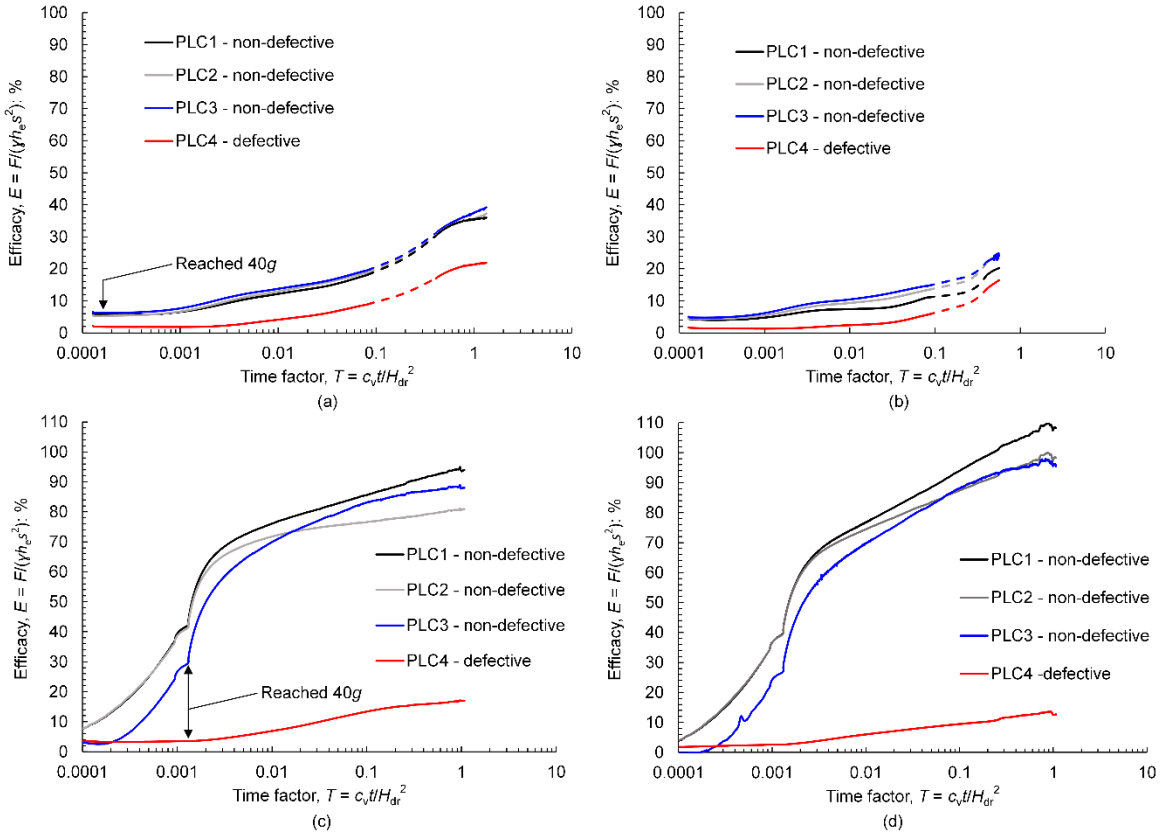

Figure 6.10: Pile load efficacy plotted against time factor: Model 1 loads measured at (a) top of pile shaft; (b) base of pile shaft; and Model 2 loads measured at (c) top of pile shaft; (d) base of pile shaft.

It is shown that loads measured near the bottom of the pile shafts in Model 1 were less than the loads measured at the top, whereas the Model 2 piles exhibited the opposite behaviour (except for the defective pile). This observation is due to the negative friction that developed above the neutral axis, the zone where soil settlement is greater than pile settlement (Poulos 2008). This is depicted in Figure 6.11, where it is shown that the neutral axis in Model 1 (Figure 6.11a) for both defective and non-defective piles was located at a relative shallow depth due to the small amount of subsoil settlement. In Model 2 (Figure 6.11b), the neutral axis of the defective pile was still quite shallow, which explains why the loads measured near its toe were consistent with loads at the top of the pile shaft. The neutral axis for non-defective piles in Model 2 was relatively deep as a result of significant subsoil settlement developing between pile heads, which induced large negative friction along the pile shaft. This negative friction resulted in loads near the bottom of the non-defective pile shafts being greater than loads measured at the top of the shafts.

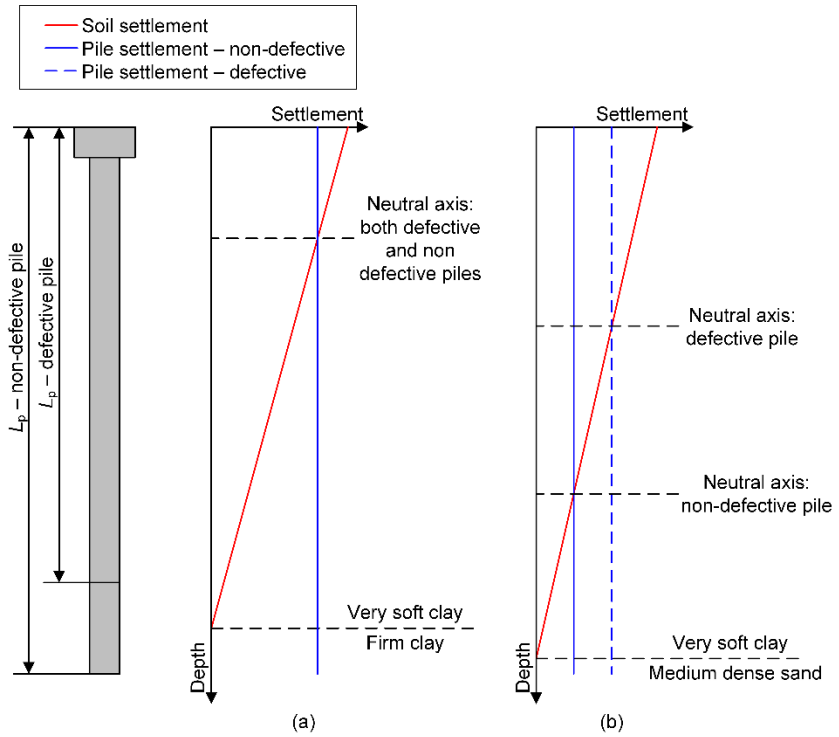

Figure 6.11: Settlement profile (indicative) along length of piles in (a) Model 1; (b) Model 2.

The load-settlement response of the piles for both models is shown in Figure 6.12 in model scale. Given that pile loads developed as the centrifuge was spun up to 40*g* and pore pressures stabilised, the initial stages of the pile load-settlement curves are not linear. The stiffness range is shown in Figure 6.12 for the stage of the test when the load-settlement curves became linear to highlight the difference in pile axial stiffnesses. The defective pile in Model 1 (Figure 6.12a) exhibited a softer load-settlement response than the non-defective piles, resulting in differential stiffness between defective and non-defective piles. The difference in stiffness between defective and non-defective piles is significantly greater for Model 2, as shown in Figure 6.12b. This difference in pile axial stiffness between defective and non-defective piles in Model 2 resulted in differential settlements at the pile head level, which propagated through the embankment fill and resulted in the localised depression forming at the embankment surface.

The load-settlement behaviour of the defective piles in both models is similar, and as noted previously, so is the efficacy they carry by the end of each test. This is due to the toes of the defective piles terminating at the same depth within clay, which was shown to have very similar strength profiles between the two models (see Figure 6.2). It is noted that the slightly higher axial stiffness of the defective pile in Model 2 is likely due to the influence of the underlying sand layer as well as the influence of the surrounding piles being stiffer and undergoing less settlement in Model 2.

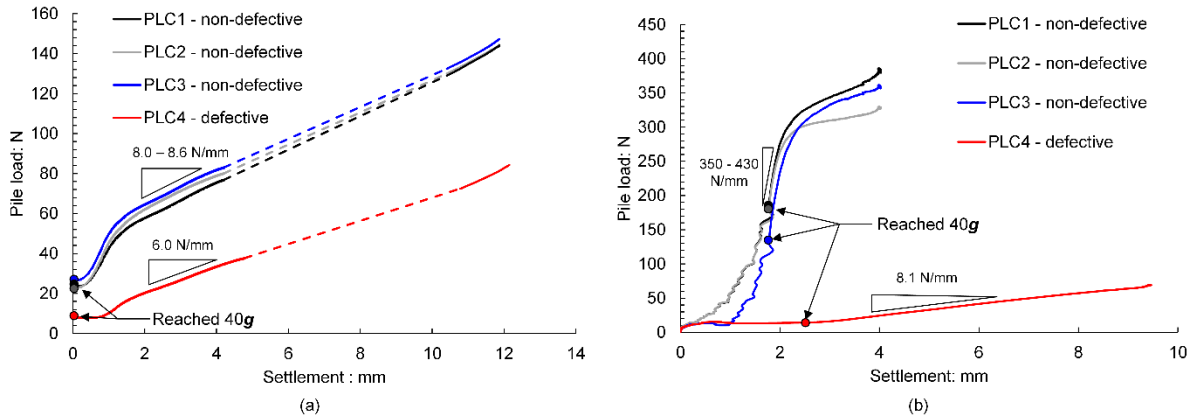

Figure 6.12: Pile load settlement response in model scale of (a) Model 1; (b) Model 2.

6.2.6 Post-test investigation

Changes in embankment sand density

Penetrometer testing was undertaken within the Model 2 embankment once the consolidation stage was complete to identify changes in sand density that arose due to shearing within the zone of soil arching. It is well established that CPT tip resistance is influenced by materials ahead of the cone to a distance that is typically in the order of several cone diameters (Gui and Bolton 1998). To reduce this depth of influence, a small 1 mm diameter steel rod with a flat base (Figure 6.13) was used rather than the more conventional centrifuge scale penetrometers that typically have diameters in the range of 7 to 10 mm.

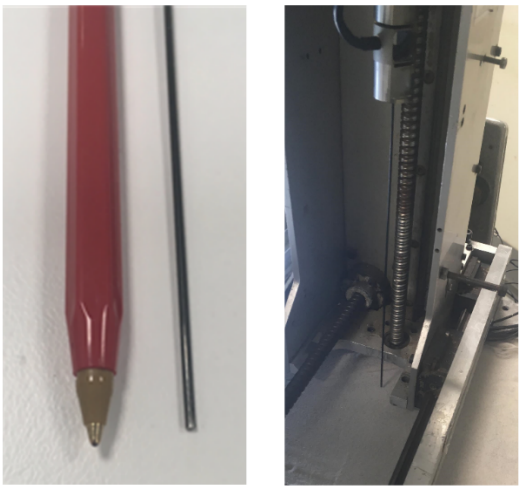

Figure 6.13: Rod penetrometer: (a) 1 mm diameter steel rod (shown adjacent to pen for scale) and (b) rod penetrometer attached via a load cell to the actuator

The rod penetrometer was jacked into the embankment sand at a penetration rate of 1 mm/s at 40*g*, with the penetration resistance measured by a load cell located at the top of the rod. Although there are

evidently limitations with this technique, including potential bowing of the slender rod, the inability to separate shaft and tip resistance and potential particle size effects, the rod penetration resistance is used here solely to qualitatively assess changes in density and zones of soil arching, rather than to provide a quantitative analysis of soil density or strength.

The locations of the rod penetrometer tests within each zone are shown in Figure 6.14 based on their proximity to the central pile in each instrumented zone. Location 1 is directly above the central pile, i.e. above the central non-defective pile in Zone 1 and above the central defective pile in Zone 2. Locations 2 to 4 increase in distance from the central pile as shown in Figure 6.14. These locations describe the penetrometer test position relative to the central pile of each zone. In Zone 1, given that all piles including the central pile are non-defective, penetrometer tests performed above any of the pile heads were considered representative of Location 1. Further, in Zone 1 any penetrometer test performed at the midpoint between two directly adjacent piles was representative of Location 2 or 4 and any penetrometer test performed at the midpoint between two diagonally adjacent piles was representative of Location 3. This allowed multiple penetrometer tests to be used for each Location in Zone 1, providing confidence in the general trends of penetrometer resistance with depth.

Figure 6.14 shows that, with the exception of Location 1 in Zone 2 (directly above the defective pile), the resistance profiles are broadly similar. Resistance increases linearly with penetration depth over the upper 35 mm, beyond which the resistance decreases slightly. A marked increase in resistance occurs at about 75 mm in Location 1 as the penetrometer senses the pile head, and at about 95 mm in Locations 2 – 4 where the penetrometer reaches the geosynthetic reinforcement.

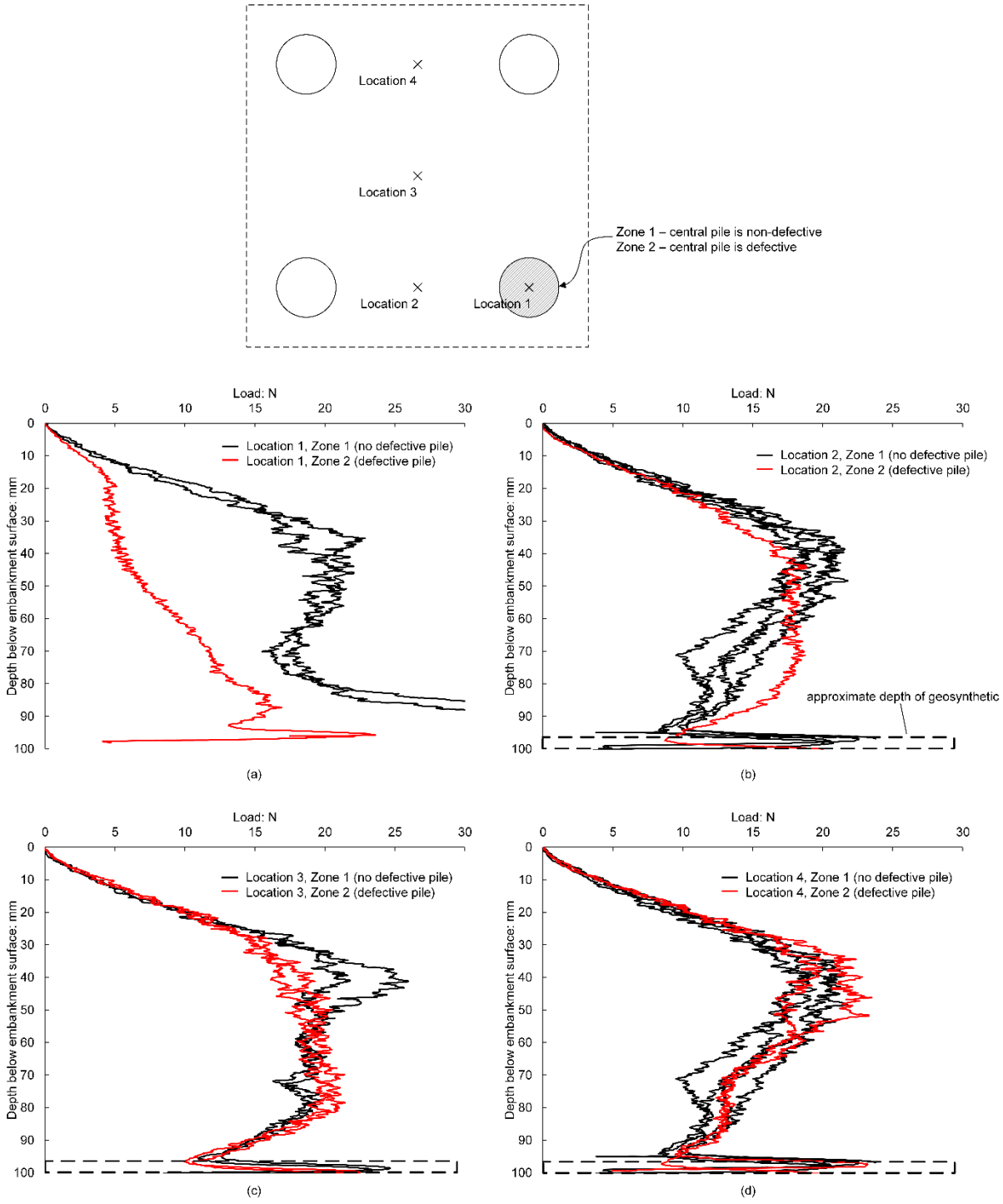

Figure 6.14: Rod penetrometers undertaken in Model 2 at (a) Location 1; (b) Location 2; (c) Location 3; (d) Location 4

The rod penetrometer response in Zone 1 may be explained by the critical height. Below the critical height, the granular soil in the embankment or LTP is undergoing shearing due to soil arching. X-ray computed tomography scans of small-scale piled embankments show that the density of soil within this zone of arching is lower than the soil above the critical height (Eskişar et al. 2012), which was also

confirmed from the CT imaging described in Chapter 3 and 4. This reduction in density may be attributed to the soil undergoing dilation as well as the volume loss from the subsoil settlement. The density of the upper approximately 35 mm of the embankment in Zone 1, where a linear increase in penetration with depth was observed, is likely to be equal to the initial sand density. Below this depth, where the soil experienced a slight reduction in penetration resistance with depth, the sand density is lower than its initial state and is representative of the zone of soil arching below the critical height.

It is noted that the penetrometer resistance is also likely influenced by the change from initial overburden stress conditions below the critical height due to soil arching. Between piles, the vertical stress below the critical height becomes less than the overburden (Potts and Zdravkovic 2010), while above the piles the vertical stress becomes greater than the overburden as soil arching develops. Given that penetrometer tests performed both above and amid piles exhibited a similar reduction in resistance below a certain height, it is considered the penetrometer resistance is predominantly influenced by the change in density due to soil arching, more so than by these changes in stress.

The rod penetrometer tests undertaken at Location 1 in Zone 2 (Figure 6.14a), directly above the defective pile, shows a linear increase in penetration resistance with depth near the embankment surface. However, the depth of this linear portion of the penetration resistance profile is significantly less than in the Zone 1 penetrometer test undertaken at the same location. This indicates that the height of disturbed soil above the pile heads, resulting from shearing and volume loss, is greater in the region directly above the defective pile compared to the non-defective pile.

The penetrometer tests undertaken at locations 2 and 3 in Zone 2 (Figure 6.14b and c) all show a linear increase in penetration resistance with depth to at least 30 mm below the embankment surface. However, the resistance profiles in these tests differ from those in Zone 1 insofar that there is no peak resistance at about 35 mm below the embankment surface, such that the resistance beyond 30 mm either increases gradually or remains approximately constant until the penetrometer reaches the geosynthetic reinforcement. This suggests that the sand in Locations 2 and 3 around the defective pile was affected by the additional settlement of the pile.

The resistance profile from the penetrometer tests at Location 4 in Zone 2 (Figure 6.14d) are similar to those from the tests in Zone 1. This similarity indicates that the sand in Location 4 was not affected by the additional settlement of the defective pile, which is to be expected given the proximity of Location 4 from the defective pile, and that location 4 is directly between two non-defective piles.

Based on (i) the characteristics of the rod penetrometer resistance profiles, (ii) the size of the localised depression and (iii) pile load measurements that suggest no additional load was carried by non-defective piles adjacent to defective piles, it is considered that the area of influence around the defective pile in the Model 2 test was limited to a region of approximately one unit cell. Beyond the boundary of the

unit cell surrounding the defective pile, the embankment was unaffected by the presence of the defective pile.

Moisture content

After both models were tested and the embankment sand removed, core samples were collected from the subsoil. These samples were dissected into approximately 10 mm thick samples and then oven dried to profile the unit weight with depth. These results are presented in Figure 6.15. It is evident that the Model 1 unit weights are greater than the Model 2 unit weights in the upper region of the very soft clay layer. This is attributed to the Model 1 very soft clay undergoing more total settlement than Model 2, and as a result, the Model 1 very soft clay has a lower void ratio by the end of the test.

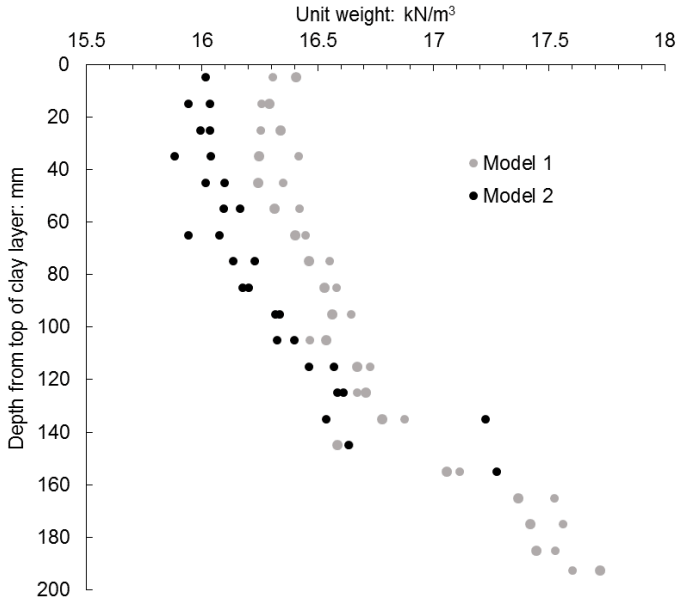

Figure 6.15: Unit weight of clay (after test) plotted against depth

Excavation

After the collection of the core samples, further examination of the Model 2 deformations and founding conditions was made by removing one side of the strongbox and excavating the clay and founding sand layers. A photo of Model 2 subsoil conditions and piles is shown in Figure 6.16a, with the sample excavated down the centreline of the strongbox. The differential settlement between non-defective piles and the defective pile (PLC4) is again evident from the post-test excavation photo.

As shown in Figure 6.16b, it was observed a thin layer (approximately 1 mm thick) of clay-sand mixture was present at the base of the pile toes in Model 2. Further, clay was present around the shafts of the piles near the pile toes. Thus, the piles were not in direct contact with clean sand. This is an important observation for numerical modelling as the presence of clay may result in a softer load-settlement

response than if piles were in direct contact with clean sand. The presence of clay beneath the pile toes is due to the piles being jacked into the sand. Given that the piles were jacked into the sand in-flight this phenomenon would likely be observed in the field (prototype) if jacked piles were installed.

The Model 2 deformed geosynthetic reinforcement profile was observed to be a smooth curved shape (Figure 6.16c), which was also shown in the surface profile in Figure 6.8b. However, upon excavation of the model, it was evident that the sand-clay interface at the base of the embankment did not exhibit the same deformation profile. Instead, sand underwent high distortion directly adjacent to the pile heads, which was not experienced at the level of the geosynthetic reinforcement. The 10 mm thick layer of sand between the pile heads and geosynthetic reinforcement, which is similar to the placement of a protective layer of fill above pile heads often utilised in the field, essentially smooths out the deformation profile. While this layer of sand may be necessary in some GRPEs to protect the geosynthetic reinforcement from damage, it may also reduce the mobilisation of strain in the reinforcement, thus reducing membrane actions. Therefore, if necessary to install a protective layer of fill between the pile heads and the reinforcement, this layer of fill should be as thin as possible. This finding is similar to the results from numerical analysis reported by Girout et al. (2018).

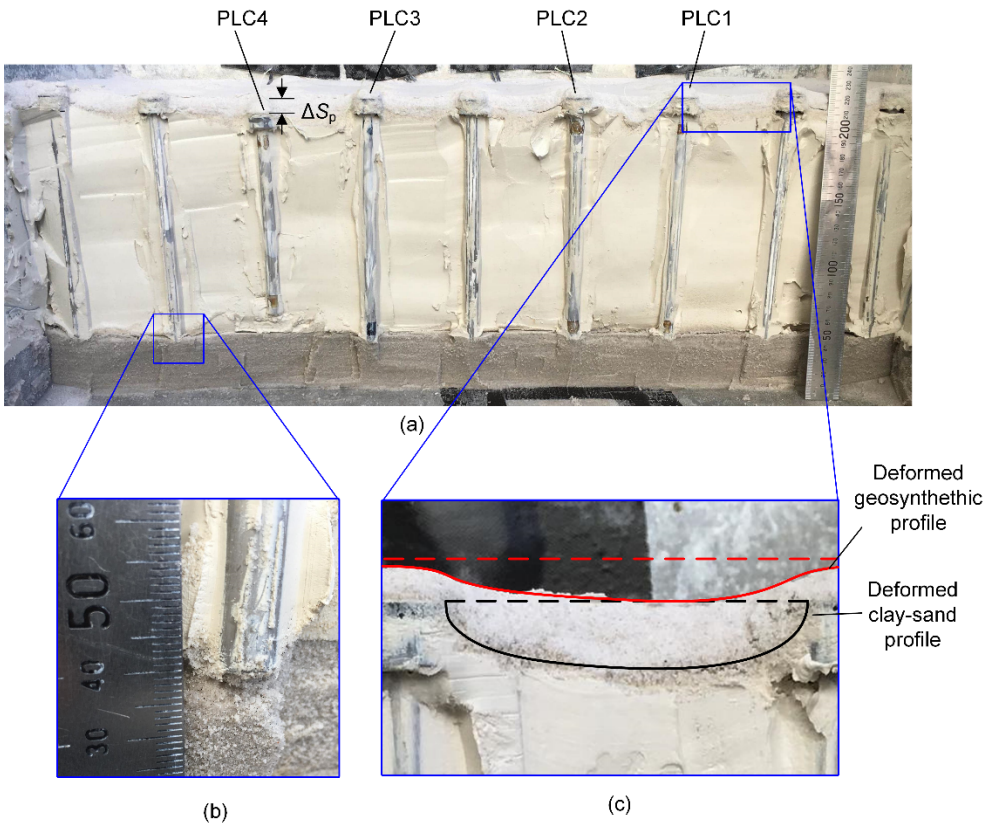

Figure 6.16: Post-test examination of Model 2 showing (a) cross-section through centreline of model; (b) pile founding conditions; (c) deformed profile between pile heads

6.3 Discussion

6.3.1 Progressive development of load transfer

It was shown in Figure 6.10 that pile loads progressively developed throughout the duration of both model tests. This observation further confirms that the development of soil arching and membrane actions within a piled embankment are time-dependent mechanisms, driven by the settlement of the subsoil, which cannot be described by the two-step design process adopted by many of the commonly used GRPE design methods (BS8006, EBGEO and CUR226). To explain the progressive development of load transfer towards piled heads, models need to be able to incorporate this subsoil settlement dependency.

Load Part A

As noted in Chapter 2 and Chapter 4, the applicability of the GRC to describe the load distribution due to soil arching within piled embankments has been reported by several authors (Ellis and Aslam 2009a, b; Zhuang et al. 2010; Zhuang et al. 2012; King et al. 2017a), where the compressible soil between piles may be thought of as the yielding trapdoor and the surrounding piles are thought of as the non-yielding support surrounding the trapdoor. To compare the results from centrifuge model testing to the GRC, the stress acting on the subsoil in the centrifuge model tests, σ'_s, is estimated by assuming loads not taken by the piles are evenly distributed on the soil surface within the pile unit cell. In doing so, σ'_s may be estimated as:

$$\sigma'_s = \frac{\gamma h_e s^2 - F}{A_{uc} - A_p} \tag{6.8}$$

Where A_{uc} is the area of the pile unit cell, A_p is the area of the pile head and F is the load measured near the top of the non-defective pile shafts (PLC1, PLC2 and PLC3).

The stress reduction ratio (SRR = σ'_s/σ'_{vo}) is plotted against the subsoil settlement in Figure 6.17 for Model 2. The prototype time and geosynthetic strain are also plotted for discrete points along PLC3 in Figure 6.17. It is evident that the arching stresses mobilised rapidly during the initial stages of the Model 2 test, although load transfer to the pile heads continued to increase over almost the entire duration of the test. Beyond 5 years (prototype time), only a small amount of additional subsoil settlement developed, with loads reaching a state of equilibrium between arching stresses, membrane actions and subsoil support prior to the end of the test after approximately 10 years.

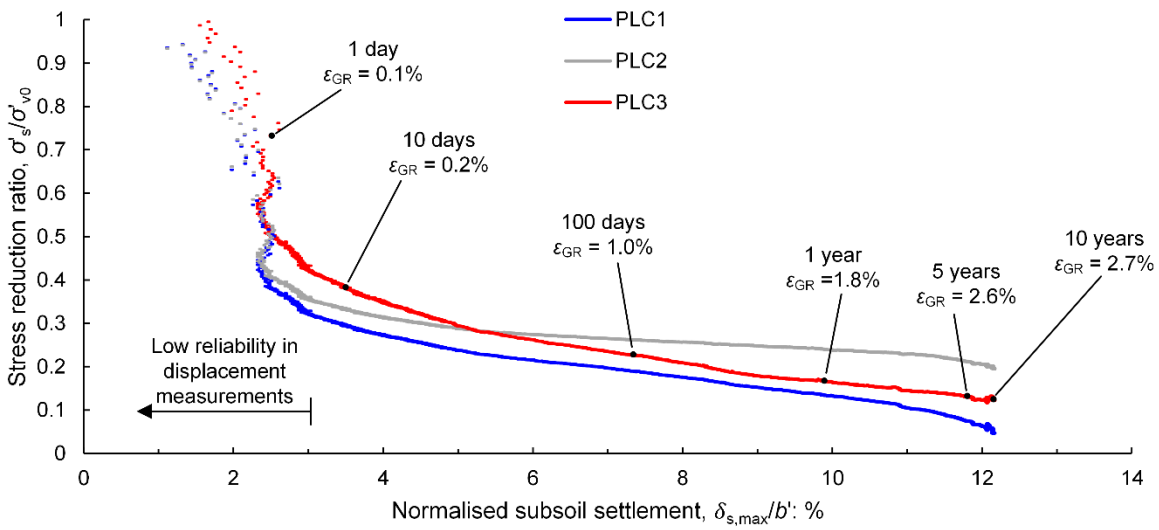

Figure 6.17: Stress reduction ratio (SRR) versus normalised subsoil settlement for Model 2 with prototype time and geosynthetic reinforcement strain

The initial arching phase in Figure 6.17 was not accurately captured as this corresponds to small geosynthetic reinforcement strains and the calculated displacements, therefore, incorporate significant error. The maximum arching, typically observed between 3% and 5% normalised displacement in the GRC framework proposed by Iglesia et al. (1999) is not evident in Figure 6.17. Instead, there is a continuous reduction in SRR with increasing subsoil settlement and no load recovery phase observed.

Given that the trapdoor tests studied by Iglesia et al. (1999) did not incorporate any geosynthetic reinforcement, the four phases of arching described by this GRC method (initial, maximum, load recovery and ultimate) are only applicable to the stresses transferred directly by arching (Load Part A) and do not include membrane actions (Load Part B). Centrifuge modelling performed by Ellis and Aslam (2009b), where it was observed characteristics of the GRC in the SRR-settlement response of a piled embankment, did not incorporate geosynthetic reinforcement within their model tests. Therefore, similar to Iglesia et al. (1999), these results only incorporated Load Part A. In piled embankments incorporating geosynthetic reinforcement, the transfer of loads towards the pile heads is due to both arching and membrane actions. As such, the progressive development of load transfer in a GRPE is expected to result in a lower SRR than would be predicted by the GRC alone, which does not consider Load Part B, particularly after sufficient subsoil settlement has occurred to develop large membrane actions. This is the case of the Model 2 embankment where a continuous reduction in the SRR is observed due to the mobilisation of membrane actions with large subsoil settlements. To include such actions in Figure 6.17, an equation that relates the stress reduction due to the geosynthetic reinforcement membrane action (σ'_{GR}) with the subsoil settlement ($\delta_{s,max}$) must be used.

Load Part B

Plane strain FE modelling by Zhuang et al. (2010) demonstrated a response similar to that of the centrifuge results presented in Figure 6.17. Zhuang et al. (2010) showed that the contribution of geosynthetic reinforcement as subsoil settles was reasonably well predicted by the plane strain equation proposed by Ellis and Aslam (2009b), which is written as:

$$\sigma'_{GR} = \frac{64J}{3(s-a)}\left(\frac{\delta_{s,PS}}{s-a}\right)^3 \tag{6.9}$$

Where σ'_{GR} is the average vertical effective stress carried by the geosynthetic reinforcement, $\delta_{s,PS}$ is the subsoil settlement between piles in a plane strain arrangement and a is the width of a square pile, which may be approximated to 0.886d if circular pile heads are used. Equation 6.9 is based on the assumption that the deflected shape of the geosynthetic between adjacent piles may be approximated by a parabola. By rearranging Equation 6.9, it may be written that:

$$\delta_{s,PS} = (s-a)\sqrt[3]{\frac{3\sigma'_{GR}(s-a)}{64J}} \tag{6.10}$$

However, the maximum deflection of the geosynthetic reinforcement will occur diagonally between piles when they are spaced on a square grid. Thus, in addition to $\delta_{s,PS}$, further sag will develop within the square section between the corners of the four pile heads within a unit cell. This additional settlement, within this central square section of geosynthetic, is approximated by a uniformly loaded square membrane pinned along its four edges as shown in Figure 6.18. The depth below the pile heads that the geosynthetic reinforcement is pinned is taken as the average displacement of the parabolic plane strain sag, equal to 2/3 the maximum height of this parabola, i.e. 2/3$\delta_{s,PS}$.

A solution to the maximum deflection at the centre of a square pinned membrane ($\delta_{s,SQ}$) with a stiffness J, is given by Leonard (1988) as:

$$\delta_{s,SQ} = 0.802\sqrt[3]{\frac{\sigma'_{GR}(s-a)^4}{16J}} \tag{6.11}$$

Thus, the maximum geosynthetic sag or subsoil settlement (assumed to be equal) in the centre of a square grid of piles may be calculated as:

$$\delta_{s,max} = {}^2/_3\,\delta_{s,PS} + \delta_{s,SQ} = 0.558\sqrt[3]{\frac{\sigma'_{GR}(s-a)^4}{J}} \tag{6.12}$$

Equation 6.12 may then be rearranged to find the stress carried by the geosynthetic reinforcement based on an amount of subsoil settlement that has occurred:

$$\sigma'_{\mathrm{GR}} = \frac{5.747 J \delta_{\mathrm{s,max}}{}^{3}}{(s-a)^4} \tag{6.13}$$

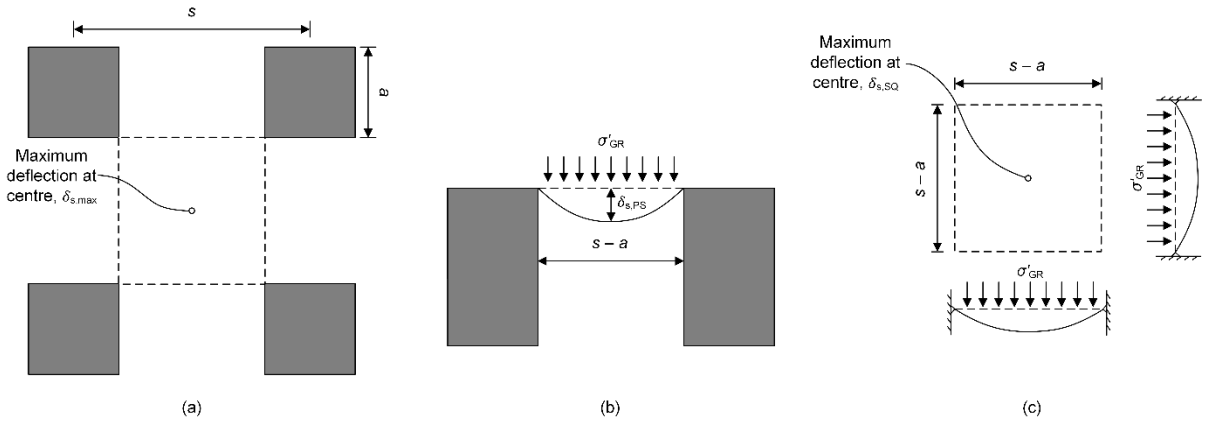

Figure 6.18: (a) Geosynthetic deflection between piles on a square grid; (b) deflection between adjacent piles; (c) deflection of a square uniformly loaded membrane

Load Part A and B

The vertical stress in the LTP soil directly above the geosynthetic reinforcement, σ'_{LTP}, may be estimated from a number of soil arching theories, which in combination with Equation 6.13, allows the resulting stress acting on the subsoil to be estimated as:

$$\sigma'_{\mathrm{s}} = \sigma'_{\mathrm{LTP}} - \sigma'_{\mathrm{GR}} \tag{6.14}$$

The stress in the LTP directly above the geosynthetic reinforcement is calculated using the GRC concept proposed by Iglesia et al. (1999), and the corresponding SRR is plotted without membrane actions (only Load Part A) in Figure 6.19 against normalised subsoil settlement. Further, the contribution of membrane action is calculated by Equation 6.13 and added to the stress reduction from arching estimated using the GRC (Load Part A + B), which is also plotted in Figure 6.19. It is shown that the combination of the GRC and membrane actions match the SRR measured from the Model 2 centrifuge test reasonably well, particularly after approximately 3% normalised subsoil settlement when subsoil settlements are more reliable. In contrast, the GRC without membrane actions overpredicts the stress acting on the subsoil.

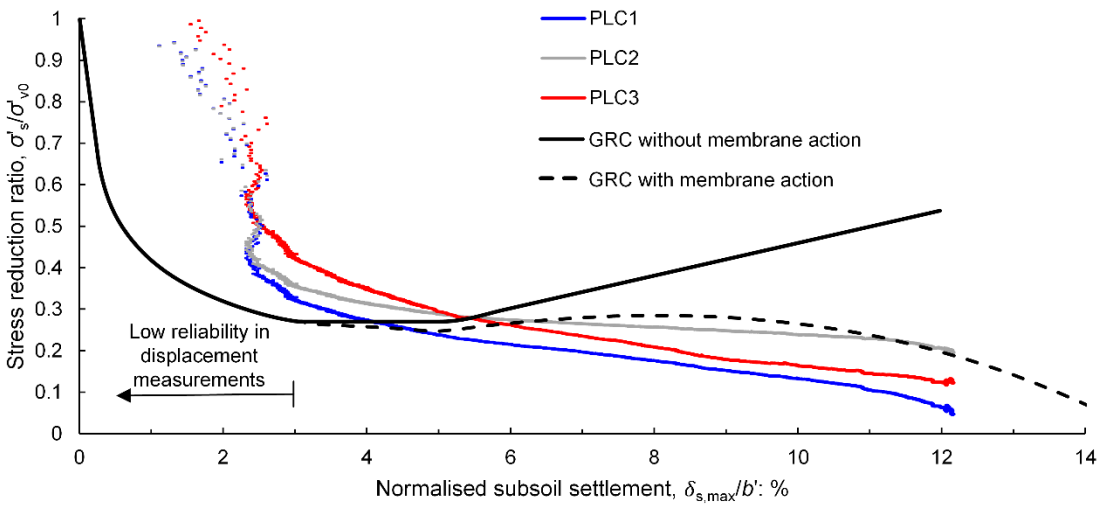

Figure 6.19: Stress reduction ratio (SRR) versus normalised subsoil settlement for Model 2 with GRC with and without membrane actions

It can be seen in Figure 6.19 that equilibrium in the centrifuge model tests between arching stresses, membrane actions and subsoil support was achieved at just over 12% normalised subsoil settlement. This state of equilibrium and the SRR-settlement behaviour of the GRPE are strongly dependent on the stiffness of the geosynthetic reinforcement. If a less stiff geosynthetic was used in the model tests, it is expected that more subsoil settlement would have been required to mobilise sufficient membrane actions to achieve equilibrium. This is demonstrated in Figure 6.20, where the arching stresses for the Model 2 embankment are estimated using the GRC and membrane actions estimated by Equation 6.13 with several different geosynthetic stiffnesses.

While some subsoil support was still provided by the end of the Model 2 embankment tests, indicating equilibrium was reached with subsoil support, the approach adopted in many design recommendations of GRPEs is to assume that subsoil support will be lost at some stage of the structures operational life. If such a design approach was adopted in combination with the above described GRC with membrane action method, the subsoil settlement required for the SRR to reduce to zero could be predicted for various geosynthetic stiffnesses. This is shown in Figure 6.20, where higher stiffness geosynthetics achieve equilibrium without subsoil support at less subsoil settlement.

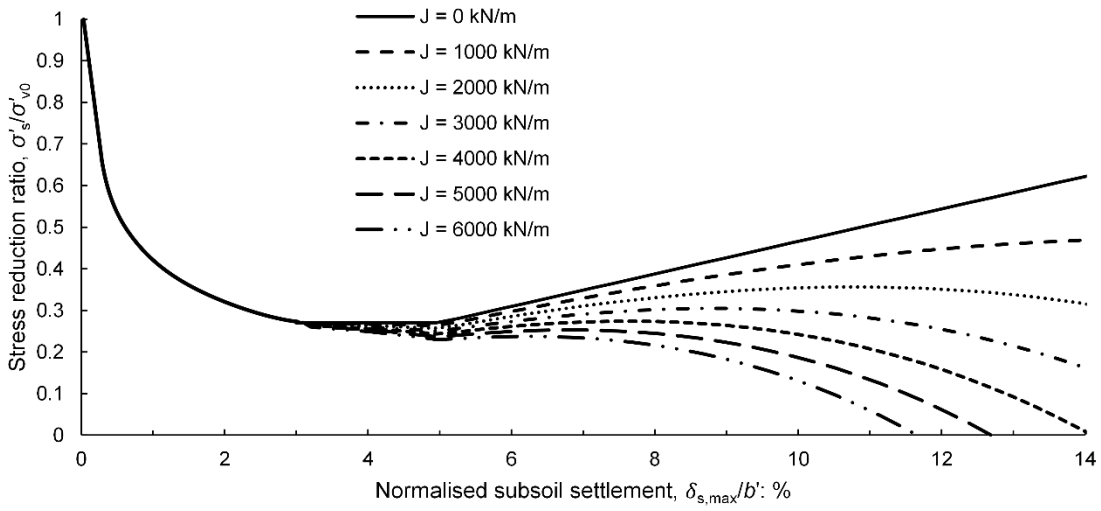

Figure 6.20: Stress reduction ratio versus normalised subsoil settlement estimated for different geosynthetic reinforcement stiffnesses

6.3.2 Critical height

Based on observations of the embankment surface during both Model 1 and 2 tests, it was concluded that $h_e > h_{cr}$ for both embankments tested (without consideration of defective piles). While kinematics within the embankment fill could not be measured to accurately determine h_{cr}, it is shown by changes in rod penetrometer resistance to be approximately 35 mm below the Model 2 embankment surface. After considering the change in embankment height above the pile heads due to subsoil settlement during the model test, the embankment surface was 102 mm above the pile heads by the end of the model test when rod penetrometer testing was undertaken. Thus, the critical height in the Model 2 embankments was approximately 67 mm above the pile heads.

The relationship adopted in BS8006 (2016) (Table 2.1) estimates the critical height for the centrifuge model geometry as 40 mm. Adopting the LDC approach (McGuire 2011), the critical height is estimated 78.3 mm. Thus, BS8006 (2016) appears to underestimate the critical height while McGuire (2011) estimates a critical height that is a closer match with the h_{cr} obtained from rod penetrometers.

6.3.3 Embankment settlement

The total embankment surface settlement (S_{total}) is the sum of the pile head settlement (S_p) and the settlement that develops within the fill due to subsoil settlement (S_e). S_{total} and S_p may be simply taken as the measurements of LDTs and SPs, respectively, within Zone 1 where no defective pile is present. S_e is then taken as the difference between S_{total} and S_p. These settlements are normalised by the total embankment surface settlement at the end of the tests ($S_{total,f}$) and plotted against the time factor in Figure 6.21.

The majority of the total settlement in the Model 1 embankment was evidently due to the pile head settlement as a result of the pile founding conditions. In Model 2, the geosynthetic reinforcement and subsoil underwent significantly more settlement relative to the pile heads due to the stiffer pile response compared to Model 1. As a result, the total settlement at the end of the Model 2 test was composed of an almost equal share of both S_p and S_e.

The settlements that developed within the embankment fill due to subsoil settlement at the base of the embankment has been estimated using the method proposed by Russell et al. (2003), described in Chapter 2, and are plotted in Figure 6.21b. The estimated S_e is based on the measured subsoil settlements shown in Section 6.2.3 and is therefore only shown for Model 2. It is evident that the estimated value of S_e from this method matches the measurements from the Model 2 LDTs and SPs closely.

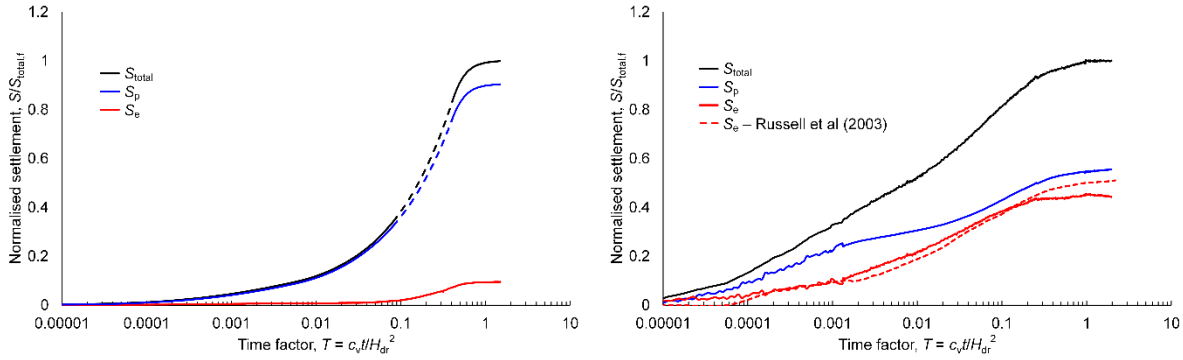

Figure 6.21: Embankment settlements (normalised) plotted against time factor for (a) Model 1; (b) Model 2)

6.4 Summary

Centrifuge tests were conducted to investigate the behaviour of GRPEs both with and without defective piles. The salient conclusions that can be drawn from this work are:

- A defective pile, floating within a layer of very soft clay, underwent uniform settlement with surrounding non-defective piles that were installed into a founding layer of firm clay. Given that no meaningful differential settlement was experienced at the pile head level, no differential settlement was observed at the embankment surface.
- A defective pile, floating within a layer of very soft clay, underwent additional settlement relative to the surrounding non-defective piles that were installed into a founding layer of medium dense sand. This additional settlement experienced at the pile head level propagated to the embankment surface and resulted in a localised depression.
- The area of embankment supported on end-bearing piles that was affected by the defective pile was approximately limited to the confines of the surrounding unit cell. Outside the boundary of

this unit cell, the arching mechanism and embankment settlements were unaffected by the presence of a defective pile.

- The load transfer towards non-defective pile heads in the Model 2 embankment progressively developed as subsoil underwent consolidation. This load development was well described by a combination of the GRC concept to estimate arching stresses and the equation given by Ellis and Aslam (2009b) to describe membrane actions, both of which are subsoil settlement dependent.

7 Numerical analysis

This chapter details the numerical investigation undertaken using the Finite Element Method (FEM) software PLAXIS 3D 2013 to further investigate the redistribution of loads and differential settlements that arise due to defective piles within GRPEs. The results from centrifuge modelling presented in Chapter 6 showed that for GRPEs supported on floating piles, where piles were founded within a firm clay layer, differential settlement was not experienced at the pile head level or embankment surface as a result of the defective pile. Whereas for the GRPE supported by end-bearing piles, where piles were founded in a medium dense sand layer, it was observed that a depression formed at the embankment surface above the defective pile.

This chapter aims to investigate the conditions that result in differential settlements developing above a defective pile. After calibrating an FEM model with the results from centrifuge modelling, a parametric study was undertaken to identify the critical conditions that may lead to a defective pile undergoing additional settlement to the surrounding non-defective piles and these differential settlements propagating to the embankment surface.

7.1 Finite element method

Numerical analysis was performed using the Finite Element Method (FEM), which in the present study utilised a continuum Lagrangian mesh-based technique for solving boundary value problems. The software PLAXIS 3D 2013 was used in the present study as it incorporates several advanced constitutive models developed specifically for simulating soil and rock behaviour. Two of the soil models incorporated within PLAXIS, the hardening soil and soft soil models, were used in the present study and are described in the following sections. PLAXIS is also capable of modelling soil-structure interaction, with the software incorporating interface elements and 2D tensile elements to model geosynthetic reinforcement.

7.1.1 Hardening soil model

Elastic perfectly plastic models provide a means to model the accumulation of irreversible strains that develop within soil under loading. However, such models are limited in their ability to model the pre-failure nonlinearity of soil, which is where hardening plasticity models provide significant advantages (Muir Wood 2004). The hardening soil (HS) model is a hardening plasticity constitutive model, which incorporates a non-fixed yield surface capable of distinguishing between shear and compression hardening (Schanz et al. 1999).

The HS model adopts a hyperbolic relationship between vertical strain (ε_1) and deviatoric stress (q) under triaxial loading. This behaviour is shown in Figure 7.1, although an approximation of this curve is made by the HS model, where q_a is the asymptotic shear strength and q_f is the ultimate deviatoric stress, the two of which are related by a failure ratio, $R_f = q_f/q_a$. The parameters E_{50} and E_{ur} depicted in Figure 7.1 are the drained triaxial secant modulus and unload/reload modulus, respectively, both of which exhibit a stress dependency defined by a power law with exponent m (shown below).

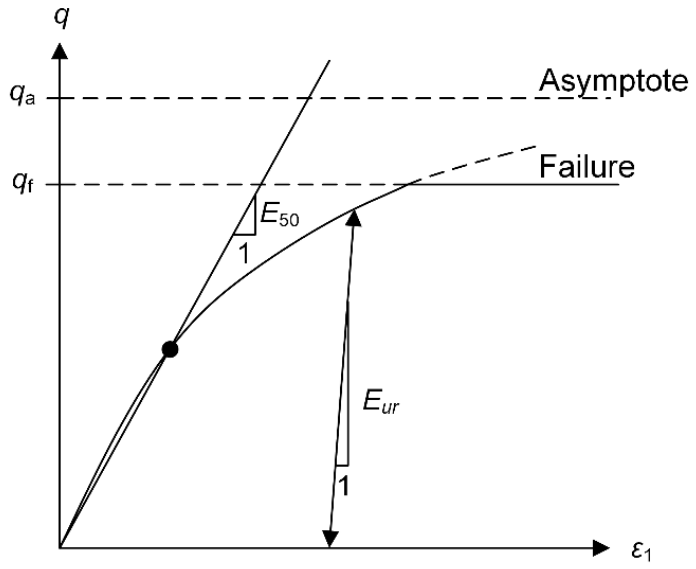

Figure 7.1: Hyperbolic deviatoric stress versus axial strain under triaxial loading, modified from Schanz et al. (1999)

The HS model adopts a shear hardening flow rule to relate the rate of plastic volumetric shear strain ($\dot{\varepsilon}_v^p$) and the rate of plastic shear strain ($\dot{\gamma}_v^p$) by the mobilised dilation angle (ψ_m), written as:

$$\dot{\varepsilon}_v^p = \sin \psi_m \dot{\gamma}_v^p \tag{7.1}$$

The flow rule in Equation 7.1 requires ψ_m to be determined. The HS model defines the mobilisation of dilation relative to the mobilised friction angle by modifying the stress-dilatancy theory proposed by Rowe (1962), as described by Schanz and Vermeer (1996). Thus, shear hardening develops as the shear strength is mobilised until the maximum shear strength is reached, which is defined using the Mohr-Coulomb failure criterion. It is noted that post-peak softening is not accounted for in the HS model.

The HS model incorporates an optional dilatancy cut off, which reduces ψ_m to zero when the void ratio reaches the maximum void ratio (e_{max}). The void ratio is estimated from the volumetric strain, which in turn is estimated from the flow rule described previously. Thus, once sufficient plastic deformation has occurred, such that the material has reached critical state as determined by $e = e_{max}$, then constant volume shearing is assumed whereby $\dot{\varepsilon}_v^p = 0$ (and $\psi_m = 0$).

Soft soils may undergo significant plastic volumetric strains under isotropic compression. This deformation is not considered by E_{50}, which primarily controls the shear yield surface. To account for this, the HS model introduces the oedometer modulus (E_{oed}) to control the cap yield surface and the associated plastic strains. The cap yield surface is taken as an ellipse in the p' -q plane, the magnitude of which is determined by the isotropic pre-consolidation stress (p_p) and the aspect ratio of the ellipse is determined by the parameter M. The parameter M is not a direct input in the HS model, instead it related to the ratio of vertical to horizontal stress in one-dimensional compression (K_0^{NC}). The yield surface in principle stress space for the HS model is shown in Figure 7.2.

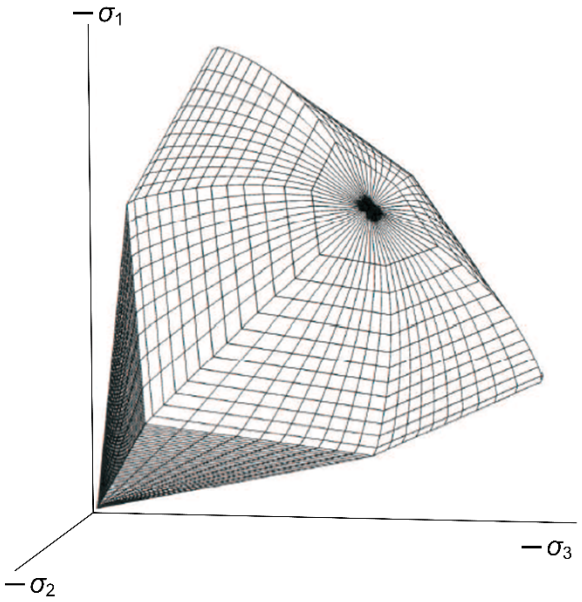

Figure 7.2: Representation of the total yield contour for the HS model in principle stress space, modified from Brinkgreve et al. (2013)

The stress dependency of the three moduli nominated in the HS model may be expressed in terms of the minor principal effective stress (σ'_3):

$$E_{50} = E_{50}^{ref}\left(\frac{\sigma'_3}{p^{ref}}\right)^m \tag{7.2}$$

$$E_{oed} = E_{oed}^{ref}\left(\frac{\sigma'_3/K_0^{NC}}{p^{ref}}\right)^m \tag{7.3}$$

$$E_{ur} = E_{ur}^{ref}\left(\frac{\sigma'_3}{p^{ref}}\right)^m \tag{7.4}$$

Where p^{ref} is the reference pressure at which moduli with the superscript ref are defined at, and m is the power law constant. For silts and sands m is typically taken as 0.5 to 1.0, and for soft clays it is taken as 1.0, which results in logarithmic compression behaviour (Schanz et al. 1999).

7.1.2 Soft soil model

The HS model may be used to model soft soils by inputting a power law constant equal to 1 (logarithmic stress-strain relationship). However, when modelling very soft soils that are expected to exhibit high compressibility under isotropic loading, such that $E_{oed} < E_{50} = 0.5$, it is more appropriate to use a model specifically developed to replicate this behaviour. The soft soil (SS) model in PLAXIS is suitable for modelling the behaviour of such highly compressible materials.

The SS model adopts a logarithmic relationship between volumetric strain (ε_v) and mean effective stress (p'), which under virgin isotropic compression (Figure 7.3) is expressed as:

$$\varepsilon_v - \varepsilon_{v0} = \lambda^* \ln\left(\frac{p'}{p'_0}\right) \tag{7.5}$$

Where subscript 0 refers to the initial condition prior to the change in stress and λ^* is the modified compression index (described below). Under isotropic unloading/reloading, the elastic strains (denoted by superscript e) may be written as:

$$\varepsilon_v^e - \varepsilon_{v0}^e = \kappa^* \ln\left(\frac{p'}{p'_0}\right) \tag{7.6}$$

Where κ^* is the modified swelling index. The indices used in Equation 7.5 and 7.6 differ from λ and κ used by Burland (1965), as λ^* and κ^* are defined in terms of volumetric strain rather than void ratio. The modified indices used by the SS model may be related to those used by Burland (1965) and more commonly known parameters by the following expressions:

$$\lambda^* = \frac{\lambda}{1+e} = \frac{C_c}{2.3(1+e)} \tag{7.7}$$

$$\kappa^* = \frac{\kappa}{1+e} = \frac{C_s}{2.3(1+e)} \tag{7.8}$$

Where C_c is the compression index and C_s is the swelling index.

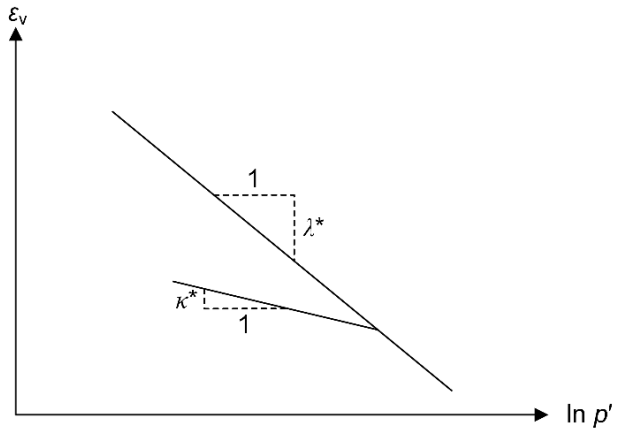

Figure 7.3: Relationship between volumetric strain and mean stress used in the soft soil model, modified from Brinkgreve et al. (2013)

The yield surface in the SS model is defined again by the Mohr-Coulomb failure criterion (fixed) and an ellipse-shaped cap in the p'-q plane, which can increase due to primary compression. This yield surface is plotted in principle stress space in Figure 7.4.

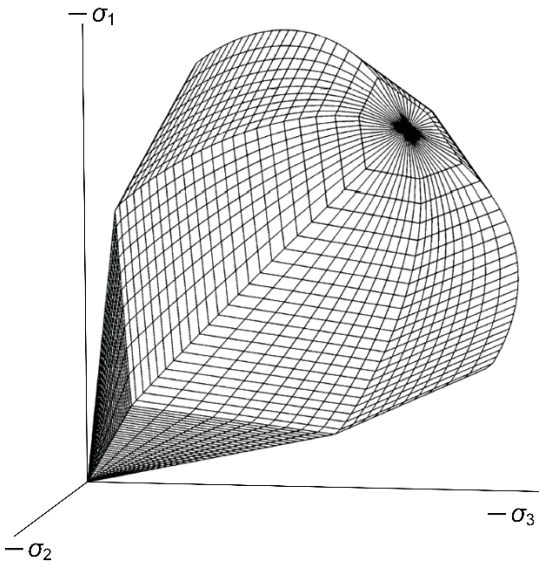

Figure 7.4: Representation of the total yield contour for the SS model in principle stress space, modified from Brinkgreve et al. (2013)

7.2 Centrifuge Model 2

This section details the calibration of an FEM model with the results from the Model 2 centrifuge test detailed in Chapter 6. The numerical modelling is focused on the area surrounding a defective pile, where it was observed that a localised depression formed at the embankment surface directly above the defective pile.

7.2.1 Materials

Clay subsoil

The clay subsoil (kaolin) was modelled using the SS model as this clay prior to the placement of the embankment was a near-normally consolidated (becoming normally consolidated once loaded by the embankment) and very soft with an undrained shear strength of less than 10 kPa. The properties of kaolin clay used for centrifuge modelling at UWA have been extensively studied over the past 25 years (Stewart 1992). Some of these parameters were previously provided in Chapters 3 and 5. While most of the parameters for UWA kaolin are consistent across studies, it has been noted by Lehane et al. (2009) that the compression index, λ, and swelling index, κ, may be up to 20% greater than the values reported by Stewart (1992), giving values of 0.26 and 0.06 respectively. The modified compression and swelling indices derived using the values reported by Lehane et al. (2009) from Equation 7.7 and 7.8, respectively, are used in the numerical analysis and presented in Table 7.1, along with other key SS model parameters.

Table 7.1: Parameters used for kaolin in Soft Soil model

Property	**Symbol**	**Value**
Modified compression index	λ^*	0.0929
Modified swelling index	κ^*	0.0214
Cohesion	c'	0.2
Friction angle	ϕ	23
Dilation angle	ψ	0
Horizontal permeability	k_x, k_y	4.9×10^{-9} m/s
Vertical permeability	k_z	2.4×10^{-9} m/s

The parameters outlined in Table 7.1 were calibrated with oedometer testing undertaken by Acosta-Martinez and Gourvenec (2006), who consolidated samples under a vertical stress of 150 kPa before undertaking conventional oedometer testing. The oedometer test with a pre-consolidation stress of p'_p = 150 kPa was modelled using the *SoilTest* module available in PLAXIS (Brinkgreve et al. 2013). The results of oedometer testing reported by Acosta-Martinez and Gourvenec (2006) and the oedometer test modelled using the SS model are shown in Figure 7.5.

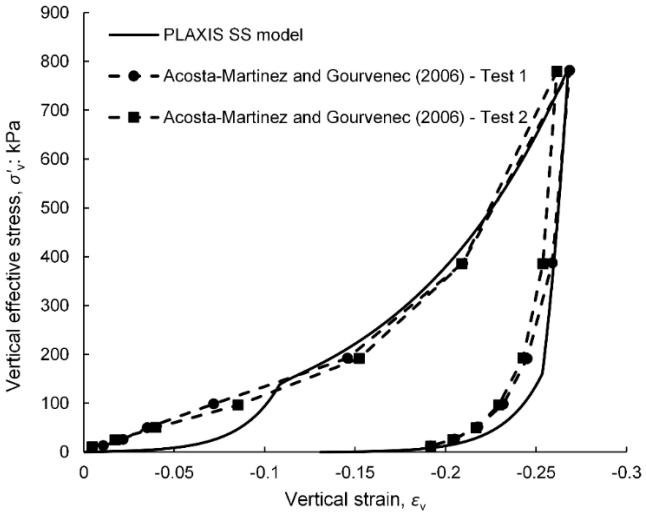

Figure 7.5: Results from oedometer tests reported by Acosta-Martinez and Gourvenec (2006) and oedometer test modelled using SS model for subsoil

The oedometer laboratory and numerical results shown in Figure 7.5 closely match for stresses greater than 150 kPa when the soil is normally consolidated. However, at relatively low stresses when the soil is overconsolidated, the SS model overestimates vertical strains compared to the results from oedometer testing. It was noted by Acosta-Martinez and Gourvenec (2006) that the measured pre-consolidation stress from testing was much lower than the stress applied to consolidate the sample. It is therefore likely that the sample experienced some disturbance or seating issues at these lower stresses. Given that at larger stresses (greater than 150 kPa) the SS model matches the results from oedometer testing very closely, the constitutive model and parameters adopted in Table 7.1 are considered appropriate for modelling the very soft clay subsoil.

Sand

UWA sand used as both the founding layer and the embankment fill was modelled using the HS model. UWA sand has some well-defined properties, as reported in previous Chapters 3 and 5, although some additional parameters are required for the HS model. It is also important to note that the sand used as a founding layer for the piles at the base of the strongbox was prepared in a medium dense state, while the embankment sand was prepared in a dense state. Therefore the material parameters used in the HS model for the two layers differ.

Calibration of the numerical model and parameters with laboratory testing was undertaken to ensure the constitutive model and parameters adopted replicated the behaviour of the sand. Bagbag et al. (2017) performed anisotropically consolidated ($\sigma'_3/\sigma'_1 = 0.5$) drained triaxial tests on UWA sand to calibrate parameters specifically for the hardening soil model. From this study, two tests were selected based on their density and average confining stress that matched closely with the conditions of the sand in the

centrifuge model. It is noted that the triaxial testing was performed on a batch of slightly coarser sand (D_{50} = 0.29 mm), with properties otherwise consistent with previously reported values for UWA sand.

Test 4 from the testing presented by Bagbag et al. (2017) was used for calibration of the embankment sand parameters. This test comprised dense sand prepared at D_r = 79% and was tested at a radial stress of 40 kPa, which is close to the initial density and horizontal stress at the base of the embankment before soil arching developed. The material parameters that were calibrated to this test are presented in Table 7.2, which correspond to the parameters recommended by Bagbag et al. (2017).

Table 7.2: Parameters used for HS model

Parameter	**Symbol**	**Embankment sand (dense)**	**Founding sand (medium dense)**
Cohesion	c'	0.2 kPa	0.2 kPa
Angle of internal friction	ϕ	39˚	36˚
Dilation angle	ψ	12 ˚	10˚
Power law	m	0.65	0.65
Drained triaxial secant modulus*	E_{50}^{ref}	25 MPa	9 MPa
Tangent primary oedometer modulus*	$E_{\mathrm{oed}}^{\mathrm{ref}}$	25 MPa	9 MPa
Unload/reload modulus*	$E_{\mathrm{ur}}^{\mathrm{ref}}$	75 MPa	27 MPa
Unload/reload Poisson's ratio	$\nu_{\mathrm{ur}}^{\mathrm{ref}}$	0.2	0.2
At rest earth pressure coefficient for normal consolidation	K_0^{NC}	0.5	0.5

*Defined at the reference minor principal effective stress of 40 kPa

Using the parameters outlined in Table 7.2, an anisotropically consolidated drained triaxial test was modelled in PLAXIS. The results of test 4 presented by Bagbag et al. (2017) and the results using the HS model with parameters for the dense embankment sand are presented in Figure 7.6. The results show close agreement with Test 4 up to 5% axial strain. After 5% axial strain, the sand undergoes post-peak softening, which corresponds to a reduction in dilation as the material within shear bands approaches critical state shearing. However, the HS constitutive model does not model strain softening and is, therefore, unable to replicate this behaviour. Given that conventional FEM can experience numerical instabilities under large deformations, it is likely other limitations of the numerical model will affect its performance more than the inability of the HS model to replicate strain softening if such deformations were to develop.

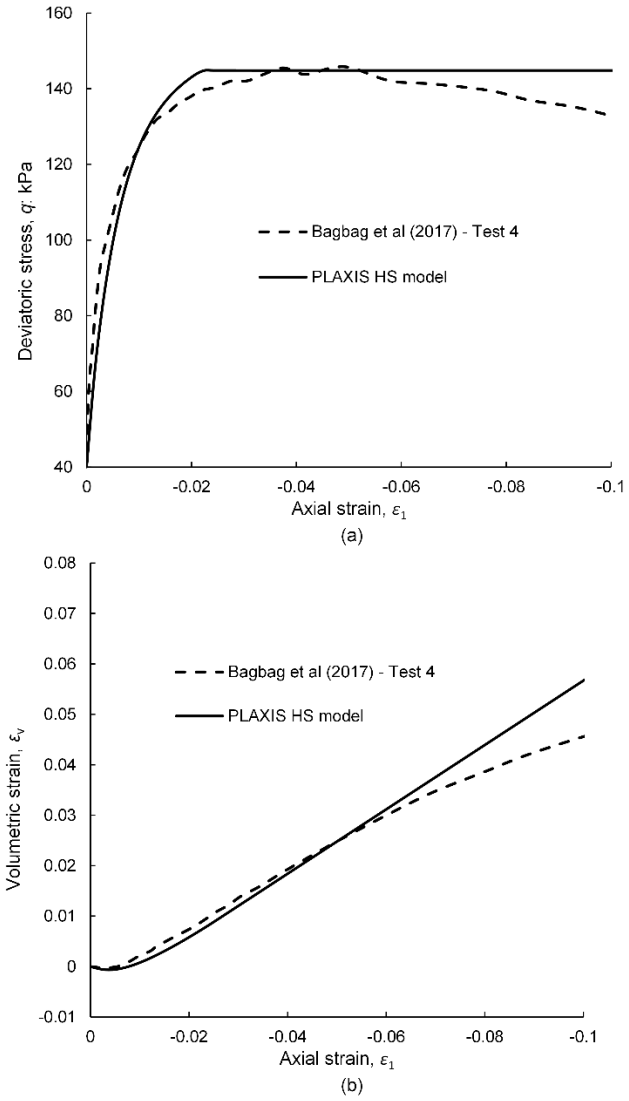

Figure 7.6: Results from anisotropic drained triaxial test for dense embankment sand, (a) deviatoric stress versus axial strain; (b) volumetric strain versus axial strain

The HS model parameters of the founding medium dense sand were calibrated based on triaxial Test 3 reported by Bagbag et al. (2017). This test comprised a medium dense sand (D_r = 42%) that was tested at a minor principle stress of σ'_3 = 40 kPa. The calibrated material parameters used in the HS model for the medium dense founding sand are also presented in Table 7.2. The results from an anisotropically consolidated drained triaxial test performed in PLAXIS using the HS model with medium dense founding sand parameters is shown along with the results of triaxial Test 3 (Bagbag et al. 2017) in Figure 7.7. The deviatoric stress versus axial strain of the HS matches the results from triaxial testing well. Again, the sand underwent some strain-softening that the HS model did not capture, although, this is after about 6% axial strain. The gradient of the volumetric strain versus axial strain plot (Figure 7.7b) is similar between HS model and triaxial results, suggesting that the dilation angle is reasonably calibrated.

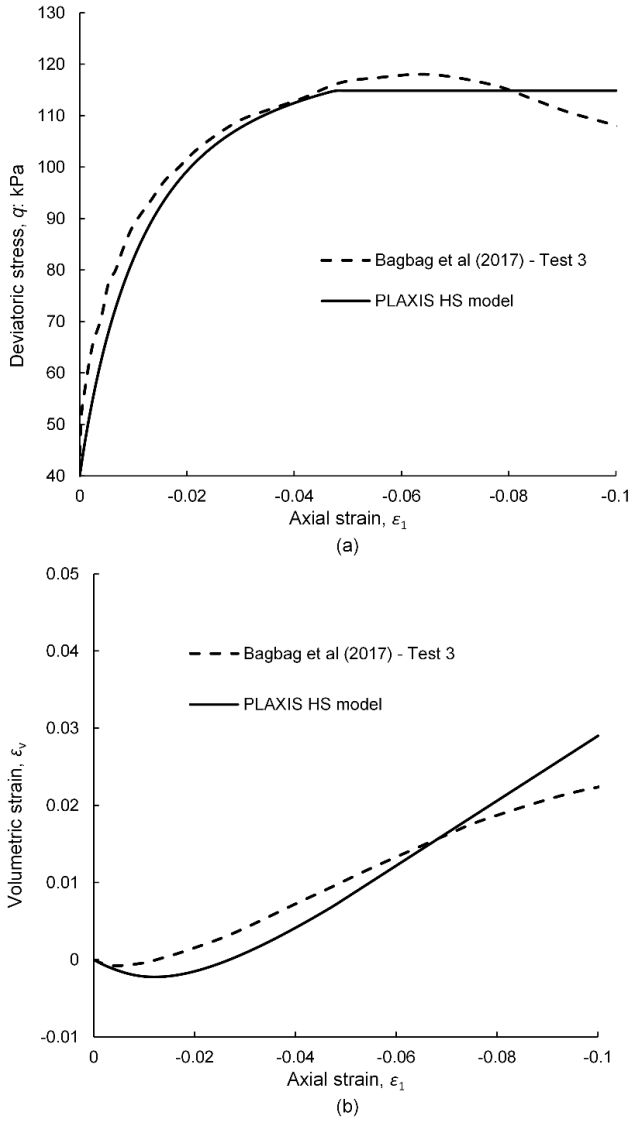

Figure 7.7: Results from anisotropic drained triaxial test for medium dense founding sand (a) deviatoric stress versus axial strain; (b) volumetric strain versus axial strain

Geosynthetic reinforcement

The geosynthetic reinforcement was modelled using a geogrid element in PLAXIS. Geogrid elements are defined in terms of axial (tensile) stiffness, *J*, which is equal to the product of the cross-sectional area and Young's Modulus of the geosynthetic. Given that the geosynthetic used in the centrifuge model tests was a geomembrane, the reinforcement was modelled as an orthotropic element with the stiffness estimated from tensile testing described in Chapter 5. The simplified bi-linear behaviour of the geosynthetic reinforcement is well replicated using an elastic-perfectly plastic model, which can be modelled using the PLAXIS geogrid elements by defining a maximum tensile force, *N*.

Table 7.3: Parameters used for geosynthetic reinforcement

Parameter	Symbol	Value
Axial stiffness	J (= EA)	3600 kN/m
Maximum tensile force	N	97.2 kN/m

The results in prototype scale from testing undertaken on the model geosynthetic and the elastic-perfectly plastic response of the geosynthetic reinforcement modelled using PLAXIS are shown in Figure 7.8. The simplified elastic-perfectly plastic model is shown to replicate the tensile tests closely.

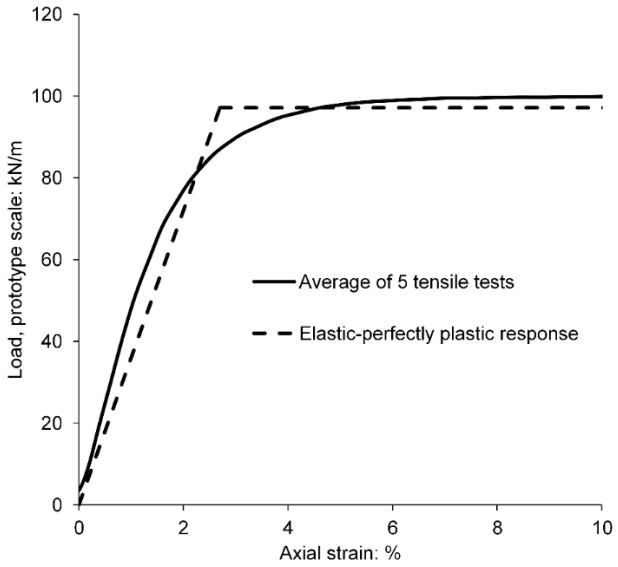

Figure 7.8: Tensile tests on model geosynthetic in prototype scale and model adopted in PLAXIS

Piles

The piles were modelled as solid linear elastic non-porous volumes, with enlarged heads attached to the top of the pile shafts. The piles used in the centrifuge model were hollow aluminium tubes with closed ends, whereas the piles were modelled as solid cylindrical elements in the numerical model. Thus, to ensure that the piles in the centrifuge model and numerical model possessed equivalent axial stiffness, the Young's Modulus, E, was scaled. This was achieved by satisfying the expression $E_{\mathrm{NM}}A_{\mathrm{NM}} = E_{\mathrm{CM}}A_{\mathrm{CM}}$, where the subscripts NM and CM denote numerical model and centrifuge model, respectively, and A is the pile shaft cross-sectional area. The Young's Modulus of aluminium may be taken as approximately 70 GPa, which results in E_{NM} = 38 GPa in order to satisfy axial stiffness equality between numerical and centrifuge models.

Interfaces

Interface elements may be used in PLAXIS when analysing soil-structure interaction problems where intense shearing is expected to develop within localised zones. In the case of GRPEs, such zones can

be expected along pile shafts and within the granular material above pile heads. At interfaces between soil and structural elements, such as a pile shaft, the mobilised strength may be less than the strength of the soil it is founded within. In the case of a pile installed in sand, the mobilised shaft friction is dependent on the grain size (Kishida and Uesugi 1987), which governs the thickness of the localised zone of shearing at the soil-pile interface (Fioravante 2002).

As noted in Chapter 5, based on the relative roughness of the shaft to the average grain size of the sand, the shaft of the piles used in the centrifuge models may be considered smooth when founded in sand. Thus, low shaft friction is expected to develop at the sand-pile interface with no dilatancy (Fioravante 2002). Interface elements were applied along the shafts of the piles to model a zone close to the pile surface with reduced strength properties. In the absence of interface tests on UWA silica sand and aluminium, the mechanical properties assigned to the interface were obtained by applying a strength reduction of $R_{inter} = 0.7$ to the properties of the adjacent sand, which is in line with typical values of $R_{inter} \approx 2/3$ (Brinkgreve et al. 2013). R_{inter} is applied to both the strength and the stiffness of the adjacent soil, thus reducing not only the axial capacity of the pile, but also the axial stiffness of the pile.

In clays, the shear resistance along the clay-pile interface is not significantly affected by the interface roughness (Lemos and Vaughan 2000). However, during the construction of the centrifuge model, the strongbox was ramped up to 40*g* and back down to 1*g* for each pile installation and for in situ penetrometer testing. Each time the model was subjected to a change in the gravitational field, a small amount of slip would have occurred along the clay-pile interface as the soil and pile undergo compression/relaxation. Thus, a strength reduction was also applied to the clay-pile interface of $R_{inter} = 0.7$ as the strength and stiffness at the interface between pile and clay is expected to be less than the soil-on-soil residual strength due to this relative movement that occurred along pile interfaces during the centrifuge model ramp-up/ramp-down.

As shown in Chapter 6, it was observed during the post-test examination of the centrifuge Model 2 that an approximately 1 mm thick (in model scale) layer of clay was present at the base of the non-defective pile toes. This was due to the installation (jacking) of the piles, which cannot be modelled in PLAXIS. The presence of clay prevented the pile toes from being in direct contact with the founding sand layer, thus, resulting in the non-defective piles exhibiting a softer load-settlement response than if they were in direct contact with clean sand. To simulate the reduced strength and stiffness at the pile toes, interface elements could be applied to the base of the pile toes, although they would assign strength and stiffness properties to the interface from the adjacent sand. Instead, a 40 mm thick (equivalent to 1 mm in model scale) volume of soft clay was modelled at the base of the pile toes using the same model and parameters as used for the clay subsoil, as shown in Figure 7.9.

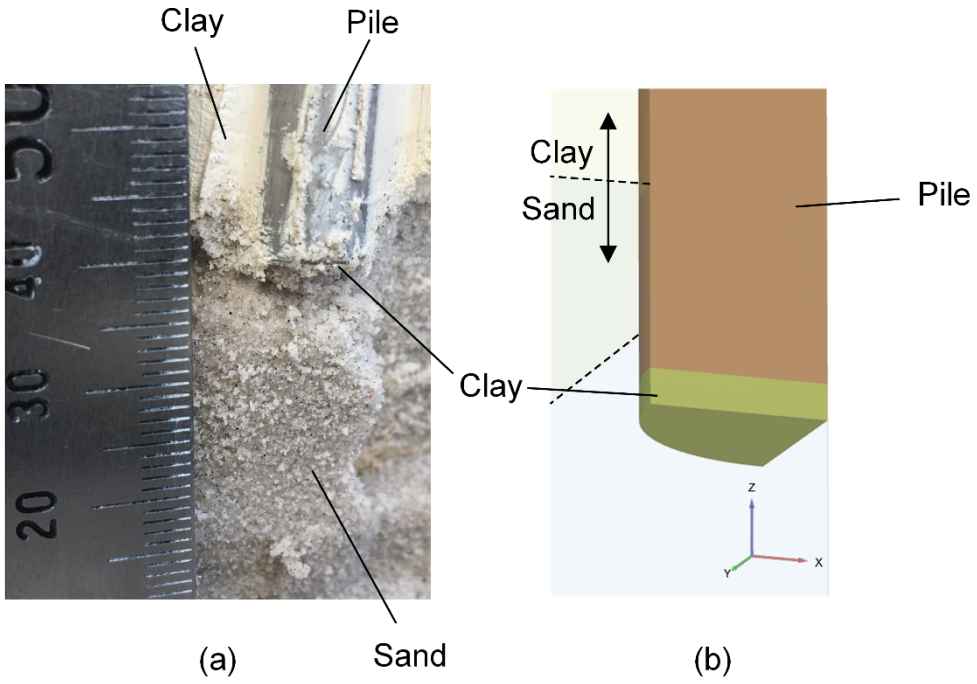

Figure 7.9: (a) Non-defective pile toe after completion of Model 2 test; (b) detail of pile toe in the numerical model

At points of displacement singularity, such as at the edge of a pile head in a piled embankment, shear bands may develop within the soil mass. Such points of high distortion cannot be easily solved using conventional FEM. One solution for addressing the non-unique displacement that develops at singularity points is to apply an interface element to introduce a failure surface (shear band), which has been shown to improve the numerical results considerably (Van Langen and Vermeer 1991). These shear bands are not zones of weakness, as they will have the same strength as the surrounding soil. As such, the soil within these zones should not have a strength reduction applied (R_{inter} = 1). Van Langen and Vermeer (1991) showed that interfaces within the soil above a trapdoor were useful in inducing slip along shear bands by creating a velocity discontinuity at the boundary. A similar approach has been adopted in the present study by applying a zero thickness interface around the edge of the pile head, which extends vertically into the embankment sand, as shown in Figure 7.10. This interface was assigned the same strength as the surrounding embankment sand material, i.e. no strength reduction.

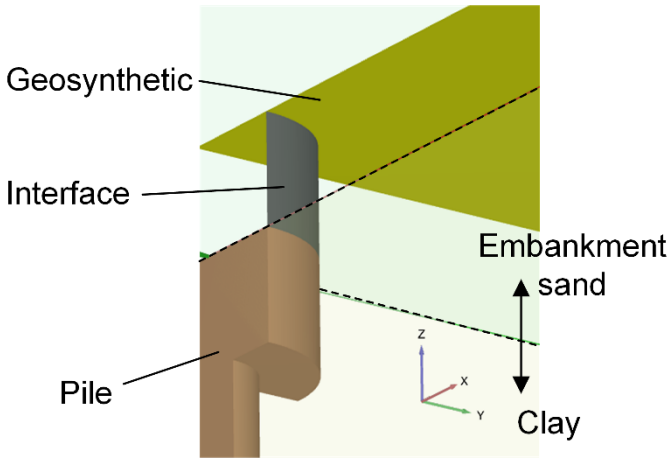

Figure 7.10: Interface above pile head

7.2.2 Model conditions

Unit cell

The present study focuses on modelling a section of embankment under the embankment centreline, away from any slopes, meaning that lateral spreading of the embankment is not considered. Under these conditions, the 3D GRPE geometry may be approximated by a 2D axisymmetric model, and has been shown to provide good agreement compared with more advanced 3D analysis (Smith and Filz 2007; Plaut and Filz 2010; Girout et al. 2014). Such approximations are based on the unit cell concept. The unit cell is the area enclosed within the centres of four piles when spaced on a square grid layout (Figure 7.11). The smallest region of the unit cell that may be modelled to approximate the 3D behaviour of a GRPE is a triangular 1/8th unit cell, which comprises three vertical planes all of which represent planes of symmetry. This triangular 1/8th unit cell may then be modelled using an axisymmetric approximation, as described by Smith and Filz (2007). However, when a defective pile is introduced, these planes bounding the triangular 1/8th unit cell no longer represent planes of symmetry, and thus, 3D analysis is required.

3D numerical models of GRPEs under the embankment centreline may also be simplified using the unit cell concept (Zhuang et al. 2012; Girout et al. 2014; Khabbazian et al. 2015), with studies typically modelling the 1/4th or 1/8th section of a unit cell (Figure 7.11). Again, this approach cannot be applied when a defective pile is introduced, as the planes of symmetry are no longer present within such small confines of the unit cell. As described in Chapter 6, the presence of a defective pile did not cause any additional load or settlement to be experienced by the piles directly adjacent to the defective pile. Further to this, the results from the rod penetrometers and the observation that the localised depression that formed at the embankment surface indicate that the effects of the defective pile did no extend beyond the adjacent non-defective piles. This means that for the Model 2 embankment, the centrelines

between four adjacent piles (when one of the piles is defective) may be assumed to be planes of symmetry, represented by the boundaries of the unit cell shown in Figure 7.11.

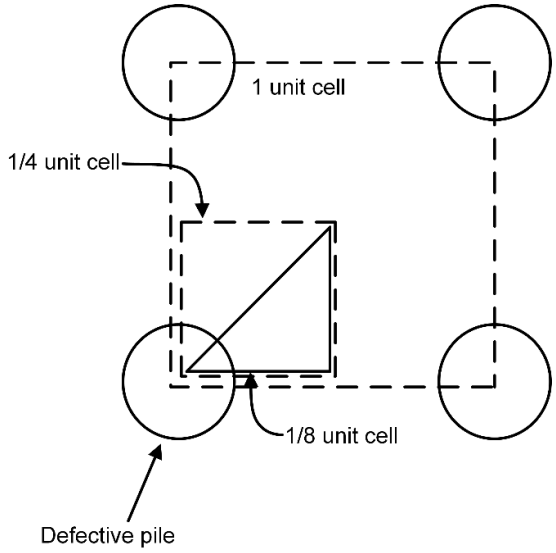

Figure 7.11: Unit cell concept for piles arranged on a square grid of piles in plan view

The smallest model that can be adopted in the analysis of the Model 2 defective pile is a triangular 1/2 unit cell. However, when the triangular geometry was modelled it was found to lead to mesh instability. While computationally more expensive, the smallest model geometry investigated in the present study was a square 1 unit cell model as it did not suffer the instabilities of a triangular model.

Boundary conditions

The vertical boundaries were restricted from horizontal movement normal to the face of the boundaries (Figure 7.12). Vertical movement was freely allowed along these boundaries with no shear stresses developing, corresponding to planes of symmetry. The horizontal boundary on the base of the model was a fully fixed boundary providing restraint in both vertical and horizontal directions as this represents the base of the strongbox. No prescribed displacements or stresses were applied to the ground surface. Groundwater flow was not allowed across any of the vertical boundaries because of symmetry, although the excess pore pressures were able to flow through the bottom boundary as a constant pressure head standpipe was connected to the founding sand layer.

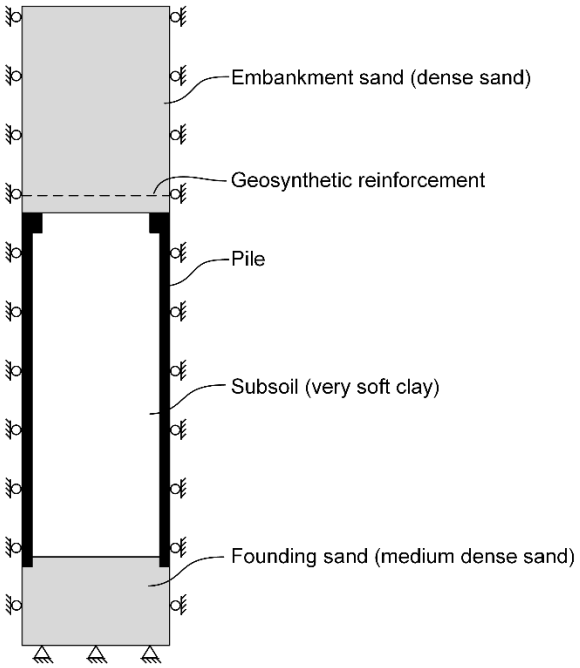

Figure 7.12: Cross-section of boundary conditions for the FEM model

Mesh

10-node tetrahedron elements were used for the soil volumes, while the geogrid was modelled using 6-node elements. Large shear strains were expected to develop in the sand directly above the pile heads and along the shafts of the piles. Thus, the mesh in these zones was locally refined within the associated volumes by a factor of 0.4 relative to the target element size, I_e. The target element size is based on the dimensions of the model and is calculated in PLAXIS using the equation:

$$I_e = \frac{r_e}{20}\sqrt{(x_{\max} - x_{\min})^2 + (y_{\max} - y_{\min})^2 + (z_{\max} - z_{\min})^2} \tag{7.9}$$

Where r_e is the relative element size, which can be varied to change the mesh fineness of the model.

Mesh density analysis

To investigate the effects of the mesh on the results of the model, analysis was performed using three values of relative fineness, r_e = 2.0, 1.6 and 1.4, which resulted in 4975, 7710 and 9830 elements respectively. The settlements at the embankment surface directly above the defective pile from the FEM model using the three mesh fineness' are plotted against time in Figure 7.13 and compared to the results from centrifuge modelling (prototype scale). It is shown that with increasing mesh fineness, the difference between calculated results reduces, and FEM results approximately approach the centrifuge model results. The model comprising 9830 (r_e = 1.4) elements calculated settlements similar to those measured in the centrifuge model, and the difference between settlements calculated reduces with increasing mesh fineness. Given that the use of a mesh any finer than r_e = 1.4 would significantly limit

the number of models that could be run as part of a parametric study, and that such a mesh fineness appears to match measured centrifuge settlements rather well, this mesh size was adopted for all models.

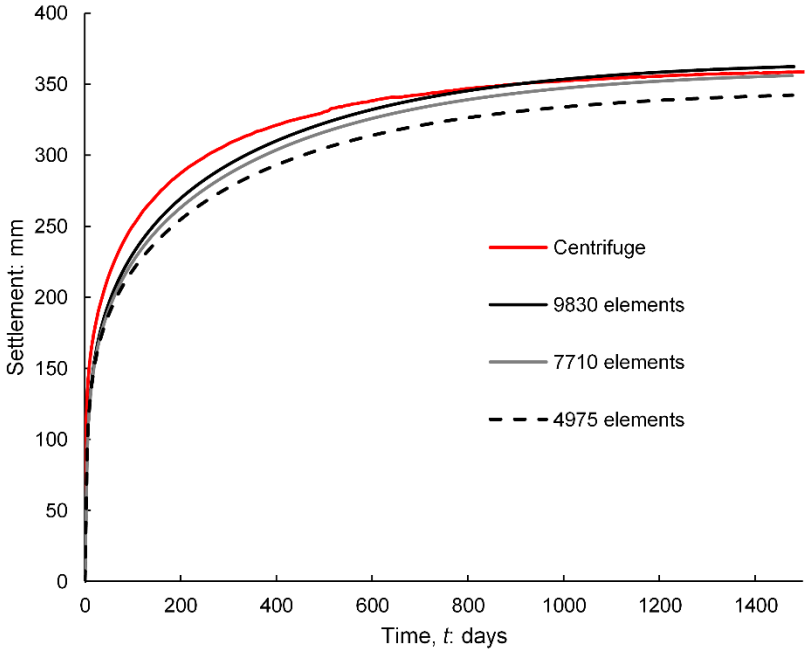

Figure 7.13: Surface settlement above defective pile from centrifuge model and FEM using different element sizes

Calculation phases

As the centrifuge model embankment was constructed at 1*g* prior to being ramped up to the target testing acceleration of 40*g*, a rapid embankment construction sequence was modelled, followed by a period of consolidation under embankment loading. To simulate this process, the following staged construction process was adopted:

1. Initial phase – The subsoil is activated (Figure 7.14a) and the initial vertical effective stresses, σ'_{v0}, is calculated based on the effective unit weight of the soil. The horizontal effective stresses are estimated using the coefficient of lateral earth pressure, K_0, which is either defined or estimated within the constitutive model for each soil type.
2. Pile installation phase – The material within the volumes representing the piles is changed to the concrete linear elastic model and interfaces are turned on (Figure 7.14b). The effective unit weight of the piles is similar to that of the clay, and thus, only small displacements will result from the loading during this stage. However, displacements are reset after this stage to compare with measurements from the centrifuge model. This phase is calculated using an elastic-plastic deformation analysis, referred to in PLAXIS as a *Plastic Calculation.* Pore pressures are not considered in this type of analysis.

3. Embankment construction phase – The embankment construction is simulated by activating the embankment volume and the geosynthetic layer (Figure 7.14c). Unlike the previous phase, pore pressures must be considered during the construction and consolidation of the embankment. The *Consolidation Calculation* type of analysis in PLAXIS was used to take pore pressures into account during embankment loading. When loading is applied using this type of analysis, the load is linearly applied over the defined time. When the embankment load was rapidly applied (1 day), the iteration process would not converge. After trialling several embankment construction periods, it was found that 5 days was the fastest construction time that would converge numerically.
4. Embankment consolidation phase – No changes to the geometry were made in this stage. The excess pore pressures from the previous stage were used as well as the same *Consolidation Calculation* type of analysis. The analysis was performed until 99% of the excess pore pressure had dissipated.

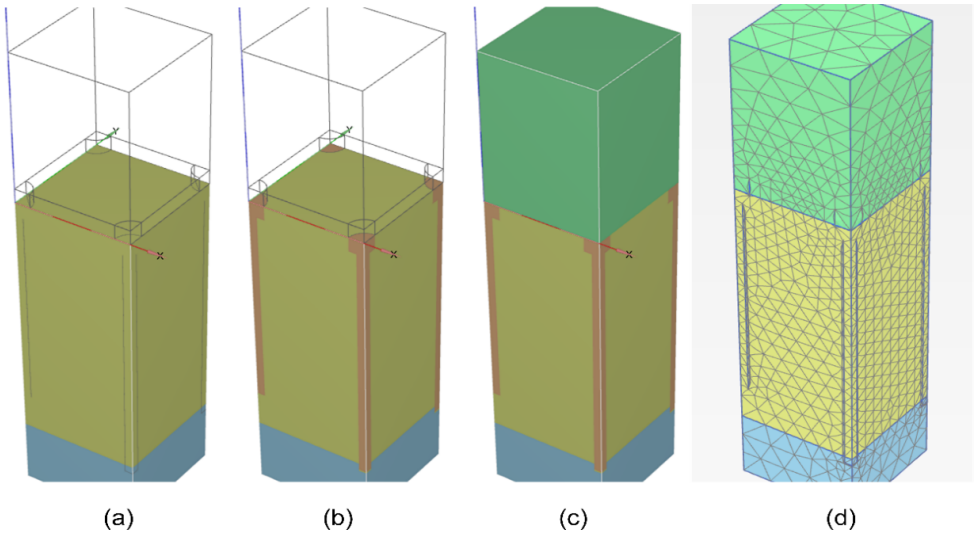

Figure 7.14: FEM model construction sequence (a) initial conditions; (b) pile volumes; (c) embankment sand activated; (d) meshed model

7.2.3 Calibrated model results

The pile head settlements calculated from the FEM model are plotted against time in Figure 7.15a along with the settlements measured from the centrifuge Model 2 at two discrete locations, defective pile and non-defective pile head settlements. It is evident that the settlement of the non-defective pile calculated by the FEM model matches the results from centrifuge model well, although FEM underpredicts the defective pile settlement by 6% by the end of consolidation. This error is considered acceptable.

The embankment surface settlements, taken directly above the defective pile and a non-defective pile, are plotted against time in Figure 7.15b. As noted previously, the settlement above the defective pile

calculated by FEM matches the results from the centrifuge model testing. However, surface settlements above non-defective piles are overestimated by the FEM model by 15% by the end of consolidation. While this alone may be considered an acceptable error, it results in the differential settlement at the embankment surface being underestimated by the FEM model. A limitation of the conventional Lagrangian FEM is that when large distortions develop it can suffer mesh distortion or introduce additional calculation errors if a re-meshing technique is applied (Więckowski 2004). This may be why the FEM model underestimates the differential settlement that occurs at the embankment surface, as the embankment sand develops localised regions of high distortion (as shown in Chapter 4) that cause the FEM model to suffer some inaccuracies.

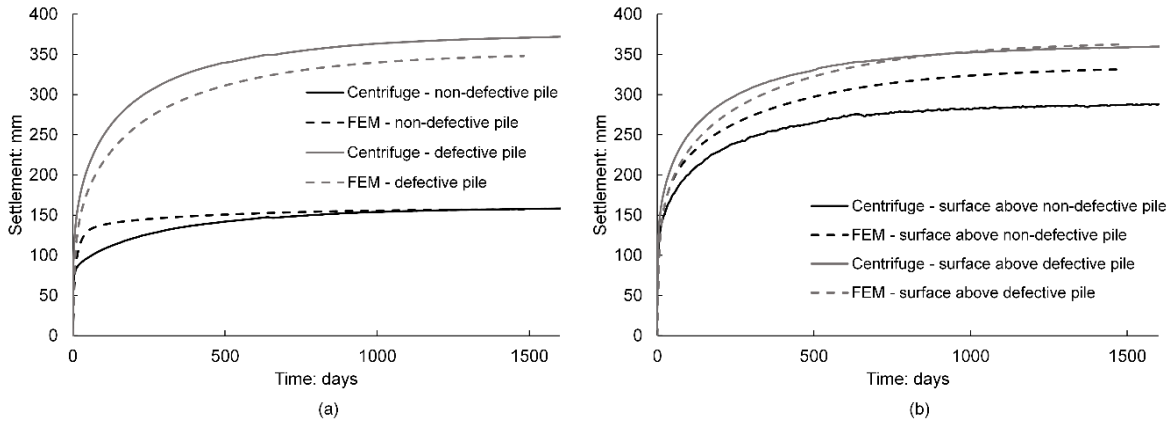

Figure 7.15: Settlements plotted against time for FEM and centrifuge Model 2 at (a) pile head level; (b) embankment surface

The pile load-settlement curves from FEM and the centrifuge Model 2 are shown in Figure 7.16 for both defective and non-defective piles. As noted in Chapter 6, load and settlement developed during the Model 2 ramp up to 40*g*. As such, the load-settlement curves from the centrifuge Model 2 are not expected to match the results from FEM closely. Although, it is shown that the FEM and centrifuge models are in relatively close agreement. The general agreement between FEM and centrifuge model pile load-settlement responses is suitable for a parametric study given that the load-settlement response of the piles in the centrifuge model incorporates some gravitational effects.

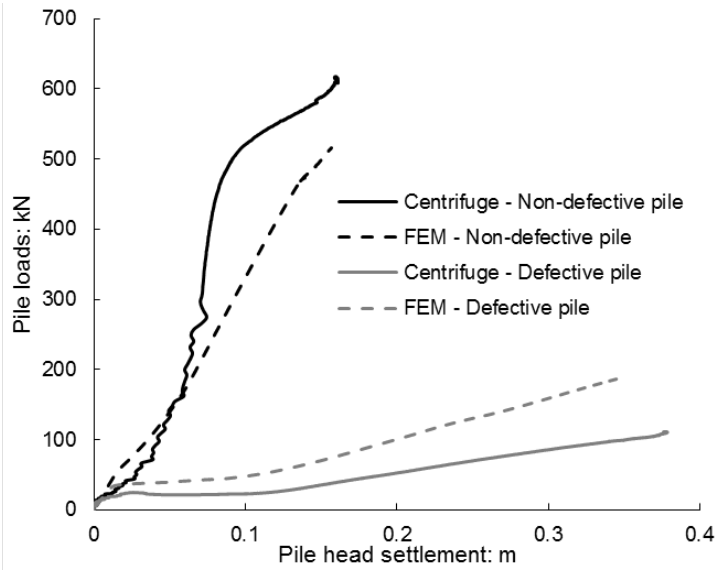

Figure 7.16: Load-settlement curves for piles from both FEM and centrifuge models

The total displacements and deviatoric strains calculated at the end of the consolidation stage of the FEM model are presented in Figure 7.17. The total displacements show how differential settlements propagated to the embankment surface from the pile head level, although as noted previously, the surface differential settlements are underestimated by the FEM model. The displacement profile at the embankment surface of the FEM model shown in Figure 7.17a is also similar to the profile of the centrifuge model, where the localised depression at the embankment surface was shown to be confined to the limits of the unit cell surrounding the defective pile. It is evident from the deviatoric strains that zones of large distortion developed above the pile heads. However, defined shear bands, which are typically much thinner ($\approx 10D_{50}$) than the zones of distortion observed, are not clearly present in Figure 7.17b. Given that the development of shear bands above pile heads within piled embankments has been observed experimentally in Chapter 4, it is likely this observation in the FEM model is a limitation of the numerical technique. This is again attributed to the inability of Lagrangian FEM to handle zones of large deformation and points of displacement singularity.

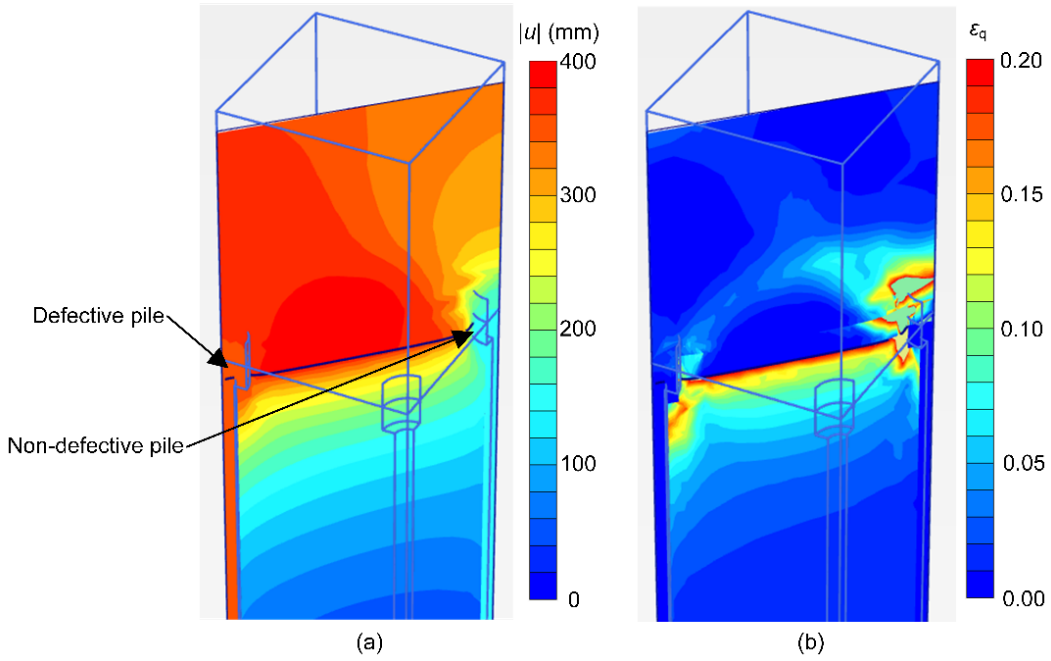

Figure 7.17: Slice taken through the middle of the unit cell of (a) total displacements; (b) deviatoric strains

7.3 Parametric study

A parametric study was undertaken to investigate the conditions that result in differential surface settlements developing due to the presence of a defective pile. It was observed in centrifuge model testing that when the difference in axial stiffness between a defective and non-defective pile is relatively small, as was the case in the Model 1 centrifuge test, differential settlement did not develop at the pile head or embankment surface. In contrast, the Model 2 centrifuge test, which comprised a greater difference in axial stiffness between defective and non-defective piles, resulted in a localised depression at the embankment surface. Based on these observations, the parametric variations focused on the axial stiffness of the defective pile and the embankment height.

7.3.1 Model parameters

The parametric study adopted the same conditions as the previously described FEM model while varying three parameters. The parameters varied as part of the parametric study are described below:

- Embankment height – Four embankment heights were modelled, h_e = 2.0, 3.1, 4.2 and 6.0 m. The critical height for the geometry adopted in the parametric study is estimated as h_{cr} = 3.1 m using the equation proposed by McGuire (2011). Thus, the parametric study comprises shallow embankments where $h_e < h_{cr}$, embankments where $h_e = h_{cr}$, embankments equal in height to the Model 2 embankment where a localised depression formed above the defective pile and tall embankments where h_e is approximately twice the critical height.

- Defective pile length – Three defective pile lengths (L_{Dpile}) were modelled to investigate whether a less severely defective pile than adopted in the centrifuge model tests still has adverse effects on the performance of an embankment. The defective pile lengths modelled were L_{Dpile} = 6.0, 6.4 and 6.8 m.
- Subsoil compressibility – The compressibility of the subsoil was varied in the parametric study, with three modified compression indices modelled, λ^* = 0.0929, 0.08, 0.06. To ensure that both compression and recompression were varied and scaled appropriately, the ratio of λ^*/κ^* = 4.3 was maintained in all models, which meant varying κ^* proportionally to λ^*.

A load test was simulated in PLAXIS to compare the axial stiffness of defective and non-defective piles in the parametric study. The load test was performed by applying a vertical load to the pile head and plotting the load-settlement curve, as shown in Figure 7.18. Given that the piles in both numerical and physical models underwent large vertical settlements, typically greater than 100 mm, it is not appropriate to take the initial tangential elastic axial stiffness of the piles as representative of the piles performance under embankment loading. Instead, the secant pile stiffness at 100 mm of displacement was adopted for the purpose of comparing pile axial stiffness of defective (K_{Dpile}) and non-defective piles (K_{NDpile}). The ratio of K_{Dpile}/K_{NDpile}, referred to as the stiffness reduction factor (R_K), as described by Poulos (2005), provides an indication of the reduction in pile axial stiffness that arises due the presence of the pile defect.

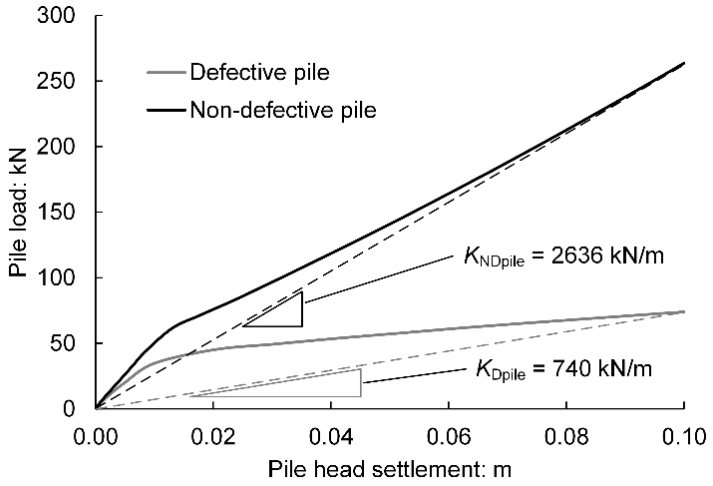

Figure 7.18: Load-settlement curves from FEM pile load test

7.3.2 Settlement

The results presented in the following section are predominantly concerned with the settlements observed at the end of the embankment consolidation when 99% of excess pore pressures induced by

the placement of embankment fill had dissipated. This indicates whether a defective pile may cause differential settlements to develop at the pile head level firstly, and secondly propagate to the embankment surface. It is noted that these settlements are associated with primary consolidation and do not consider creep.

Defective pile length

The pile head differential settlements (ΔS_{pile}), calculated as the difference in pile head settlement directly above the defective pile and the diagonally opposite non-defective pile within the unit cell at the end of embankment consolidation, are plotted against the stiffness reduction factor for all models in Figure 7.19. It is evident that a strong relationship exists between ΔS_{pile} and R_K. Defective piles with a length of 6.0 m and an R_K less than 0.4 resulted in significant differential settlement developing between the defective and non-defective pile heads. Piles that were only slightly defective, e.g. defective piles with a length of 6.8 m, still experienced a reduction in axial stiffness. However, with an increasing R_K (becoming less defective), pile head differential settlements between defective and non-defective piles reduced, such that less than 50 mm of pile head differential settlement developed for defective piles that exhibited an R_K greater than 0.7.

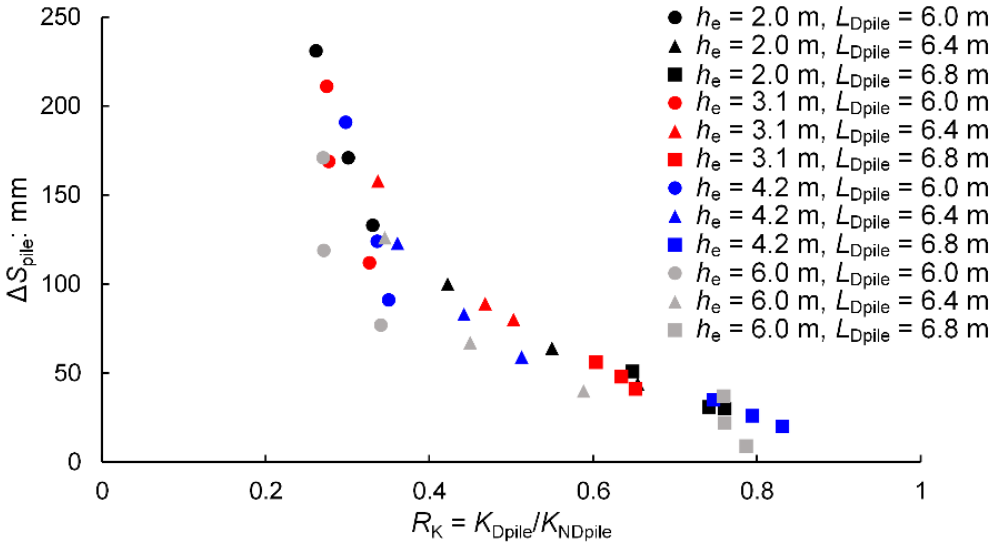

Figure 7.19: Pile head differential settlement versus stiffness reduction factor

The results shown in Figure 7.19 suggest that the embankment height does not significantly affect the amount of differential settlement that develops between pile heads. However, it is noted that less differential settlement typically developed for the embankments with a height of 6.0 m compared to other embankment heights. As will be shown later, embankments with h_e = 6.0 were the only embankments that consistently experienced no differential settlement at the embankment surface. This suggests that if an embankment is of sufficient height, loads may be redistributed away from a defective

pile towards non-defective piles, which consequently reduces the differential settlement between pile heads.

Embankment height

The differential surface settlements (ΔS_{surf}), calculated as the difference in embankment surface settlement directly above the defective pile and the diagonally opposite non-defective pile at the end of embankment consolidation, are plotted in Figure 7.20 against pile head differential settlement for the four embankment heights modelled. It should be noted that in models where $h_e < h_{cr}$ (i.e. h_e = 2.0 m) the maximum surface settlement did not always occur directly above the defective pile. Such cases are indicated by open symbols in Figure 7.20a and do not represent the maximum differential surface settlement. Thus, while it appears in Figure 7.20a that small or no surface differential surface settlement developed in some cases where h_e = 2.0 m, significant differential surface settlement still occurred at the embankment surface between piles due to the embankment height being less than the critical height.

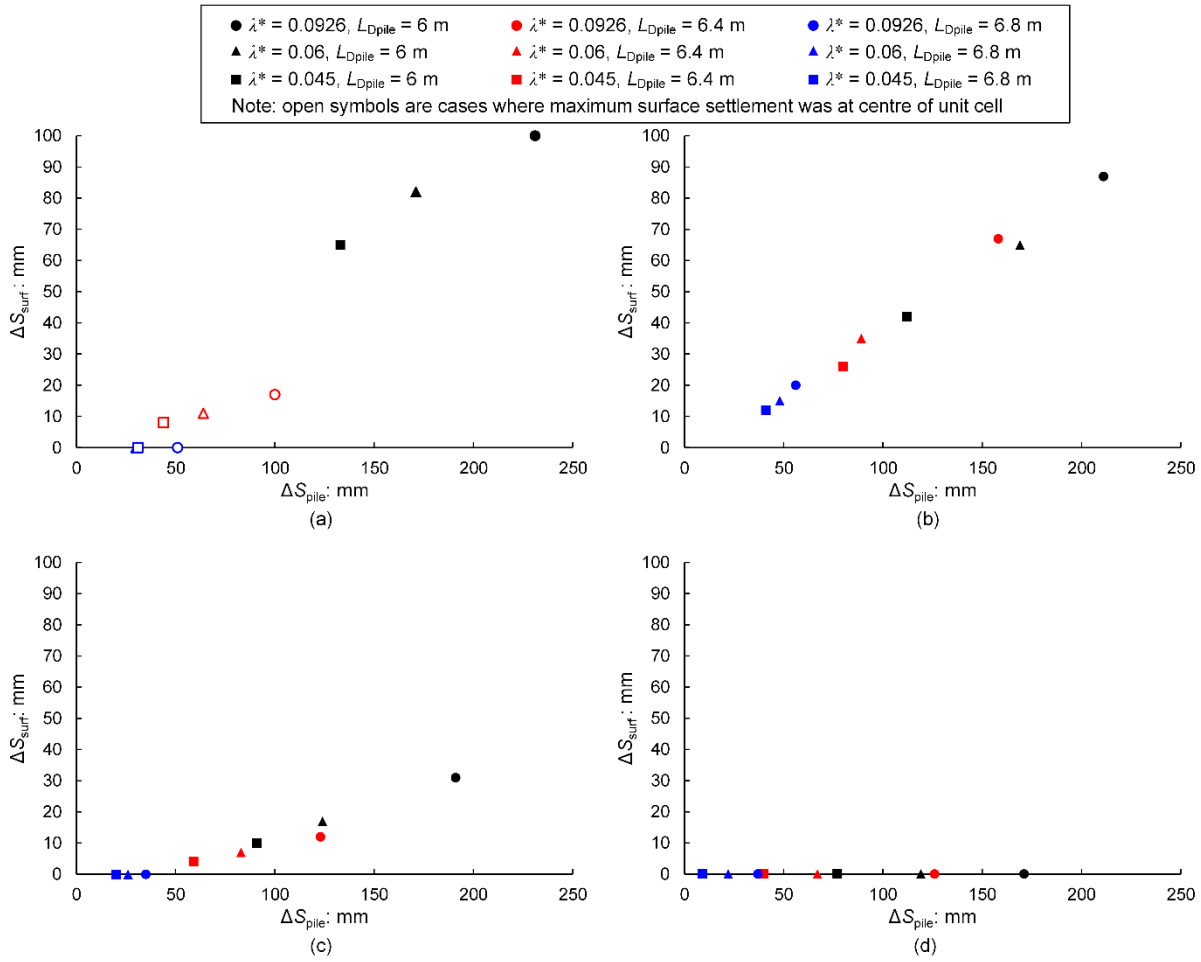

Figure 7.20: Differential surface settlement versus differential pile head settlement for (a) h_e = 2.0 m; (b) h_e = 3.1 m; (c) h_e = 4.2 m; (d) h_e = 6.0 m

Embankments with a height equal to the critical height (where h_e = 3.1 m), as determined by the method proposed by McGuire (2011), all experienced differential surface settlement due to the defective pile undergoing additional settlement relative to the surrounding non-defective piles, as shown in Figure 7.20b. This is due to the embankment height being insufficient to dissipate these differential settlements between pile heads, and as such, even small differential pile head settlements of approximately 50 mm resulted in some differential surface settlement. This observation suggests that any differential pile head settlement that develops in shallow embankments, where h_e is approximately equal to h_{cr}, will result in differential surface settlement being experienced. While differential surface settlement was experienced in all cases in Figure 7.20b, the differential surface settlement was less than 50% of the differential settlement experienced between defective and non-defective piles.

As shown in Chapter 6, a localised depression formed above the defective pile in Model 2 where h_e = 4.2 m. This was also observed in FEM models with defective piles of length L_{Dpile} = 6.4 m, with each of these models experiencing greater than 50 mm of differential pile head settlement (Figure 7.20c). However, when defective pile lengths of L_{Dpile} = 6.8 m were modelled with embankments where h_e = 4.2 m, less than 50 mm of differential pile head settlement developed, and no differential settlement was experienced at the embankment surface. Where differential surface settlement was experienced in embankments with h_e = 4.2 m it was always less than 20% of the differential settlement that developed between defective and non-defective piles. This reduction from differential settlement experienced between pile heads to what was experienced at the embankment surface is greater for embankments with h_e = 4.2 m compared to those with h_e = 3.1 m. This observation shows that with increasing embankment height there is greater thickness for embankment soil to undergo shearing, and hence volume change (dilation), which in turn reduces differential settlements caused by a defective pile.

Models with h_e = 6.0 m did not experience any differential settlement at the embankment surface, irrespective of how much differential settlement developed between pile heads, as shown in Figure 7.20d. This suggests that if an embankment is of sufficient height, then a plane of equal settlement will still develop even in the presence of a defective pile, albeit, the height of this plane will be greater than h_{cr} due to the defective pile.

Slices of total displacements taken diagonally through the modelled unit cell are shown in Figure 7.21 for the four embankment heights with otherwise the same parameters as the original FEM model described in Section 7.2. It is evident that with increasing embankment height, the differential settlement that develops between defective and non-defective pile heads reduces. With sufficient height above the pile heads, a plane of equal settlement develops within the embankment, as observed for the embankment with a height of 6.0 m.

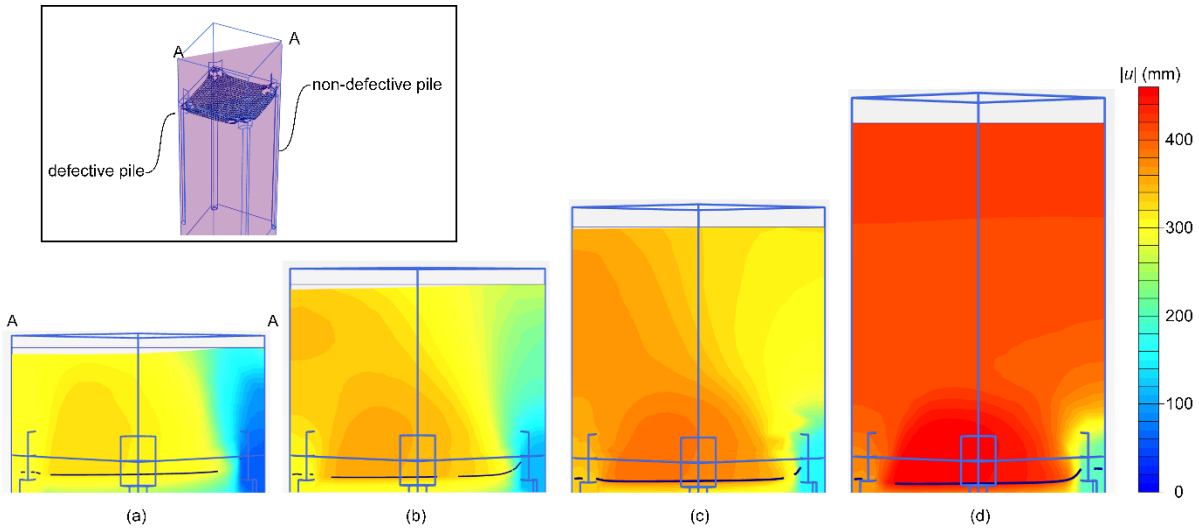

Figure 7.21: Total displacements at the end of consolidation for (a) h_e = 2.0 m; (b) h_e = 3.1 m; (c) h_e = 4.2 m; (d) h_e = 6.0 m, with otherwise unchanged parameters from the original Model 2 FEM setup

Subsoil compressibility

Results from Figure 7.20 indicate that while the compressibility of the subsoil affected the magnitude of differential settlement and pile axial stiffness, it did not ultimately influence whether a defective pile did or did not result in surface differential settlement over the range of λ^* and κ^* values modelled. Essentially, if differential surface settlement developed with a subsoil stiffness of $\lambda^* = 0.0929$, then differential surface settlement also developed when the same model was run with a stiffer subsoil where $\lambda^* = 0.045$. Increasing subsoil stiffness such that the subsoil is no longer representative of a soft clay may result in a shallow defective pile not exhibiting a significant reduction in axial stiffness, and as a result, surface differential settlements may not develop. However, results from the parametric study show that small changes in subsoil compressibility have less of an impact on whether a defective pile results in differential settlement compared to embankment height or defective pile length.

7.3.3 Load transfer

The efficacies of both defective and non-defective piles considering Load Part A and B are plotted in Figure 7.22 against the stiffness reduction factor for the four embankment heights modelled. For each model run as part of the parametric study, there are two points plotted in Figure 7.22, one for the defective pile and another non-defective pile loads. The pile loads were taken at the end of embankment consolidation and estimated from stress points approximately 0.5 m below the top of the pile head, which is similar in location to where loads were measured within pile shafts in the centrifuge model tests. In measuring pile loads within the pile shaft, there is some variability amongst results due to differences in measurement locations depending on the FEM mesh. It is also noted that results have not been separated in Figure 7.22 based on the subsoil compressibility. Given that a stiffer subsoil will carry

more load (increased Load Part C), there is some scatter amongst results as subsoil compressibility does effect E_{A+B}. Also plotted in Figure 7.22 is the linear regression trendline for both defective and non-defective pile efficacies. While the E_{A+B}-R_k behaviour may be better represented by another relationship, likely a higher order power law, the linear relationship is presented to simply show general trends.

Both defective and non-defective piles supporting embankments with a height of 2.0 m (Figure 7.22a) were found to carry similar loads. Where a significant difference between defective and non-defective pile axial stiffness was modelled ($R_k < 0.4$) at this embankment height, defective piles carried slightly less load than non-defective piles. However, when R_k was greater than 0.4, all piles were found to carry a consistent efficacy of between 50 and 65%. This is likely due to the shallow height of the embankment not allowing arching to fully develop. Even though non-defective piles had the geotechnical capacity to carry a significantly greater load, the mobilised arching stresses within such shallow embankments could not facilitate any additional load transfer towards the pile heads.

Embankments with a height of 3.1 m (Figure 7.22b) exhibited a trend where defective piles carried greater efficacy with increasing values of R_k while non-defective piles carried less efficacy with increasing values of R_k. This behaviour was also evident for embankments with heights of 4.2 m and 6.0 m, with the E_{A+B}-R_k trendline for non-defective piles becoming steeper with increasing height. This behaviour suggests that when a defective pile carries less load due to its relatively softer load-settlement response, an adjacent non-defective pile may carry some additional load. This transfer of additional load towards the non-defective pile develops increasingly with greater embankment heights. However, this contradicts the observation that no significant difference was observed between loads measured in non-defective piles adjacent to or far away from a defective pile in the Model 2 centrifuge test. This is likely due to the relatively small amount of load transfer towards a non-defective pile adjacent to a defective pile that occurs for an embankment where $h_e = 4.2$ m, evidenced by the relatively low gradient of the trendline drawn for non-defective piles in Figure 7.22c.

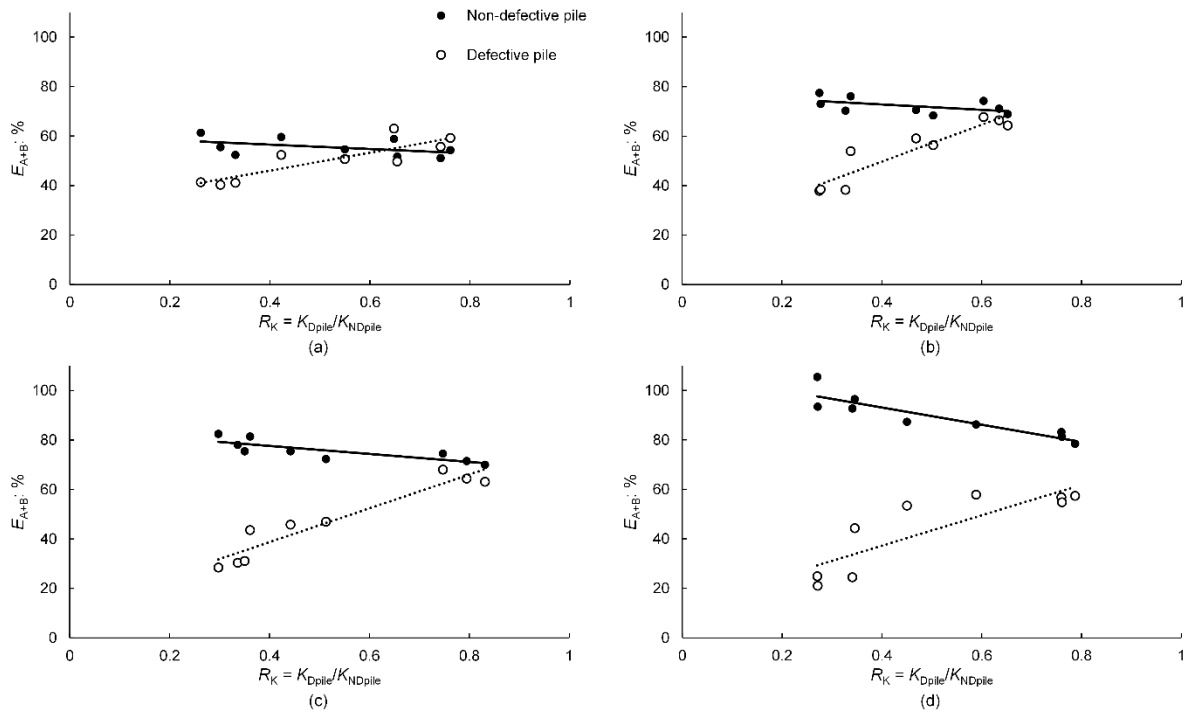

Figure 7.22: Pile efficacy considering Load Part A and B versus stiffness reduction factor for (a) h_e = 2.0 m; (b) h_e = 3.1 m; (c) h_e = 4.2 m; (d) h_e = 6.0 m

7.3.4 Geosynthetic reinforcement

The effect of geosynthetic stiffness on reducing differential settlements due to a defective pile was also investigated. This analysis was not performed as part of the full parametric study as it would have required many additional models. Instead three FEM models were analysed with a geosynthetic stiffness of J = 7200 kN/m (twice that used in the centrifuge model tests). These models comprised defective pile lengths of 6 m, 6.4 m and 6.8 m with parameters otherwise unchanged from the initial calibrated FEM model based on the Model 2 centrifuge test.

Differential settlement at the embankment surface versus differential settlement at the pile head level, both taken at the end of primary consolidation, is plotted in Figure 7.23 for the three models with a stiffer geosynthetic (J = 7200 kN/m) along with the corresponding models with the original geosynthetic stiffness (J = 3600 kN/m). It is evident that even a very stiff geosynthetic was not able to reduce differential settlements at the pile head or embankment surface substantially. While there is some reduction in differential settlement due to the stiffer geosynthetic reinforcement, this reduction is small and does not reduce differential settlements from an intolerable level to a tolerable level. This suggests that in the event that a defective pile is identified during construction, utilising stiffer geosynthetics or placing additional layers of geosynthetic reinforcement is not a practical or economical remedial option.

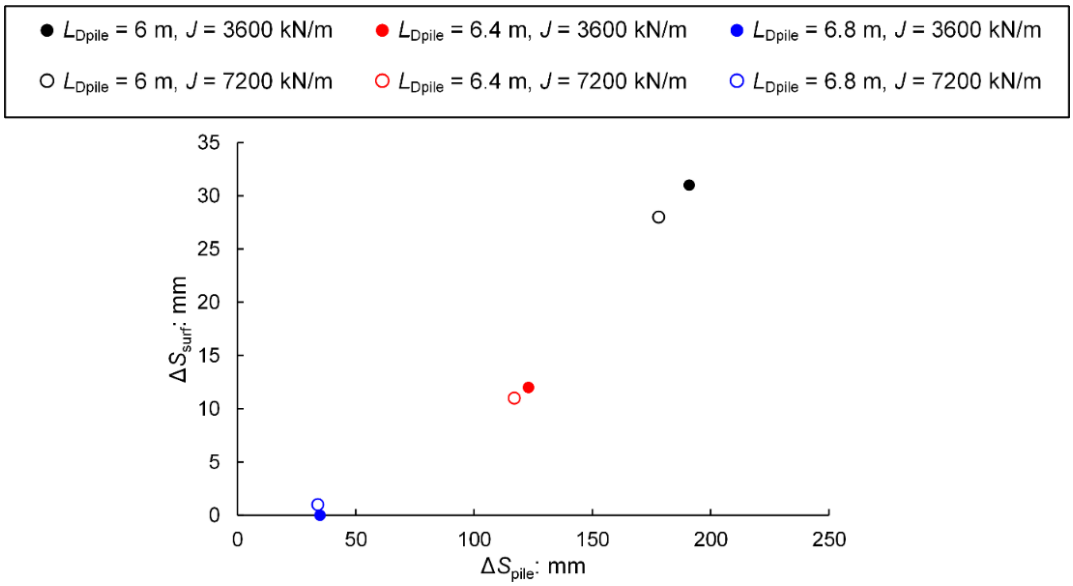

Figure 7.23: Differential surface settlement versus differential pile head settlement

7.4 Summary of findings

FEM modelling of GRPEs was undertaken based on the geometry and materials used within the centrifuge Model 2 detailed in Chapters 5 and 6. The initial model was calibrated based on laboratory testing of materials and validated against results from centrifuge modelling. Limitations were identified with the numerical model, which included the inability of the model to handle large and/or localised deformations as well as the failure of the soil constitutive model to replicate the strain softening behaviour exhibited in triaxial tests on sand.

The FEM model was able to replicate the general behaviour of the Model 2 centrifuge embankment. Settlements calculated from the FEM were in relatively close agreement with those measured from centrifuge modelling around the defective pile, both at the base and surface of the embankment. However, it was shown that the FEM model underestimated the differential surface settlement. This was attributed to the inability of the FEM to accurately model large deformations within the embankment sand. Thus, the results from the subsequent parametric analysis were interpreted qualitatively to understand general mechanisms and behaviour.

A parametric study was undertaken where the defective pile length, embankment height and subsoil compressibility were varied, resulting in 36 models being run. The key findings from the parametric study may be summarised as:

- Embankment height does not have a significant impact on whether differential settlement develops between defective and non-defective pile heads.

- The stiffness reduction factor has a strong influence on whether differential pile head settlement develops. As the stiffness reduction factor reduces (i.e. a defect becomes more severe/extensive), the defective pile undergoes more settlement, and thus, more differential settlement develops between pile heads.
- For a given stiffness reduction factor, whether differential surface settlement is or is not experienced at the embankment surface is strongly dependent on the embankment height. Differential settlements, either between piles or subsoil-piles, reduce with height above the pile heads due to shearing and volume change of the embankment material. Thus, higher embankments are less likely to experience adverse effects from the presence of a defective pile.
- Shallow embankments, where the embankment height is approximately equal to or less than the critical height, may be prone to differential settlements developing at the embankment surface if there is any difference in load-settlement response between piles.
- For shallow embankment heights, non-defective piles adjacent to a defective pile may carry some additional load due to their proximity to the defective pile; however, this additional load is likely to be small. With increasing embankment height, this additional load carried by non-defective piles will increase as there is a greater thickness of embankment material to facilitate this load transfer away from the defective pile and towards non-defective piles.

8 Research findings and practical outcomes

The research work presented in this thesis was undertaken to investigate the progressive development of soil arching in GRPEs as subsoil settles and defective piles settle. A combination of physical modelling at two scales and numerical modelling was performed to achieve the aims of the study. The findings are outlined in the following chapter as well as some of the practical outcomes from the current investigation. Based on these outcomes, several topics are proposed as possible areas for future research.

8.1 Research summary

8.1.1 Scope of research

It has been shown that the soil arching mechanism within GRPEs is time dependent as it progressively develops as subsoil undergoes consolidation. However, current design recommendations fail to consider this aspect and instead predict an arching stress that corresponds to a single state of arching, typically maximum or ultimate arching within the GRC framework proposed by Iglesia et al. (1999). These soil arching models are also unable to explain many of the phenomenon associated with soil arching in GRPEs, such as the development of a plane of equal settlement within the embankment at some height above the pile heads and the propagation of total settlement above this plane of equal settlement to the embankment surface. The clear majority of existing soil arching models have been shown to be based on assumed failure surfaces, without any observed soil kinematics, and contradict much of the observed soil arching behaviour.

Soil arching is also dependent on the settlement of pile heads. Pile heads may undergo differential settlement to each other when an individual pile is installed with a defect and exhibits a softer load-settlement response compared to the surrounding non-defective piles. Whether this differential settlement at the pile head level transpires to differential settlement being experienced at the embankment surface is essential to the performance of a GRPE. The ability of an LTP to redistribute loads towards and away from a defective pile and reduce differential settlements is a complex soil-structure-geosynthetic interaction problem.

The research undertaken was directed at addressing the knowledge gaps associated with the issues outlined above. The specific aims of the research were:

- To investigate how soil arching within an LTP progressively develops as subsoil undergoes consolidation.
- To examine how soil arching within an LTP gradually develops as an individual pile (defective pile) undergoes additional settlement relative to surrounding piles (non-defective piles).

- To investigate what conditions may lead to a defective pile causing adverse effects on the performance of a GRPE.

8.1.2 Research observations

The research undertaken to meet the aims outlined above comprised three major studies, 1*g* model tests, centrifuge model tests and numerical analysis. The methodology of these studies and important observations associated with them are described below.

1g small-scale model tests

Small-scale models were built to replicate the soil arching mechanism within a mass of granular material overlying pile heads on a scale where non-destructive imaging could be undertaken. Details of the experimental setup and measurment techniques were provided in Chapter 3. Models were built that simulated the progressive settlement of subsoil, and in some model tests, the progressive displacement of a single defective pile. Unfortunately, it was not feasible to use geosynthetic reinforcement at such scales due to the difficulty in manufacturing an appropriately scaled material, and as such, only the soil arching mechanism without geosynthetic reinforcement was studied.

Three forms of CT imaging were undertaken with different sources of radiation, including laboratory X-rays, neutrons and synchrotron X-rays. It was found that monochromatic synchrotron produced X-rays with an energy of 60 keV resulted in reconstructed volumes of the fine-grained sand with high image texture, i.e. high density of voxel information. The quality of these images was attributed to the high brilliance, coherent and low energy monochromatic X-ray beam achieved at the Australian Synchrotron IMBL facility.

With such high image texture, it was possible to apply the image correlation technique known as Digital Volume Correlation (DVC) to pairs of reconstructed CT volumes. DVC divides CT volumes into sub-volumes and applies cross-correlation between pairs of volumes to estimate the shift in similar voxel patterns. This shift is indicative of the displacement each sub-volume has undergone between CT scans, the accuracy of which can achieve sub-voxel accuracy. By progressively simulating subsoil consolidation within the small-scale models between CT scans, the incremental three-dimensional displacement vector field was obtained corresponding to different stages of subsoil settlement. This displacement vector field was then used to calculate the shear and volumetric strain fields within the sand mass overlying pile heads.

With three-dimensional displacement, shear strain and volumetric strain fields, which are the first to have been obtained for granular materials within piled embankments experimentally, insight was gained into the kinematics of soil arching in piled embankments and how it progressively develops with subsoil

settlement. Analysis of the soil arching kinematics were presented in Chapter 4. Some of the observations from this analysis include:

- The failure surfaces within the sand mass overlying pile heads indicate a mechanism develops that is analogous to that of a bearing failure beneath a circular shallow foundation, although vertically mirrored. Similar to shallow foundations, the failure mechanism is dependent on the soil state, including relative density and initial mean stress.
- Unlike the assumption made in many soil arching models where it is considered that a stable arch develops between pile heads, the observed failure surfaces above pile heads did not resemble an arch-like shape. Instead, failure surfaces in the form of shear bands were observed to develop above pile heads within the LTP granular material, which in the case of dense sand, interacted with the failure surfaces propagating from adjacent pile heads.
- The observed failure mechanisms within the model tests explain the observation of the progressive development of soil arching in piled embankments. The progressive development of soil arching may be attributed to the mobilisation of friction and dilation angles with relative shearing within shear bands. This mobilisation of strength with subsoil settlement is similar again to the progressive failure of a shallow foundation placed on dense sand, where a peak resistance is observed followed by an ultimate/residual resistance.
- It is evident from model tests that a plane of equal settlement (i.e. the critical height) develops at some height above the failure surfaces. At the top of the failure surfaces, there is still some differential settlement within the sand mass. This differential settlement requires some further height above the failure surfaces for a plane of equal settlement to form. Thus, $h_{cr} > h_{fs}$.
- Shearing was shown to continue with increasing subsoil settlement along the same failure surfaces that developed initially after small subsoil settlements. No sequential failure surfaces developed over the range of normalised subsoil settlements typical of a piled embankment. This shows that a plane of equal settlement develops regardless of how much subsoil settlement occurs. In trapdoor tests, the development of sequential failure surfaces that propagate to the soil surface after sufficient trapdoor displacement prevents the development of a plane of equal settlement.
- The failure surfaces observed also explain how settlements propagate above the critical height to the embankment surface. Arching models that assume a stable arch between piles cannot explain how this occurs because such an arch cannot remain stable while permitting displacements to propagate to the embankment surface. In the observed soil arching mechanism, shearing occurs along failure surfaces that allow settlements to propagate to the embankment surface, even after large amounts of subsoil settlement without a “breakdown of arching” that would occur with other commonly assumed arching models. It has been shown that subsoil

settlement will always result in some embankment surface settlement, although this settlement may be reduced by utilising highly dilative material within the LTP.

- The same failure surfaces as observed in tests without a defective pile developed above the defective pile head, albeit, the magnitude of strain within these failure surfaces was typically less in shear bands propagating from a defective pile head.
- The height above pile heads for a plane of equal settlement to develop was increased when a defective pile was present. The height of sand in the model tests allowed this plane of equal settlement to develop for models both with and without defective piles.
- The presence of a defective pile was shown not to affect the amount of total settlement that propagated above the critical height to the embankment surface.

Centrifuge model tests

Centrifuge model testing was performed on two model tests, the first of which (Model 1) modelled a GRPE supported on floating piles and the second (Model 2) modelled a GRPE supported on end-bearing piles (detailed in Chapter 5). While both model tests comprised piles installed into a founding stratum, Model 1 pile toes were founded within a firm clay while Model 2 pile toes were founded within a medium dense sand. Each model included two instrumented zones: Zone 1 comprised piles installed to the same depth and Zone 2 comprised a single pile installed short of the founding stratum and the surrounding piles, representative of a defective pile that exhibits a softer load-settlement response to the surrounding non-defective piles.

The models were constructed with the principle of replicating materials and processes as accurately as possible without incorporating surrogate materials to simulate mechanisms. To do so, the soft clay in both model tests was modelled by consolidating kaolin slurry in-flight to create a layer of clay with an OCR of 1.5. Piles were pushed into the prepared subsoil in-flight, replicating the installation of jacked full-displacement piles. Further, a low-density polyethylene geomembrane was used to simulate the geosynthetic reinforcement, which was shown to exhibit a similar axial stiffness to common high-strength prototype geotextiles used for basal reinforcement.

The results from these two centrifuge model tests were presented in Chapter 6. Some of the observations from this testing include the following:

- A defective pile, floating within a layer of very soft clay, underwent uniform settlement with the surrounding non-defective piles that were installed into a founding layer of firm clay. Given that no meaningful differential settlement was experienced at the pile head level, no differential settlement was observed at the embankment surface.
- A defective pile, floating within a layer of very soft clay, underwent additional settlement relative to the surrounding non-defective piles that were installed into a founding layer of

medium dense sand. Some of the additional settlement experienced at the pile head level propagated to the embankment surface, resulting in a localised depression forming above the defective pile.

- The area of the Model 2 embankment affected by the defective pile was approximately limited to the confines of the surrounding unit cell. Outside the boundary of this unit cell (defined in Chapter 1), the arching mechanism and embankment settlements were unaffected by the presence of a defective pile.
- The load transfer towards non-defective pile heads in the Model 2 embankment progressively developed as subsoil underwent consolidation. This load development was well described by a combination of the GRC concept to estimate arching stresses and an equation that was developed to estimate the progressive mobilisation of membrane actions. This equation for membrane actions approximated the geosynthetic sag as the sum of a cable deflecting between two pinned supports and a square membrane deflecting between four pinned edges, both under a uniform pressure.
- Given that uniform settlement was experienced in both model tests in areas where no defective piles were present, it is established that the height of the embankment was greater than the critical height, i.e. $h_e > h_{cr}$.
- Given that differential settlement was experienced at the embankment surface in Model 2 above the defective pile, the embankment height must have been insufficient for a plane of equal settlement to develop at this location of the embankment. The critical height was therefore locally increased due to the defective pile to a height greater than the embankment height, i.e. $h_e < h_{cr,def}$.

Numerical analysis

The finite element software PLAXIS was used to model the behaviour of GRPEs with defective piles. A unit cell was modelled to replicate the behaviour of the Model 2 centrifuge test in the zone where a defective pile was present (Zone 2). The constitutive models were first calibrated with laboratory testing, from which it was shown that the models and parameters used generally simulated the behaviour of the materials well. However, the granular embankment material (silica sand) exhibited strain softening under triaxial loading, which was not modelled by the hardening soil model, or any other soil constitutive model, available in PLAXIS 3D 2013. This was identified as a limitation of the numerical analysis.

The unit cell modelled the quarter volumes of four piles, one of which was a defective pile while the other three were non-defective piles. The results from the calibrated FEM model generally matched the displacements measured over the duration of the centrifuge model test. It was shown that the differential settlement that occurred at the embankment surface was underestimated by the FEM model, which was

considered to likely be a result of the inability of Lagrangian mesh-based FEM techniques to model localised deformations with high accuracy (Więckowski 2004). It was also noted that the pile load-settlement response was difficult to measure due to a significant portion of pile load and settlement occurring while the centrifuge ramped up to 40*g*. Nevertheless, the pile load-settlement response of the piles (both defective and non-defective) from the FEM model was in general agreement with the results from centrifuge modelling.

With a calibrated model, a parametric study was undertaken to qualitatively assess the effects of varying certain parameters on the performance of GRPEs with a single defective pile. The parameters that were varied were subsoil compressibility (C_c and C_r), defective pile length and embankment height. Details of the numerical analysis and the outcomes from this modelling were presented in Chapter 7. The following observations were made based on the results from the numerical analysis:

- Embankment height does not have a significant impact on whether differential settlement develops at the base of the embankment between defective and non-defective pile heads.
- The stiffness reduction factor has a strong influence on whether differential pile head settlement develops or not. As a defect becomes more severe, the defective pile undergoes more settlement, and thus, more differential settlement develops between pile heads.
- For a given pile defect, the amount of differential surface settlement experienced at the embankment surface is strongly dependent on the embankment height. Higher embankments are less likely to experience adverse effects from the presence of a defective pile.
- Shallow embankments, where the embankment height is approximately equal to or less than the critical height, are likely to experience differential surface settlement if a defective pile undergoes additional settlement to non-defective piles.
- For shallow embankment heights, non-defective piles adjacent to a defective pile may support some additional load due to their proximity to the defective pile; however, this additional load is likely to be small. With increasing embankment height, this additional load carried by non-defective piles will increase as there is a greater thickness of embankment material to facilitate this load transfer away from the defective pile towards the non-defective piles.
- Increasing the stiffness of geosynthetic reinforcement does not significantly reduce the settlement of a defective pile or the resulting differential settlement experienced at the embankment surface. Thus, using a stronger and stiffer geosynthetic or multiple layers of reinforcement is not a suitable remedial option for a defective pile.

8.2 Practical outcomes from research

8.2.1 Design based on subsoil settlement - Interaction diagram

Based on the observations from their centrifuge model testing, Ellis and Aslam (2009b) suggested that the design of GRPEs could be undertaken using an "interaction diagram". Such an approach would account for the progressive mobilisation of arching stresses, membrane actions and subsoil support. In their proposed diagram, Ellis and Aslam (2009b) characterised the arching stresses by the GRC method (Iglesia et al. 1999). While Ellis and Aslam (2009b) did not provide a framework to characterise the mobilisation of membrane actions and subsoil support, the general behaviour was described where Load Part A, B and C would eventually reach a state of equilibrium (if properly designed) after a certain amount of subsoil settlement. While the interaction diagram was only suggested for the purpose of discussion by Ellis and Aslam (2009b), it is considered that if such a method was developed then it would be possible to estimate the settlement required for stresses resulting from these three mechanisms (Load Part A, B and C) to reach equilibrium without any additional settlement. This would allow the design of GRPEs to consider serviceability requirements, where the pile geometry and geosynthetic reinforcement could be optimised to satisfy settlement tolerances.

The progressive development of load transfer observed in the Model 2 centrifuge test provides a further argument for the interaction diagram approach. It was shown in this test that equilibrium between arching, membrane and subsoil actions was not achieved until almost 10 years in prototype time after the commencement of the test, highlighting the time dependency GRPEs exhibit. Based on the agreement between this approach and the Model 2 centrifuge test results, a preliminary method is outlined below to estimate the stress distribution within a GRPE using an interaction diagram approach.

Load Part A

It was shown in Chapter 4 that the failure surfaces that develop above a pile head within LTP granular material are analogous to the failure surfaces that occur beneath a shallow foundation, although vertically mirrored. Similar to the response of a shallow foundation, the arching stress-settlement response within piled embankments typically exhibits a peak arching stress after a certain amount of settlement followed by a reduction in stress with increasing settlement. For the case of shallow foundations, there is no analytical solution for the progressive load-settlement response at present. This is also the case for the arching stress-settlement response in piled embankments. Even if a semi-analytical model was developed for estimating this stress-settlement response in piled embankments, it would require extensive validation, and therefore, time before it could be implemented in a design method. Thus, at this point in time, empirical solutions must be adopted in place of a more rigorous analytical solution if an interaction diagram design method is to be used.

As shown in Chapter 4, the development of sequential failure surfaces typically observed in trapdoor tests with ongoing trapdoor displacement does not occur in piled embankments. However, several studies have shown that the GRC, which was developed for trapdoor tests, is well suited to characterising the arching stress-displacement response of GRPEs (Ellis and Aslam 2009b; Zhuang et al. 2010; King et al. 2017a). It is noted that typical subsoil settlements beneath a GRPE do not exceed 15% normalised settlement/relative displacement. It is considered likely that the corresponding stages of the GRC for a trapdoor test (less than 15% relative displacement) is within the region of the GRC where trapdoor tests have not mobilised vertical Terzaghi-like failure surfaces. Instead the load recovery stage of the GRC has been mobilised. The behaviour of the load recovery stage in a trapdoor test may be attributed to post-peak shearing within the failure surfaces, which was also observed in the small-scale piled embankment model tests. This may explain why the GRC developed for trapdoor tests matches the behaviour of soil arching within piled embankments. Within the range of subsoil settlements typically experienced beneath a GRPE, soil above active trapdoors and within GRPEs undergo similar aching failure surfaces. With larger subsoil settlements, the two mechanisms may diverge as the soil above active trapdoors develops sequential failure surfaces that propagate to the surface, while the soil within GRPEs does not.

Given that the GRC has been shown by others, and the present study, to characterise the progressive development of soil arching in GRPEs well within the typical range of subsoil settlements, its use is recommended to estimate Load Part A. This is achieved by converting the three-dimensional geometry of the GRPE to an equivalent axisymmetric unit cell geometry so that the two-dimensional parameters of the Iglesia et al. (1999) GRC can be applied, as described by King et al. (2017a).

Load Part B

A solution was provided in Chapter 6 for the mobilisation of membrane actions as subsoil undergoes settlement based on piles in a square grid. This solution approximated the maximum deflection of a geosynthetic in the middle of four piles as the combination of the plane strain parabolic deflection between adjacent piles and the deflection of a square membrane between the corners of four piles. Both deflections were estimated assuming a uniformly applied stress σ'_{GR} causes the geosynthetic to sag. The stress σ'_{GR} is the net vertical stress carried by the geosynthetic and is the difference between the vertical stress acting at the base of the LTP between piles directly above the geosynthetic reinforcement (σ'_{LTP}) and the vertical stress acting on the surface of the subsoil (σ'_{s}). In deriving the geosynthetic sag solution, it was assumed that the stresses σ'_{GR}, σ'_{LTP} and σ'_{s} all act uniformly over the area above the subsoil. For completeness, the geosynthetic sag under a uniformly applied load is provided again:

$$\sigma'_{GR} = \frac{5.747 J \delta_{s,max}{}^{3}}{(s-a)^4} \tag{8.1}$$

Axisymmetric modelling of a geosynthetic under uniform vertical stress was undertaken by Smith (2005) using the finite difference software package FLAC to investigate the load-deflection response of the geosynthetic. The arrangement of the axisymmetric model is shown in Figure 8.1a. Smith (2005) modelled a geosynthetic with a stiffness of J = 1167 kN/m and varied the pile head radius (r_c) and total model radius (r_t). Considering that the total model radius is equal to half the equivalent area axisymmetric unit cell diameter (r_t = 1.128s/2) and the pile head radius is half the pile head diameter, the deflections predicted by Equation 8.1 may be compared to the results of axisymmetric modelling performed by Smith (2005). These results are plotted using normalised stresses and displacements in Figure 8.1b. While the axisymmetric model and Equation 8.1 approximate the geosynthetic deflection using different geometrical simplifications, it is shown that the two estimate similar deflections under a range of pile geometries.

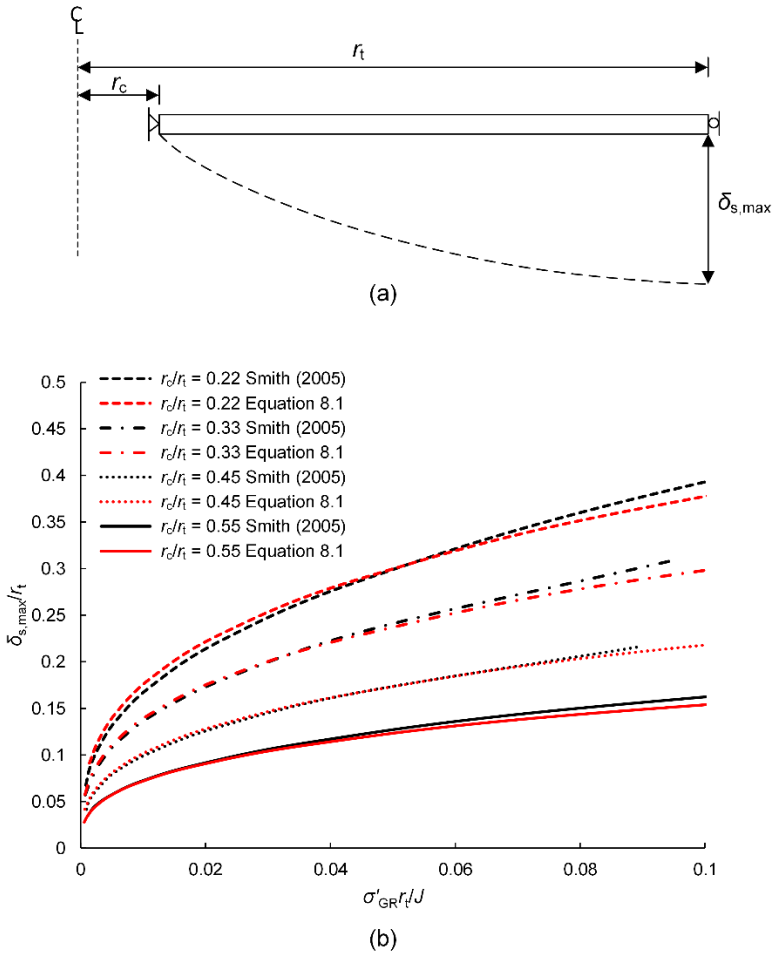

Figure 8.1: (a) Axisymmetric model used by Smith (2005); (b) results of numerical analysis compared with Equation 8.1

Load Part C

King et al. (2017b) described a method for estimating the subsoil settlement due to primary consolidation using Terzaghi's one-dimensional consolidation theory. In this method, the average percentage of consolidation completed was calculated using the equation:

$$U = 1 - \sum_{m=0}^{\infty} \frac{2}{M^2} e^{(-M^2 T)} \tag{8.2}$$

Where $M = \pi(2m + 1)/2$. Equation 8.2 may be solved iteratively to account for the mobilisation and progressive development of Load Part A and B. This can be done using a macro-enabled spreadsheet, which estimates the settlement over a small time-step. This settlement is then used to estimate a stress acting on the subsoil based on the GRC.

With the development of an equation that characterises the mobilisation of membrane actions with subsoil support (Equation 8.1) it is possible to estimate the stress acting on the subsoil from the mobilisation of Load Part A and B, i.e. $\sigma'_s = \sigma'_{LTP} - \sigma'_{GR}$. Thus, an interaction diagram can estimate the stress acting on the subsoil, which coupled with Terzaghi's one-dimensional consolidation theory, can be used to estimate subsoil settlement with time. With the known subsoil settlements, it is also possible to evaluate the embankment surface settlement with time using the method proposed by Russell et al. (2003).

While equilibrium within an interaction diagram may be achieved with some subsoil support, the assumption is often made that subsoil support will be lost at some stage of the structures operational life. This may occur due to, among other things, subsoil creep or primary consolidation resulting from changes in the effective stress state (e.g. due to changes in the water table). With the interaction diagram approach described above, it is possible to estimate the settlement that occurs during the construction period, prior to the placement of rigid structures, pavements or tracks. The remaining settlement required for the stress reduction ratio to reduce to zero (i.e. Load Part C = 0) may then be calculated, which is strongly dependent on the stiffness of the geosynthetic reinforcement. An example is provided below to highlight the features of an interaction diagram design approach.

Example

An example is provided below using the same geometry and properties as used in the example given by King et al. (2017b). An embankment is used with piles at 2.5 m centre-to-centre spacing with 0.8 m wide square pile caps support an embankment overlying a 7 m thick, soft clay deposit, the details of which are shown in Figure 8.2. For this example, the compressibility of the subsoil (OCR and C_c) and the rate of consolidation (c_v) will be varied to investigate how these properties affect the serviceability performance of an embankment.

The first step in a design based on an interaction diagram is to develop the GRC to estimate the contribution of Load Part A as subsoil undergoes consolidation. Using the method outlined by Iglesia et al. (1999), key parameters for the GRC can be estimated by transforming the GRPE geometry to an equivalent axisymmetric unit cell. Some of these parameters include:

- Initial vertical stress, $\sigma'_{v0} = 42.4$ kPa
- Stress on subsoil at maximum arching (minimum stress), $\sigma'_{s,min} = 12.9$ kPa
- Load recovery index, $\lambda = 5.261$
- Stress acting on the subsoil at ultimate arching, $\sigma'_{s,ult} = 29.2$ kPa

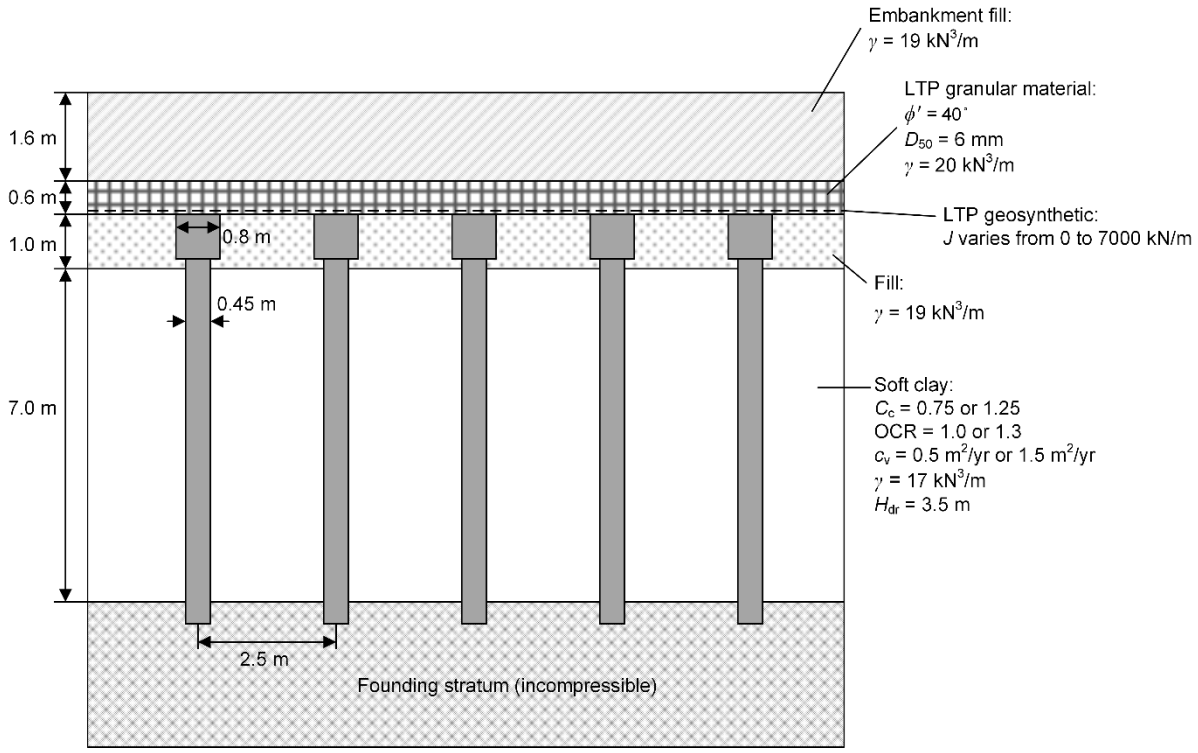

Figure 8.2: Example GRPE geometry, ground conditions and material properties

The GRC framework proposed by Iglesia et al. (1999) suggests that maximum arching occurs between 3% and 5% relative displacement while also providing several other plotting parameters (refer to the original manuscript for details). Along with some curve fitting techniques, it is possible to obtain a continuous GRC to plot σ'_{LTP} vs $\delta_{s,max}$, which is plotted using normalised parameters and shown as a solid line in Figure 8.3 ($J = 0$ kN/m). The load-deflection behaviour of the geosynthetic reinforcement is accounted for by Equation 8.1, which is used to estimate σ'_{GR} as subsoil undergoes consolidation for a range of geosynthetic stiffnesses. The contribution of the geosynthetic reinforcement is then added to the GRC (Load Part A) to develop the interaction diagram for various geosynthetic stiffnesses ranging from 0 kN/m (no reinforcement) up to 7000 kN/m, the results of which are also plotted in Figure 8.3.

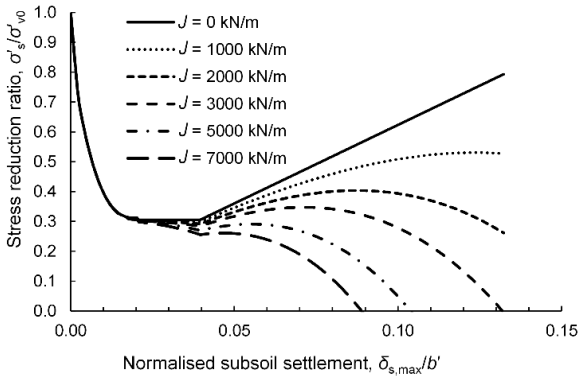

Figure 8.3: Interaction diagram for various geosynthetic stiffnesses

With the interaction diagram presented in Figure 8.3, it is possible to estimate the associated time-settlement plots for different subsoil conditions for each of the geosynthetic stiffnesses using one-dimensional consolidation theory. The results of this analysis performed using an iterative method to account for the progressive mobilisation of arching and membrane actions are presented in Figure 8.4 up to a period of t = 10 years. In this analysis, the interaction between the soft subsoil and piles is ignored, and it is assumed that the fill is placed instantly at t = 0 years.

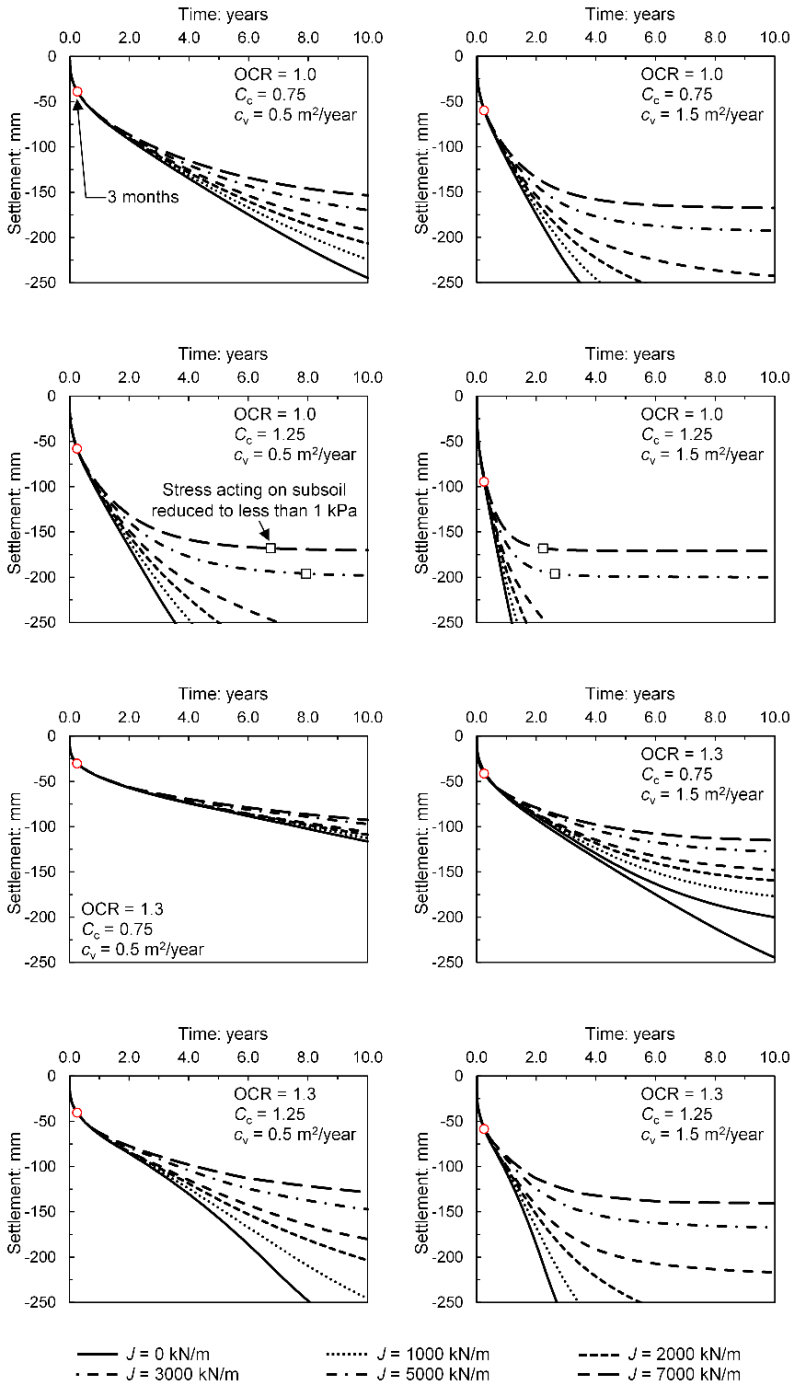

Figure 8.4: Settlement vs time plots for different values of OCR, C_c and c_v

It is shown in Figure 8.4 that in some cases equilibrium was achieved where settlements essentially ceased within 10 years. This equilibrium either resulted from primary consolidation approaching completion or by the loss of subsoil support. For normally consolidated clay with C_c = 1.25, the stress acting on the subsoil reduced to less than 1 kPa when a geosynthetic with a stiffness of either 5000 kN/m or 7000 kN/m was used. This observation indicates that subsoil support was lost when the subsoil

was highly compressible and resulted in the stiff geosynthetic undergoing sufficient sag to reduce the stress acting on the subsoil to essentially zero.

A construction period of 3 months is assumed for the purposes of discussion, which is indicated by a hollow red circle in Figure 8.4. It is evident that some subsoil settlement occurs during this construction period, which is greater for more compressible (higher values of C_c or lower values of OCR) or more permeable (higher values of c_v) subsoil. However, in all cases presented in Figure 8.4 equilibrium (loss of subsoil support or end of primary consolidation) was not achieved during construction, and post-construction settlements occurred. Using the method proposed by Russell et al. (2003), it is then possible to estimate the post-construction embankment surface settlement. This was performed for two cases, the results of which are shown in Figure 8.5. For this analysis, it was assumed that pile heads did not undergo settlement, and as such $S_{total} = S_e$. It is noted that models to estimate pile head settlement could be easily incorporated.

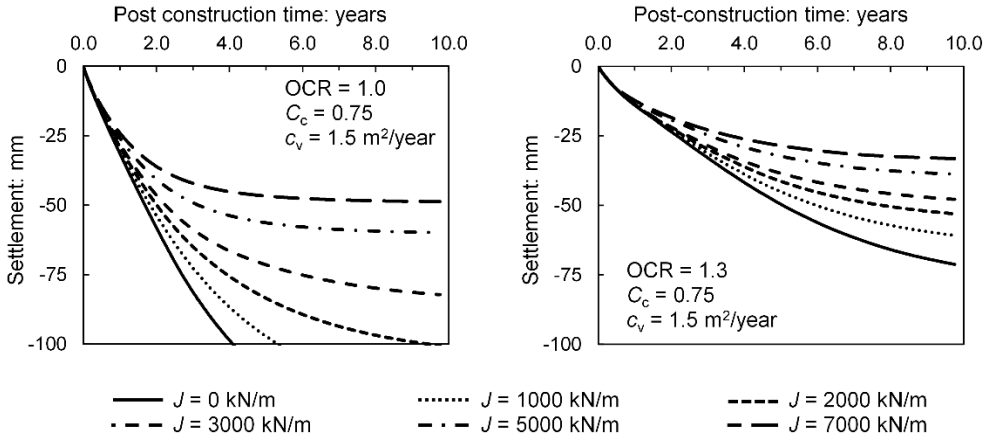

Figure 8.5: Post construction embankment surface settlement

From the results presented for the two cases in Figure 8.5, it is evident that excessive surface settlements (greater than 50 mm) would develop for both cases if geosynthetic reinforcement was not used. For the case shown in Figure 8.5 where the subsoil is slightly overconsolidated (OCR = 1.3), a stiff geosynthetic with J = 7000 kN/m is required to achieve post-construction settlements of approximately 30 mm, which is a typical requirement of many road and rail infrastructure projects. For the same conditions and geosynthetic stiffness where the soil is normally consolidated, post-construction settlements of approximately 50 mm occur. It is noted that this analysis does not consider creep effects, which would likely result in additional subsoil settlements. A prudent assumption to account for creep effects would be to assume subsoil loss will occur over the duration of the projects design life.

The settlements presented in Figure 8.5 highlight the difficulty for GRPEs to satisfy post-construction settlement requirements, which is not considered in many design methods such as BS8006 (2016), EBGEO (2011) or CUR226 (2016). These design methods typically prioritise ultimate limit state

conditions, e.g. ensuring the geosynthetic reinforcement has sufficient tensile strength to carry the imposed loads (Load Part B). While this should be ensured in the design of any GRPE, consideration must be given to satisfying serviceability requirements. For the cases presented in Figure 8.5, it would likely be required to adopt a higher replacement ratio with a stiff geosynthetic reinforcement or allow for a longer construction period to ensure that post-construction settlements could be reduced to below 30 mm.

It should be noted that CUR226 (2016) recommends that compressible material or sand without compaction is placed between pile heads. In doing so, the geosynthetic reinforcement undergoes sag almost instantly upon the placement of any overlying LTP or embankment fill, which mobilises membrane actions. While this is a valuable construction recommendation, existing design methods do not provide a means to quantify the benefit of adopting such an approach. With an interaction diagram, it is possible to calculate these membrane actions that are mobilised during the construction period. By placing compressible material between pile heads this approach increases the amount of subsoil settlement that occurs during the construction period, and thus, reduces the time and settlement required post-construction for equilibrium to be achieved.

8.2.2 Height of load transfer platform

There are benefits in using granular material within the LTP that exhibit high peak friction and dilation angles. In the model test presented in Chapter 4, dense sand led to a lower critical height and less settlement propagated from the settlement plate to the sand surface compared to the material that did not undergo as much dilation (medium dense sand). However, due to the expense to procure high-quality granular material, it is often desirable to reduce the volume of these materials within a project. As such, many design guidelines recommend a minimum height above the pile heads where high-quality granular materials must be placed, which is the height of the LTP (h_{LTP}). Above h_{LTP}, lower quality fill materials are often used as a cheaper alternative to these expensive, high-quality granular materials. The height above the pile heads where such high-quality granular materials are to be placed typically coincides with the minimum embankment height. For example, CUR226 (2016) recommends that for a height of $0.66(s_d - d)$ above the pile heads, which corresponds to their prediction of the critical height, granular material should exhibit a critical state friction angle of $\phi_{cv} \geq 35^{\circ}$. Above this height, a lower quality material may be used with $\phi_{cv} \geq 30^{\circ}$. This concept is demonstrated in Figure 8.6.

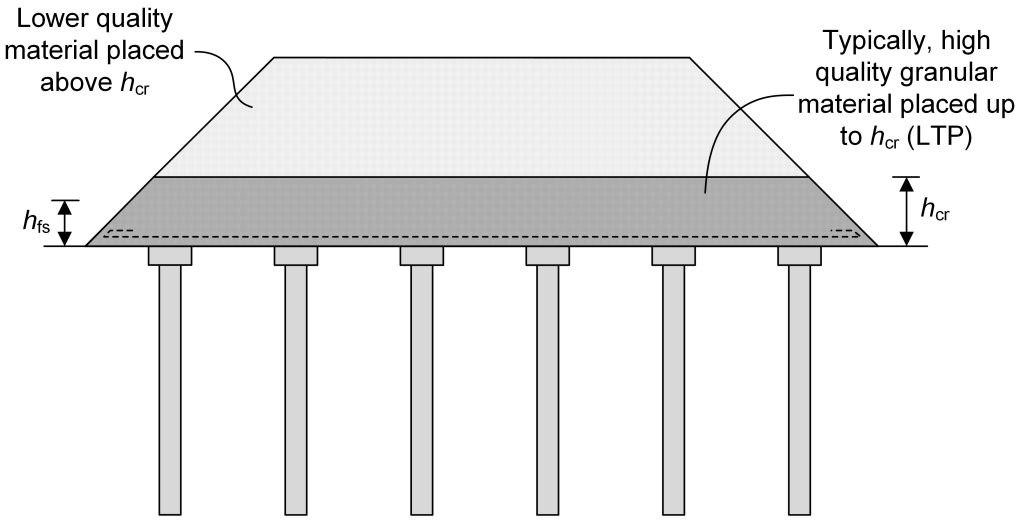

Figure 8.6: Placement of high-quality granular material directly above pile heads

It was shown in Chapter 4 that the height at which failure surfaces extend into the LTP above pile heads is less than the height at which a plane of equal settlement forms above pile heads, i.e. $h_{fs} < h_{cr}$. Given that the failure surfaces do not extend to the height at which a plane of equal settlement forms and the majority of shearing and load transfer occurs in the thickness of granular material below h_{fs}, it may be more economical to place high-quality granular material only up to a height of h_{fs} rather than h_{cr}. It is noted that granular fill materials should still be used above h_{fs} up h_{cr} as differential settlements will still cause some shearing in this thickness of material, although this granular material could be of lower quality and exhibit relatively lower friction and dilation angles. Given that above h_{cr} there is a uniform settlement profile within the embankment fill, fill materials above this height do not have to possess any specific friction or dilation properties for the purpose of load transfer or differential settlement reduction. Standard select fill can be used in accordance with local earthworks specifications above h_{cr}.

8.2.3 Critical height

While a method for estimating the critical height was not developed as part of this research, insight was gained into how the critical height develops. As such, comments can be made regarding the appropriateness of the assumptions made by some methods for estimating the critical height. Methods for estimating the critical height, or minimum permitted embankment height, adopted in the national design guidelines BS8006 (2016), EBGEO (2011) and CUR226 (2016) all estimate a height based on the clear spacing between piles. The ratio between the clear spacing and critical height is based on some assumed kinematics, without an in-depth understanding of the soil arching mechanism or observed kinematics. Further, these methods do not consider the mechanical properties of the granular material used within the LTP, which was shown in Chapter 4 to affect the critical height.

It has been shown that the critical height develops at some height above the height at which the failure surfaces extend into the LTP. The relationship between h_{fs} and h_{cr} is currently not well understood and is outside the scope of this research. However, it is anticipated that by studying this relationship, and how differential settlements reduce with height above h_{fs}, then an analytical model can be developed to estimate h_{cr}. Such a model would need to consider the deviatoric response of the LTP granular material.

For now, it seems appropriate to rely upon empirically derived relationships for estimating h_{cr} that are based on results from physical modelling, rather than relationships based on incorrect or assumed kinematics. The most reliable method for estimating h_{cr} in the author's opinion, at present, is the relationship proposed by McGuire (2011). This method is based on bench-scale model tests and has been shown to agree well with physical model testing and case studies (King et al. 2017b). Centrifuge modelling performed by Fagundes et al. (2015) also showed that the relationship for estimating h_{cr} proposed by McGuire (2011) was a better match with experimental results than the relationship proposed by BS8006 (2016).

8.2.4 Design around a defective pile

It has been shown that in many cases a defective pile will exhibit a softer load-settlement response to non-defective piles, and as a result, may undergo additional settlement to these other non-defective piles when installed within a group connected by an overlying LTP. In the event that a defective pile does undergo additional settlement, the height required for a plane of equal settlement to develop within the embankment will be increased from h_{cr} to $h_{cr,def}$. The magnitude of this increase will primarily depend on the severity of the pile defect and the additional settlement the defective pile experiences because of its defect.

With the increasing demand to construct GRPEs with shallow embankment heights, where h_e is approximately less than $1.5h_{cr}$, there is a significant risk that embankments will experience differential surfaces settlements if the underlying piles exhibit any differential axial stiffness. It is therefore essential that shallow height embankments are subjected to strict quality assurance (QA) and quality control (QC) practices to ensure that all piles exhibit consistent axial stiffness and undergo uniform settlement. In the event that a defective pile is installed within a shallow height embankment, the following remedial actions may be implemented:

- Install replacement pile(s). Consideration must be given to how the replacement pile will behave and interact with the LTP. For example, if the replacement pile is installed adjacent to the defective pile, the span between the replacement pile and the furthest adjacent non-defective pile must be such that the critical height above these piles is less than the embankment height.
- Or, increase the thickness of the LTP/embankment and do not install a replacement pile. While it may not be possible for the finished embankment surface to extend above a certain level,

there may be an opportunity to break the piles back, construct pile heads and place the base of the LTP at a lower level.

- Or, perform site testing/trials and rigorous analysis to confirm that the defective pile will not undergo additional settlement to the surrounding non-defective piles. If this can be established, then no remedial actions need to be undertaken. It is noted that conventional finite element analysis alone may not be sufficient to confirm this due to the limitations with these techniques as outlined in Chapter 7.

It was shown in Chapter 7 that increasing the stiffness of geosynthetic reinforcement does not significantly reduce differential settlements between a defective and non-defective piles at the pile head level or embankment surface. Thus, increasing the stiffness of the geosynthetic or placing multiple layers of reinforcement is unlikely to reduce differential settlements enough to satisfy design requirements.

It has been shown that tall GRPEs, where h_e is approximately greater than $2h_{cr}$, may have a sufficient thickness of fill materials for a plane of equal settlement to develop even in the event that a defective pile is installed and h_{cr} increases locally to $h_{cr,def}$. Thus, there is a greater level of redundancy in tall GRPEs, and there may be an ability for piles to exhibit differential stiffness while not affecting the performance of the embankment. However, if the granular material is placed only up to a height of h_{cr} with predominantly fine-grained materials used in the embankment fill above this height, these fine-grained materials will not reduce differential settlements as efficiently as coarse-grained materials. Thus, for tall GRPEs where a defective pile is installed, it is recommended that:

- Place granular material up to a height within the embankment of at least $2h_{cr}$, with the high-quality granular material used to a height of at least $2h_{fs}$.
- Or, install a replacement pile with the same considerations as outlined for shallow embankments.
- Or, confirm that the defective pile will not undergo additional settlement relative to the non-defective piles with the same considerations as outlined for shallow embankments.

It is noted that the analysis undertaken and recommendations presented are based on there being only one defective pile installed. In the event that multiple defective piles are identified within close proximity to each other, then replacement piles should be installed. Further testing and analysis is required to study the interaction between multiple defective piles.

8.3 Further research

While the aims of the study have been achieved, there remains the need for further research into the field of GRPEs. The research undertaken as part of this study has provided insight that may be used by

others to advance the state of knowledge regarding the mechanisms that occur within GRPEs. This research has also raised additional questions that warrant further study. Some topics that require further study are described below:

- There is a need to develop an arching method that considers the progressive development of soil arching stresses within a GRPE as subsoil settles. Ideally, this would be an analytical method, although such a method seems unlikely to be developed soon. It is therefore expected that an empirical method, potentially a chart based solution, would provide the most suitable method in place of a more rigorous analytical solution. It is envisaged that a chart based solution could be developed from a suite of physical model tests, which would preferably comprise centrifuge modelling to ensure scaling laws are satisfied.
- Reliable numerical techniques to simulate the behaviour of GRPEs need to be developed. Currently, mesh-based methods, such as conventional FEM, suffer mesh distortion in the LTP material overlying pile heads due to the localised strain that occurs around the singularity points. Further, it has been shown that strain softening may occur within these localisations, and as such, advanced constitutive models are needed. Meshfree methods or Eulerian-Lagrangian methods such as smoothed particle hydrodynamics (SPH) or material point method (MPM) may provide a means to deal with mesh distortion; however, such methods typically do not incorporate more advanced constitutive models.
- The relationship between the height above pile heads at which a plane of equal settlement develops and the height that failure surfaces extend into the LTP needs to be investigated. It was shown that the two are not equal and that the critical height is greater than the maximum height of failure surfaces. However, estimating the height above the failure surfaces that is required for a plane of equal settlement to develop was not investigated.
- Design charts should be developed to assist engineers in determining whether a defective pile will cause additional settlement at the embankment surface. In the research undertaken for this thesis, only two physical model tests were performed, which provided insight into what parameters influence the behaviour of a GRPE with a defective pile. However, to develop such design charts, additional physical modelling is required. Alternatively, a numerical analysis that that can be shown to model the behaviour of GRPEs with defective piles accurately could be used to develop these design charts if such modelling was calibrated with physical model tests, like those undertaken as part of this research.

9 Conclusions

Research has been undertaken into the progressive development of soil arching within GRPEs as subsoil and defective piles undergo settlement. Modelling, both physical and numerical, was undertaken to address the aims of the thesis. Small-scale 1*g* physical models were imaged using Synchrotron X-ray CT, the results of which were used to calculate three-dimensional displacement fields within a mass of sand overlying pile heads. While these small-scale models provided an opportunity to visualise soil arching kinematics, several scaling issues were identified while testing at 1*g*. To account for many of the limitations associated with the scaling of small-scale model tests, centrifuge modelling was performed on two models. A numerical model was then calibrated with the results obtained from centrifuge model tests. The calibrated numerical model was used to perform a parametric study investigating more arrangements and conditions that could be tested using centrifuge modelling.

The principal conclusions from this research may be divided into those relating to the behaviour of GRPEs with and without defective piles. Conclusions relating to GRPEs without defective piles may be summarised as:

- The failure mechanism within an LTP above pile heads is analogous to that of a shallow circular foundation, although vertically mirrored. Similar to shallow foundations, the failure mechanism is dependent on the soil state, including relative density and initial mean stress.
- The failure surfaces associated with soil arching in GRPEs do not take the form or resemble a simple arch-like shape, which is the assumption made by many soil arching models. Instead, failure surfaces in the form of shear bands were observed to develop above pile heads within the LTP granular material, which in the case of dense sand, interacted with the failure surfaces propagating from adjacent pile heads.
- The observed failure mechanism within the model tests explains the observation of the progressive development of soil arching in piled embankments. The progressive development of soil arching may be attributed to the mobilisation of strength with relative shearing within shear bands.
- Based on the observed soil arching mechanism, the progressive development of soil arching stresses for dense granular materials that exhibit high peak friction angles, high rates of dilation and post-peak softening can be expected to display similar arching-displacement responses as characterised by the GRC framework proposed by Iglesia et al. (1999): a maximum (or peak) state of arching develops after a small amount of subsoil settlement, followed by a load recover (or softening) stage with increasing subsoil settlement until an ultimate (or residual) state of arching is achieved.

- The critical height of a GRPE is dependent on not only the clear spacing between piles and the pile head geometry but also on the deviatoric response of the LTP granular material. This is not considered by most critical height theories currently available.
- Once sufficient subsoil settlement has occurred for the full critical height to be realised additional subsoil settlement will not affect the critical height.
- The critical height within GRPEs does not correspond with the height at which failure surfaces extend above pile heads into the LTP or embankment fill. Instead, the critical height is greater than the height of failure surfaces.
- The progressive development of load transfer towards pile heads within a GRPE was shown to be due to the mobilisation of soil arching and membrane actions. As noted, the development of soil arching stresses is well characterised by the GRC framework proposed by Iglesia et al. (1999). A method has been proposed for estimating the mobilisation of membrane actions as subsoil undergoes consolidation, which was shown to match experimental and numerical results.

Conclusions relating to defective piles supporting GRPEs may be summarised as:

- The same failure surfaces that develop above non-defective piles still develop above defective piles, albeit, with less strain mobilised within these failure surfaces when the defective pile undergoes additional settlement to non-defective piles.
- A plane of equal settlement may still develop above a defective pile, however, the height above the pile heads at which this plane forms is typically greater than the critical height for non-defective piles.
- Provided the embankment height is sufficient for a plane of equal settlement to develop, the presence of a defective pile does not affect the amount of total settlement that propagates above the critical height to the embankment surface.
- Whether a defective pile experiences differential settlement, and how much additional settlement, is dependent on the difference in axial stiffness between defective and non-defective piles. In the centrifuge modelling performed, it was shown that for floating piles a defective pile did not undergo additional settlement to the non-defective piles.
- As the stiffness reduction factor reduces (i.e. a defect becomes more severe/extensive), the defective pile undergoes more settlement, and thus, more differential settlement develops between pile heads.
- For the pile arrangement modelled (both centrifuge and numerical), it was shown that the piles and embankment surface outside of the unit cell surrounding a defective pile were not affected by the presence of a defective pile.
- Embankment height does not have a significant impact on whether differential settlement develops between defective and non-defective pile heads.

- For a given stiffness reduction factor, whether differential surface settlements is or is not experienced at the embankment surface is strongly dependent on the embankment height. Differential settlements, either between piles or subsoil-piles, reduce with height above the pile heads due to shearing and volume change of the embankment material. Thus, higher embankments are less likely to experience adverse effects from the presence of a defective pile.
- Shallow embankments, where the embankment height is approximately equal to the critical height, may be prone to differential settlements developing at the embankment surface if there is any difference in load-settlement response between piles.
- For shallow embankment heights, non-defective piles adjacent to a defective pile may carry some additional due to their proximity to the defective pile; however, this additional load is likely to be small. With increasing embankment height, this additional load carried by non-defective piles will increase as there is a greater thickness of embankment material to facilitate this load transfer away from the defective pile and towards non-defective piles.
- Increasing the stiffness of geosynthetic reinforcement is not an efficient or reliable remediation method when a defective pile is installed. Instead, the thickness of high-quality granular material above the pile heads should be increased or a replacement pile installed.

References

Abdrabbo, F., and Abouseeda, H. (2002). "Effect of construction procedures on the performance of bored piles." *Proceedings of Deep Foundations 2002: An International Perspective on Theory, Design, Construction, and Performance*, Orlando, Florida, 1438-1454.

Acosta-Martinez, H., and Gourvenec, S. (2006). "One-dimensional consolidation tests on kaolin clay." *Centre for Offshore Foundations Systems, The University of Western Australia*, GEO: 06385.

Adrian, R. J. (2005). "Twenty years of particle image velocimetry." *Experiments in fluids*, 39(2), 159-169.

Almeida, M., Ehrlich, M., Spotti, A., and Marques, M. (2007). "Embankment supported on piles with biaxial geogrids." *Proceedings of the Institution of Civil Engineers - Geotechnical Engineering*, 160(4), 185-192.

Altaee, A., and Fellenius, B. H. (1994). "Physical modeling in sand." *Canadian Geotechnical Journal*, 31(3), 420-431.

Anderson, I. S., McGreevy, R. L., and Bilheux, H. Z. (2009). "Neutron imaging and applications." Springer Science + Business Media, New York, USA.

Arthur, J., Dunstan, T., Al-Ani, Q., and Assadi, A. (1977). "Plastic deformation and failure in granular media." *Géotechnique*, 27(1), 53-74.

Aslam, R. (2008). "Centrifuge modelling of piled embankments." PhD thesis, University of Nottingham.

Bagbag, A. A., Lehane, B. M., and Doherty, J. P. (2017). "Predictions of footing and pressuremeter response in sand using a hardening soil model." *Proceedings of the Institution of Civil Engineers - Geotechnical Engineering*, 170(6), 479-492.

Banhart, J. (2008). "Advanced tomographic methods in materials research and engineering." Oxford University Press, Oxford, UK.

Baudouin, G., Thorel, L., and Rault, G. (2010). "3D load transfer in pile-supported earth platforms over soft soils: Centrifuge modeling." *Proceedings of 7th international Conference on Physical Modelling in Geotechnics*, 1303-1308.

Bay, B. K., Smith, T. S., Fyhrie, D. P., and Saad, M. (1999). "Digital volume correlation: three-dimensional strain mapping using X-ray tomography." *Experimental mechanics*, 39(3), 217-226.

Been, K., and Jefferies, M. G. (1985). "A state parameter for sands." *Géotechnique*, 35(2), 99-112.

Bienen, B., Ragni, R., Cassidy, M. J., and Stanier, S. A. (2015). "Effects of consolidation under a penetrating footing in carbonate silty clay." *Journal of Geotechnical and Geoenvironmental Engineering*, 141(9), 04015040.

Blanc, M., Rault, G., Thorel, L., and Almeida, M. (2013). "Centrifuge investigation of load transfer mechanisms in a granular mattress above a rigid inclusions network." *Geotextiles and Geomembranes*, 36, 92-105.

Blanc, M., Thorel, L., Girout, R., and Almeida, M. (2014). "Geosynthetic reinforcement of a granular load transfer platform above rigid inclusions: comparison between centrifuge testing and analytical modelling." *Geosynthetics International*, 21(1), 37-52.

Blight, G. (1986). "Pressures exerted by materials stored in silos: part I, coarse materials." *Géotechnique*, 36(1), 33-46.

Bolton, M. (1986). "The strength and dilatancy of sands." *Géotechnique*, 36(1), 65-78.

Briançon, L., and Simon, B. (2012). "Performance of pile-supported embankment over soft soil: full-scale experiment." *Journal of Geotechnical and Geoenvironmental Engineering*, 138(4), 551-561.

Brinkgreve, R., Engin, E., and Swolfs, W. (2013). "Plaxis 3D 2013 Manual." Plaxis BV, Delft, the Netherlands.

Brooks, R. A., and Di Chiro, G. (1976). "Beam hardening in x-ray reconstructive tomography." *Physics in Medicine & Biology*, 21(3), 390-398.

Brunke, O., Brockdorf, K., Drews, S., Müller, B., Donath, T., Herzen, J., and Beckmann, F. (2008). "Comparison between X-ray tube based and synchrotron radiation based μCT." *Proceedings of Developments in X-Ray Tomography VI*, San Diego, USA, SPIE.
BS8006 (1995). "BS8006." British Standard Institution, London, UK.
BS8006 (2010). "BS8006-1." British Standard Institution, London, UK.
BS8006 (2016). "BS8006-1:2010+A1:2016." British Standard Institution, London, UK.
Buckingham, E. (1914). "On physically similar systems; illustrations of the use of dimensional equations." *Physical review*, 4(4), 345.
Burland, J. B. (1965). "The yieding and dilation of clay." *Géotechnique*, 15(1), 211-214.
Carmignato, S., Dewulf, W., and Leach, R. (2018). "Industrial X-ray computed tomography." Springer, Swtizerland.
Chen, L. T., Poulos, H., and Loganathan, N. (1999). "Pile responses caused by tunneling." *Journal of Geotechnical and Geoenvironmental Engineering*, 125(3), 207-215.
Chen, R., Wang, Y., Ye, X., Bian, X., and Dong, X. (2016). "Tensile force of geogrids embedded in pile-supported reinforced embankment: A full-scale experimental study." *Geotextiles and Geomembranes*, 44(2), 157-169.
Chen, W. F. (1975). "Limit analysis and soil plasticity." Ross Publishing, Plantation, FL, USA.
Chen, Y. M., Cao, W. P., and Chen, R. P. (2008). "An experimental investigation of soil arching within basal reinforced and unreinforced piled embankments." *Geotextiles and Geomembranes*, 26(2), 164-174.
Cheong, J. (2002). "Physical testing of jack-up footings on sand subjected to torsion." BE Honours thesis, The University of Western Australia.
Chevalier, B., Combe, G., and Villard, P. (2012). "Experimental and discrete element modeling studies of the trapdoor problem: influence of the macro-mechanical frictional parameters." *Acta Geotechnica*, 7(1), 15-39.
Chevalier, B., and Otani, J. (2011). "Arching observation in three-dimensional trapdoor problem with x-ray CT and discrete element method." *Soils and foundations*, 51(3), 459-469.
Chew, S., Phoon, H., Le Hello, B., and Villard, P. (2006). "Geosynthetic reinforced piled embankment: large-scale model tests and numerical modeling." *Proceedings of 8th International conference on geosynthetics, Geosynthetics*, Yokohama, Japan, 18-22.
Chow, S. H., Le, J., Forsyth, M., and O'Loughlin, C. D. (2018a). "Capacity of vertical and horizontal plate anchors in sand under normal and shear loading." *Proceedings of 9th International Conference on Physical Modelling in Geotechnics*, London, UK.
Chow, S. H., O'Loughlin, C. D., Gaudin, C., and Lieng, J. T. (2018b). "Drained monotonic and cyclic capacity of a dynamically installed plate anchor in sand." *Ocean Engineering*, 148, 588-601.
Chung, S. F., Randolph, M. F., and Schneider, J. A. (2006). "Effect of penetration rate on penetrometer resistance in clay." *Journal of geotechnical and geoenvironmental engineering*, 132(9), 1188-1196.
Cocjin, M., Gourvenec, S., White, D., and Randolph, M. (2014). "Tolerably mobile subsea foundations–observations of performance." *Géotechnique*, 64(11), 895-909.
Collin, J. (2007). "US State-of-practice for the design of the geosynthetic reinforced load transfer platform in column supported embankments." *Proceedings of Geo-Denver 2007*, Denver, Colorado, USA.
Colreavy, C., O'Loughlin, C. D., and Randolph, M. F. (2016). "Experience with a dual pore pressure element piezoball." *International Journal of Physical Modelling in Geotechnics*, 16(3), 101-118.
Conte, E., Donato, A., and Troncone, A. (2013). "Progressive failure analysis of shallow foundations on soils with strain-softening behaviour." *Computers and Geotechnics*, 54, 117-124.
Costa, Y. D., Zornberg, J. G., Bueno, B. S., and Costa, C. L. (2009). "Failure mechanisms in sand over a deep active trapdoor." *Journal of Geotechnical and Geoenvironmental Engineering*, 135(11), 1741-1753.
Cryer, C. (1963). "A comparison of the three-dimensional consolidation theories of Biot and Terzaghi." *The Quarterly Journal of Mechanics and Applied Mathematics*, 16(4), 401-412.

Cui, Z. D., Yuan, Q., and Yang, J. Q. (2017). "Laboratory model tests about the sand embankment supported by piles with a cap beam." *Geomechanics and Geoengineering*, 13(1), 64-76.
CUR226 (2010). "Dutch design guideline for piled embankments (in Dutch)." SBR CURnet & CRC press, Delft, the Netherlands.
CUR226 (2016). "Dutch design guideline for piled embankments." SBR CURnet & CRC press, Delft, the Netherlands.
Darve, F., Servant, G., Laouafa, F., and Khoa, H. (2004). "Failure in geomaterials: continuous and discrete analyses." *Computer methods in applied mechanics and engineering*, 193(27-29), 3057-3085.
Das, B. M., and Larbi-Cherif, S. (1983). "Bearing capacity of two closely-spaced shallow foundations on sand." *Soils and foundations*, 23(1), 1-7.
De Catania, S., Breen, J., Gaudin, C., and White, D. J. (2010). "Development of a multiple axis actuator control system." *Proceedings of 7th International Conference on Physical Modelling in Geotechnics*, Zurich, Switzerland, 325-330.
de Lima, L. C. (2017). "Construction Effects on the Side Shear of Drilled Shafts." PhD thesis, University of South Florida.
Deb, K., Basudhar, P., and Chandra, S. (2007). "Generalized model for geosynthetic-reinforced granular fill-soft soil with stone columns." *International Journal of Geomechanics*, 7(4), 266-276.
Deltares, and Van Eekelen, S. J. M. (2015). "Concentric Arches Model Spreadhseet." <https://publicwiki.deltares.nl/display/PE/Piled+embankments>. (18th April, 2018).
Desrues, J., Lanier, J., and Stutz, P. (1985). "Localization of the deformation in tests on sand sample." *Engineering fracture mechanics*, 21(4), 909-921.
Dewoolkar, M. M., Santichaianant, K., and Ko, H.-Y. (2007). "Centrifuge modeling of granular soil response over active circular trapdoors." *Soils and Foundations*, 47(5), 931-945.
Diemoz, P., Bravin, A., and Coan, P. (2012). "Theoretical comparison of three X-ray phase-contrast imaging techniques: propagation-based imaging, analyzer-based imaging and grating interferometry." *Optics express*, 20(3), 2789-2805.
Dierick, M., Masschaele, B., and Van Hoorebeke, L. (2004). "Octopus, a fast and user-friendly tomographic reconstruction package developed in LabView." *Measurement Science and Technology*, 15(7), 1366-1370.
Dubsky, S., Hooper, S. B., Siu, K. K., and Fouras, A. (2012). "Synchrotron-based dynamic computed tomography of tissue motion for regional lung function measurement." *Journal of The Royal Society Interface*, 9(74), 2213-2224.
Dunnicliff, J. (1988). "Geotechnical instrumentation for monitoring field performance." John Wiley & Sons, New York.
Dyson, G., and Randolph, M. (2001). "Monotonic lateral loading of piles in calcareous sand." *Journal of Geotechnical and Geoenvironmental Engineering*, 127(4), 346-352.
EBGEO (2011). "Recommendations for Design and Analysis of Earth Structures using Geosynthetic Reinforcements." German Geotechnical Society, Wilhelm Ernst & Sohn, Berlin, Germany.
Ellis, E., and Aslam, R. (2009a). "Arching in piled embankments: comparison of centrifuge tests and predictive methods-part 1 of 2." *Ground Engineering*, 42(6), 34-38.
Ellis, E., and Aslam, R. (2009b). "Arching in piled embankments: comparison of centrifuge tests and predictive methods-part 2 of 2." *Ground Engineering*, 42(7), 28-30.
Elsinga, G. E., Scarano, F., Wieneke, B., and van Oudheusden, B. W. (2006). "Tomographic particle image velocimetry." *Experiments in fluids*, 41(6), 933-947.
Engesser, F. (1882). "Ueber den Erdduck gegen innere Stützwande (Tunnelwande)." *Deutsche Bauzeitung*, 16, 91-93.
Eskişar, T., Otani, J., and Hironaka, J. (2012). "Visualization of soil arching on reinforced embankment with rigid pile foundation using X-ray CT." *Geotextiles and Geomembranes*, 32, 44-54.
Evans, C. H. (1983). "An examination of arching in granular soils." MSci. thesis, Massachusetts Institute of Technology.
Fagundes, D. F., Almeida, M. S., Girout, R., Blanc, M., and Thorel, L. (2015). "Behaviour of piled embankment without reinforcement." *Proceedings of the Institution of Civil Engineers - Geotechnical Engineering*, 168(6), 514-525.

Fagundes, D. F., Almeida, M. S., Thorel, L., and Blanc, M. (2017). "Load transfer mechanism and deformation of reinforced piled embankments." *Geotextiles and Geomembranes*, 45(2), 1-10.
Feld, J. (1948). "Early history and bibliography of soil mechanics." *Proceedings of Second International Conference on Soil Mechanics and Foundation Engineering*, Rotterdam, Netherlands, 1-7.
Filz, G. M., Sloan, J., McGuire, M. P., Collin, J., and Smith, M. E. (2012). "Column-supported embankments: settlement and load transfer." *Proceedings of Geotechnical Engineering State of the Art and Practice from GeoCongress 2012*, Oakland, USA, ASCE, 54-77.
Filz, G. M., and Smith, M. E. (2006). "Design of bridging layers in geosynthetic-reinforced, column-supported embankments." Virginia Transportation Research Council, Charlottesville, Virginia, USA.
Finnie, I. M. S., and Randolph, M. F. (1994). "Punch-through and liquefaction induced failure of shallow foundations on calcareous sediments." *Proceedings of International Conference on Behaviour of Offshore Structures*, Boston, MA, USA, 217-230.
Fioravante, V. (2002). "On the shaft friction modelling of non-displacement piles in sand." *Soils and Foundations*, 42(2), 23-33.
Foray, P., Balachowski, L., and Rault, G. (1998). "Scale effect in shaft friction due to the localization of deformations." *Proceedings of International Conference Centrifuge 98*, Tokyo, Japan, 211-216.
Garbe, U., Randall, T., Hughes, C., Davidson, G., Pangelis, S., and Kennedy, S. (2015). "A new neutron radiography/tomography/imaging station DINGO at OPAL." *Physics Procedia*, 69, 27-32.
Garnier, J., Gaudin, C., Springman, S. M., Culligan, P. J., Goodings, D. J., Konig, D., Kutter, B. L., Phillips, R., Randolph, M. F., and Thorel, L. (2007). "Catalogue of scaling laws and similitude questions in geotechnical centrifuge modelling." *International Journal of Physical Modelling in Geotechnics*, 7(3), 1-23.
Gaudin, C., O'loughlin, C., Randolph, M., and Lowmass, A. (2006). "Influence of the installation process on the performance of suction embedded plate anchors." *Géotechnique*, 56(6), 381-391.
Gaudin, C., White, D., Boylan, N., Breen, J., Brown, T., De Catania, S., and Hortin, P. (2009). "A wireless high-speed data acquisition system for geotechnical centrifuge model testing." *Measurement Science and Technology*, 20(9), 095709.
Giroud, J.-P. (1981). "Designing with geotextiles." *Matériaux et Construction*, 14, 257-272.
Giroud, J. (1995). "Determination of geosynthetic strain due to deflection." *Geosynthetics International*, 2(3), 635-641.
Girout, R., Blanc, M., Dias, D., and Thorel, L. (2014). "Numerical analysis of a geosynthetic-reinforced piled load transfer platform–validation on centrifuge test." *Geotextiles and Geomembranes*, 42(5), 525-539.
Girout, R., Blanc, M., Thorel, L., and Dias, D. (2018). "Geosynthetic reinforcement of pile-supported embankments." *Geosynthetics International*, 25(1), 37-49.
Girout, R., Blanc, M., Thorel, L., Fagundes, D. F., and Almeida, M. S. (2016). "Arching and deformation in a piled embankment: centrifuge tests compared to analytical calculations." *Journal of Geotechnical and Geoenvironmental Engineering*, 142(12), 04016069.
Gniel, J., and Haberfield, C. (2014). "Design, construction and performance of a tied-wall embankment supported on concrete column ground improvement." *Proceedings of International Conference on Geotechnical Engineering: Soil-Structure Interaction, Underground Structures and Retaining Walls*, St Petersburg, Russia, IOS Press, 18-27.
Gourvenec, S., and Randolph, M. F. (2010). "Consolidation beneath circular skirted foundations." *International Journal of Geomechanics*, 10(1), 22-29.
Gui, M., and Bolton, M. (1998). "Geometry and scale effects in CPT and pile design." *Geotechnical site characterization. Edited by PK Robertson and PW Mayne. Balkema, Rotterdam*, 1063-1068.
Gureyev, T. E., Nesterets, Y., Ternovski, D., Thompson, D., Wilkins, S. W., Stevenson, A. W., Sakellariou, A., and Taylor, J. A. (2011). "Toolbox for advanced X-ray image processing." *Proceedings of Advances in Computational Methods for X-Ray Optics II*, San Diego, USA, SPIE.
Hainsworth, J., and Aylmore, L. (1983). "The use of computer assisted tomography to determine spatial distribution of soil water content." *Soil Research*, 21(4), 435-443.

Hall, C., Hausermann, D., Maksimenko, A., Astolfo, A., Siu, K., Pearson, J., and Stevenson, A. (2013). "Detectors for the imaging and medical beam line at the Australian synchrotron." *Journal of Instrumentation*, 8(6), C06011.

Halvordson, K., Plaut, R., and Filz, G. (2010). "Analysis of geosynthetic reinforcement in pile-supported embankments. Part II: 3D cable-net model." *Geosynthetics International*, 17(2), 68-76.

Han, J., Wang, F., Al-Naddaf, M., and Xu, C. (2017). "Progressive Development of Two-Dimensional Soil Arching with Displacement." *International Journal of Geomechanics*, 17(12), 04017112.

Handy, R. L. (1985). "The arch in soil arching." *Journal of Geotechnical Engineering*, 111(3), 302-318.

Harris, H. G., and Sabnis, G. (1999). "Structural modeling and experimental techniques." CRC press, Boca Raton, FL, USA.

Hewlett, W., and Randolph, M. (1988). "Analysis of piled embankments." *Ground Engineering*, 22(3), 12-18.

Hong, W. P., Hong, S., and Song, J. S. (2011). "Load transfer by punching shear in pile-supported embankments on soft grounds." *Marine Georesources & Geotechnology*, 29(4), 279-298.

Hong, W. P., Lee, J. H., and Lee, K. W. (2007). "Load transfer by soil arching in pile-supported embankments." *Soils and foundations*, 47(5), 833-843.

House, A., Oliveira, J., and Randolph, M. (2001). "Evaluating the coefficient of consolidation using penetration tests." *International Journal of Physical Modelling in Geotechnics*, 1(3), 17-26.

Huang, J., and Han, J. (2009). "3D coupled mechanical and hydraulic modeling of a geosynthetic-reinforced deep mixed column-supported embankment." *Geotextiles and Geomembranes*, 27(4), 272-280.

Iglesia, G. R. (1991). "Trapdoor Experiments on the Centrifuge: A Study of Soil Arching in Geomaterials and Similitude in Geotechnical Models." PhD thesis, Massachusetts Institute of Technology.

Iglesia, G. R., Einstein, H. H., and Whitman, R. V. (1999). "Determination of vertical loading on underground structures based on an arching evolution concept." *Proceedings of Geo-Engineering for Underground Facilities*, University of Illinois, Illinois, USA, 495-506.

Iglesia, G. R., Einstein, H. H., and Whitman, R. V. (2013). "Investigation of soil arching with centrifuge tests." *Journal of Geotechnical and Geoenvironmental engineering*, 140(2).

Jacobsz, S. (2016). "Trapdoor experiments studying cavity propagation." *Proceedings of 1st Southern African Geotechnical Conference*, Durban, South Africa, CRC Press, 159-165.

Janssen, H. (1895). "Versuche über getreidedruck in silozellen (in German)." *Zeitschrift des Vereines deutscher Ingenieure*, 1045-1049.

Jenck, O., Dias, D., and Kastner, R. (2005). "Soft ground improvement by vertical rigid piles two-dimensional physical modelling and comparison with current design methods." *Soils and Foundations*, 45(6), 15-30.

Jenck, O., Dias, D., and Kastner, R. (2007). "Two-dimensional physical and numerical modeling of a pile-supported earth platform over soft soil." *Journal of Geotechnical and Geoenvironmental Engineering*, 133(3), 295-305.

Jin, P., Bouman, C. A., and Sauer, K. D. (2015). "A Model-Based Image Reconstruction Algorithm With Simultaneous Beam Hardening Correction for X-Ray CT." *IEEE Transactions on Computational Imaging*, 1(3), 200-216.

Jones, B., Plaut, R., and Filz, G. (2010). "Analysis of geosynthetic reinforcement in pile-supported embankments. Part I: 3D plate model." *Geosynthetics International*, 17(2), 59-67.

Jones, C., Lawson, C., and Ayres, D. (1990). "Geotextile reinforced piled embankments." *Proceedings of 4th International Conference on Geotextiles: Geomembranes and Related Products. Rotterdam: AA Balkema*, 155-160.

Kak, A. C., and Slaney, M. (2001). "Principles of computerized tomographic imaging." Society for Industrial and Applied Mathematics, Philadelphia, PA, USA.

Kempfert, H., Göbel, C., Alexiew, D., and Heitz, C. (2004). "German recommendations for reinforced embankments on pile-similar elements." *Proceedings of EuroGeo3*, Munich, Germany, 279-284.

Khabbazian, M., Kaliakin, V. N., and Meehan, C. L. (2015). "Column supported embankments with geosynthetic encased columns: validity of the unit cell concept." *Geotechnical and Geological Engineering*, 33(3), 425-442.
King, D. J., Bouazza, A., Gniel, J. R., Rowe, R. K., and Bui, H. H. (2017a). "Load-transfer platform behaviour in embankments supported on semi-rigid columns: implications of the ground reaction curve." *Canadian Geotechnical Journal*, 54(8), 1158-1175.
King, D. J., Bouazza, A., Gniel, J. R., Rowe, R. K., and Bui, H. H. (2017b). "Serviceability design for geosynthetic reinforced column supported embankments." *Geotextiles and Geomembranes*, 45(4), 261-279.
King, D. J., Bouazza, A., Gniel, J. R., Rowe, R. K., and Bui, H. H. (2018). "Geosynthetic reinforced column supported embankments and the role of ground improvement installation effects." *Canadian Geotechnical Journal*, 55(6), 792-809.
Kishida, H., and Uesugi, M. (1987). "Tests of the interface between sand and steel in the simple shear apparatus." *Géotechnique*, 37(1), 45-52.
Kitazume, M., and Maruyama, K. (2007). "Internal stability of group column type deep mixing improved ground under embankment loading." *Soils and Foundations*, 47(3), 437-455.
Kong, L., and Zhang, L. (2004). "Lateral or torsional failure modes in vertically loaded defective pile groups." *Proceedings of GeoSupport 2004: Drilled Shafts, Micropiling, Deep Mixing, Remedial Methods, and Specialty Foundation Systems*, Orlando, Florida, USA, 625-636.
Kulhawy, F. H., and Mayne, P. W. (1990). "Manual on estimating soil properties for foundation design (Report EL-6800)." Electric Power Research Institute, Palo Alto, CA, USA, 306.
Kumar, A., and Saran, S. (2003). "Closely spaced footings on geogrid-reinforced sand." *Journal of geotechnical and geoenvironmental engineering*, 129(7), 660-664.
Kutter, B., Chang, J., and Davis, B. (1994). "Collapse of cavities in sand and particle size effects." *Proceedings of Centrifuge 94*, Singapore, 809-815.
Ladanyi, B., and Hoyaux, B. (1969). "A study of the trap-door problem in a granular mass." *Canadian Geotechnical Journal*, 6(1), 1-14.
Lai, H.-J., Zheng, J.-J., Zhang, R.-J., and Cui, M.-J. (2018). "Classification and characteristics of soil arching structures in pile-supported embankments." *Computers and Geotechnics*, 98, 153-171.
Langhaar, H. L. (1980). "Dimensional analysis and theory of models." Robert E. Krieger publishing company, Huntington, New York, USA.
Lavasan, A. A., and Ghazavi, M. (2012). "Behavior of closely spaced square and circular footings on reinforced sand." *Soils and Foundations*, 52(1), 160-167.
Lee, S., Leung, C., and Chow, Y. (2005). "Performance of oil tank foundation." *Proceedings of Geo-Frontiers 2005, Advances in Deep Foundations*, Austin, Texas, USA.
Lehane, B., O'Loughlin, C., Gaudin, C., and Randolph, M. (2009). "Rate effects on penetrometer resistance in kaolin." *Géotechnique*, 59(1), 41.
Lemos, L. J. L., and Vaughan, P. R. (2000). "Clay–interface shear resistance." *Géotechnique*, 50(1), 55-64.
Leonard, J. W. (1988). "Tension structures: Behavior and analysis."
Low, B., Tang, S., and Choa, V. (1994). "Arching in piled embankments." *Journal of Geotechnical Engineering*, 120(11), 1917-1938.
Mandel, J. (1953). "Consolidation Des Sols (Étude Mathématique)." *Géotechnique*, 3(7), 287-299.
Marston, A., and Anderson, A. (1913). "The Theory of Loads on Pipes in Ditches And Tests of Cement and Clay Drain Tile and Sewer Pipe." Iowa Engineering Experiment Station, Ames Hill, New York.
Martin, C., and Randolph, M. (2006). "Upper-bound analysis of lateral pile capacity in cohesive soil." *Géotechnique*, 56(2), 141-145.
McGuire, M. P. (2011). "Critical height and surface deformation of column-supported embankments." PhD thesis, Virginia Polytechnic Institute and State University.
Meyerhof, G. (1951). "The ultimate bearing capacity of foudations." *Géotechnique*, 2(4), 301-332.
Michalowski, R. L., Wojtasik, A., Duda, A., Florkiewicz, A., and Park, D. (2018). "Failure and Remedy of Column-Supported Embankment: Case Study." *Journal of Geotechnical and Geoenvironmental Engineering*, 144(3), 05017008.

Mitchell, J. K., and Soga, K. (2005). "Fundamentals of soil behavior." John Wiley & Sons, New York, USA.
Morton, J., O'Loughlin, C., and White, D. (2014). "Strength assessment during shallow penetration of a sphere in clay." *Géotechnique Letters*, 4(4), 262-266.
Mroueh, H., and Shahrour, I. (2002). "Three ‐ dimensional finite element analysis of the interaction between tunneling and pile foundations." *International Journal for Numerical and Analytical Methods in Geomechanics*, 26(3), 217-230.
Muir Wood, D. (2004). "Geotechnical modelling." Spon Press, New York, USA.
Naughton, P. (2007). "The significance of critical height in the design of piled embankments." *Proceedings of Geo-Denver*, Denver, CO, USA, ASCE.
O'Beirne, C., O'Loughlin, C., and Gaudin, C. (2015). "Soil response in the wake of dynamically installed projectiles." *Géotechnique Letters*, 5(3), 153-160.
Oh, Y. I., and Shin, E. C. (2007). "Reinforcement and arching effect of geogrid-reinforced and pile-supported embankment on marine soft ground." *Marine Georesources and Geotechnology*, 25(2), 97-118.
Okyay, U., Dias, D., Thorel, L., and Rault, G. (2014). "Centrifuge modeling of a pile-supported granular earth-platform." *Journal of Geotechnical and Geoenvironmental Engineering*, 140(2), 1-12.
Ovesen, N. K. (1979). "The scaling law relationship." *Proceedings of 7th European conference on soil mechanics and foundation engineering*, London, UK, Britsh Geotechnical Society, 319-323.
Pearlman, S., and Porbaha, A. (2006). "Design and monitoring of an embankment on controlled modulus columns." *Journal of the Transportation Research Board*, 1975, 96-103.
Perkins, S. W., and Madson, C. R. (2000). "Bearing capacity of shallow foundations on sand: A relative density approach." *Journal of geotechnical and geoenvironmental engineering*, 126(6), 521-530.
Petrovic, A., Siebert, J., and Rieke, P. (1982). "Soil bulk density analysis in three dimensions by computed tomographic scanning." *Soil Science Society of America Journal*, 46(3), 445-450.
Plaut, R., and Filz, G. (2010). "Analysis of geosynthetic reinforcement in pile-supported embankments. Part III: Axisymmetric model." *Geosynthetics International*, 17(2), 77-85.
Potts, V., and Zdravkovic, L. (2010). "Finite-element study of arching behaviour in reinforced fills." *Proceedings of the Institution of Civil Engineers - Ground Improvement*, 163(4), 217-229.
Poulos, H. (1997). "Behaviour of pile groups with defective piles." *Proceedings of 14th International Conference on Soil Mechanics and Foundation Engineering*, Hamburg, Germany, 871-876.
Poulos, H. G. (2005). "Pile Behavior—Consequences of Geological and Construction Imperfections." *Journal of geotechnical and geoenvironmental engineering*, 131(5), 538-563.
Poulos, H. G. (2008). "A practical design approach for piles with negative friction." *Proceedings of the Institution of Civil Engineers - Geotechnical Engineering*, 161(1), 19-27.
Poulos, H. G., and Davis, E. H. (1974). "Elastic solutions for soil and rock mechanics." John Wiley & Sons, New York, USA.
Raffel, M., Willert, C. E., Wereley, S. T., and Kompenhans, J. (2007). "Particle Image Velocimetry 2nd eds." Springer, Berlin, Germany.
Randolph, M., and Hope, S. (2004). "Effect of cone velocity on cone resistance and excess pore pressures." *Proceedings of International Symposium on Engineering Practice and Performance of Soft Deposits*, Osaka, Japan, 147-152.
Randolph, M., and House, A. (2001). "The complementary roles of physical and computational modelling." *International journal of physical modelling in geotechnics*, 1(1), 1-8.
Randolph, M. F., Low, H. E., and Zhou, H. (2007). "In situ testing for design of pipeline and anchoring systems." *Proceedings of Offshore Site Investigation and Geotechnics, Confronting New Challenges and Sharing Knowledge*, London, UK, Society of Underwater Technology.
Rault, G., Thorel, L., Neel, A., Buttigieg, S., Derkx, F., Six, G., and Okyay, U. (2010). "Mobile tray for simulation of 3D load transfer in pile-supported earth platforms." *Proceedings of International Conference on Physical Modelling in Geotechnics*, Zurich, Switzerland, Taylor and Francis, London, 261-266.

Rogbeck, Y., Alén, C., Franzén, G., Kjeld, A., Oden, K., Rathmayer, H., Want, A., and Oiseth, E. (2003). "Nordic guidelines for reinforced soils and fills." Nordic Geosynthetic Group & Nordic Industrial Fund, Sweden.

Roscoe, K. H., Schofield, A. N., and Wroth, C. P. (1958). "On The Yielding of Soils." *Géotechnique*, 8(1), 22-53.

Rowe, P. W. (1962). "The stress-dilatancy relation for static equilibrium of an assembly of particles in contact." *Proceedings of the Royal Society of London A*, 269(1339), 500-527.

Roy, M., Tremblay, M., Tavenas, F., and Rochelle, P. L. (1982). "Development of pore pressures in quasi-static penetration tests in sensitive clay." *Canadian Geotechnical Journal*, 19(2), 124-138.

Rui, R., Van Tol, A., Xia, Y., Van Eekelen, S., and Hu, G. (2016). "Investigation of soil-arching development in dense sand by 2D model tests." *Geotechnical Testing Journal*, 39(3), 415-430.

Russell, D., Naughton, P., and Kempton, G. (2003). "A new design procedure for piled embankments." *Proceedings of 56th Canadian Geotechnical Conference*, Winnipeg, Canada, 858-865.

Russell, D., and Pierpoint, N. (1997). "An assessment of design methods for piled embankments." *Ground Engineering*, 30(10).

Sahdi, F., Gaudin, C., White, D. J., and Boylan, N. (2014). "Interpreting T-bar tests in ultra-soft clay." *International Journal of Physical Modelling in Geotechnics*, 14(1), 13-19.

Santichaianaint, K. (2002). "Centrifuge modeling and analysis of active trapdoor in sand." PhD thesis, University of Colorado at Boulder.

Scarano, F., and Riethmuller, M. L. (1999). "Iterative multigrid approach in PIV image processing with discrete window offset." *Experiments in Fluids*, 26(6), 513-523.

Schanz, T., and Vermeer, P. (1996). "Angles of friction and dilatancy of sand." *Géotechnique*, 46(1), 145-151.

Schanz, T., Vermeer, P., and Bonnier, P. (1999). "The hardening soil model: formulation and verification." *Proceedings of Beyond 2000 in computational geotechnics*, Amsterdam, The Netherlands, 281-296.

Schneebeli, G. (1957). "Une analogie mécanique pour l'étude de la stabilité des ouvrages en terrea deux dimensions'." *Proceedings of 4th International Conference on Soil Mechanics and Foundation Engineering*, London, UK, 228-232.

Sliwinski, Z., and Fleming, W. (1983). "The integrity and performance of bored piles." *Proceedings of International conference on advances in piling and ground treatment for foundations*, London, United Kingdom, Thomas Telford Publishing, 211-223.

Sloan, J. A. (2011). "Column-supported embankments: full-scale tests and design recommendations." PhD thesis, Virginia Polytechnic Institute and State University.

Smith, M., and Filz, G. (2007). "Axisymmetric numerical modeling of a unit cell in geosynthetic-reinforced, column-supported embankments." *Geosynthetics International*, 14(1), 13-22.

Smith, M. E. (2005). "Design of bridging layers in geosynthetic-reinforced column-supported embankments." PhD thesis, Virginia Polytechnic Institute and State University.

Spangler, M. G., and Handy, R. L. (1973). "Soil engineering." Intext Press Inc., New York.

Springman, S., Bolton, M., Sharma, J., and Balachandran, S. (1992). "Modelling and instrumentation of a geotextile in the geotechnical centrifuge." *Proceedings of International Symposium on Earth Reinforcement Practice*, Kyushu, Japan.

Stanier, S., and White, D. (2013). "Improved image-based deformation measurement in the centrifuge environment." *Geotechnical Testing Journal*, 36(6), 915-928.

Stewart, D., and Randolph, M. (1994). "T-bar penetration testing in soft clay." *Journal of Geotechnical Engineering*, 120(12), 2230-2235.

Stewart, D. P. (1992). "Lateral loading of piled bridge abutments due to embankment construction." PhD thesis, Department of Civil Engineering, University of Western Australia.

Stone, K., and Wood, D. M. (1992). "Effects of dilatancy and particle size observed in model tests on sand." *Soils and Foundations*, 32(4), 43-57.

Stuart, J. (1962). "Interference between foundations, with special reference to surface footings in sand." *Géotechnique*, 12(1), 15-22.

Sully, J. P., Robertson, P. K., Campanella, R. G., and Woeller, D. J. (1999). "An approach to evaluation of field CPTU dissipation data in overconsolidated fine-grained soils." *Canadian geotechnical journal*, 36(2), 369-381.

Tanaka, T., and Sakai, T. (1993). "Progressive failure and scale effect of trap-door problems with granular materials." *Soils and Foundations*, 33(1), 11-22.

Teh, C., and Houlsby, G. (1991). "Analytical study of the cone penetration test in clay." *Géotechnique*, 41(1), 17-34.

Terzaghi, K. (1936). "Stress distribution in dry and in saturated sand above a yielding trap-door." *Proceedings of 1st International Conference of Soil Mechanics and Foundation Engineering*, Harvard University, Cambridge, USA.

Terzaghi, K. (1943). "Theoretical soil mechanics." John Wiley and Sons, New York, USA.

Van Eekelen, S. J. M., Bezuijen, A., and Alexiew, D. (2010). "The Kyoto Road Piled Embankment: 3/2 Years of Measurements." *Proceedings of 9th International Conference on Geosynthetics*, Guaruja, Brazil, 1941-1944.

Van Eekelen, S. J. M., Bezuijen, A., Lodder, H. J., and van Tol, A. F. (2012a). "Model experiments on piled embankments. Part I." *Geotextiles and Geomembranes*, 32, 69-81.

Van Eekelen, S. J. M., Bezuijen, A., Lodder, H. J., and van Tol, A. F. (2012b). "Model experiments on piled embankments. Part II." *Geotextiles and Geomembranes*, 32, 82-94.

Van Eekelen, S. J. M., Bezuijen, A., and Van Tol, A. F. (2011). "Analysis and modification of the British Standard BS8006 for the design of piled embankments." *Geotextiles and Geomembranes*, 29(3), 345-359.

Van Eekelen, S. J. M., Bezuijen, A., and Van Tol, A. F. (2013). "An analytical model for arching in piled embankments." *Geotextiles and Geomembranes*, 39, 78-102.

Van Eekelen, S. J. M., Bezuijen, A., and van Tol, A. F. (2015). "Validation of analytical models for the design of basal reinforced piled embankments." *Geotextiles and Geomembranes*, 43(1), 56-81.

Van Langen, H., and Vermeer, P. (1991). "Interface elements for singular plasticity points." *International journal for numerical and analytical methods in geomechanics*, 15(5), 301-315.

Vardoulakis, I. (1980). "Shear band inclination and shear modulus of sand in biaxial tests." *International Journal for Numerical and Analytical Methods in Geomechanics*, 4(2), 103-119.

Vardoulakis, I., Graf, B., and Gudehus, G. (1981). "Trap‐door problem with dry sand: A statical approach based upon model test kinematics." *International Journal for Numerical and Analytical Methods in Geomechanics*, 5(1), 57-78.

Vermeer, P. (1990). "The orientation of shear bands in biaxial tests." *Géotechnique*, 40(2), 223-236.

Vesic, A. B. (1963). "Bearing capacity of deep foundations in sand." *Highway Research Board, National Academy of Sciences*, 39.

Vesic, A. S. (1973). "Analysis of ultimate loads of shallow foundations." *Journal of Soil Mechanics and Foundations Division, ASCE*, 99(1), 45-73.

Villard, P., Le Hello, B., Chew, S., Nancey, A., Delmas, P., Loke, K., and Mannsbart, G. (2004). "Use of high strength geotextiles over piles results from a full scale test'." *Proceedings of 3rd European Geosynthetics Conference*, Munich, Germany.

Viswanadham, B., and König, D. (2004). "Studies on scaling and instrumentation of a geogrid." *Geotextiles and Geomembranes*, 22(5), 307-328.

Watson, P. G. (1999). "Performance of skirted foundations for offshore structures." PhD thesis, University of Western Australia.

Weber, T. M., Laue, J., and Springman, S. M. (2006). "Centrifuge modelling of sand compaction piles in soft clay under embankment load." *Proceedings of 6th International Conference on Physical Modelling in Geotechnics*, Hong Kong, 603-608.

Weiler, W. A., and Kulhawy, F. H. (1982). "Factors affecting stress cell measurements in soil." *Journal of the Geotechnical Engineering Division*, 108(12), 1529-1548.

Wellington, S. L., and Vinegar, H. J. (1987). "X-ray computerized tomography." *Journal of Petroleum Technology*, 39(08), 885-898.

Westerweel, J., and Scarano, F. (2005). "Universal outlier detection for PIV data." *Experiments in Fluids*, 39(6), 1096-1100.

White, D., and Take, W. (2005). "Discussion on “Application of Particle Image Velocimetry (PIV) in centrifuge testing of uniform clay”." *International Journal of Physical Modelling in Geotechnics*, 5(4), 27-31.
White, D. J., Take, W. A., and Bolton, M. D. (2003). "Soil deformation measurement using particle image velocimetry (PIV) and photogrammetry." *Géotechnique*, 53(7), 619-632.
Więckowski, Z. (2004). "The material point method in large strain engineering problems." *Computer Methods in Applied Mechanics and Engineering*, 193(39-41), 4417-4438.
Wong, E. Y.-w. (2004). "Behaviour of large-diameter bored pile groups with defects." M.Phil., Hong Kong University of Science and Technology.
Wong, P., and Muttuvel, T. (2012). "Design of embankments supported on controlled modulus columns." *International Journal of Geotechnical Engineering*, 6(2), 207-213.
Xing, H., Zhang, Z., Liu, H., and Wei, H. (2014). "Large-scale tests of pile-supported earth platform with and without geogrid." *Geotextiles and Geomembranes*, 42(6), 586-598.
Xradia. 2011. XMReconstructor Cone Beam 10, Xradia. Inc, Pleasanton, California, USA.
Xu, C., Song, S., and Han, J. (2016). "Scaled model tests on influence factors of full geosynthetic-reinforced pile-supported embankments." *Geosynthetics International*, 23(2), 140-153.
Yamaguchi, H., Kimura, T., and Fuji, N. (1976). "On the influence of progressive failure on the bearing capacity of shallow foundations in dense sand." *Soils and Foundations*, 16(4), 11-22.
Yin, J.-H., and Zhu, J.-G. (1999). "Elastic viscoplastic consolidation modelling and interpretation of pore-water pressure responses in clay underneath Tarsiut Island." *Canadian Geotechnical Journal*, 36(4), 708-717.
Zaeske, D. (2001). "Zur Wirkungsweise von unbewehrten und bewehrten mineralischen Tragschichten über pfahlartigen Gründungselementen (in German)." Univeristy Kassel, Hesse, Germany.
Zhang, L., and Wong, E. Y. (2007). "Centrifuge modeling of large-diameter bored pile groups with defects." *Journal of Geotechnical and Geoenvironmental Engineering*, 133(9), 1091-1101.
Zhuang, Y., and Ellis, E. (2014). "Finite-element analysis of a piled embankment with reinforcement compared with BS 8006 predictions." *Géotechnique*, 64(11), 910-917.
Zhuang, Y., Ellis, E., and Yu, H. (2012). "Three-dimensional finite-element analysis of arching in a piled embankment." *Géotechnique*, 62(12), 1127.
Zhuang, Y., Ellis, E. A., and Yu, H.-S. (2010). "Plane strain FE analysis of arching in a piled embankment." *Proceedings of the Institution of Civil Engineers - Ground Improvement*, 163(4), 207-215.